Université d'Ottawa · University of Ottawa

CHARACTERIZATION AND APPLICATION OF OPTICAL FIBERS

1. Application of Optical Fibers in Gas Concentration and Radiation Dose Measurements

2. Polarization Effects in Fiber Communication Systems

By

Ping Lu

Thesis submitted to
the Faculty of Graduate and Postdoctoral Studies
in partial fulfillment of the requirements for the Degree of
DOCTOR OF PHILOSOPHY

Ottawa-Carleton Institute for Physics
University of Ottawa
Ottawa, Canada
October 2001

Abstract

The thesis consists of two research directions: Optical fiber applications in gas concentration and radiation dose measurements; and polarization effects in fiber optic communication systems.

Part I of the thesis presents two optical fiber applications. 1) An infrared (IR) fiber bundle has been designed and fabricated to measure gas concentrations in a chemical vapor deposition (CVD) chamber using Fourier transform infrared spectroscopy. This fiber bundle covers the IR range from 0.5 to 20 μm and reduces the light beam divergence in the CVD chamber, which makes it possible to measure gas concentrations in a region near the substrate surface. Semi-ellipsoid mirrors have been designed and used to increase the collection efficiency of infrared radiation and to compensate the loss introduced by the fiber bundle. 2) A fiber optic radiation sensor based on radiation-induced fiber loss is reported. The gamma radiation-induced loss spectra in various fibers have been studied. Among all the fibers tested, 5% P-doped fiber shows the highest sensitivity to gamma radiation. The wavelength and dose rate dependence of radiation-induced loss in 5% P-doped fiber are investigated and the possibility of using this fiber as a radiation sensor for radiation therapy is discussed.

Part II of the thesis examines two polarization effects, polarization mode dispersion (PMD) and polarization dependent loss (PDL), in fiber optic communication systems based on the waveplate models. A new waveplate model, capable of generating any PMD and PDL values, is proposed to overcome the limitations of the conventional waveplate model. Using both models the statistical distributions of PDL and differential group delay (DGD) have been studied considering the presence of biased elliptical birefringence. The principal state of polarization (PSP) of an optical pulse is proposed for a fiber having both PMD and PDL. PMD and PDL of a pulse for a fiber consisting of two polarization maintaining fiber segments are calculated, and the pulse distortions due to PMD and PDL are analyzed. PMD and PDL impact on digital communication systems have been studied in terms of system Q factor, bit error rate (BER) and system outage probability. The acceptable PMD values in a system with PDL are discussed for various power margins. The Q factor distributions due to PDL and its combination with PMD have been measured experimentally and compared to numerical simulations.

Acknowledgements

I would like to thank my supervisors, Dr. Xiaoyi Bao and Dr. Liang Chen, for their guidance with this research. Their encouragement and support are very much appreciated.

I would like to thank Prosensys Inc., Saint John Regional Hospital and NBTel, and in particular Dr. Tom Whidden, Mr. Narayan Kulkarni, Mr. John Stears and Dr. Roger Cormier, for their collaboration in this work.

I want to thank Mr. Donald Hornibrook at UNB for machining the ellipsoid mirrors and fiber connectors. I also want to thank Dr. Alexander Tomashuk at General Physics Institute (Russia) and Prof. Abraham Katzir at Tel Aviv University (Israel) for providing optical fibers.

I appreciate the financial support from Prosensys Inc, NBTel, NSERC, CIPI, CFI and Univ. of Ottawa. I also appreciate the support of equipment from Gamble Technologies Limited, Agilent Technologies, NBTel and Prosensys Inc.

I would like to thank all members in our fiber optics group, and in particular Mr. David Waddy, my research partner.

Finally, I would like to thank my wife, Dongmei, my son, Dajian, and other relatives for their understanding and patience throughout the years.

Contents

List of Figures

List of Tables

List of Acronyms

BER	bit error rate
CCD	charge-coupled device
CVD	chemical vapor deposition
DGD	differential group delay
DOP	degree of polarization
DTGS	deuterated triglycine sulfate
EDFA	erbium-doped fiber amplifier
FBG	fiber Bragg grating
FT-IR	Fourier transform infrared
FUT	fiber under test
IM-DD	intensity modulation with direct detection
I/O	input/output
IR	infrared
JME	Jones matrix eigenanalysis
KRS-5	$TlBr_{0.5}I_{0.5}$
LED	light emission device
MCT	mercury cadmium telluride
MM	multimode
NBOHC	non-bridging oxygen hole center
NEP	noise equivalent power
OADM	optical add-drop multiplexer
OC	optical carrier
PDF	probability density function
PDL	polarization dependent loss
PMD	polarization mode dispersion

PMF	polarization maintaining fiber
POHC	phosphorus-oxygen-hole center
PSP	principal state of polarization
rms	root mean square
SM	single-mode
SNR	signal to noise ratio
SOP	state of polarization
TEOS	tetraethoxysilane
UV	Ultraviolet
WDM	wavelength division multiplexing

Chapter 1

Introduction

This thesis consists of two research directions: 1) Optical fiber applications for gas concentration and radiation dose measurements; and 2) Polarization effects in fiber optic communication systems. The first part has been carried out in collaboration with Prosensys Inc. and Saint John Regional Hospital, and the second part has been conducted in collaboration with NBTel.

The first research direction is mainly experimental work done to solve the problems faced by the specific needs of industries and hospitals. The motivation of the development of infrared (IR) fiber bundles is to overcome the drawbacks of the current sensing system that limits the realization of real time monitoring and control of thin film deposition on large substrates. In semiconductor industry the technique of Fourier transform infrared (FT-IR) spectroscopy is used to monitor the chemical processes in the chemical vapor deposition (CVD) chamber, where the thin film is deposited on the substrate. The process is as follows: the IR light beam from a FT-IR spectrometer is launched into a CVD chamber. After interacting with reactive gases in the chamber the IR light beam is collected by a photodetector at the distal side of the chamber. The gas concentrations therein are measured to control incoming gas flows (tetraethoxysilane and Ozone). There are a few drawbacks of the current system that limit the real-time monitoring and control of thin film deposition quality, especially for large substrates (diameter larger than 300 mm) [1, 2]. The first drawback is the low collecting efficiency of IR radiation from the light source (< 4%). The signal to noise ratio (SNR) of the whole system is proportional to this efficiency. Consequently, high SNR is required for short signal processing time. The total thin film deposition time can be as short as 3 minutes, but the current system

needs about 30 seconds to obtain one absorption spectrum (16 scans). Clearly, the current system is not suitable for real-time control. Another drawback of the current system is the large divergence angle of the IR light beam in the chamber. It has been shown that the reactive gases, which determine the thin film quality, are distributed near the substrate surface (within a few millimeters above the substrate) [3]. When a highly divergent light beam passes near the substrate, it will be either blocked or reflected by the substrate and therefore cannot be collected by the photodetector. Other drawbacks such as the difficulty of optical alignment and system inflexibility will be discussed in chapter 3. To solve these problems, we proposed the following system improvements: 1) Semi-ellipsoid mirrors are designed and machined to improve the collecting efficiency of IR radiation from the light source, and 2) IR fiber bundles are designed and fabricated to link the FT-IR spectrometer to the CVD chamber. This link reduces the divergence angle of the light beam in the chamber and makes the optical alignment easier.

This thesis also presents the study of gamma radiation effects in various optical fibers. The radiation effects in optical fibers have been studied for two reasons: 1) To study the performance of fiber optic data transmission under radiation fields, and 2) To explore the potential of using optical fibers as radiation dosimeters, which is the focus of the research of this thesis. The radiation damage suffered by lead glass, Ge-doped silica and pure silica fibers has been investigated [4, 5]. In this study, the dose rate dependence, wavelength dependence and the recovery of radiation-induced loss in various optical fibers are studied to determine their effects on radiation dose measurement. As a result, the radiation-induced loss spectra of normal single-mode (SM), normal multi-mode (MM), P-doped and Ge-doped fibers are measured. At certain wavelengths the radiation-induced loss in P-doped fiber is linear with the total absorbed dose and is independent of dose rate. The sensitivity of P-doped fiber to gamma radiation is more than 100 times higher than that of normal SM fiber (SMF28). This suggests that P-doped fiber is a good candidate for radiation dose measurement with high sensitivity and large dynamic range.

The second research direction focuses on investigating the polarization effects in fiber optic communication systems. The fundamental limitations of a fiber optic communication system

include fiber loss, chromatic dispersion and some nonlinear effects when the bit rate is relatively low (2.5 Gbits/second or lower) [6]. With the development of high bit rates (≥ 10 Gbits/second) and more complex fiber optic communication systems, polarization mode dispersion (PMD) and polarization dependent loss (PDL) become additional obstacles [7-9]. PMD introduces pulse broadening [10] and it can be up to 20 ps in installed fibers [11]. PDL causes power fluctuation and it can be up to 0.4 dB in fiber components [12-14]. The interaction of PMD and PDL causes further system impairments [9, 13]. Due to the stochastic perturbations of environmental factors, such as temperature and vibration, PMD and PDL have been studied statistically and can be described in the following aspects:

1) PMD is expressed by principal states of polarization (PSP's) and differential group delay (DGD), where DGD is the difference of time delays when lightwave transmits along the two orthogonal PSP's. Both PSP and DGD are wavelength and time dependent. The average of DGD over wavelength or time is called PMD [7, 15].
2) The statistical distribution of DGD is Maxwellian without PDL, and it is the combination of Gaussian and Maxwellian with high PDL [16, 17].
3) Due to the interaction of PMD and PDL there are some anomalous phenomena, such as pulse narrowing with finite DGD and pulse broadening with zero DGD [18, 19].
4) System impact due to PMD has been studied both in the analog and digital systems. For analog systems it has been shown that the pulse broadening due to PMD is a Rayleigh distribution [20]. For digital systems the impact of PMD has been studied in terms of system outage probability [8] and the statistical distributions of eye-opening [11] and Q factor [21].

Due to the mode-coupling effect in single-mode fibers, most studies of PMD and PDL are based on the use of a waveplate model [8, 9, 12, 13, 15, 17-19, 22-24], where a fiber is treated as a concatenation of N polarization maintaining fiber (PMF) segments. The DGD of each PMF segment is uniformly distributed within a finite range. However, this waveplate model has upper limits of DGD and PDL. The maximum DGD (or PDL) value can be generated by this model is $N \cdot \beta_{max}$ (or $N \cdot \alpha_{max}$), where β_{max} (or α_{max}) is the maximum DGD (or PDL) in each

PMF segment. As a result this model yields zero probability in the DGD (or PDL) range exceeding $N \cdot \beta_{max}$ (or $N \cdot \alpha_{max}$). This would induce errors in examining the system impact due to PMD because high BER occurs for large DGD (or PDL) values. Considering this limitation of the conventional waveplate model, a new waveplate model is proposed in this thesis. In the new model, the range of DGD values for each PMF segment is unlimited. In addition, the birefringence of each PMF segment is assumed to be elliptical. Using both waveplate models, the statistical DGD distributions are examined in chapter 7. So far the statistical properties of PDL have not been studied theoretically. In chapter 8, the statistical PDL distributions are studied for the first time using both waveplate models. The influence of PMD on PDL distribution is studied as well.

Previous studies of PMD and PDL are based on the concepts of PSP, DGD and PDL for one single frequency. However, they are all frequency dependent. It is worthwhile to study the PSP, PMD and PDL for an optical pulse spectrum range, rather than one single frequency. The concepts of PSP, PMD and PDL for an optical pulse are proposed in chapter 9. It is found that for a fiber consisting of two PMF segments, the effective PMD of a pulse can be either larger than the sum of the two DGDs of the two PMF segments or less than the DGD difference of the two PMF segments, depending on the pulse width. The effective PDL of a pulse can be less than the PDL difference of the two PMF segments.

The system impact due to PMD and PDL has been studied extensively, which include PMD and PDL induced pulse broadening [9, 20], system PMD limitation in the presence of chromatic dispersion and frequency chirp [8, 23], statistical distribution of Q factor in the presence of PMD [21] and system outage probability due to PMD [8]. So far the system impacts due to PDL alone and the combination of PMD and PDL have not been studied quantitatively in terms of system outage probability [8] and system PMD limitation in the presence of PDL. In chapter 10, the statistical distributions of both Q factor and BER due to PMD, PDL and their combination are studied. The system outage probabilities due to PMD and PDL are examined at various power margins and the system PMD limitation in the presence of PDL is discussed. The

Q factor distributions in the presence of PDL and its combination with PMD are measured experimentally and compared with numerical simulations.

The thesis is organized as follows:

- **Chapter 1** is the introduction of the thesis (this chapter).

Part 1: Application of optical fibers in gas concentration and radiation dose measurements

- **Chapter 2** presents the principles of FT-IR spectroscopy, chemical processes of thin film deposition in a CVD chamber, infrared fiber properties and radiation effects in optical fibers. This chapter provides background information related to part 1 of the thesis.
- **Chapter 3** describes the current system configuration used for monitoring the chemical processes in a CVD chamber using FT-IR spectroscopy. The limitations of the current configuration for real-time control of thin film deposition on large substrates are discussed.
- **Chapter 4** describes the system improvements for measuring gas concentrations in a CVD chamber. The improvements include the using of a semi-ellipsoid mirror to increase the light collection efficiency and an IR fiber bundle to decrease the beam divergence in the CVD chamber. Experiment results with the improved system are presented.
- **Chapter 5** presents the studies of gamma radiation effects in various optical fibers. Details concerning the experiment configuration, measurement results and data processing are included. The possibility of using P-doped silica fibers as fiber optic radiation dosimeters is discussed.

Part 2: Polarization effects in fiber optic communication systems

- **Chapter 6** provides an introduction to PMD and PDL effects in fiber optic communication systems.
- **Chapter 7** examines the statistics of DGD. A new waveplate model is proposed in this chapter to overcome the limitations of the conventional waveplate model. The statistical distributions of DGD in the presence of PDL and biased birefringence are studied.
- **Chapter 8** examines numerically the statistical distribution of PDL in the presence of PMD for the first time. The new model proposed in chapter 7 is used as well. The difference of PDL distributions using the two waveplate models are compared.
- **Chapter 9** presents the concepts of PSP, PMD and PDL for an optical pulse. The effective PMD and PDL of a pulse for a fiber consisting of two PMF segments are calculated. Pulse broadenings when pulses are launched to different PSP's are discussed.
- **Chapter 10** studies the impact of PMD and PDL on an *intensity modulation with direct detection* (IM-DD) fiber optic communication system (10 Gbits/second). The Q factor distribution and system outage probability due to PMD and PDL are studied. The system PMD limitations in the presence of PDL with various power margins are discussed.
- **Chapter 11** is the summary of the thesis and suggestions for future work.

Chapter 2

Overview of the Current Studies of Thin Film Deposition Monitoring and Fiber Optic Radiation Sensors

2.1 Introduction

The research described in part 1 has been conducted in collaboration with Prosensys Inc. and Saint John Regional Hospital. In this study, optical fibers have been used for gas concentration measurements in a chemical vapor deposition (CVD) chamber, and also for measuring radiation doses commonly used in radiation therapy.

Section 2.2 describes the basic principles of Fourier transform infrared (FT-IR) spectroscopy. The infrared (IR) light sources and detectors used in FT-IR spectroscopy are described in section 2.3. The chemical processes of thin film deposition in a CVD chamber and the absorptions of reactive gases in the middle IR are introduced in section 2.4. The chemical, optical and mechanical properties of IR fibers are introduced in section 2.5. Section 2.6 briefly introduces the phenomenon of radiation-induced attenuation in optical fibers and section 2.7 presents the research efforts on fiber optic radiation dosimeters. These sections are intended to provide the fundamental issues relevant to the first part of this thesis.

2.2 FT-IR spectrometer

Most interferometers used in IR spectrometry today are based on the Michelson interferometer, which was originally designed by Michelson in 1891 [25]. In a Michelson interferometer, a light beam is split into two paths and then recombined after a certain path

difference. Fig. 2.1 shows the simplest configuration of a Michelson interferometer consisting of two perpendicular mirrors; one is fixed and the other is movable. When the movable mirror is moved at a constant velocity, the intensity at the detector has both constant (DC) and modulated (AC) components. For a broadband IR light source and a 50:50 beam splitter, the AC component, $I(\delta)$, can be written as [25]

$$I(\delta) = \int_{-\infty}^{+\infty} B(\bar{\upsilon})\cos(2\pi\bar{\upsilon}\delta)\cdot d\bar{\upsilon}, \tag{2.1}$$

where δ is the path difference of the two beams, $\bar{\upsilon}$ is the wavenumber (reciprocal of wavelength λ) and $B(\bar{\upsilon})$ is the spectral intensity at wavenumber $\bar{\upsilon}$. From Eq. 2.1 the spectral intensity, $B(\bar{\upsilon})$, can be obtained by the following Fourier transform:

$$B(\bar{\upsilon}) = \int_{-\infty}^{+\infty} I(\delta)\cos(2\pi\bar{\upsilon}\delta)\cdot d\delta = 2\int_{0}^{+\infty} I(\delta)\cos(2\pi\bar{\upsilon}\delta)\cdot d\delta. \tag{2.2}$$

For the absorbance measurement of a sample, the spectral intensity $B(\bar{\upsilon})$ before the sample is placed in front of the detector is measured first. Then the sample is placed just at the front of the detector and the spectrum intensity $B'(\bar{\upsilon})$ is measured. The absorbance spectrum $A(\bar{\upsilon})$ of the sample is

$$A(\bar{\upsilon}) = 1 - \frac{B'(\bar{\upsilon})}{B(\bar{\upsilon})}. \tag{2.3}$$

This is the ideal model of an FT-IR interferometer. In practice, the path difference between the light beams reflected back from the two mirrors cannot vary from zero to infinity and the beam splitting ratio is not exactly 50:50 for all wavelengths. For a practical FT-IR spectrometer, the spectrum signal to noise ratio (SNR) and the optical throughput must be considered. The optical throughput of an optical system (including FT-IR spectrometer) is defined as the product of the beam area and its solid angle at any focus [25]. In a spectrometer the throughput is limited by the mirror areas and the maximum angle allowed in the spectrometer, which is determined by its required spectral resolution [25]. The optical throughput of a detector is

determined by its area and its maximum acceptance angle, which is typically less than 45^0. For an optical system, the effective optical throughput is the minimum optical throughput of the components in the system.

The SNR of a FT-IR spectrometer can be expressed as [25, 26]

$$SNR = \frac{U_{\bar{\upsilon}}(T) \cdot \Theta \cdot \Delta\bar{\upsilon} \cdot t^{1/2} \cdot \xi}{NEP}, \tag{2.4}$$

where $U_{\bar{\upsilon}}(T)$ is the spectral energy density of the light source at wavenumber $\bar{\upsilon}$ and temperature T, Θ is the optical throughput of the spectrometer, $\Delta\bar{\upsilon}$ is the resolution of the spectrometer, t is the measurement time, ξ is the total system efficiency ($\xi < 1$) and NEP is the noise equivalent power of the detector. Eq. 2.4 shows that the SNR of an FT-IR spectrometer is proportional to its optical throughput and the spectral energy density of the source.

2.3 IR light sources and detectors

The IR light sources (Glowbars) used for FT-IR spectroscopy have a broadband IR spectrum range. They are essentially resistors made of SiC and other materials possessing high emission coefficients in the IR. The IR spectral energy density of the source can be treated like a blackbody and may be written as [27]

$$U_{\bar{\upsilon}}(T) = \varepsilon_{\bar{\upsilon}} \frac{C_1 \bar{\upsilon}^3}{\exp(C_2 \bar{\upsilon} / T) - 1} \qquad \left(W / sr \cdot cm^2 \cdot cm^{-1}\right), \tag{2.5}$$

where $\varepsilon_{\bar{\upsilon}}$ is the spectral radiation coefficient, T is the temperature of the glowbar in Kelvin, and C_1 and C_2 are the first and the second radiation constants respectively. The total optical power emitting from the glowbar is (Stefan-Boltzmann law)

$$P = \varepsilon\sigma T^4 \cdot A_{glowbar}, \tag{2.6}$$

where $A_{glowbar}$ is the area of the source, ε (<1) is the source emissivity and σ is the Stefan-Boltzmann constant (σ=5.67 x 10^{-8} J $m^{-2}s^{-1}K^{-4}$). For a glowbar, the values of $\varepsilon_{\tilde{\nu}}$ and ε vary within the 0.8 to 0.95 range.

The detectors used for FT-IR spectroscopy are made of mercury cadmium telluride (MCT) and pyroelectric deuterated triglycine sulfate (DTGS). The advantages of MCT detectors are high detectivity, high optical absorption coefficient, high quantum efficiency and short response time [28-31]. They can detect IR radiation from 1 to 25 μm. However, MCT detectors require very low operating temperature to reduce their thermal noise, therefore liquid nitrogen is needed. Because of low price, wide spectral response range, room temperature operation, no wavelength selectivity, high detectivity and absorption coefficient, pyroelectric DTGS IR detectors are widely used for routine absorption and reflection spectrum measurements with FT-IR spectrometers [31, 32]. Compared to MCT photo detectors, the response time of DTGS detectors is longer and the detectivity is lower depending on the detector size and packaging. Both types of detectors are used for our experiments.

2.4 Absorptions of reactive gases in the middle IR

The reactive gases fed into the CVD chamber for silica thin film deposition on a wafer are Tetraethoxysilane (TEOS or $Si(OC_2H_5)_4$) and Ozone (O_3). Nitrogen gas is also fed into the chamber to change the chamber pressure. The chemical reactions to obtain silica film mainly include the following chemical processes [33]:

$$\begin{aligned}
(C_2H_5O)_3SiOC_2H_5 + O_3 &\rightarrow (C_2H_5O)_3SiOOC_2H_5 + O_2 \\
(C_2H_5O)_3SiOOC_2H_5 &\rightarrow (C_2H_5O)_3SiOH + C_2H_4O \\
C_2H_4O + O^- &\rightarrow CO + CO_2 + H_2O \\
(C_2H_5O)_3SiOH &\rightarrow SiO_2 + H_2O + CO_2
\end{aligned} \tag{2.7}$$

Most of these reactive gases and intermediates have strong absorptions in the near and middle IR spectrum region. Fig. 2.2 shows the absorbance spectra of TEOS and Ozone and Fig. 2.3 shows the absorption spectrum of fed gases and intermediates in the CVD chamber during thin film deposition [1, 2]. As evidenced by Figs. 2.2 and 2.3, the absorption peaks of gases in the CVD chamber occur within 600-4000 cm^{-1} (2-17 μm) range.

The current configuration used for measuring the gas concentrations in a CVD chamber is shown in Fig. 2.4. IR light beam from an FT-IR spectrometer is launched to the chamber through an IR glass window. After interacting with the reactive gases in the chamber the light beam reaches the IR detector located at the distal side of the chamber. The FT-IR spectrometer is attached to the CVD chamber directly to maintain a stable optical beam transmission path from the spectrometer to the detector. As will be discussed in chapter 3, large beam divergence and low light collection efficiency of the current configuration significantly limit the real-time monitoring of thin film deposition. We have improved the system by using IR fibers to link the spectrometer to the CVD chamber. The subsequent advantages of using IR fibers in the system are discussed in detail in chapter 4. In next section the properties of commonly used IR fibers will be introduced.

2.5 Properties of IR fibers

Commercially available IR fibers are chalcogenide fibers (As-Se-Te, As_2S_3, etc), fluoride glass fibers (CaF_2, MgF_2, and ZrF_4, etc) and halide fibers (NaCl, KCl and AgCl+AgBr, etc). The optical, mechanical and chemical properties of these IR fibers are introduced in this section.

Most chalcogenide fibers have good chemical properties including strong resistance to water and non-oxidizing acids. Although chalcogenide fibers have high transmission in the wavelength range from 1 to 6 μm, they have strong absorptions around 3 and 4 μm due to impurities such as water and H_2S in the chalcogenide glass [34]. A typical loss spectrum of chalcogenide glass (As_2S_3) is shown in Fig. 2.5 [35]. The refractive index of chalcogenide glass

varies from 2.1 to 2.9, which introduces a reflection loss from 23% to 42% (Fresnel reflection). The minimum bending radius of chalcogenide fiber is approximately 10 cm for a core diameter of 700 μm. The numerical aperture (N.A.) of chalcogenide varies from 0.5 to 0.7 [35].

Fluoride glass fibers are synthesized with compounds such as ZrF_4, HfF_4 and AlF_3. In order to make the fluoride glass stable, doping materials (BaF_4, LaF_3 etc) must also be added in the glass. The mechanical properties of fluoride glass fibers are inferior to those of chalcogenide and halide fibers. The minimum bending radius of fluoride glass fiber is about 10 cm for a core diameter of 250 μm. Hence, to have the same minimum bending radius the core diameter of fluoride fibers is smaller than those of chalcogenide and halide fibers. In some applications where large fiber diameters are needed, fluoride fiber bundles are used. Fluoride glass fibers can transmit light from visible to 3.5 μm wavelength range. Fig. 2.6 shows the attenuation spectrum of ZrF_4 [36]. The high transmission of fluoride fiber in the visible region makes it easier for optical alignment in our system. The refractive index of fluoride glass is ~ 1.5, which introduces a reflection loss of 9% at the fiber ends (Fresnel reflection). The numerical aperture of ZrF_4 fiber is 0.21 [36].

Halide crystalline fibers, such as KCl, KRS-5 ($TlBr_{0.5}I_{0.5}$) and silver halide ($AgCl_xBr_{1-x}$) are the most commonly used IR fibers for IR transmission beyond 10 μm. Unlike chalcogenide and fluoride glass fibers, halide materials are polycrystalline and they do not vitrify. KRS-5 and AgClBr fibers are extruded through a wire die by applying high pressure on the rods of these crystals. This method has some difficulties in making core-cladding structure. Hence, most halide fibers only have fiber core, the surrounding air acts as the fiber cladding. The transmittance of KRS-5 and AgClBr fibers in the IR are similar, see Fig. 2.7. Silver halide fibers have high transmission in the wavelength range from 3.5 to 20 μm [37]. The refractive index of silver halide is 2.4, which introduces a reflection loss of 43% at the fiber ends. Since the mechanical strength of KRS-5 fibers is not sufficient for practical use, silver halide fibers are the most widely used middle IR fibers in spectrum measurement and high power CO_2 laser delivery. However, silver halide crystal is not chemically stable, it reacts with most metals and

is UV sensitive (being darkened when exposed to UV light). Because of this drawback, silver halide fibers must be protected in black plastic tubings. Fortunately, the mechanical strength of silver halide fibers is strong enough for most industrial and laboratory applications. The minimum bending radius of silver halide fiber is less than 5 cm for a core diameter of 700 μm. The practical numerical aperture of silver halide fiber is 0.5 [37].

2.6 Radiation-induced attenuation in optical fibers

When optical fibers are exposed to nuclear or X-ray radiation, the losses in the fibers increase due to radiation induced ionization and formation of color centers [38, 39]. Color centers refer to the trapping of electrons or holes by the defects in fibers. This effect can strongly degrade fiber optic systems, such as fiber optic data transmission and fibroscopy in nuclear environments [40-42]. However, based on the dependence of fiber loss on radiation dose, this mechanism can be explored to fabricate fiber optic radiation sensors.

In the last two decades, much research work has been conducted to study the radiation effects in optical fibers for two main purposes. The first is to use optical fibers in the information transmission system under strong radiation fields where their radiation resistance is a key issue [40-42]. The second is to explore the possibility of using this effect to fabricate fiber optic radiation sensors under various radiation environments, such as nuclear site tanks and nuclear reactors where higher loss in fibers due to the radiation field is favored [4, 5, 43-45]. Compared to conventional dosimeters such as Si diodes and ionization chambers, the advantages of fiber optic dosimeters include high sensitivity, small size, distributed sensing capability and real-time measurements.

2.7 Current studies of fiber optic radiation sensors

Fiber optic methods of measuring radiation dose include radio-photo luminescence, thermo-luminescence, and radiation induced loss [43, 46]. Among these methods the radiation induced loss method has been widely studied because the following two reasons: 1) Free choice of

measurement wavelength and fiber material; and 2) Option of a distributed sensor. Optical fibers that have been tested for radiation measurement are mainly lead glass [43], Ge-doped silica [45] and pure silica fibers [4]. The radiation-induced losses in these fibers have been studied and their applications for radiation dose measurement have been investigated. So far, none have addressed the radiation dose measurements at low dose rates for the application in radiation therapy. For a practical fiber optic dosimeter based on the radiation-induced loss, characteristics such as sensitivity, wavelength, dose rate, temperature and loss recovery must be studied.

Sensitivity is defined in this thesis as the radiation-induced loss divided by the product of the total absorbed dose and the fiber length, i.e. $sensitivity = \alpha / D \cdot L$, in the unit of $dB/(m.Gy)$, where α is the radiation induced loss, D is the total dose and L is the fiber length. High sensitivity is one of the requirements of dosimeters used in radiation therapy because the total dose for a cancer patient is only 2 Gy per day. The radiation-induced loss is dependent on parameters such as wavelength, dose rate, and temperature. The strong wavelength dependence results from the different color centers, which give different absorption coefficients [47]. For rapidly decaying color centers, the associated radiation-induced losses are also dose rate dependent. This dose rate dependence is critical for dosimeter applications where the dose rate of the radiation field is unknown. The temperature dependence of radiation-induced loss is important for applications where fibers experience temperature fluctuations. For radiation therapy, this impact is insignificant as radiation rooms typically maintain stable operating temperatures. When the fiber is no longer exposed to radiation, its radiation-induced loss decreases with time, and this characteristic is known as the recovery of the fiber. This is caused by the decaying of color centers initially produced by the radiation-induced ionization in fibers.

In chapter 5, gamma radiation induced loss spectra in normal single-mode, normal multi-mode, P-doped and Ge-doped fibers are studied. The characteristics discussed above of P-doped fibers are examined and the possibility of using P-doped fibers as fiber optic dosimeters is discussed.

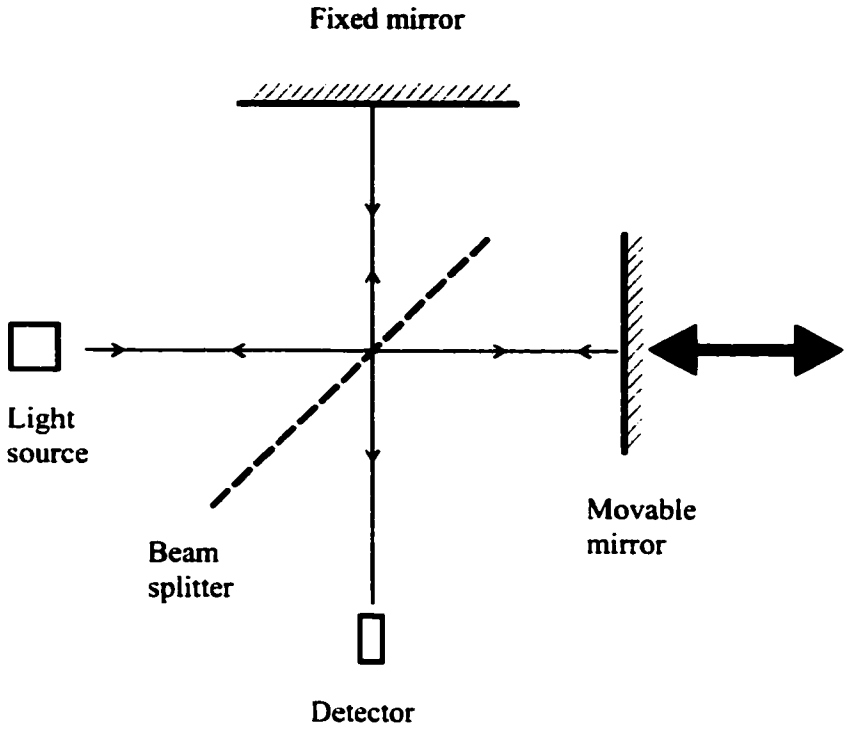

Figure 2.1 Schematic of a Michelson interferometer.

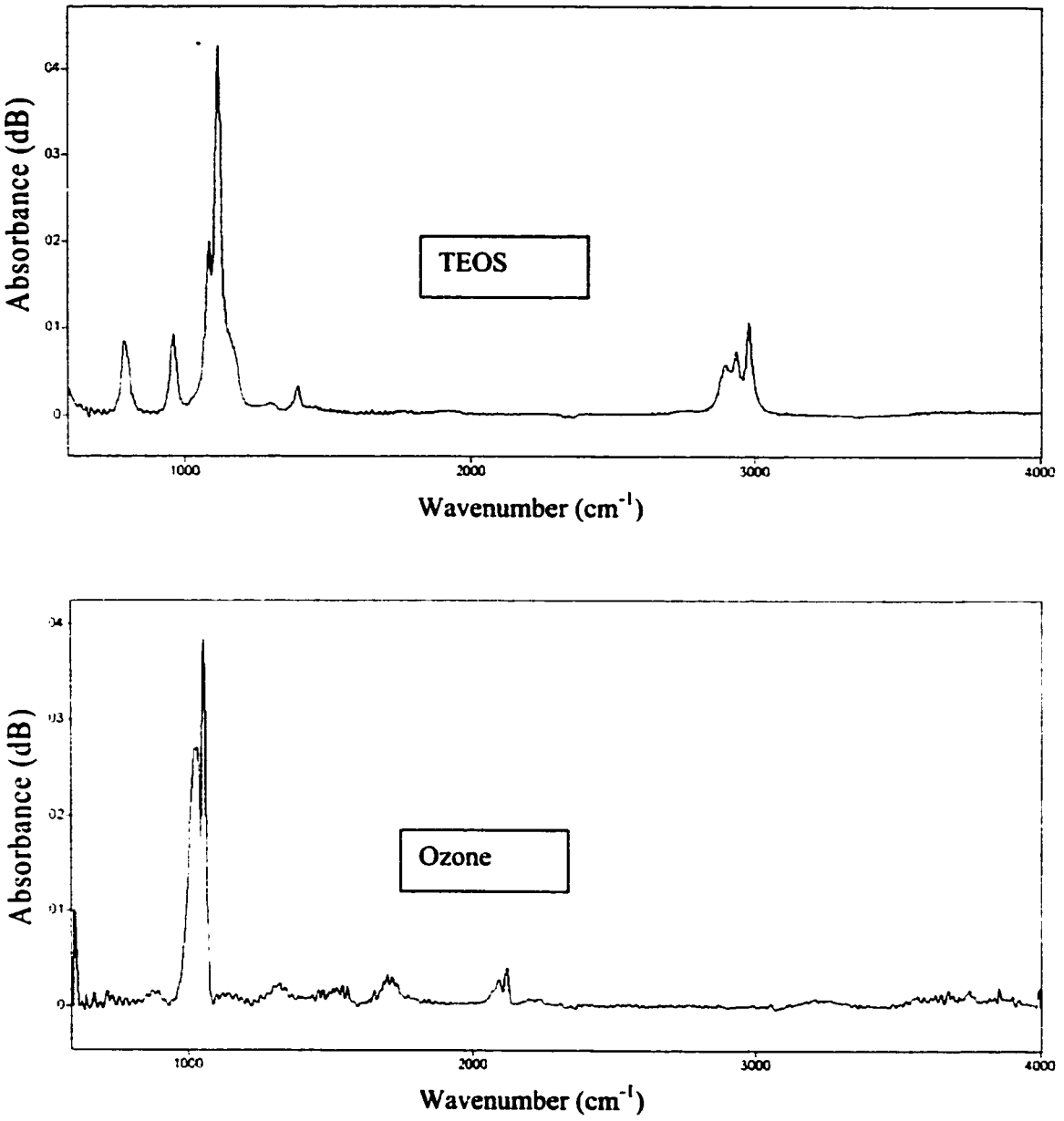

Figure 2.2 Absorption spectra of TEOS and Ozone in the infrared.

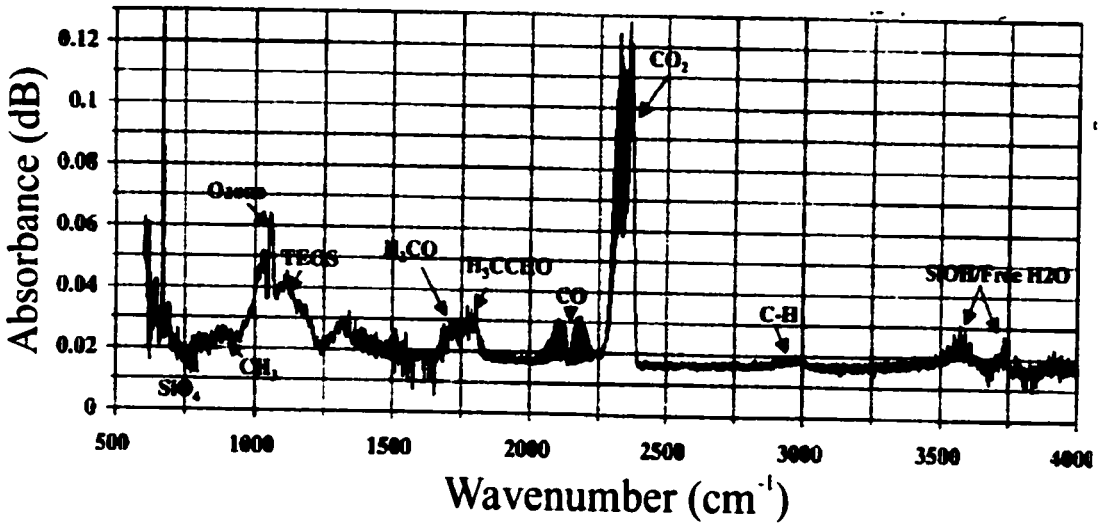

Figure 2.3 Absorption peaks of fed gases and some intermediates in the CVD chamber during thin film deposition.

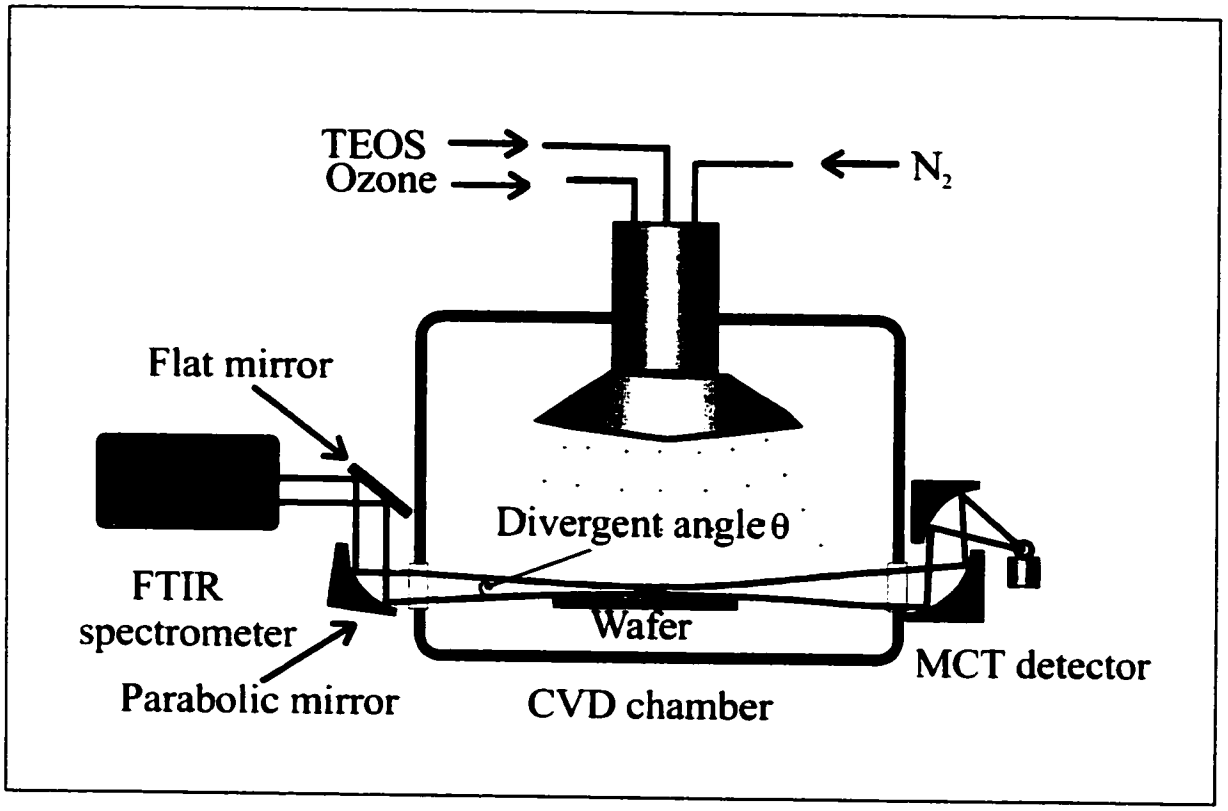

Figure 2.4 Configuration for gas concentration measurement in a CVD chamber using FT-IR spectroscopy.

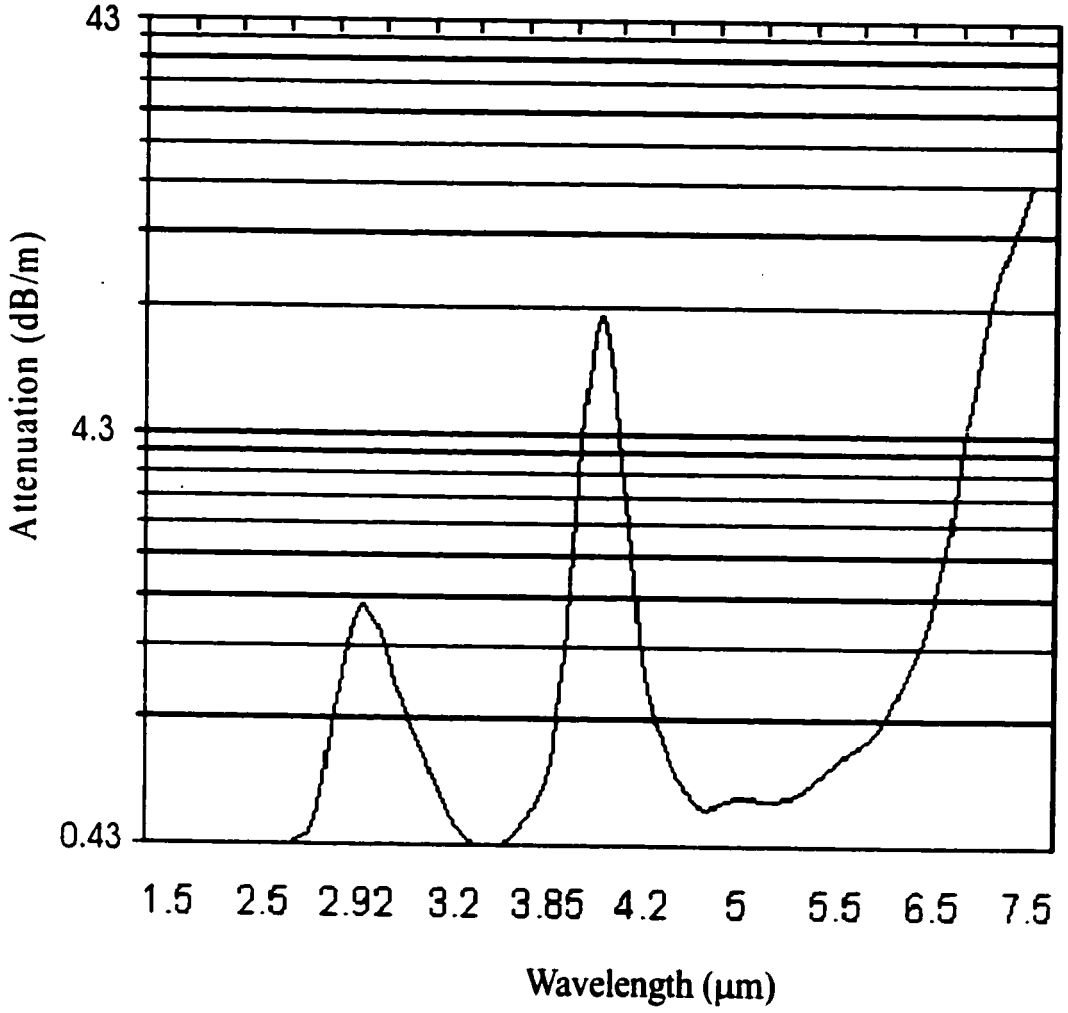

Figure 2.5 Attenuation spectrum of As_2S_3.

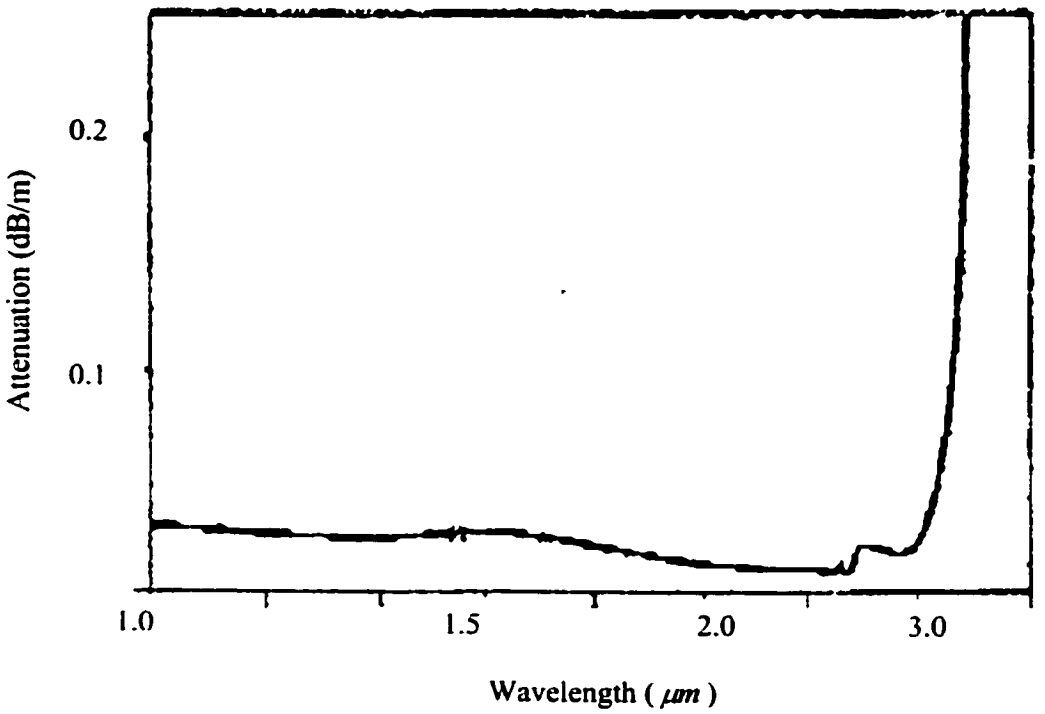

Figure 2.6 Attenuation spectrum of ZrF_4 fiber.

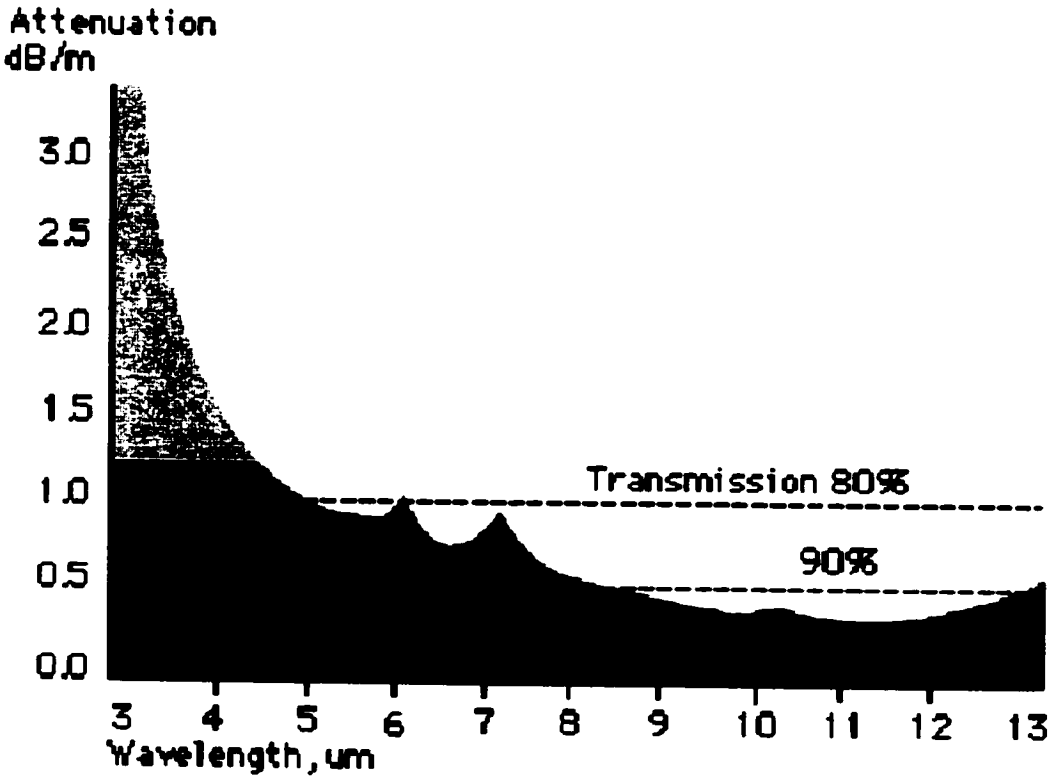

Figure 2.7 Attenuation spectrum of silver halide fiber.

Chapter 3

Monitoring of Chemical Processes in a CVD Chamber Using FT-IR Spectroscopy

3.1 Introduction

The measurements of gas concentration in a CVD chamber using the technique of FT-IR spectroscopy are analyzed in this chapter. Section 3.2 presents the system configuration used in our experiments. Section 3.3 analyzes the light collection efficiencies of the spectrometer using various parabolic mirrors. Section 3.4 examines the interaction between light beam and reactive gases in a CVD chamber using a two-dimensional model. The limitations of current configuration for real-time monitoring and control of thin film deposition on large substrates are discussed. Section 3.5 is a short summary of this chapter.

3.2 System configuration

Fig. 3.1 shows the configuration for monitoring chemical processes in a CVD chamber using a FT-IR spectrometer. The IR light from a SiC glowbar is collimated by a parabolic mirror and launched into a Michelson interferometer, where the light beam is split into two beams by a 50:50 beam splitter. Two beams are reflected by two corner cubes respectively. One of the corner cubes is at a fixed location and the other one is movable. Two light beams with a certain path difference are recombined at the beam splitter and are focused at the chamber center with a parabolic mirror. After passing through the CVD chamber the light beams are focused to a MCT or DTGS detector with two parabolic mirrors. When the light beam passes through the CVD chamber it interacts with the reactive gas mixture and the absorption spectrum

of the gas mixture is measured with the FT-IR spectrometer. The measurement results (gas concentrations obtained from the absorption spectrum) can be used for the real-time control of N_2, O_3 and TEOS flow rates to get uniform gas distribution over large substrate surface. Therefore, real-time gas concentration measurements are needed and the total processing time to get an absorption spectrum should be as short as possible. It has been shown that some intermediates, such as silanol ($(C_2H_5O)_3SiOH$), only exist within a thin (a few millimeters) boundary layer above the substrate [1, 2]. Fast measurements of intermediate concentrations are critical for real-time control of thin film deposition because the thin film quality and deposition speed are determined by intermediates directly. To achieve this, we need to increase the signal to noise ratio (SNR) of the absorption spectrum, as well as to design the optics to realize the light beam reaching the thin layer. A potential solution of measuring the gas concentrations in this thin layer by using IR fibers is provided from this work.

3.3 Collection efficiency of IR radiation

The SNR of a FT-IR spectrometer is proportional to the optical power at the detector and the throughput of the whole system (Eq. 2.4). The throughput is defined as the product of light beam area and the solid angle at any focus [25, 26]. In section 3.4, we will show that increasing the throughput will not allow the current configuration to measure gas concentrations in the region near the substrate. To increase the SNR of the gas absorption spectrum can be achieved by launching more optical power to the FT-IR spectrometer. The optical power that can be collected by the parabolic mirror in Fig. 3.1 is:

$$P \approx \frac{A_{mirror}}{4\pi f^2} P_0 \tag{3.1}$$

where A_{mirror} is the area of the parabolic mirror, f is the focal length of the parabolic mirror. P_0 is the optical power of the glowbar. The area of the mirror is limited by the windows of the spectrometer and the CVD chamber. Typically the window of a FT-IR spectrometer is about 50 cm^2 (the light beam in the spectrometer is 8 cm in diameter). The focal length of the parabolic mirror is around 10 cm. The focal length of the parabolic mirror is chosen due to two facts: 1) The focal length should be as small as possible to get high P value in Eq. 3.1; and 2) the focal

length should be large enough in order to reduce the off-axis effect induced by the finite size of the light source, i.e. $f >> d$ ($d = 4mm$ is the dimension of the glowbar). Using Eq. 3.1 the collection efficiency (P/P_0) is ~ 4% for the current system. Such a low collection efficiency is due to the fact that the glowbar emits IR light in a 4π solid angle and the parabolic mirror only receives a small portion. Increasing the mirror size is not the solution of increasing the collection efficiency because: 1) Larger parabolic mirror means larger beam diameter in the spectrometer and in the CVD chamber. In next section it will be seen that a larger light beam is useless in measuring the interested gas mixture in the CVD chamber; and 2) If the area of the parabolic mirror is increased, the focal length of the mirror must be increased as well to keep the same light beam divergence in the spectrometer.

Another possible method of increasing the spectrometer SNR is to increase the optical power of the glowbar. As shown in Eq. 2.6, the optical power of a glowbar can be increased by increasing its temperature and/or its area. Increasing the glowbar temperature will shorten its lifetime and using a larger glowbar will introduce off-axis effect in the system, which is due to the finite size of the glowbar and the small focal spot of the parabolic mirror. When a glowbar with finite size is placed at the focus of a parabolic mirror, the light beam after the mirror is divergent, see Fig. 3.2. It is obvious that, for a given focal length of the parabolic mirror, the larger of the glowbar the larger of the divergent angle. Light beam divergence should be as small as possible in order to get high spectral resolution [25]. In next section we will show that a highly divergent light beam will not pass through the CVD chamber and the divergence makes it impossible to measure the gas concentrations in the region near the substrate surface. Also, large divergence makes it hard to get small focal points at both the chamber center and the detector. There are two kinds of glowbars commercially available, see Fig. 3.3. The one used in this experiment is type A with the dimension of $4 \times 4 \times 2\ cm^3$ (central hollow).

Form above analysis we can see that both a larger parabolic mirror and a larger glowbar for higher power are not proper solutions to increase the spectrum SNR. In order to launch more optical power to the spectrometer, i.e. to increase the SNR of the spectrum and maintain a light beam with small divergence in the spectrometer, a semi-ellipsoid mirror is proposed in this

study (The term "semi-ellipsoid mirror" used in this thesis refers to half of an ellipsoid with one focus inside and with the other focus outside of the half-ellipsoid), see Fig. 3.4. The light from one focus (point A) will pass through the other focus (point B) after being reflected by the ellipsoid surface. If the glowbar is placed at location A, more than 50% of the optical power can be collected at location B. Comparing the collection efficiency of the parabolic mirror (~ 4%) in Fig. 3.1, the potential improvement of light collection efficiency by using a semi-ellipsoid mirror is evident. The design, fabrication and performance of semi-ellipsoid mirrors will be discussed in chapter 4.

3.4 The interaction of IR light beam with reactive gases

3.4.1 Light beam transmission in the CVD chamber

The gas concentrations in the CVD chamber are not uniformly distributed, and they are dynamically changing during thin film deposition [1, 2]. As explained in the previous section, the intermediates are located within a few millimeters above the wafer. Fig. 3.5 shows the concentration distribution of one intermediate, silanol ($(C_2H_5O)_3SiOH$), in the CVD chamber [1, 2]. We can see that silanol is only distributed within a 3 mm thin layer above the substrate. In order to measure gas concentrations in this thin layer the light beam must interact with gases in this region.

For the current system, the light beam profile in the CVD chamber is measured with an IR power meter. The small power meter is mounted on an X-Y-Z positioner placed in the CVD chamber. The detector of the power meter has a window of only 0.6 mm in diameter. By moving the location of the detector in the chamber the light beam intensity profile is observed. First, the light beam profile at the chamber center is measured. Fig. 3.6 shows the locations around focal area where the detector is moved horizontally (or vertically) and the corresponding beam intensities. From the beam intensity distribution the shape of the light beam at the chamber center is obtained, see Fig. 3.7. We can see that light beam profile is the image of the glowbar with some distortions. The area of the image is about 140 mm^2 with central hollow. Secondly, the light beam profile at the chamber window is measured with the same procedure.

The light beam shape at the chamber window is similar to Fig. 3.7 with an area of 50 cm^2. Knowing the light beam dimensions at the chamber window and at the chamber center and the diameter of the CVD chamber, the light beam divergence in the chamber is calculated. It is 0.4 rad for current system shown in Fig. 3.1. Light beam with large divergence will not all pass through the chamber and reach the detector if the substrate is placed near the focal spot at the chamber center, see Fig. 3.8. Part of it will be either reflected (in shadowed area A) or blocked (in shadowed area B) by the wafer.

If the distance between the wafer surface to the focal spot (center) is h, the diameter of the light beam at the chamber window is D, the diameter of focal spot at the center of the CVD chamber is 12 mm (give the same area as the image shown in Fig. 3.7) and the wafer diameter is 300 mm. Assuming that the light within the two shadowed areas in Fig. 3.8 cannot pass through the chamber and the intensity distribution at beam intersection is Gaussian, the percentage of optical power that can pass through the CVD chamber is shown in Fig. 3.9. From Fig. 3.9 we can see that when h is 2 mm, only 30%, 14% and 4% of the optical power can reach the detector when the beam diameter at the chamber window is 25.4, 51 and 80 mm respectively. Here we can see that the larger of parabolic mirror in the spectrometer (the larger of beam diameter at chamber window) the lower optical power transmission through the chamber. For the purpose of real-time monitoring and control of thin film deposition, we need strong signal (absorption of the interested gases) at the detector to reduce the data processing time. Clearly the current optical arrangement with low light collection efficiency and large beam divergence needs to be improved. Further more, the focal spot above the wafer is central hollow, which will lose more optical power for interaction with intermediates. The improvement of the current configuration may be done by increasing the light collection efficiency, reducing the beam diameter and divergence. This can be realized by an IR fiber bundle and a semi-ellipsoid mirror.

3.4.2 A two-dimensional model

The intermediates in the CVD chamber are distributed very close to the substrate (within a thin boundary layer above the substrate, see Fig. 3.5). The current system (with large beam diameter and divergence) cannot effectively sample this thin boundary layer since this boundary area constitutes only a small fraction of the total area sampled. Here a two-dimensional model is used to examine the interaction between the light beam and the reactive gases in the thin boundary layer above the substrate. The model is shown in Fig.3.10. The substrate diameter is D. The intermediate distribution is assumed to be the same as shown in Fig. 3.5. The width of the IR beam at the focal spot is H and the beam divergent angle is θ. The distribution of light beam intensity is assumed to be Gaussin, i.e. the light intensity, $I(x,r)$, at point A is

$$I(x,r) = P(x)\cdot\exp(-\frac{r^2}{b^2}), \tag{3.2}$$

where $b = H/2 + x\cdot\tan\theta$ is half of beam width (intensity drops to e^{-1} of the maximum) and $P(x)$ is a coefficient that satisfies

$$\int_{-\infty}^{\infty} I(x,r)dr = \text{constant}. \tag{3.3}$$

Eq. 3.3 ensures that the optical power at any beam intersection is constant. If the constant is unity, then $P(x)$ can be written as

$$P(x) = \left(\sqrt{\pi}(H/2 + x\cdot\tan\theta)\right)^{-1}. \tag{3.4}$$

The thin boundary layer of intermediates is shown in the dashed rectangular region in Fig. 3.10. The data of the intermediate concentration, $C(x,r)$, is obtained from Fig. 3.5. In this model we assume that the gas concentration only depends on the distance away from the wafer surface, i.e. $C(x,r) = C(r)$. The parameter, r, used in Fig.3.10 is related to the distance, y, between point A and the wafer surface as $r = y - (H + D\cdot\tan\theta)/2$. The two shadowed regions

in Fig. 3.10 indicate the interaction regions between the IR beam and the intermediate species. The absorption signal strength of the intermediates increases with both the IR beam intensity $I(x,r)$ and intermediate concentration $C(x,r)$ in two interaction regions. So the integral of the product of beam intensity and intermediate concentration over the two interaction regions can be considered as the signal strength of the intermediate species above the substrate. The integral of $P(x,r)\cdot C(x,r)$ over the two interaction regions for various substrate diameters, beam divergence angles and beam diameters at the focal spot are shown in Figs. 3.11 and 3.12.

Fig. 3.11 shows the signal strengths of the intermediate absorption when substrate diameters are 200, 250 and 300 mm respectively. The beam diameter, H, at focal spot for Fig. 3.11 is 12 mm. It is clear from Fig.3.11 that the signal strength strongly depends on the beam divergence angle. Generally speaking the signal strength depends on the sizes of two shadowed areas in Fig. 3.10 and the beam intensity in these areas. For a very small divergence angle (near zero) the signal strength is stronger for large substrate than that for small substrate, because the two shadowed areas increase with substrate and the light beam intensity is independent of the substrate dimension. However, when beam divergence increases the beam intensity in the two shadowed areas is weaker for large substrate than that for small substrate. When divergence increases up to a certain value, the signal strength can be smaller for larger substrate. Fig.3.12 shows signal strengths with various the beam diameters at the focal spot. The substrate diameter is 300 mm in this case. From Fig. 3.12 we can see that the signal strongly depends on the beam diameter and divergence angle. Comparing Fig. 3.11 and Fig. 3.12 we may conclude that the signal strength relevant to intermediates in the thin layer is dominated by the beam divergence and the beam diameter.

For current configuration shown in Fig. 3.1, the light beam divergence angle and diameter in the CVD chamber is 0.4 rad and 12 mm respectively. From Figs. 3.11 and 3.12 we can see that the signal strength related to intermediate within the thin layer above the substrate is zero, even for small substrate (200 mm in diameter).

3.5 Conclusion

The current configuration for measuring the gas concentrations in a CVD chamber is analyzed. By using the technique of FT-IR spectroscopy the current system can monitor the gas concentrations in the chamber by measuring the gas absorptions in middle IR range. For the requirements of real-time monitoring and control of thin film deposition in the chamber the current system has following limitations: 1) Low collection efficiency of radiation from the light source (4%). Due to this low efficiency the current system needs about 30 seconds to obtain one absorption spectrum (with 16 scans average) to get the desired spectrum SNR. But the whole thin film process can be as short as a few minutes. Clearly the current system is not suitable for real-time monitoring and control. 2) Large beam divergence and diameter. Due to this limitation the current system can't effectively measure gas concentrations in the region that is close to the substrate (within a few millimeters above the substrate). The measurement of gas concentrations in this region is critical for real-time control of thin film deposition, because the reactive gases in this region determine the thin film quality and deposition speed.

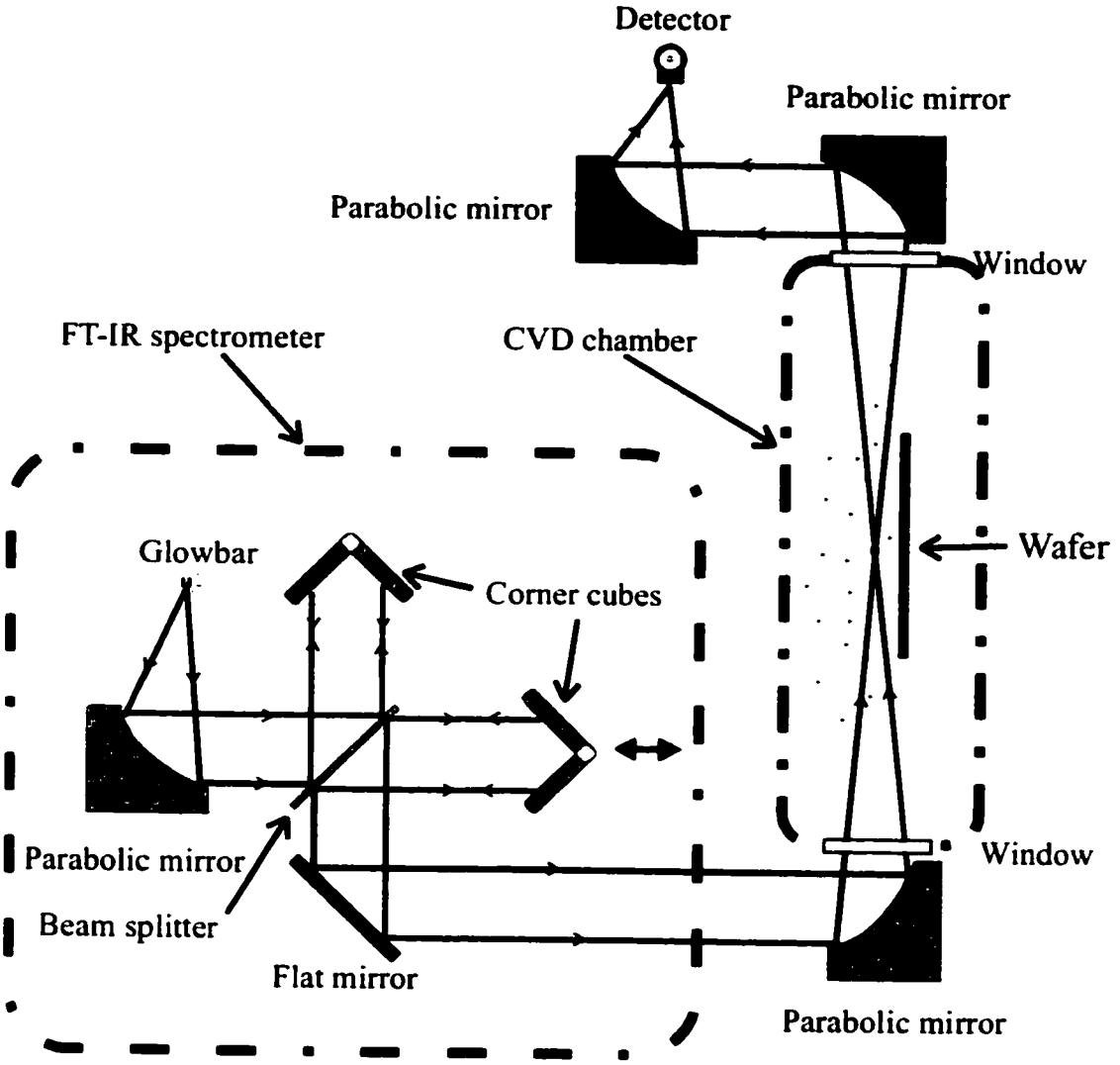

Figure 3.1 Infrared beam transmission in the system for measuring gas concentrations in a CVD chamber.

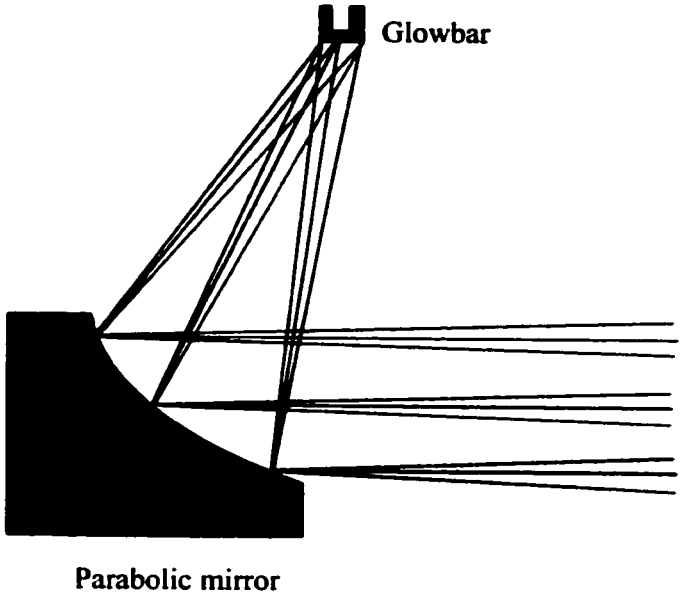

Figure 3.2 Light beam divergence due to the off-axis effect.

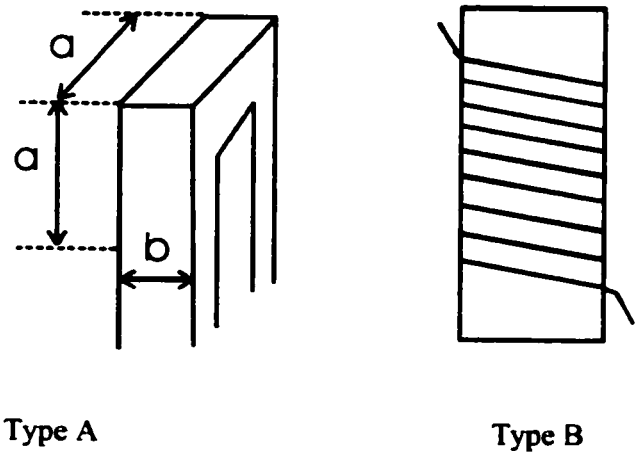

Figure 3.3 SiC infrared light sources (glowbar). The one used in our experiments is type A and $a = 4mm, b = 2mm$.

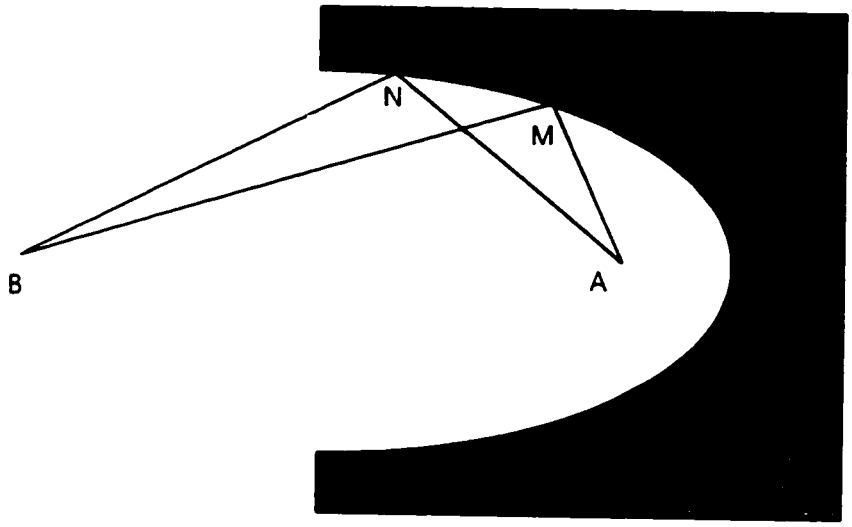

AM+MB=AN+NB=constant

Figure 3.4 Principle of an semi-ellipsoid mirror. Light from focus A will be reflected to focus B.

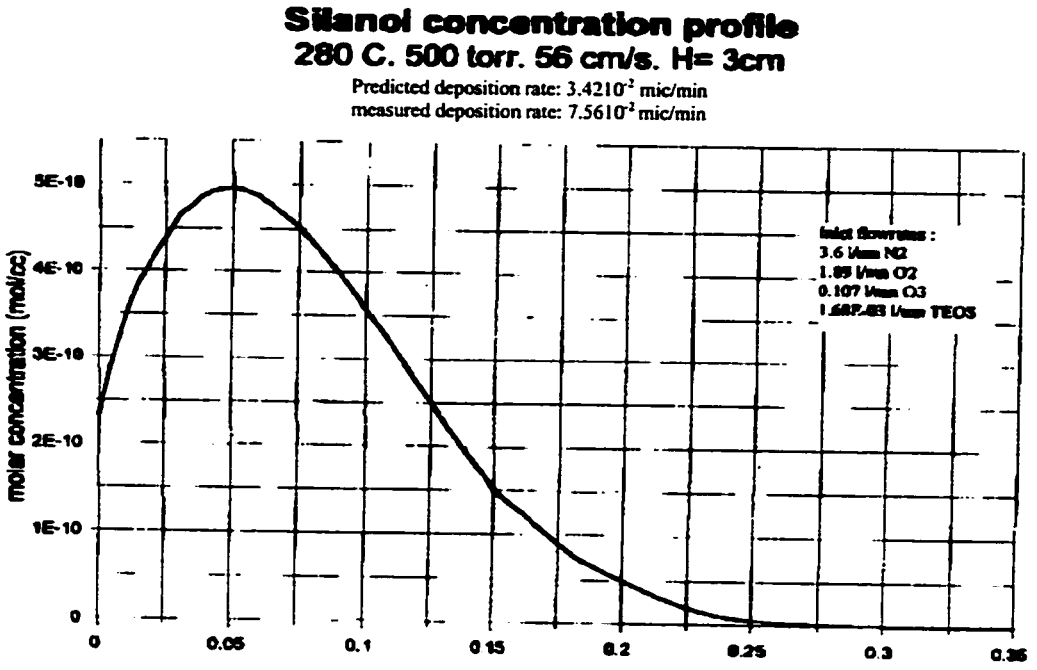

Distance from wafer surface (cm)

Figure 3.5 Concentration of silanol vs. the distance from wafer.

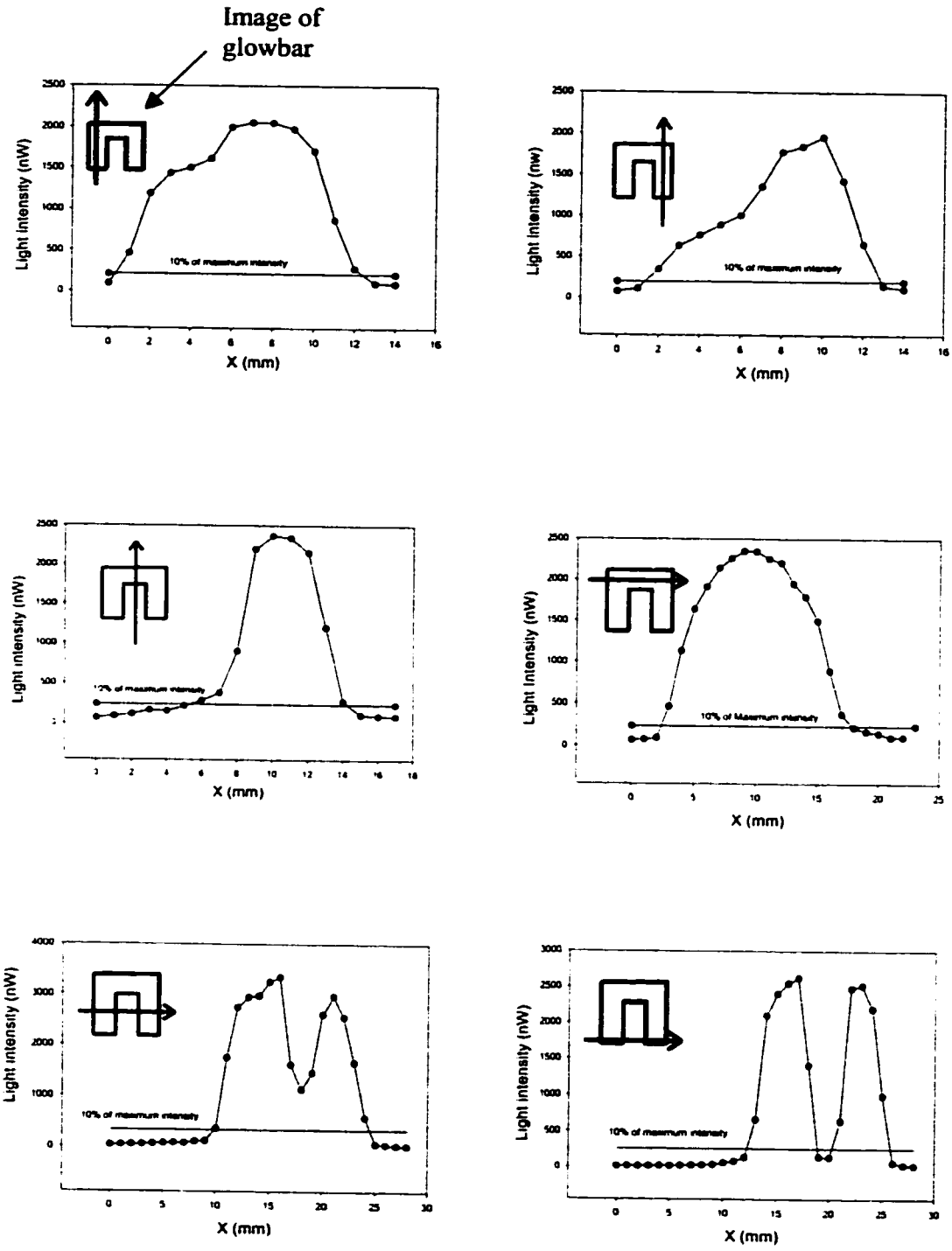

Figure 3.6 Measurements of focus shape at the center of the CVD chamber.

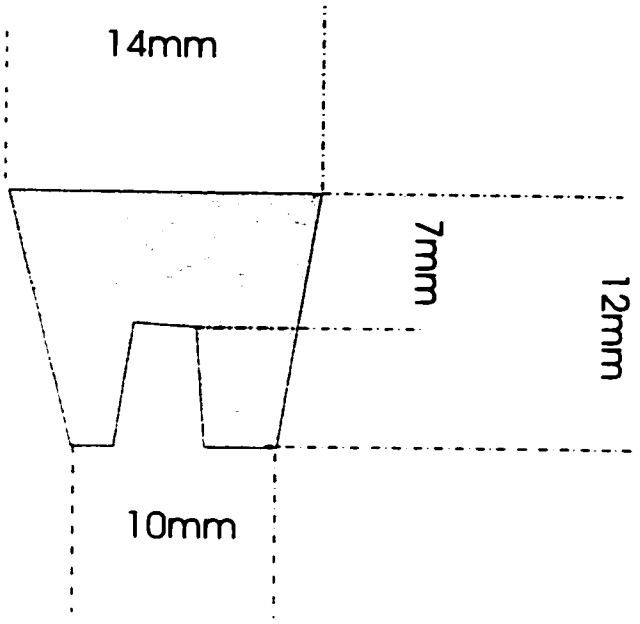

Figure 3.7 The shape of focus at the center of the CVD chamber.

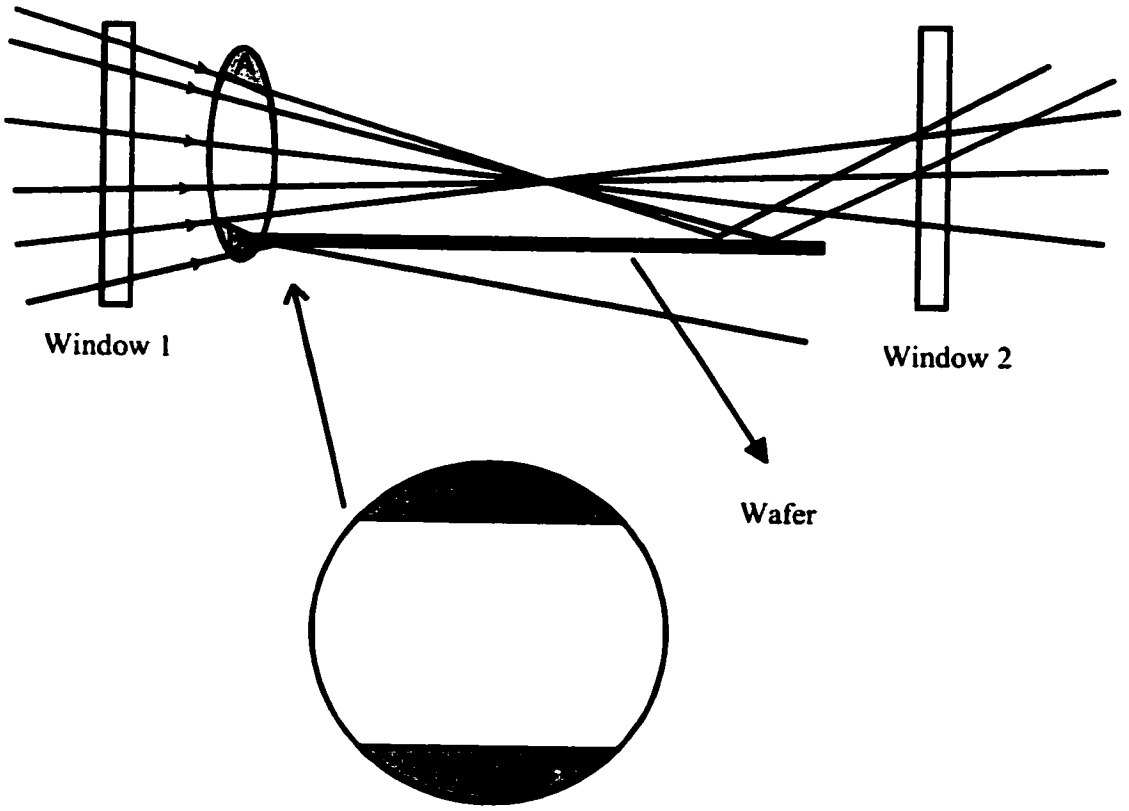

Figure 3.8 Light beam transmission in a CVD chamber. Part of the beam is blocked or reflected by the wafer.

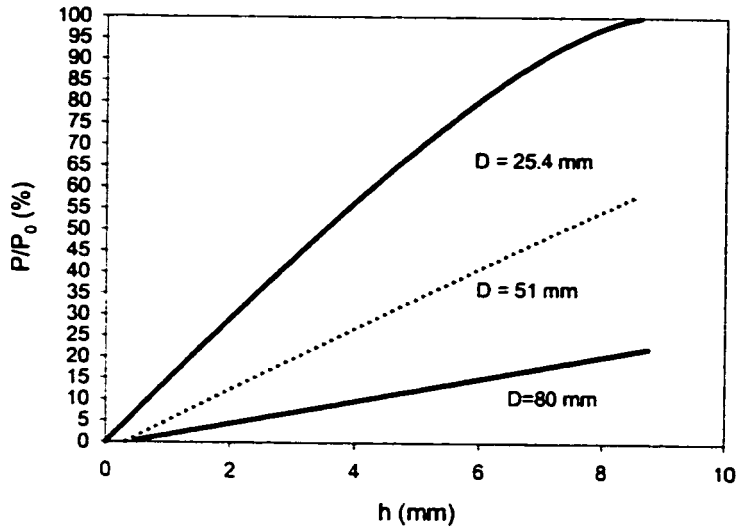

Figure 3.9 Optical power transmittance through a CVD chamber vs. the distance between the wafer surface and the focus of the light beam, h. D is the beam diameter at the chamber window.

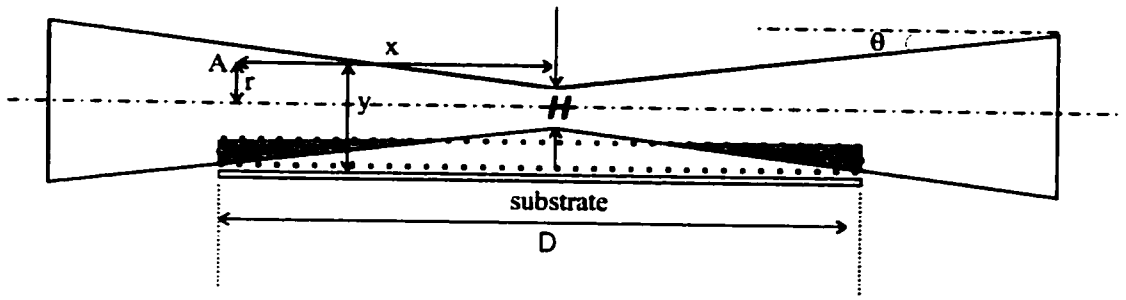

Figure 3.10 A two dimensional model of the interaction between infrared beam and reactive intermediates above the substrate.

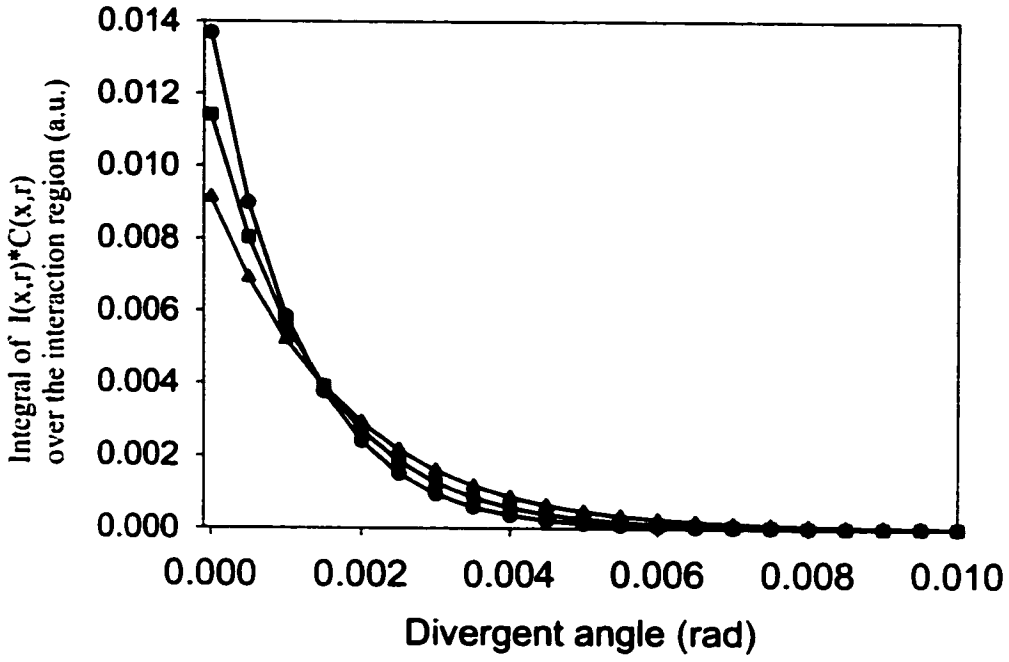

Circular: D=300 mm, rectangular: D=250 mm, triangle: D=200 mm

Figure 3.11 Signal strengths with various substrate diameters.

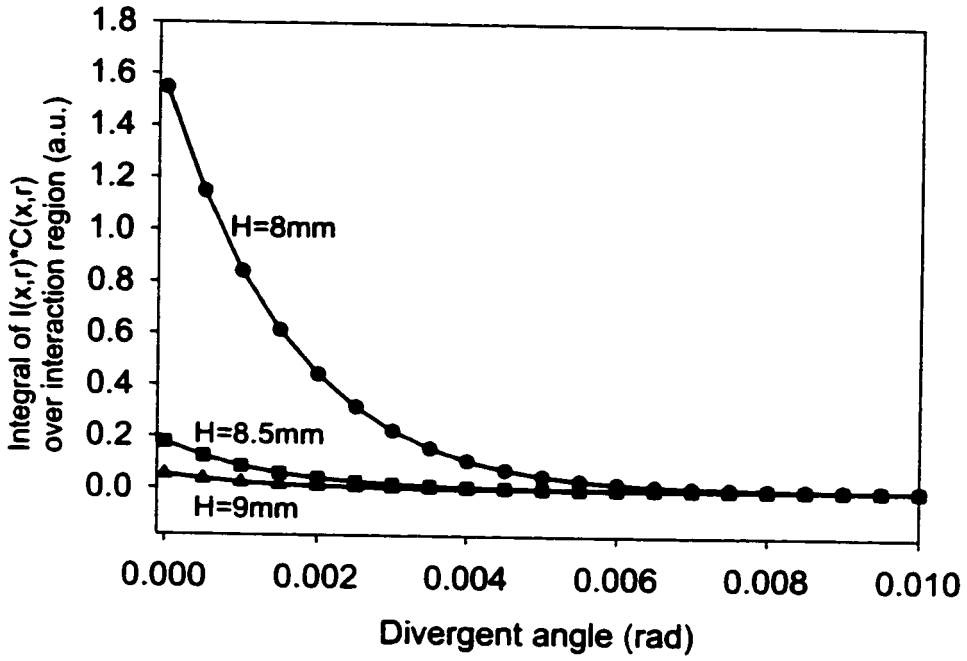

Figure 3.12 Signal strengths with various beam diameters at the focus.

Chapter 4

System Improvements for Monitoring the Thin Film Deposition in a CVD chamber

4.1 Introduction

The system improvements for measuring gas concentrations in a CVD chamber are presented in this chapter. Section 4.2 describes the design and fabrication of an IR fiber bundle. By using two modified SMA connectors the fiber bundle is epoxy free and covers the wavelength range from visible to 20 μm (10000 to 500 cm^{-1}). The effective throughput of the improved system with the IR fiber bundle is discussed in section 4.3. Section 4.4 presents the design and experimental test of semi-ellipsoid mirrors. Section 4.5 presents the measurement of gas concentrations in a CVD chamber using an improved configuration with an IR fiber bundle. The advantages of using an IR fiber bundle in the improved system are discussed in section 4.6. Section 4.7 is a short summary of this chapter.

4.2 Design and fabrication of an IR fiber bundle

4.2.1 Selection of IR fibers

As introduced in chapter 2, optical fibers that have acceptable mechanical properties in the mid-IR spectrum region are silver halide, metal fluoride and chalcogenide fibers. Silver halide fibers exhibit the highest transmittance around 10 μm and high losses at low wavelengths (<3 μm). Metal fluoride fibers have a high transmittance from the visible to 3.5 μm, however, beyond 5 μm the transmittance decreases dramatically [34]. The transmission range of

chalcogenide fibers is wider than that of the fluoride fibers, but loss in the visible region and beyond 10 μm is high. As well, chalcogenide fibers usually exhibit strong absorption peaks around 4 μm due to the presence of water and hydrogen impurities [34], see Fig. 2.5. These absorptions can introduce measurement errors if the gases being monitored also have features in this region. We have chosen as a test process the reaction between tetraethoxysilane (TEOS) and ozone that produces thin films of silicon dioxide. This process is commonly employed for semiconductor device manufacture. Optical fibers to be used for the monitoring of gas concentrations in the TEOS/ozone CVD process must have high transmission, over the entire mid-IR range, from 2 to 17 μm, since mixtures of TEOS, ozone and reactive intermediates have strong absorptions in different parts of the range, see Figs. 2.2 and 2.3. As shown in Figs. 2.5, 2.6 and 2.7, no single mid-IR fiber has high transmittance through this entire range. As a result, a fiber bundle consisting of different types of fibers must be designed to properly determine the spectrum of the gas mixture in this CVD process. Two types of mid-IR fibers; zirconium fluoride and silver halide fibers are selected for inclusion within the bundle, based on the following considerations: 1) Zirconium fluoride fibers have high transmittance from the visible to 3.5 μm and silver halide fibers have high transmittance from 3.5 to 20 μm. Thus a bundle composed of these two fibers covers the wavelength range that is required for measurements in a TEOS/ozone CVD process; 2) Fluoride fibers have high transmittance in the visible range, which makes it easy to perform the optical alignment using a laser diode (0.63 μm).

4.2.2 Fabrications of modified SMA connectors and an IR fiber bundle

The configuration of the fiber bundle is shown in Fig. 4.1. Two silver halide fibers and six zirconium fluoride fibers are placed in parallel and are installed in two modified SMA connectors at the bundle ends. The connectors are specially designed and machined for this fiber bundle. Because silver halide fibers react with most metals we use titanium as the connector material. A critical difference between these connectors and standard SMA connectors is that no epoxy is needed to mount the fiber in the modified connector. Standard SMA connectors require some epoxy to fix the fiber within the connector and the epoxy contacts the fiber in some areas. This is not an issue for non-spectroscopic applications, since

the fiber has a cladding and an acrylate jacket. However, in spectroscopic applications the silver halide fibers can have no cladding since this gives rise to spurious absorptions in the spectral data. When the silver halide fibers are installed in a standard SMA connector, the epoxy fixative will touch the fiber core and induce selective losses due to the absorption of the epoxy in the mid-IR. In fact a fiber bundle had been built with standard SMA connectors and some epoxy is used to mount the fibers in the connectors. The transmission spectrum of the whole bundle shows strong absorption around 2800-3000 cm^{-1}, see Fig. 4.2. The configuration of a modified SMA connector is shown in Fig. 4.3. The connector consists of a male and female part as shown. One end of the male part is slotted and threaded to fit into the female part that is also threaded and compression on the fiber bundle takes place, holding the fibers in the connector. The other end of the male part is also threaded and is fixed to Teflon tubing to protect the fibers. Before the fibers are put into the connector, the silver halide fibers are cut by a microtome and the zirconium fluoride fibers are polished using lapping oil and lapping papers. Using two modified SMA connectors, two silver halide fibers and six zirconium fibers, a one-meter long fiber bundle is fabricated. Measuring the transmission spectrum of this fiber bundle it is found that the absorption due to epoxy in Fig. 4.2 is removed.

4.3 Effective throughput

As mentioned in section 2.2 the SNR of an optical system is proportional to the throughput of the system (Eq. 2.4), which is the minimum throughput of the components in the system. Using IR fibers in the system will introduce some power loss in the system. This power loss can be compensated partially by using a semi-ellipsoid mirror. Another factor that may be of concern is the effective throughput of the system with IR fibers. The optical components in the monitoring system include a FT-IR spectrometer, an IR fiber bundle and a detector. The effective throughput of the system is the minimum throughput of these three components.

The throughput of the FT-IR spectrometer, Θ_s, is [25, 48]

$$\Theta_s = \frac{2\pi A_M \Delta\bar{\upsilon}}{\bar{\upsilon}_{max}} \tag{4.1}$$

where A_M is the area of the mirrors in the spectrometer being illuminated, $\Delta\bar{\upsilon}$ is the desired resolution of the measurement and $\bar{\upsilon}_{max}$ is the maximum wavenumber in the spectrum. For the spectrometer used in our system, $A_M = 50cm^2$, $\bar{\upsilon}_{max} = 4000cm^{-1}$. If the resolution $\Delta\bar{\upsilon}$ is 4 cm^{-1}, then the throughput of the spectrometer, Θ_s, is $3.14\times10^{-1}cm^2sr$.

The throughput of fiber, Θ_f, is the product of the fiber end area, A_f, and the maximum acceptance solid angle of the fiber, $\Omega_{f\,max}$. It can be written as

$$\Theta_f = A_f \cdot \Omega_{f\,max} \tag{4.2}$$

Considering the relation between maximum acceptance solid angle and the numerical aperture of optical fibers, the throughput of a fiber can also be written as

$$\Theta_f = \pi A_f (N.A.) = \pi A_f \sin\theta_c, \tag{4.3}$$

where θ_c is the maximum acceptable angle of the fiber.

The end area of silver halide fiber used in our studies is $3.85\times10^{-3}cm^2$, the practical acceptance angle of silver halide fiber is around 55^0 [49]. Using Eqs. 4.2 and 4.3 the throughput of one silver halide fiber is $1.03\times10^{-2}cm^2sr$. The end area of Zirconium Fluoride fiber used in our experiment is 0.49×10^{-3} cm^2 and the maximum acceptance angle is 12^0. Using Eqs. 4.2 and 4.3 the throughput of one zirconium fluoride fiber is 0.07×10^{-2} cm^2sr. In the fiber bundle we fabricated there are two silver halide fibers and 6 zirconium fluoride fibers. The effective throughput of the fiber bundle, Θ_b, is the sum of all fiber throughputs in the bundle, and it is $2.48\times10^{-2}cm^2sr$.

The detector used in the system is a MCT photo detector with a area of 1 mm^2. The maximum acceptance angle of the detector is 45^0. The calculation of the throughput of the

detector is the same for a fiber. Using Eqs. 4.2 and 4.3 the throughput of the detector, Θ_d is $1.44\times10^{-2}cm^2sr$. The throughputs of the spectrometer, fiber bundle and the detector are listed in table 4.1

Table 4.1 Throughputs of the spectrometer, the fiber bundle and the detector used in the monitoring system

Component	FT-IR spectrometer	Fiber bundle	Detector
Throughput ($\times10^{-2}cm^2sr$)	31.4	2.48	1.44

From table 4.1 we can see that the effective throughput of the system is limited by the detector. A fiber bundle in the system will not decrease the effective throughput.

4.4 Semi-ellipsoid mirrors

4.4.1 Design and fabrication of semi-ellipsoid mirrors

As discussed in section 3.3, semi-ellipsoid mirrors have the potential of increasing light collection efficiency. In order to test the performance of semi-ellipsoid mirrors experimentally, two semi-ellipsoid mirrors are designed, machined and polished. The dimensions of the two mirrors are shown in Fig. 4.4. The major axis and the minor axis of the large mirror are 250 mm and 105 mm respectively. The major axis and the minor axis of the small mirror are 140 mm and 60 mm respectively. Two different sizes of semi-ellipsoid mirrors are designed in order to see the off-axis effect due to the finite size of the light source. For an ellipsoid it can be shown that the distance between the focus and the center of the cavity, c, is

$$c=\sqrt{a^2-b^2} \tag{4.4}$$

where a is half of the major axis and b is half of the minor axis of the ellipsoid. In the two semi-ellipsiod mirrors we designed, c is 110.7 mm for the large mirror and it is 63.2 mm for the

small mirror. The determination of the dimensions of the mirrors is based on the following considerations: 1) The dimensions of the mirrors should be much larger than that of the glowbar ($4\times4\times2mm^3$) in order to reduce the off-axis effect; and 2) When a light source is placed at one focus, the maximum convergence angle at the other focus should be less than or equal to the acceptance angle of the optical fiber. The practical acceptance angle of silver halide fiber is 55^0 and the angle Φ in Fig. 4.4 is 25.4^0. These two semi-ellipsoid mirrors are machined and polished by using the UNB machine shop facilities. The inner surfaces are coated with gold to increase its the reflectivity in the IR. The facilities at the UNB machine shop are not for optical machining and polishing. The shapes of the semi-ellipsoid mirrors and inner surface polishing are not as good as were expected.

4.4.2 Improvement of light collection efficiency

Conventional FT-IR spectrometer optics uses parabolic mirrors to collect the IR light from a Glowbar. This light is then directed to the interferometer. As discussed in section 3.3, typically the mirrors can collect only about 4% of the IR light. Such a low launching efficiency is due to the fact that the glowbar emits IR radiation in a 4π solid angle and the parabolic mirror can only collect a small portion. In this section, the improvement of light collection efficiency is shown experimentally by using semi-ellipsoid mirrors. In the experiment, the semi-ellipsoid mirror is used to collect the IR light from a Glowbar as the input to the FT-IR spectrometer with the help of another parabolic mirror, see Fig. 4.5.

As shown in Fig.4.5, a practical Michelson interferometer has two optical inputs and two optical outputs. Two corner cubes are used to form the two arms with a optical path difference. One corner cube is fixed and the other is movable. In this experiment the IR light beam is launched to the spectrometer through input 1 and the output light beam is collected through output 2. A DTGS detector is used to convert the optical signal from output 2 to an electrical signal. After a A/D converter the data is stored in a computer. First, the glowbar is placed at one focal point inside the large semi-ellipsoid (Fig. 4.5) and the IR light is focused at the other focal point (point A). Point A is also the focal point of a parabolic mirror that is used to deliver the

parallel light beam to the interferometer (input 1). The output spectrum trace is labeled as (a) in Fig. 4.6. In order to compare this result with ordinary FT-IR optics, the semi-ellipsoid mirror is removed and the same glowbar is placed at point A. The output spectrum trace of this test is shown as (b) in Fig. 4.6. These results clearly show that the semi-ellipsoid mirror increases the intensity of the spectrum by a factor of at least 2. The absorption peak at 2400 cm^{-1} in Fig. 4.6 is due to CO_2 and the absorptions from 3500 to 4000 cm^{-1} and from 1300 to 2000 cm^{-1} are due to water. These artifacts are present since the experiment is performed in an open-air environment. It should also be noted that the semi-ellipsoid mirror is not optically polished and the shape may not be exactly ellipsoid since the UNB machining facility is not optimized for the production of optical components. Further signal improvement should therefore be possible if the mirror is machined in the correct shape and is polished to optical standards.

The use of this semi-ellipsoid mirror is expected to improve the signal to noise ratios in spectral determinations using fiber optic I/O, since the increased source intensity can compensate for IR beam intensity losses by attenuation of the fiber and reflections at the fiber ends.

The same setup shown in Fig. 4.5 is used to test the collection efficiency of the small semi-ellipsoid mirror shown in Fig. 4.4. It is found that the signal intensity from output 2 of the interferometer is half of that using the big semi-ellipsoid mirror. The focal spot at point A is almost twice as that when the big semi-ellipsoid mirror is used. This is due to the off-axis effect shown in Fig. 3.2. The small mirror shows stronger off-axis effect than the big mirror.

4.5 Gas concentration measurement

The experimental configuration used to measure the gas concentration (TEOS) in a CVD chamber with our fiber bundle and an FT-IR is shown in Fig. 4.7. The FT-IR spectrometer is a BOMEM MB104 with a ZnSe beam-splitter. The optical windows of the CVD chamber are ZnSe. The cross section of the light beam from the spectrometer is 80 mm at the entrance window to the CVD chamber. A parabolic mirror (M1) is used to direct the light beam into a

fiber launcher which consists of two parabolic mirrors (M2 and M3) and one X-Y-Z positioner. One end of the fiber bundle with the modified SMA connector is connected to the fiber launcher through a SMA adapter. The position of the fiber bundle is adjusted for maximum optical power by using the X-Y-Z positioner in the launcher. The other end of the fiber bundle is connected to another X-Y-Z positioner located on one side of the CVD chamber. The light from the fiber bundle is delivered to the CVD chamber through a parabolic mirror (M4). The locations of M4 and the X-Y-Z positioner are adjusted to focus the IR beam at the center of the CVD chamber. The other two parabolic mirrors (M5 and M6) are used to collect the light exiting the CVD chamber and to launch it to a MCT detector. In a practical system, designing a fiber bundle unit that can be fitted directly to the various mirrors can eliminate the two X-Y-Z positioners, thus reducing unit cost.

Unfortunately, the semi-ellipsoid mirror could not be used in our test of the fiber bundle based I/O configuration for measuring the TEOS concentration in the chamber. This is due to the fact that the FT-IR spectrometer used in this study has only one open output (or input) window. The other input (or output) window is specially designed to collect the light beam from an internal light source and there is insufficient space in the spectrometer for the semi-ellipsoid mirror and a parabolic mirror unit. However, from the experiment result in Section 4.4 (Fig. 4.6), we know that with the semi-ellipsoid mirror the signal level will be doubled compared to tests performed without the semi-ellipsoid mirror. This provide the evidence that the semi-ellipsoid mirror has the potential of improving the current system further.

Using the configuration in Fig. 4.7, the absorption spectrum of TEOS in a CVD chamber under typical operating conditions is determined (Fig. 4.8). The spectrum shows the characteristic absorptions of TEOS between 600 and 3000 cm^{-1}. The absorption peak at 2400 cm^{-1} in Fig. 4.7 is an artifact due to CO_2. Examining the spectrum in Fig. 4.8 it is apparent that the spectral peaks between 1400 to 600 cm^{-1} are well-defined and that the SNR in this range is higher than that observed between 3400 and 1600 cm^{-1}. We believe that this difference in the signal to noise ratio is an artifact caused by the presence of ZnSe components in the optical design as the transmission spectrum with the fiber bundle outside the CVD chamber has shown

low absorption in this region [Fig. 4.2]. The fiber bundle is designed to transmit IR light from visible through the mid-IR, however absorptions by the ZnSe beam-splitter in the FT-IR spectrometer and the ZnSe windows of the CVD chamber detrimentally affect the performance of the system in the near IR. As a result, the signal to noise ratio at higher wavenumbers is poorer than in the spectral regions near or below 1000 cm^{-1}.

4.6 Light beam characterization in the CVD chamber

As discussed in section 3.4, light beam passing through the CVD chamber with large divergence is not suitable for real-time monitoring of the gas concentration above the wafer.The characteristics of the IR beam in the CVD chamber with the fiber bundle are measured using the method described in section 3.4.1 The experimental data are summarized and are shown in table 4.2. These data clearly show that by using the fiber bundle the divergence of light beam in the CVD chamber is reduced and the IR beam has a smaller focal point diameter.

Table 4.2. Light beam characterizations in the CVD chamber before and after a fiber bundle is used

Configuration	Beam diameter at side windows of the chamber (mm)	Focal point diameter (mm)	Divergence angle of light beam in the chamber (rad.)
Without fiber bundle	80	12	0.4
With fiber bundle	20	4	0.1

The significance of this for the use of a fiber bundle based FT-IR probe of CVD chambers is that areas closer to the wafer surface can be sampled more effectively, providing the experimental data with greater sensitivity to the reactive intermediate compounds that are only

present close to the wafer surface. It should be noted that the total optical power reaching the MCT detector when the fiber bundle is employed is lower than without the fiber bundle in place (loss is around 15 dB). The main loss occurs in the launching unit (fiber launcher) shown in Fig. 4.7. The launcher consists of two parabolic mirrors (M3 and M4) and the focal point of the launching mirror (focal point of M3) is 3-4 mm in diameter. A comparison of this value with the diameter of the fiber bundle (1.5 mm) shows that only a small portion of the optical power can be launched into the fiber bundle in the configuration tested. Such coupling between the broadband light source (such as a Glowbar) and optical fibers needs further improvement. Other sources of loss include the reflections at the fiber ends and attenuation in the fibers.

Using the two-dimensional model described in section 3.4.2 and the parameters in table 4.2, Fig. 4.9 shows signal strengths (integral of $I(x,r)\times C(x, r)$ over the interaction region shown in Fig. 3.10) for the configurations before and after the IR fiber bundle is used. The diameter of the substrate is 300 mm and the loss due to the introduction of the fiber bundle is 15 dB. We can see that the signal strength relevant to the intermediates is significantly stronger for the improved system.

4.7 Conclusion

The preliminary studies presented in this chapter lead to the following conclusions: 1) Mid-IR fiber bundles can be used in the spectroscopic measurements of the gas concentrations in a CVD chamber; 2) The semi-ellipsoid mirror increases the light collection efficiency by a factor of at least 2, which has the potential of improving the performance of conventional FT-IR spectrometers and holds promise as spectrometer components that permit the deployment of mid-IR fiber optic I/O in a variety of sampling configurations; 3) The absorption spectrum of TEOS in a CVD chamber has been measured by using an IR fiber bundle interfaced to a conventional FT-IR spectrometer; and 4) Using a fiber bundle in the monitoring system the beam focal spot in the CVD chamber decreases from 12 mm to 4 mm and the beam divergence drops from 0.4 rad to 0.1 rad, which has the potential of measuring the gas concentrations in the region that is close to the substrate surface.

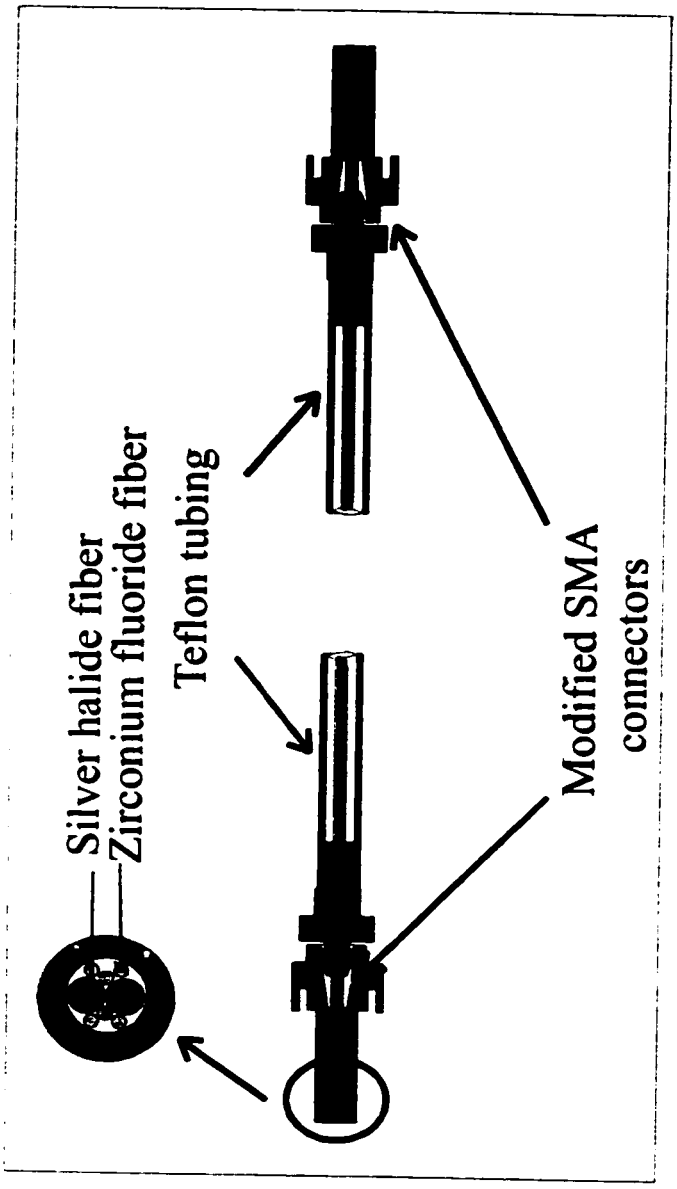

Figure 4.1 The configuration of an infrared fiber bundle composed of two silver halide fibers and six zirconium fluoride fibers.

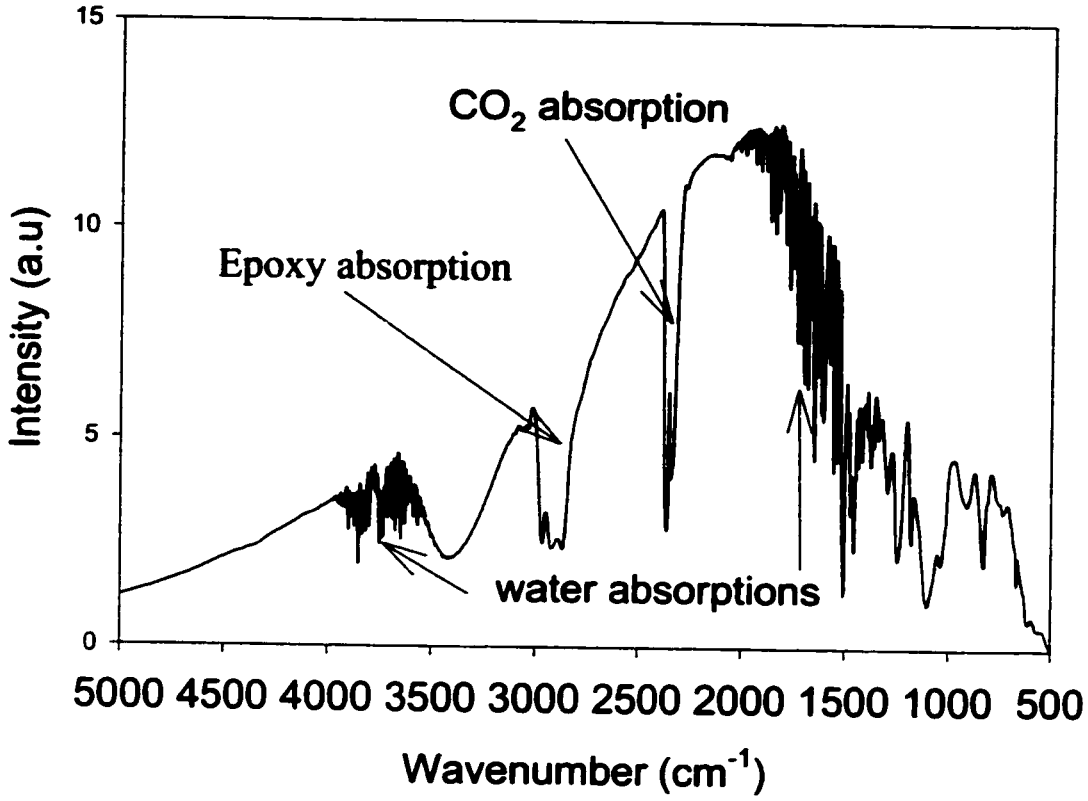

Figure 4.2 Epoxy absorption peak at 2800-3000 cm^{-1}.

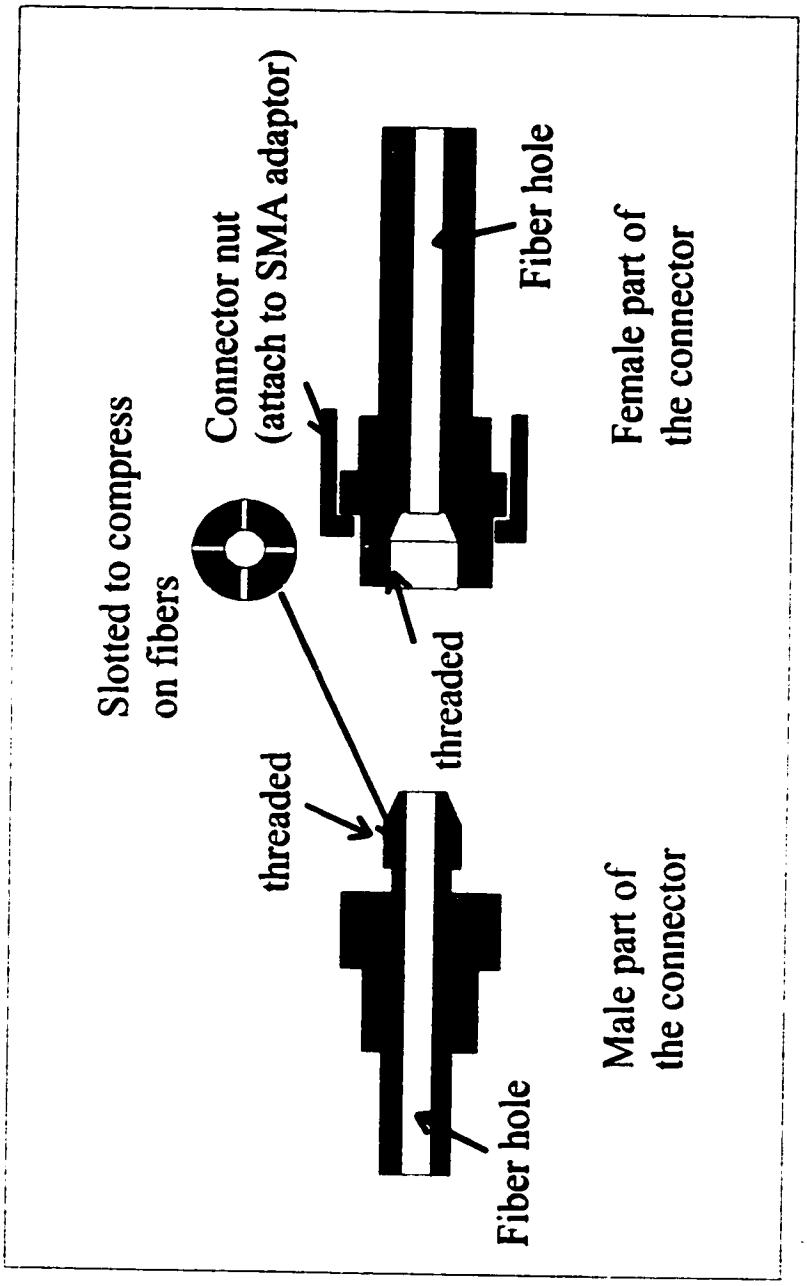

Figure 4.3 Configuration of the modified SMA connector.

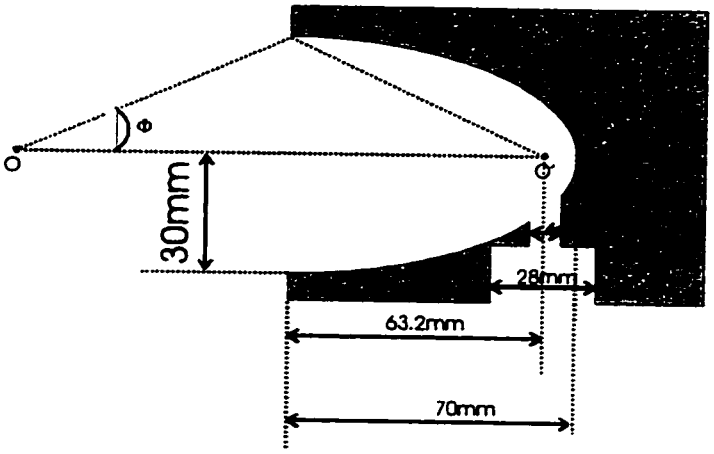

(a) small semi-ellipsoid mirror

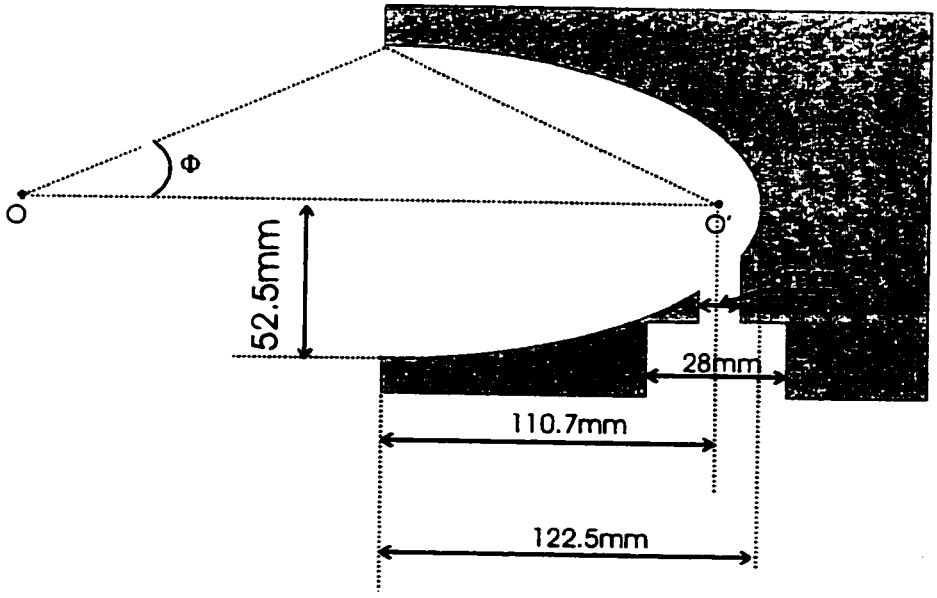

(b) large semi-ellipsoid mirror

Figure 4.4 Shapes and dimensions of two semi-ellipsoid mirrors.

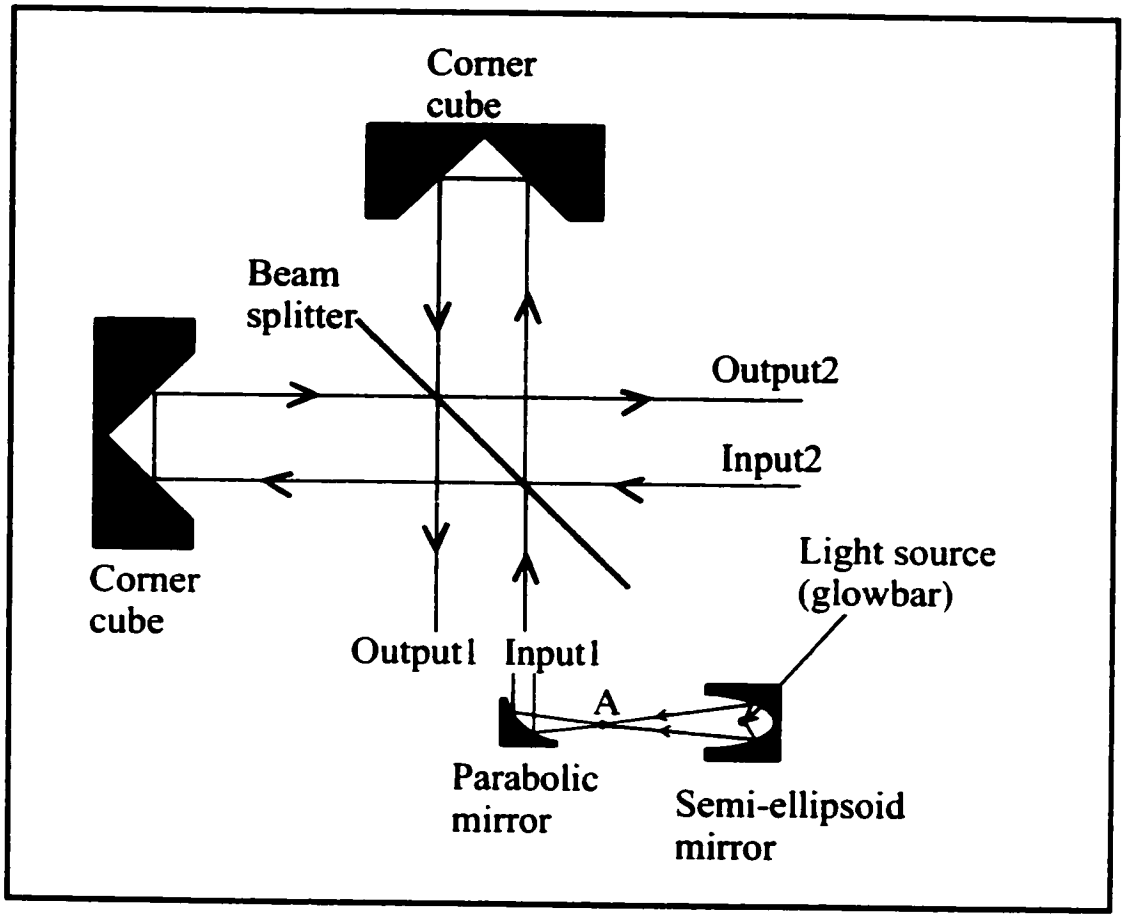

Figure 4.5 Configuration for testing the performance of a semi-ellipsoid mirror with a FT-IR spectrometer.

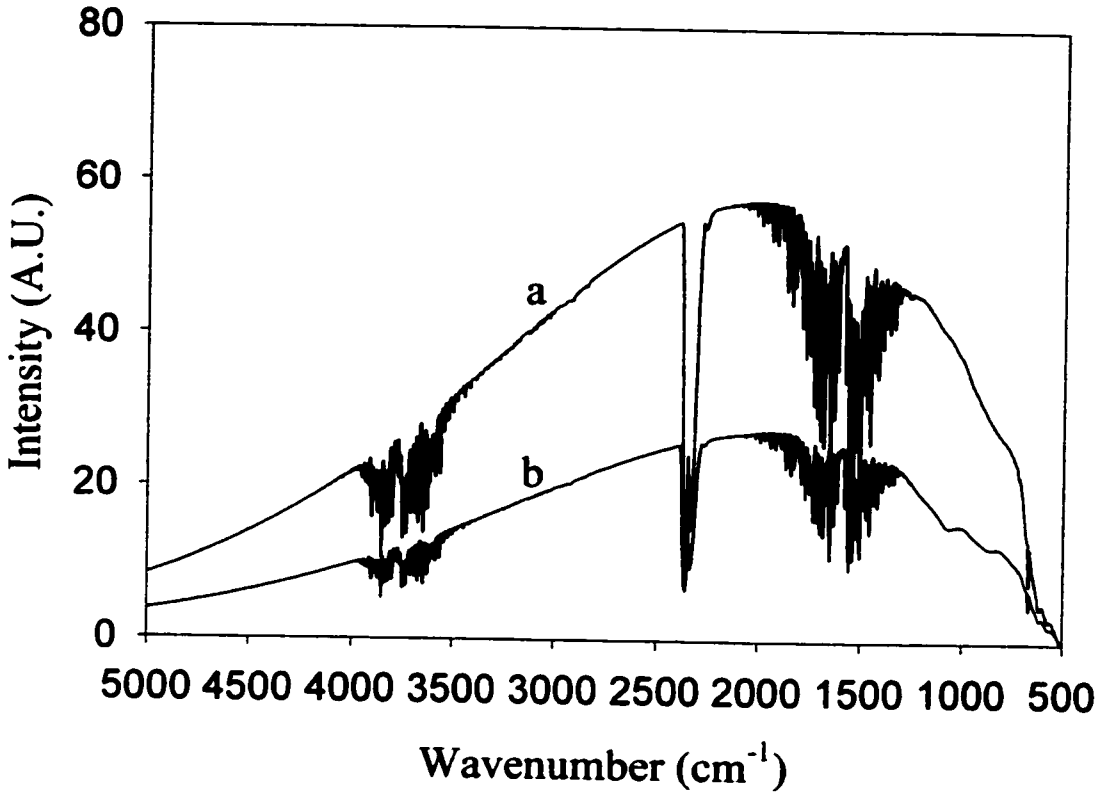

Figure 4.6 The output spectra of the FT-IR spectrometer with (a) and without (b) the use of the semi-ellipsoid mirror.

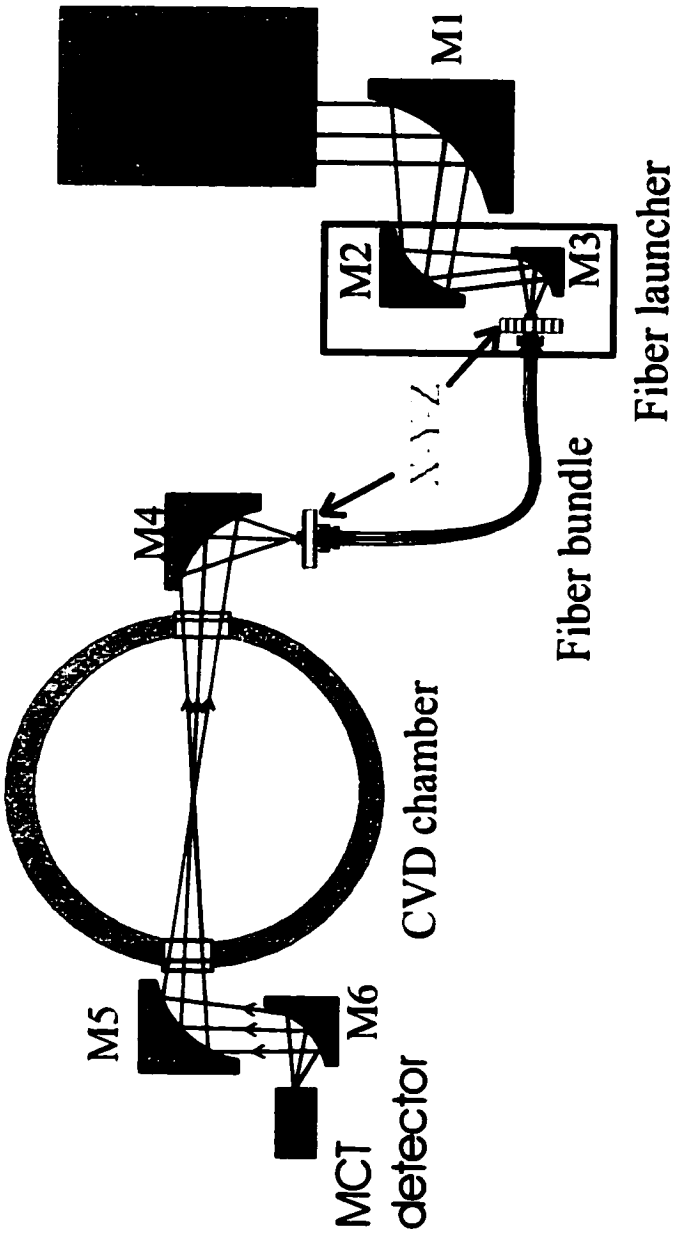

Figure 4.7 Experimental setup for measuring the gas (TEOS) concentration in a CVD chamber with an infrared fiber bundle and a FT-IR spectrometer.

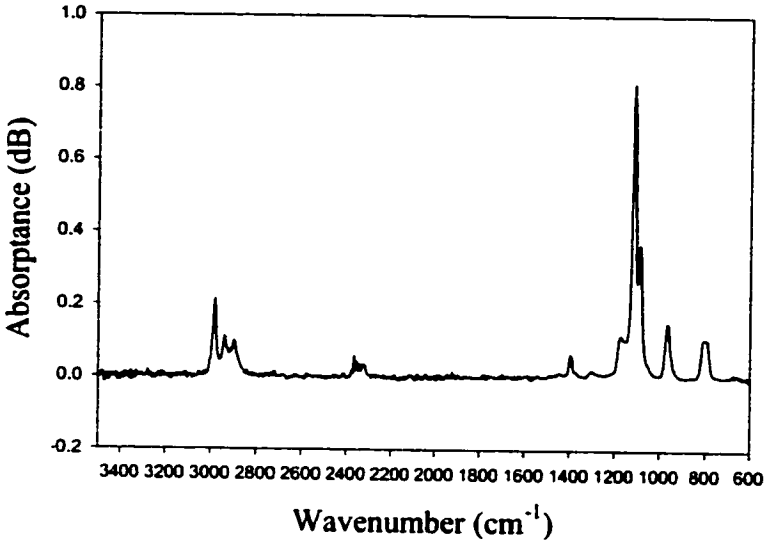

Figure 4.8 The absorption spectrum of TEOS in the CVD chamber measured by the improved system with an infrared bundle.

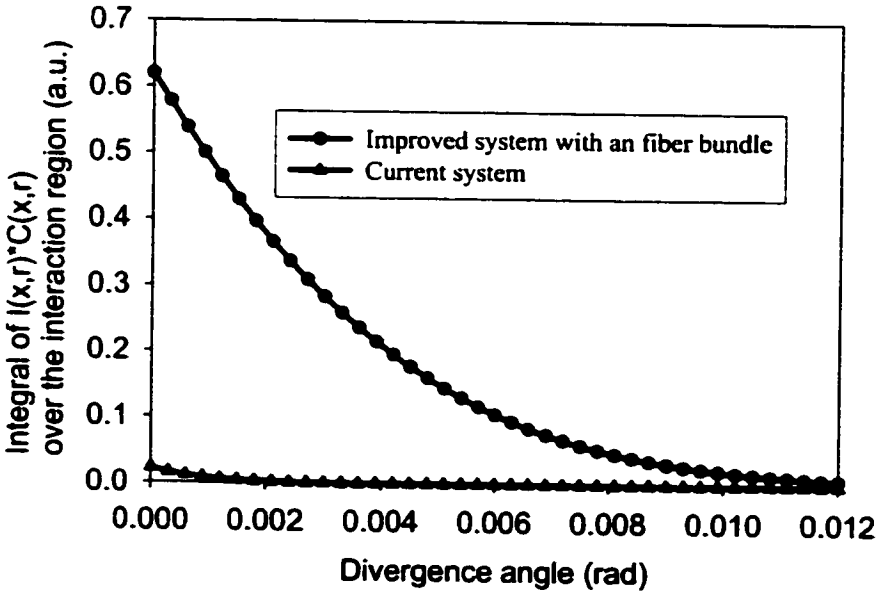

Figure 4.9 Comparison of signal strengths before and after the system is improved with an infrared fiber bundle.

Chapter 5

Gamma-Induced Attenuation in Optical Fibers – Fiber Optic Radiation Dosimeters

5.1 Introduction

When optical fibers are exposed to nuclear or X-ray radiation, their losses increase due to the radiation induced ionization and formation of color centers [38, 39]. This effect can strongly reduce the performance of the fiber optic systems, such as fiber optic data transmission and fibroscopy in nuclear environments, without compensation or careful design of systems [40-42]. However, based on the dependence of fiber loss on radiation dose, this mechanism can be explored to fabricate fiber optic radiation sensors [4, 5, 43].

In this chapter the gamma radiation induced loss spectra in single mode (SM) and multi-mode (MM) fibers, P-doped MM fibers, Ge-doped SM and MM fibers are studied. Section 5.2 briefly describes the experimental setup and the fiber samples that are tested. Section 5.3 shows the measurement procedure and experiment results. Section 5.4 discusses the possibility of using P-doped fibers as fiber optic radiation sensors. Section 5.5 is the summary of this chapter.

5.2 Experimental setup and fiber samples

5.2.1 Experimental setup

The experimental setup for measuring the gamma radiation induced loss in optical fibers is shown in Fig. 5.1. A 2×2 MM fiber coupler is used to couple the light from the light source (an

incandescent bulb, temperature of about 2800 to 3000 K) to a 20 meters MM fiber cable that transmits the light to the fiber under test (FUT) located in the radiation room. The light from the FUT is collected by another fiber cable that is connected to a CCD fiber optic spectrometer. The spectrometer has a resolution of 1 nm, and is used to capture the light spectrum every 15 to 30 seconds. The incandescent bulb is driven by a stabilized power supply to reduce the optical power fluctuation. An optical power meter is connected to another arm of the fiber coupler to monitor the source power fluctuations. During experiments the optical power typically fluctuates within the range of $\pm 1\%$ from visible to near infrared. Thus the loss spectrum has an inherent error of $\pm 1\%$. The laser diodes shown in Fig. 5.1 are used for studying photo-bleaching effects in optical fibers after gamma irradiation. Each fiber sample is cleaved and inspected with a fiber viewer to ensure that the surface is flat to minimize Fresnel end face reflections, and then fixed with a bare fiber ST connector. The FUT is coiled into loops of diameter of about 5 cm.

The experiments are conducted at the Radiation Oncology Department of Saint John Regional Hospital, New Brunswick, Canada. A Theratron 780 Cobalt-60 gamma source (1.25MeV) is used to irradiate the FUT. The dose rate from this machine is calibrated with an ionization chamber placed in a water phantom. The chamber itself is calibrated by the National Standards Laboratory. A 10×10 cm^2 field is used for the exposures at all times. In order to facilitate the study of the effect of dose rate on the fiber loss, the dose rate is varied by both varying the distance between the cobalt-60 source and the FUT as well as using appropriate lead thickness to attenuate the intensity of the beam. The total exposure dose for each fiber sample is controlled by varying the exposure time for different dose rates. The FUT coil is placed at the center of the field on a $30 \times 30 \times 1$ cm^2 thick water equivalent solid-gel (superflab). Another 0.3 cm thick superflab layer is placed on the coil to achieve maximum dose build up and uniformity of exposure. The whole assembly is than placed on a water equivalent polymethyl methacrylate block of $30 \times 30 \times 20$ cm^3 to achieve adequate back scattering gamma radiation and reproducible dosimetric conditions. A diode dosimeter calibrated with the ionization chamber is placed at the center of the field to monitor the dose rate at the fiber coil. The spectrometer is computer controlled and the experimental data (absorption spectrum) is recorded for further processing.

The dose rates of the Cobalt-60 radiation on the fiber sample can vary from 0.1 Gy/min to 3.0 Gy/min (One Gy is equal to one joule of energy deposited in one kg of a material). The optical power coupled to the tested fiber sample is controlled as low as possible (about 2 to 6 μW) in order to prevent photo-bleaching effects, if any, from occurring during irradiation. Before the fiber is exposed to gamma radiation, a transmission spectrum of the light output of the fiber is recorded as a reference for relative loss measurement. The transmission spectrum measured during and after irradiation is compared with this reference and the loss is considered to be due to radiation exposure. All the measurements are performed at room temperature (~ 20 ^{0}C).

The wavelength range of the fiber optic spectrometer is 300 nm to 900 nm. However, in this experiment, we show only the absorption spectra from 460 nm to 700 nm because at wavelengths shorter than 460 nm, the intensity of the light source is relatively weak and the radiation induced fiber loss is high. As a result, the signal due to radiation at shorter wavelength is too weak to be detected. At wavelengths longer than 700 nm no evident absorption peaks are observed even at a total dose of 10 Gy.

5.2.2 Optical fiber samples

Optical fibers that have been tested and the parameters of these fibers are listed in table 5.1.

5.3 Experiment procedure and results

5.3.1 Normal single-mode fiber

A 12 m long SM silica fiber is irradiated by gamma rays for five minutes at the dose rate of 0.5 Gy/min. The radiation-induced loss spectrum is shown in Fig. 5.2. Absorption peaks are observed at 472, 502 and 540 nm. The fiber is then allowed to recover for 3 minutes at room temperature. The loss spectrum after recovery is shown in Fig. 5.3. Fig. 5.4 shows the radiation-induced loss vs. total dose. As we can see that at 472 and 502 nm the induced loss has a linear relationship with total dose. The slopes, and thus the sensitivities are 0.004 dB/Gy.m and 0.0014 dB/Gy.m at wavelengths of 472 nm and 502 nm respectively.

Table 5.1 Optical fibers tested under gamma-ray radiation

Fiber Type	Core Diameter (μm)	Cladding Diameter (μm)	Coating	Core Dopant (concentration)	Cladding Dopant (concentration)	Manufacturer
SM-silica (Corning SMF-28)	9	125	Acrylate	Ge (3 mole %)	No dopant	Corning[1]
MM-silica (Corning 62.5/125)	61	125	Acrylate	Ge (N.A.)	No dopant	Corning
Ge-SM-18	3.6	125±2	Acrylate	Ge and P (GeO_2: 18 mole %)	F and P (N.A.)	INO[2]
Ge-MM-11	25±1	125±2	Acrylate	Ge and P (GeO_2: 11 mole %)	F and P (N.A.)	INO
P-MM-10	21	125±2	Acrylate	P_2O_5 (10 mole %)	F and P (N.A.)	INO
P-MM-05	40	125±2	Acrylate	P_2O_5 (5 mole %)	F and P (N.A.)	INO
P-MM-01	30	50	Acrylate	P_2O_5 (1 mole %)	Depressed F-doped (N.A.)	FORC[3]

Note: *: N.A., not available.

1. Corning, Corning Incorporated. USA
2. INO: INO, Quebec, Canada
3. FORC: Fiber Optics Research Center at the General Physics Institute, Russia

5.3.2 Normal multi-mode fiber

The gamma radiation effects in normal MM fibers are tested under the dose rates of both 0.5 Gy/min and 3.0 Gy/min. At dose rate of 0.5 Gy/min, a 12.7 m long MM fiber is irradiated for 5 minutes and then allowed to recover for 3 minutes. The radiation-induced loss at 0.5 Gy/min is shown in Fig. 5.5 and its recovery spectrum is shown in Fig. 5.6. Comparing Figs. 5.3 and 5.6 it is clear that normal MM fiber recovers more than normal SM fiber for the same total dose level. The absorption peaks in normal MM fibers are at the same wavelengths as those in SM fibers but with higher induced loss for the same dose level. The radiation induced loss vs dose at 472 and 505 nm in normal MM fibers is shown in Fig. 5.7. At 472 nm the radiation-induced loss has a non-linear relationship with total dose, while at 505nm the loss is linear with total dose. At the dose rate of 3.0 Gy/min, the radiation-induced loss on normal MM fibers is shown in Fig. 5.8. The loss vs. total dose at the absorption peaks is shown in Fig. 5.9. At the dose rate of 3.0 Gy/min we can see that the absorption peaks appear at shorter wavelengths compared to those at the dose rate of 0.5 Gy/min. This phenomenon needs to be studied further. Similar to those at the dose rate of 0.5 Gy/min, the radiation- induced loss at the 469 nm peak also shows nonlinear dependence on the total dose. While the radiation loss at 500 nm shows linear dependence on total dose. After 3.25 minutes of irradiation, the normal MM fiber recovers from most of the loss within in one minute (see Fig. 5.10). As a comparison, with 0.5Gy/min after three minutes recovery, the MM fiber still holds one half of the loss induced by the radiation field.

5.3.3 Ge-doped optical fibers

Ge-doped fibers are tested at the dose rate of 0.5 Gy/min. A 0.99 m long SM Ge-doped fiber is irradiated by gamma rays for five minutes at the dose rate of 0.5 Gy/min. The radiation-induced loss spectrum is shown in Fig. 5.11. Fig. 5.12 shows the radiation-induced loss vs. dose at 470 nm and 504 nm absorption peaks. After being irradiated the fiber is then allowed to recover for 3 minutes. No evident recovery effect is found. The induced loss has a linear relationship with total dose. The slopes, and thus the sensitivities are 0.068 dB/Gy.m and 0.02 dB/Gy.m at 470 and 504 nm respectively. The Ge-doped MM fiber with a length of 1.2 m is

irradiated at the dose rate of 0.5 Gy/min for twenty minutes. The absorption spectra are shown in Fig. 5.13 (the first ten minutes) and the radiation-induced loss vs. total dose is shown in Fig. 5.14. Similar to Ge-doped SM fiber, the recovery of Ge-doped MM fiber is not evident. It is clear from Fig. 5.14 that the loss of Ge-doped MM fiber at 470 nm is not linear with the total dose, but the loss at 505 nm is linear with total dose. The sensitivity of the Ge-doped MM fibers at 470 nm is 0.01 dB/Gy.m and it is 0.006 dB/Gy.m at 505 nm.

5.3.4 P-doped optical fibers

There are three types of P-doped fibers tested in the experiment with different dopant concentrations. All of the P-doped fibers are tested at the dose rates of 0.1, 0.2, 0.5 and 1.0 Gy/min. The radiation induced attenuation spectra of 1%, 5% and 10% P-doped fibers at various dose rates are shown in Figs. 5.15, 5.16 and 5.17. Figs. 5.15 to 5.17 show that there are at least four absorption bands around 470, 502, 540 and 600 nm in all P-doped fibers at all dose rates. Some experiments also show a weak absorption peak at 640 nm (Figs. 5.15b, 5.15c, 5.16d and 5.17d). According to the optical absorption spectrum of P-doped silica glass after gamma ray irradiation [47], the color centers that are associated to P_2O_5-dopant are phosphorus-oxygen-hole center (POHC) and PO_3^{2-}, PO_4^{4-} and PO_2^{2-} radicals. POHC is formatted by the trapping of a hole by two non-bridging oxygen atoms [47]. The four bands observed in this experiment, 470nm, 502nm, 540nm and 600nm, are not attributed to the P_2O_5-dopant in the fiber. This conclusion is confirmed by observing the gamma-induced loss spectrum in normal MM fibers. All the absorption bands mentioned above are observed with lower induced loss than that observed in P-doped fibers (Figs. 5.5, 5.8). The P_2O_5 dopant in the fiber has changed the absorbing intensities and induced loss. The P_2O_5 dopant in silica fiber may help the photons (gamma) to produce more free electrons to form color centers that associate with the defects in the silica. The absorption band near 470 nm has been reported before [50, 51] for Ge-doped fibers. It is defined as a GeX color center but its absorption mechanism is not clear so far. The reason that the 470 nm peak appears in our P-doped fiber absorption spectrum is that GeO_2 doping is used during fiber manufacture in order to achieve higher refractive index in the fiber core to form waveguides. This is true for all the communication fibers, both single mode and

multi-mode. The 600 nm band with a "shoulder" (Figs. 5.15c, 5.16d and 5.17d) is attributed to Non-Bridging Oxygen Hole Centers (NBOHC, trapping a hole by a non-bridging oxygen) [52]. The bands at 502 nm and 540 nm need to be further identified. They may be attributed to the defects in Ge-doped silica or some other impurities. The reason why we did not find absorption peaks attributed to POHC defect and PO_3^{2-}, PO_4^{4-} and PO_2^{2-} radicals may be due to the fact that number of these defect and radicals are less than other defects, such as GeX centers and NBOHCs, and/or the total dose (1.5 Gy) in this study may not be high enough to produce strong absorption peaks that are attributed to P-related defects and radicals.

Looking closely at the fiber loss in the spectrum peaks of 470 nm in Figs. 5.15-17, we find that the radiation induced loss increases with dose rate (0.1 - 0.5 Gy/min), but decreases at high dose rate (1.0 Gy/min) for all three different P-doping levels. On the other hand the fiber loss at 600 nm shows little dose-rate-dependence at dose rates from 0.1 to 0.5 Gy/min, but increases at 1.0 Gy/min. This indicates that there may be some relationship between the two color centers, GeX and NBOHC that are attributed to the absorptions at 470 nm and 600 nm respectively. The dose-rate dependence of the two absorption bands (470 nm and 600 nm) may be explained as follows: the gamma radiation initially generates NBOHCs, but the NBOHCs decay by releasing electrons either thermally or by photo-bleaching. Meanwhile GeX center formation is increased by trapping these electrons. At low dose rates there is enough time for this color- center conversion to occur during the irradiation process, hence we find a stronger absorption (high fiber loss) at 470 nm which is related to GeX centers. But at higher dose rate there may not be enough time for the NBOHC →GeX conversion to take place, so the NBOHC concentration in the fiber is relatively higher. Therefore a stronger absorption is generated at high dose rate (1.0 Gy/min) at 600 nm and a reduced absorption at 470 nm. A similar phenomenon was also found in Ge-doped silica fibers (conversion of Ge(1) centers to GeX centers) [50, 51].

Through this experiment we find that all the P-doped fibers show similar absorption behavior and among them the 5% P-doped fiber shows the greatest sensitivity (dB/(m.Gy) => induced loss per meter fiber and per Gy). This may be due to its much larger fiber core (40 μm) than those of 1% P-doped and 10% P-doped fibers (21 μm and 30 μm respectively). A larger

fiber core results in an increased absorption of photons (gamma ray) for the same dose rate. As a result, more color centers are formed and the radiation-induced fiber loss can increase.

After the three types of P-doped fibers are irradiated by gamma ray the loss spectra are monitored for up to 10 minutes and no evident recovery effects are observed for all P-doped fibers. This means the gamma-induced loss in P-doped fibers is permanent or the recovery is long term. The diode lasers shown in Fig. 5.1 with the wavelengths of 630, 670, 780 and 840 nm are used to examine the "photo bleaching" effect after the recovery of the P-doped fibers. No evident "photo bleaching" is found for all types of fiber samples. This may due to the fact that the wavelengths of the diode lasers are longer than that associated with the color centers (470, 502 and 600 nm). The photon energy is not high enough to "erase" the color centers.

The gamma-induced fiber loss vs. total dose at different absorption peaks for various dose rates are shown in Fig. 5.18. From Figs. 5.15-17 it can be seen that 5% P-doped fiber shows the highest fiber loss due to gamma irradiation. Fig. 5.18 only shows the loss-dose relationship of 5% P-doped fiber.

5.4 Possibility of using P-doped fibers as radiation sensors

Section 5.3 shows that 5% P-doped fiber has the highest loss among all the fibers that are tested. This section examines the possibility of using this fiber as the sensing component of a dosimeter for low dose levels.

To be qualified as a fiber optic dosimeter, the radiation induced fiber loss should have a linear relation to the total dose within the region of application. In order to study this effect, we checked the correlation between the total dose and the induced loss at various dose rates for different absorption peaks. Figs. 5.18a, 5.18b, 5.18c and 5.18d show the radiation-induced loss in 5% P-doped fiber at four different bands with different dose rates. In Fig. 5.18a we can see that the induced loss of this fiber at 470 nm strongly depends on the dose rate. At the dose rates of 0.2 Gy/min and 0.5 Gy/min the induced fiber loss increases exponentially with total dose, while at both

low and high dose rates (0.1 Gy/min and 1.0 Gy/min) the fiber loss increases linearly with the total dose within 1.6 Gy range. The induced fiber losses at 502 nm and 540 nm (Figs. 5.18b and 5.18c) show excellent linear relationships with total absorbed dose and little dose rate dependence, a quality desired of a practical dosimeter. The sensitivities of all fibers tested around 502 nm are listed in table 5.2. The sensitivity of 5% P-doped fiber at 502 nm is 0.15 dB/Gy.m. As a comparison, the sensitivity of standard SM communication fiber (much cheaper than P-doped fiber and widely used) at 502 nm is only 0.0014 dB/Gy.m, which is approximate 100 times lower than that of 5% P-doped fiber.

In summary, 5% P-doped fibers possess the following properties required for radiation sensors: 1) Small size; 2) High sensitivity; 3) Linear relationship between induced loss and total dose; 4) No dose-rate dependence of induced loss at certain wavelengths; and 5) No recovery of induced loss. These properties make 5% P-doped fiber a good candidate to measure radiation dose in radiation therapy applications.

Table 5.2 Sensitivities of optical fibers to gamma radiation (dB/Gy/m)
(based on the absorption peak of each fiber sample)

Fiber type	Normal SM	Normal MM	Ge-SM	Ge-MM	1% P-doped	5% P-doped	10% P-doped
Sensitivity (dB/Gy/m)	0.0014 @502 nm	0.004 @505 nm	0.02 @504 nm	0.006 @505 nm	0.09 @507 nm	0.15 @502 nm	0.11 @ 504 nm

5.5 Conclusion

Ge-doped, P-doped, normal single-mode (SM) and multi-mode (MM) optical fibers are exposed to Cobalt-60 gamma radiation at dose rates of 0.1 to 3.0 Gray(Gy)/min, typical radiotherapy dose rates. A CCD-based fiber optic spectrometer is used to measure the real-time absorption spectra of these fibers in the visible region. Experimental results have shown that P-

doped fiber is the most radiation-sensitive and normal SM fiber is the least radiation-sensitive of the fibers tested. At the wavelength of 502 and 540 nm, the radiation induced loss in P-doped fiber shows a linear relationship with the total dose with no dose-rate dependence. This indicates that dose rates have no influence on a fiber optic dosimeter operating at these wavelengths. The radiation induced losses in normal MM fibers, Ge-doped MM fibers and Ge-doped SM fibers are shown to be dose rate dependent. Compared to standard communication fiber (SMF-28), P-doped fiber is at least 100 times more sensitive to gamma irradiation. This suggests that P-doped fiber is a good candidate for fiber optic dosimetry operating at 502 nm or 540 nm in radiation therapy applications.

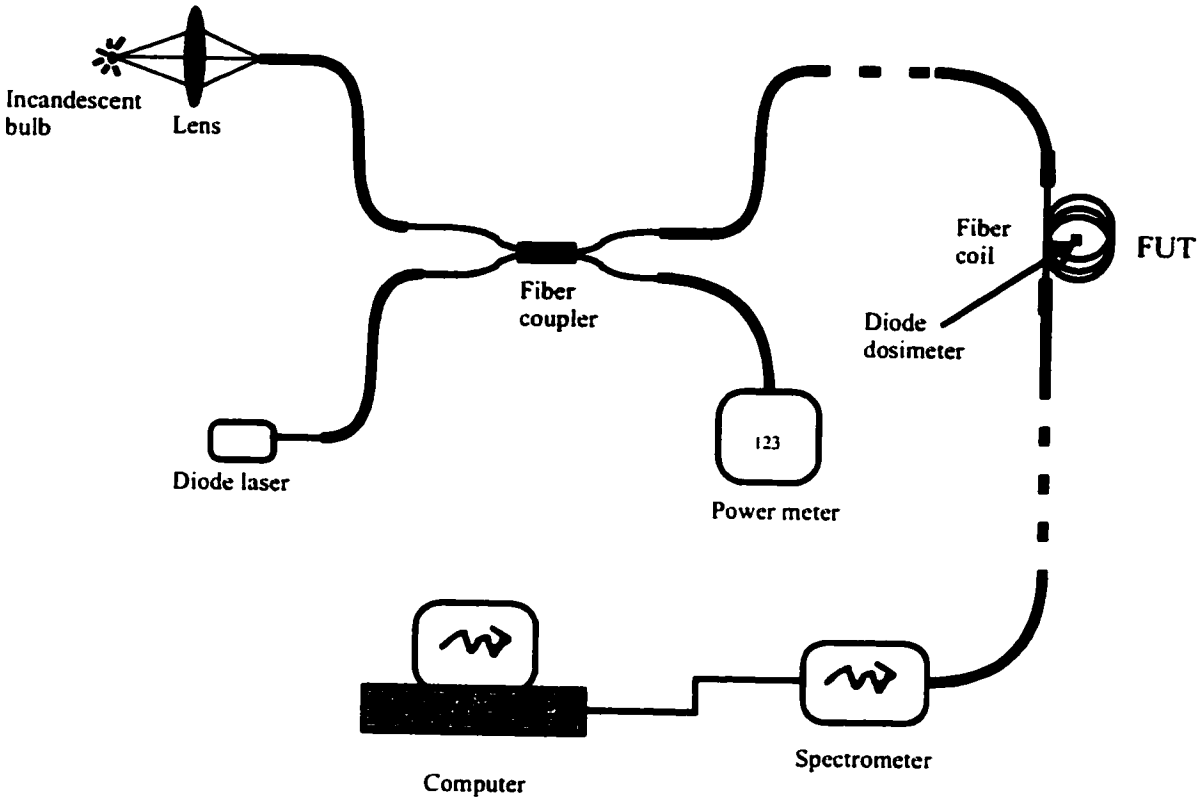

Figure 5.1 Setup of measuring the gamma ray induced attenuation in optical fibers.

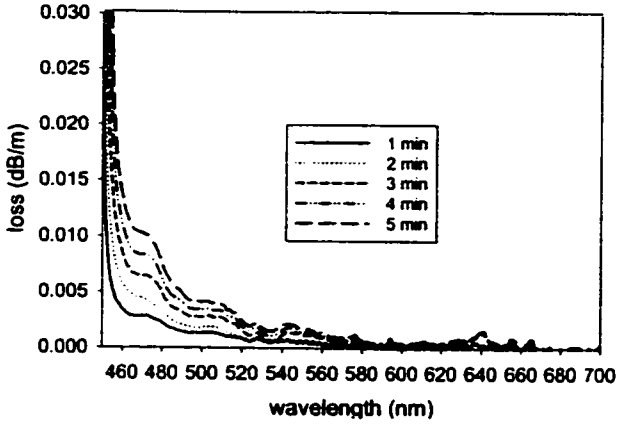

Figure 5.2 Gamma radiation induced loss of SM fiber (SMF 28) at the dose rate of 0.5 Gy/min.

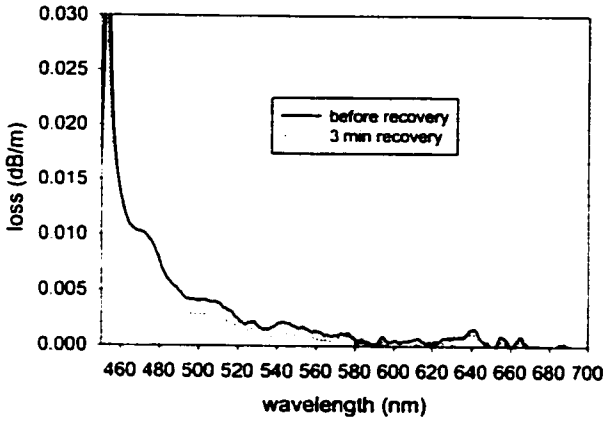

Figure 5.3 Recovery of SM fiber after 5 minutes irradiation at the dose rate of 0.5 Gy/min.

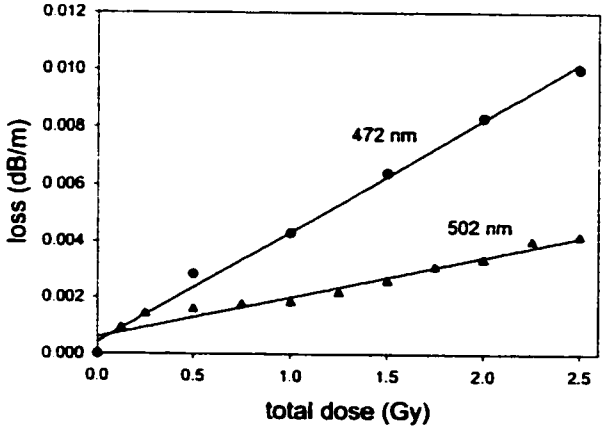

Figure 5.4 Loss vs. dose of SM fiber at the dose rate of 0.5 Gy/min.

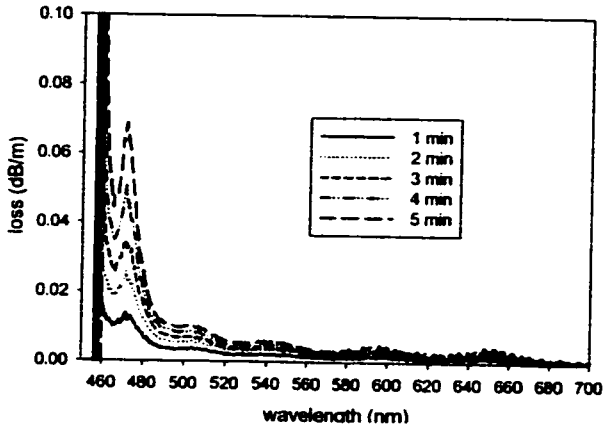

Figure 5.5. Gamma radiation induced loss of MM fiber at the dose rate of 0.5 Gy/min.

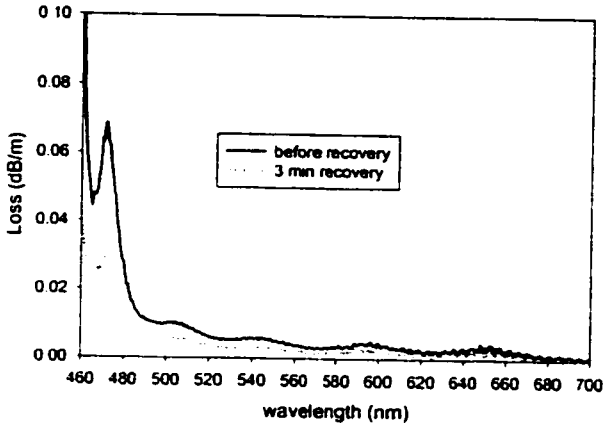

Figure 5.6 Recovery of MM fiber after 5 minutes irradiation at the dose rate of 0.5 Gy/min.

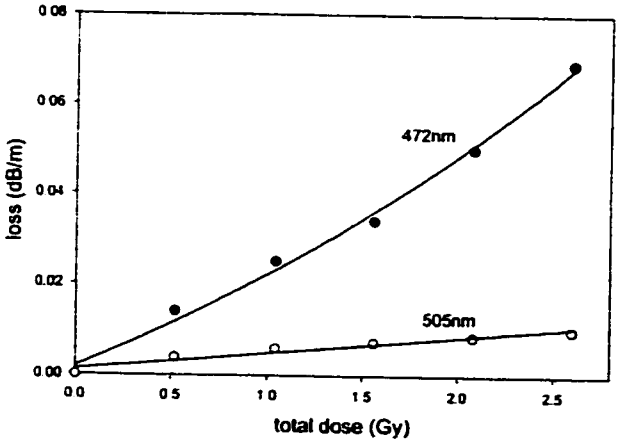

Figure 5.7 Loss vs. dose of MM fiber at the dose rate of 0.5 Gy/min.

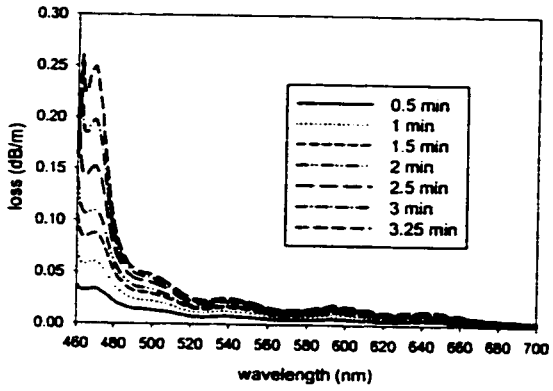

Figure 5.8 Gamma radiation induced loss of MM fiber at the dose rate of 3.0 Gy/min.

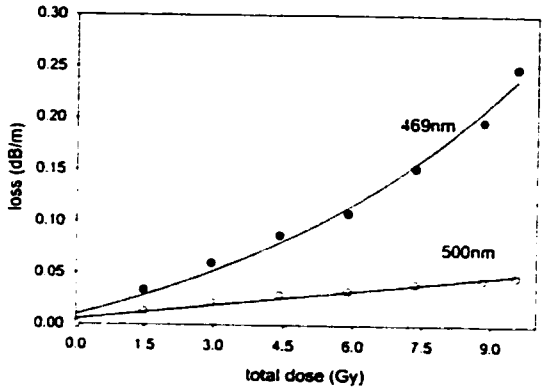

Figure 5.9 Loss vs. dose of MM fiber at the dose rate of 3.0 Gy/min.

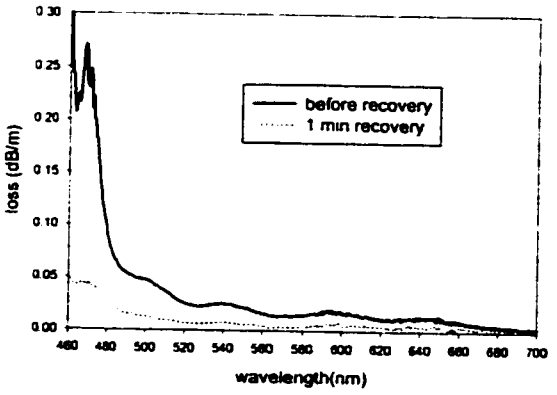

Figure 5.10 Recovery of MM fiber after 3.25 min irradiation at the dose rate of 3.0Gy/min.

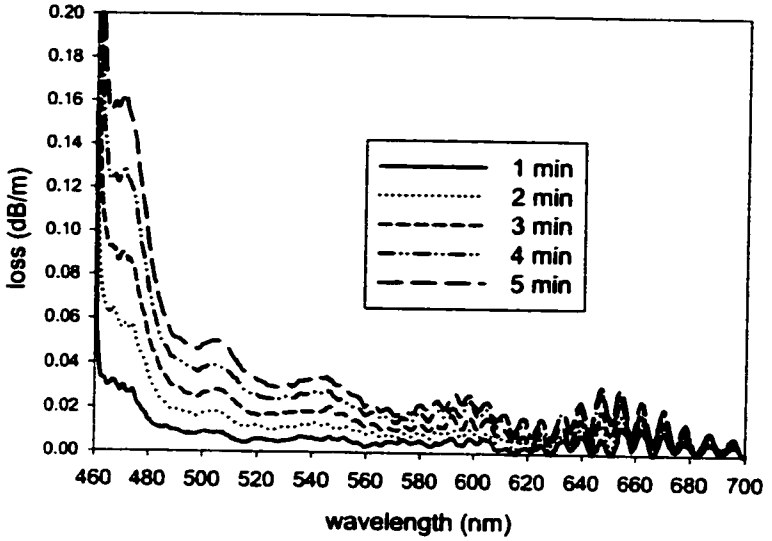

Figure 5.11 Gamma radiation induced loss of Ge-doped SM fiber at the dose rate of 0.5 Gy/min.

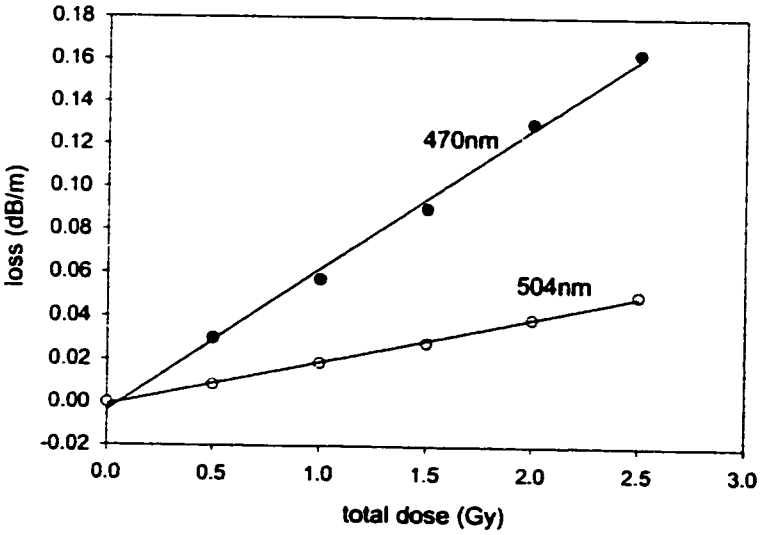

Figure 5.12 Loss vs. dose of Ge-doped SM fiber at the dose rate of 0.5 Gy/min.

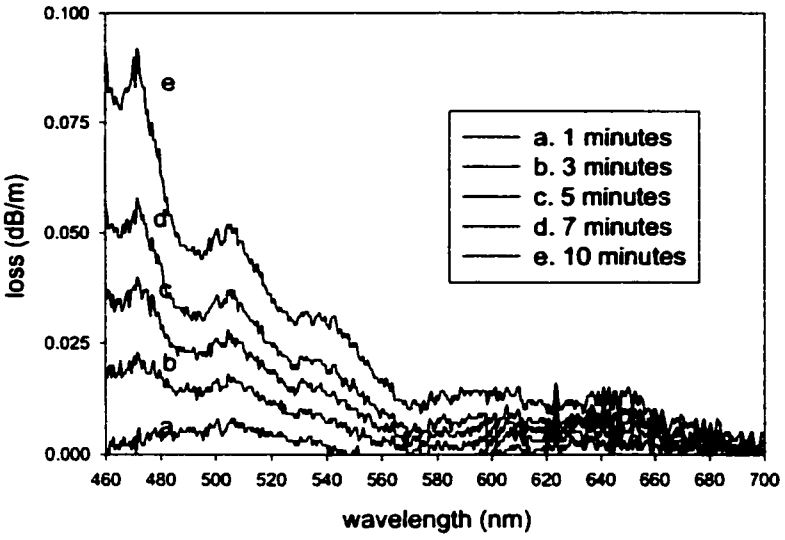

Figure 5.13 Gamma radiation induced loss of Ge-doped MM fiber at the dose rate of 0.5 Gy/min

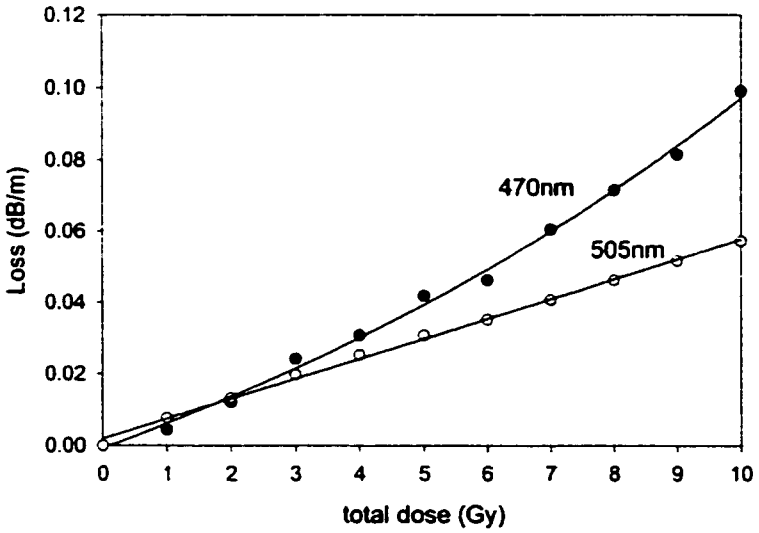

Figure 5.14 Loss vs. dose of Ge-MM fiber at the dose rate of 0.5 Gy/min

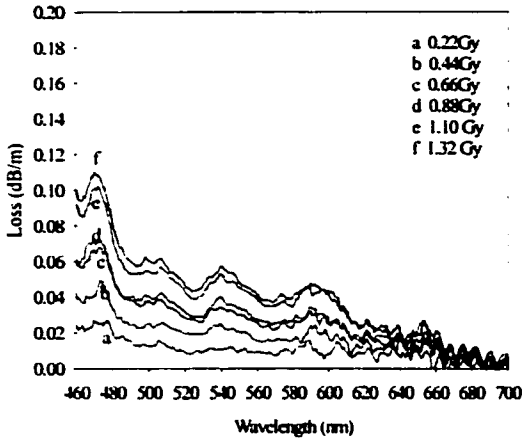

a) Dose rate of 0.1Gy/min

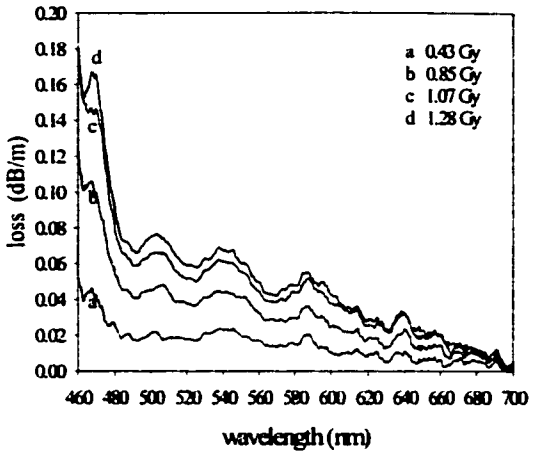

b) Dose rate of 0.2 Gy/min

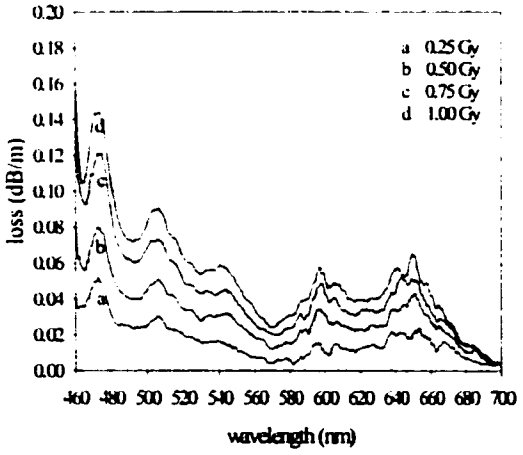

c) Dose rate of 0.5 Gy/min

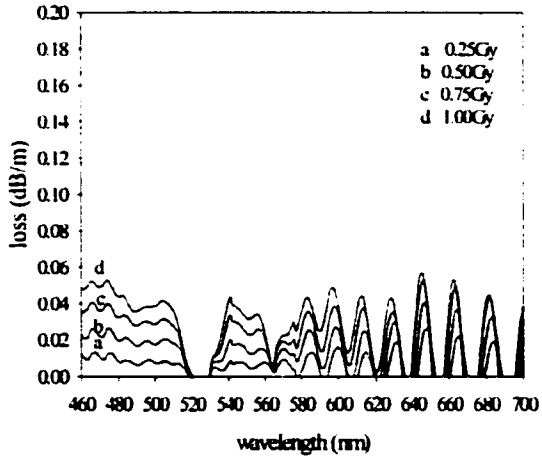

d) Dose rate of 1.0 Gy/min

Figure 5.15 Radiation induced absorption spectra of 1 mole % P-doped silica fiber at various dose rates.

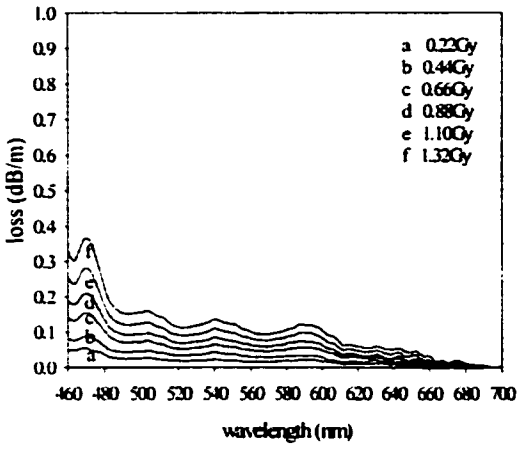

a) Dose rate of 0.1Gy/min

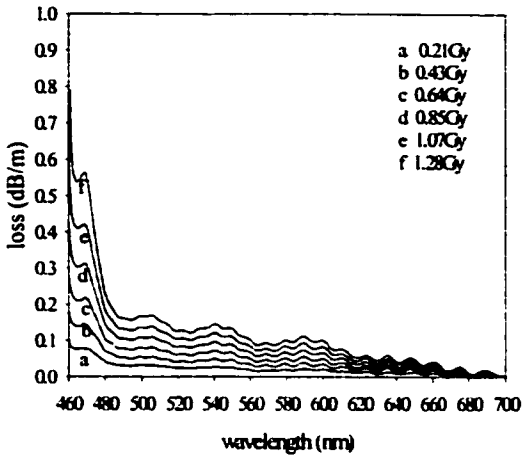

b) Dose rate of 0.2Gy/min

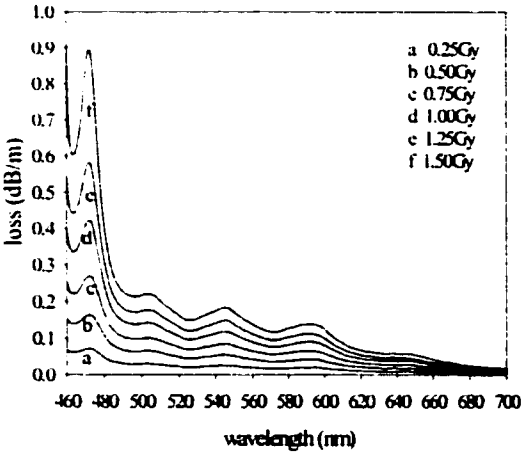

c) Dose rate of 0.5Gy/min

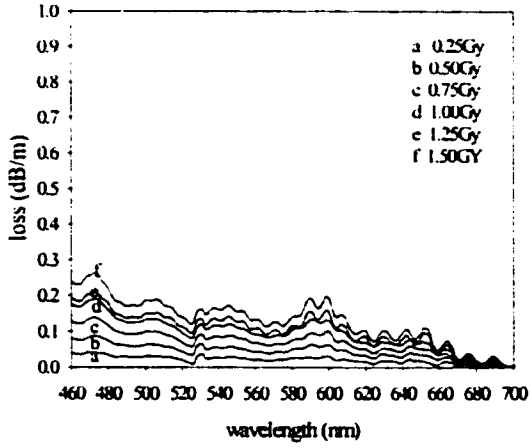

d) Dose rate of 1.0 Gy/min

Figure 5.16 Radiation induced absorption spectra of 5 mole % P-doped silica fiber at various dose rates.

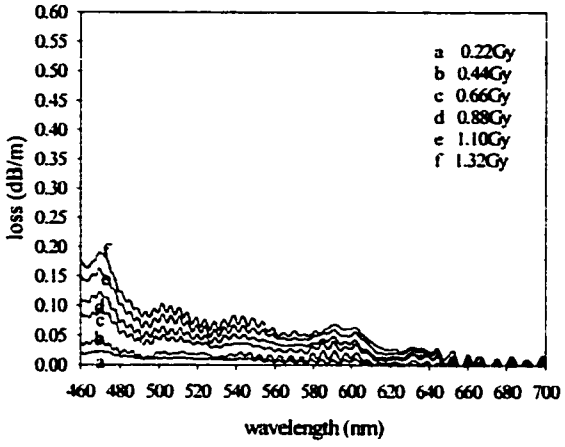

a) Dose rate of 0.1Gy/min

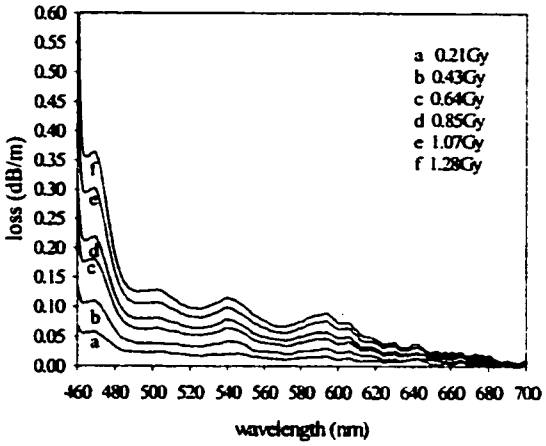

b) Dose rate of 0.2Gy/min

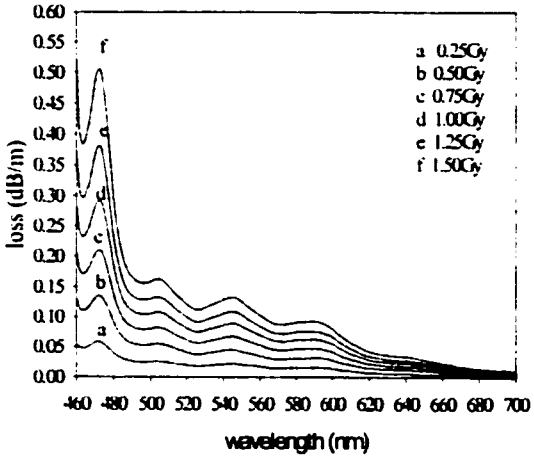

c) Dose rate of 0.5Gy/min

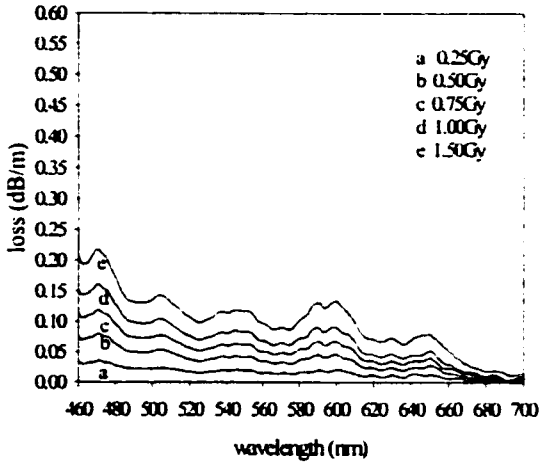

d) Dose rate of 1.0 Gy/min

Figure 5.17 Radiation induced absorption spectra of 10 mole % P-doped fiber at various dose rates.

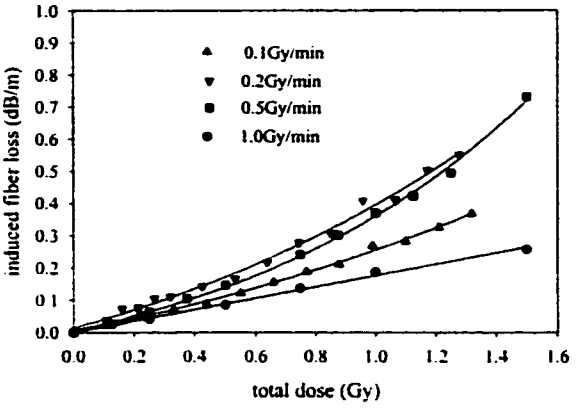

a) Induced loss of 5 mole % P-doped fiber at 470nm vs total dose

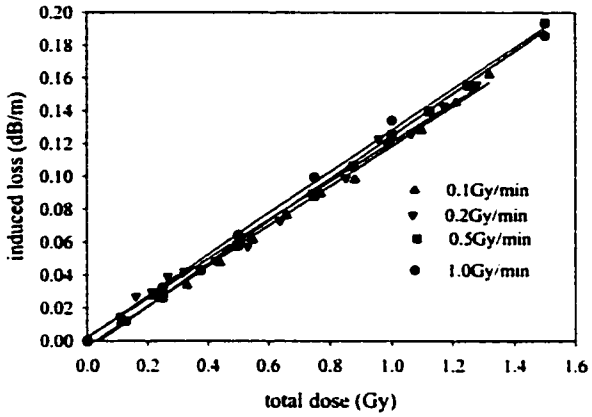

b) Induced loss of 5 mole % P-doped fiber at 502nm vs total dose

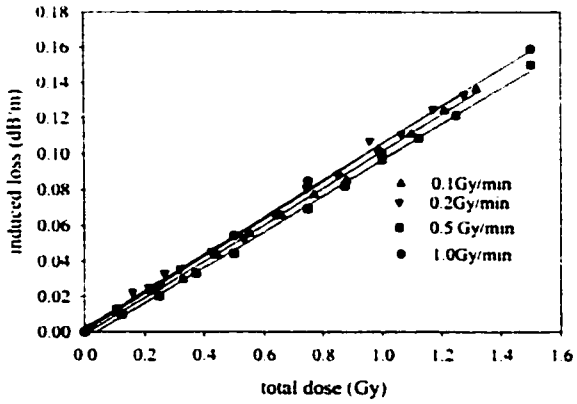

c) Induced loss of 5%P-doped silica fiber at 540nm vs total dose

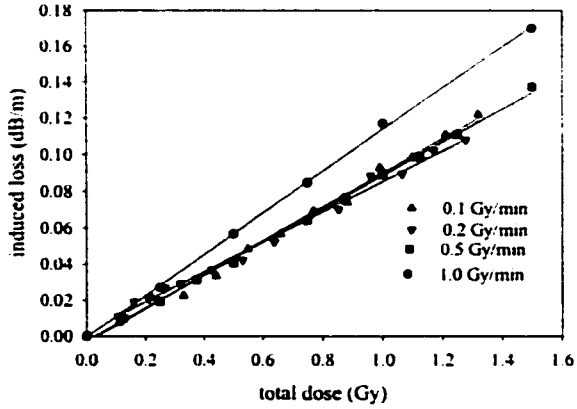

d) Induced loss of 5 mole % P-doped fiber at 600nm vs total dose

Figure 5.18 Radiation induced fiber loss (dB/m) vs total dose (Gy) at various dose rates. Here we only show the results of 5 mole % P-doped fiber which has the highest sensitivity. Other P-doped fibers show similar results but with lower sensitivity.

Chapter 6

Overview of the Studies of Polarization Effects in Fiber Optic Communication Systems

6.1 Introduction

Fiber optic communication systems are capable of transmitting high data rates over long distances. Part 2 of the thesis examines various aspects of two polarization effects, polarization mode dispersion (PMD) and polarization dependent loss (PDL), in fiber optic systems. These two polarization effects limit the transmission capacity of high speed communication systems.

6.2 Fiber optic communication systems

Fiber optic communication systems are lightwave systems that employ optical fibers for information transmission. A typical fiber optic communication system includes three major parts: optical transmitter, optical fibers and optical receiver, see the block diagram in Fig. 6.1 [53].

At the optical transmitter end, the electrical signal, which is initially in the form of a binary digital signal, is converted by modulating the optical carrier wave. The modulator acts as an optical switch. When a bit "1" of electrical signal is input into the modulator, the modulator switches on and a optical bit "1" is generated. When there is no electrical signal given to the modulator it switches off that corresponds to optical bit "0". The laser can also be modulated directly by modulating the injection current of the semiconductor laser. Due to the rise and fall times of the modulator a series of bits is represented by a series of pulses that may include

frequency chirp. A pulse is chirped if its carrier frequency changes with time [6]. The optical signal (a series of bits or pulses) is then launched into optical fibers through a coupler. Due to the loss and dispersions in the fibers the pulses may be distorted when transmitting in the fiber.

At the receiver end the optical signal is launched into a photodetector that converts the optical signal into an electrical signal with some distortions. For an *intensity modulation with a direct detection system* (IM/DD) the demodulation is done by a decision circuit that identifies bits as "1" or "0". There usually exists a threshold current in the circuit. If the current from the photo detector is higher than this threshold a "1" bit is declared and if the current from the photo detector is lower than the threshold a "0" bit is declared. The decision time, t_d, of sampling the current is controlled the clock signal. An error bit is generated if the decision circuit declares a "1" bit as a "0" bit or declares a "0" bit as a "1" bit due to the signal distortion. The bit error rate (BER) is defined as the number of error bits divided by the total number of bits. The sources of errors may include the distortion of pulses in transmission, the noise of the detector and the distortion of the clock signal etc. The noises from the detector include thermal noise, shot noise, spontaneous-emission noise and the *beatings* of spontaneous-emission noise against itself, signal and shot noise [54].

The second part of the thesis mainly studies the pulse distortion when the pulses transmit in optical fiber and how the distortion affects a fiber optic communication system. For low bit rate fiber optic communication systems (2.5 Gbits/second and below) the bit rate and transmission distance are limited by fiber loss and fiber chromatic dispersion. Fiber losses include the absorption of the glass material, Rayleigh scattering and fiber imperfections etc. Fiber loss is usually expressed in the unit of dB as

$$\alpha = -10\log_{10}\left(\frac{P_{out}}{P_{in}}\right), \tag{6.1}$$

where P_{out} is the optical power at the fiber output end when the optical power P_{in} is launched to the fiber. Sometimes fiber loss is expressed by the loss per kilometer. Due to the fiber loss, the optical signal is attenuated and the signal to noise ratio (SNR) at the receiver is decreased, and

as a result the BER of the whole system is increased. Presently the fiber loss is compensated by using optical amplifiers, such as Erbium-doped fiber amplifiers (EDFAs).

Another limitation factor of system bit rate and distance is the fiber chromatic dispersion. Chromatic dispersion refers to the frequency dependence of the refractive index of the material. As a result, the group velocity is frequency dependent. As we know that a pulse consists of different frequency components, when the different frequency components of the pulse travel at slightly different group velocities, the output pulse is broadened. The direct result of pulse broadening is the decreasing of the optical power of bit "1" at the decision time, and resulting in a higher BER. Pulse broadening also spreads the energy (power of bit "1" or bit "0") in one bit slot into adjacent slots causing intersymbol interference. The pulse broadening, σ_b^2, can be expressed as the difference between the output *rms* pulse width and the input *rms* pulse width given by

$$\sigma_b^2 = \sigma_{out}^2 - \sigma_{in}^2 = \left[\frac{\int_{-\infty}^{\infty} t^2 P_{out}(t)dt}{\int_{-\infty}^{\infty} P_{out}(t)dt} - \left[\frac{\int_{-\infty}^{\infty} tP_{out}(t)dt}{\int_{-\infty}^{\infty} P_{out}(t)dt}\right]^2\right] - \left[\frac{\int_{-\infty}^{\infty} t^2 P_{in}(t)dt}{\int_{-\infty}^{\infty} P_{in}(t)dt} - \left[\frac{\int_{-\infty}^{\infty} tP_{in}(t)dt}{\int_{-\infty}^{\infty} P_{in}(t)dt}\right]^2\right], \tag{6.2}$$

where $P_{out}(t)$ and $P_{in}(t)$ are the optical powers at the fiber output and input. Chromatic dispersion is a fixed value once a system is determined. It can be compensated either by using a piece of fiber with opposite chromatic dispersion or by shifting the fiber dispersion to let the minimum chromatic dispersion being located at the operating frequency range [11]. The chromatic dispersion effect can also be compensated by introducing a frequency chirp in the pulse [6].

With the development of high speed fiber optic communication systems, the bit rate can be as high as 10 Gbits/second (OC192) and 40 Gbits/second (OC768). When fiber loss and chromatic dispersion are compensated, other factors, such as the fiber nonlinear effects,

polarization mode dispersion (PMD) and polarization dependent loss (PDL), limit the system capacity. The interaction of these limiting factors in fiber optic communication systems is complex and makes their compensation difficult [11]. This part of the thesis mainly studies the polarization effects (PMD and PDL) in fiber optic communication systems, which include the properties of PMD and PDL, their interaction and system impact.

6.3 Polarization mode dispersion

6.3.1 Single-mode fiber and birefringence

A lightwave that can propagate a long distance in optical fiber is composed of many discrete modes. A mode refers to a specific solution of the wave equations (Maxwell equations) that satisfies the appropriate boundary conditions and has the property that its spatial distribution does not change with propagation [6]. A single mode fiber refers to a fiber that can only support one fundamental transmission mode. This fundamental mode is a transverse wave and is called HE_{11} mode. The polarization states of the HE_{11} mode, $\vec{\varphi}$, can be any states. In a x-y-z coordinate system with the lightwave transmitting along z-direction, $\vec{\varphi}$ can be decomposed to x- and y-directions as

$$\vec{\varphi} = \varphi_x \vec{i} + \varphi_y \vec{j}, \tag{6.3}$$

where $\vec{i}$ and $\vec{j}$ are unitary vectors in the x- and y-directions and $\varphi_x^2 + \varphi_y^2 = 1$. In a perfect single mode fiber, light propagates with a constant group velocity that is independent of polarization states. In other words, the two polarization states along $\vec{i}$ and $\vec{j}$ are degenerate. In practice, the asymmetry of the fiber core and external strain on the fiber break this degeneracy and induce a difference of effective refractive index, Δn, known as the fiber birefringence, see Fig. 6.2.

$$\Delta n = |n_x - n_y| \tag{6.4}$$

where n_x and n_y are the effective refractive indices when the polarization is along the x- and y-directions. Due to this refractive index difference, the lightwave propagates with different velocities when its polarization is along the x- and y-directions.

6.3.2 Principle states of polarization and differential group delay

The birefringence in single mode fibers changes with both wavelength and environmental perturbations, such as temperature, vibration and strain. For a long single mode fiber the description and analysis of the birefringence effect are complicated due to the arbitrary variation of spatial orientation of birefringence. In 1986 Poole *et al* proposed the concept of the principal state of polarization (PSP) [7]. It has been shown by Poole *et al* that for every fiber having PMD there exists at every wavelength an orthogonal pair of input principal states of polarization (PSP's) whose output states of polarization (SOP's) are independent of wavelength to the first order. This means that when a wide input pulse is launched to one of the PSP's the pulse distortion is minimal. Furthermore, if a chirp-free pulse is launched to one of the two PSP's, the time delay is either maximum or minimum [7]. The PSP that gives the minimum time delay is called the fast PSP and the other is called the slow PSP. The difference of time delays when the pulse travels along the fast and the slow PSP's is defined as the differential group delay (DGD). The concept of PSP is very useful for understanding the PMD effects in fibers with high mode coupling (a fiber is highly mode coupled if the fiber length is much longer than the length scale over which the birefringence orientation changes). For instance, in the first-order approximation of PMD (DGD is constant over the spectrum of the pulse), the pulse broadening can be simply expressed as [56]

$$\Delta\sigma = \sigma_{out} - \sigma_{in} = \sqrt{\sigma^2{}_{in} + \tau^2\gamma(1-\gamma)} - \sigma_{in}, \tag{6.5}$$

where γ ($0 \le \gamma \le 1$) is the relative power launched to the fast (or slow) PSP and τ is the DGD of the fiber. When equal powers are launched to the two PSP's ($\gamma = 1/2$) the maximum pulse broadening occurs and when all the power is launched to either the fast or the slow PSP ($\gamma = 1$ or 0) there is no pulse broadening.

Due to environmental perturbations, the PSP's and DGD in single mode fibers change with time and frequency. The averages of DGD over frequency and over time at a single frequency are equivalent and are called PMD [15].

6.3.3 Measurements of PMD and SOP

The methods of DGD and PMD measurements include the fixed-analyzer method (wavelength scanning method), the Jones matrix eigenanalysis (JME) method, the interferometric method, the Poincare arc method, the modulation phase shift method and the pulse delay method [57]. The Jones matrix eigenanalysis method and the interferometric method are most commonly used

Polarized light can be represented by a two-element vector, the elements of which specify the magnitude and phase of the x- and y-components of the electric field at a particular point in space [58]. The Jones vector has the form

$$\vec{E} = \begin{pmatrix} E_x \\ E_y \end{pmatrix} = \begin{pmatrix} E_{0x} e^{i\delta_x} \\ E_{0y} e^{i\delta_y} \end{pmatrix} \tag{6.6}$$

where the real quantities E_{0x} and E_{0y} represent the maximum amplitudes and δ_x and δ_y represent the phases. The transmission properties of a two-port optical device can be described by the complex two-by-two Jones matrix, $T(\omega)$, which relates the input and output Jones vectors [58]. That is:

$$\vec{E}_{out} = T(\omega)\vec{E}_{in}. \tag{6.7}$$

The Jones polarization calculus can only deal with fully polarized light. For partially polarized light, it is often represented in Stokes four parameters, S_0, S_1, S_2 and S_3. S_0 is the total optical power (both polarized and unpolarized), S_1 is the power through a linear horizontal polarizer minus the power through a linear vertical polarizer, S_2 is the power through a linear plus 45^0 polarizer minus the power through a linear minus 45^0 polarizer, and S_3 is the power through a right circular polarizer minus the power through left circular polarizer. The degree of polarization can be written as [57]:

$$DOP = \frac{\sqrt{S_1^2 + S_2^2 + S_3^2}}{S_0} \tag{6.8}$$

The Jones matrix eigenanalysis (JME) method is based on the measurement of the Jones matrices of the fiber under test at two closely spaced frequencies. The DGD of the fiber at the intermediate frequency can be determined from the two matrices even in the presence of PDL [13, 59]. The Agilent 8509B polarization analyzer, which is based on the JME method, is used to measure the SOP and DGD in this thesis. A block diagram of this test set is shown in Fig.6.3. A laser with frequency ω is launched to the polarization analyzer that splits the light into four separate beams. The four beams pass through different polarizing and retarding elements and reach four photo detectors [57]. From the signals of the four detectors (four Stokes parameters), the SOP and degree of polarization (DOP) of the light are obtained. The Jones matrix of the fiber under test at frequency ω is determined by measuring the output SOPs (port 3) that correspond to the fixed input SOPs (port 2) and using the relation of the SOP and Jones matrix as shown in Eq. 6.7. By tuning the laser frequency to $\omega + \Delta\omega$ and measuring the Jones matrix at frequency $\omega + \Delta\omega$, the DGD of the fiber at frequency $\omega + \Delta\omega/2$ can be obtained [57]. The JME method is usually used in the laboratory because it requires a stable environment (during the measurement, the fiber under test should be stable).

The detailed description of the interferometric PMD measurement method can be found in many publications [57, 60]. This method gives the rms value of DGD over a spectrum range of the light source (LED). Light from a LED source passing through the fiber is launched to a Michelson interferometer and is then collected by a detector. The signal from the detector is recorded when one arm of the michelson interferometer scans over a certain range. If the PMD of the fiber under test is larger than the coherence time of the LED source, the fringe pattern will have a main peak and two satellite peaks. The main peak corresponds to the equal delays in the arms of the interferometer and the two satellite peaks corresponds to the DGD of the fiber. For a fiber with high mode coupling, the fringe pattern of the interferometer consists of a series of peaks instead of two satellite peaks and the rms DGD can be obtained from the distribution of these peaks [57, 60]. Because this method does not depend on the polarization states in the fibers (which is very sensitive to the temperature, strain etc.), it is widely used for field testing.

In chapter 7 the Poincare arc method is also used to measure the DGD orientation in fibers and components. The DGD vector, $\bar{\Omega}(\omega)$, is measured by measuring the Stokes vector, $\bar{S}(\omega)$, and using the following equation [61],

$$\frac{d\bar{S}}{d\omega} = \bar{\Omega} \times \bar{S}. \tag{6.9}$$

From the trajectory of Stokes vectors at different frequencies the DGD vector can be calculated.

6.4 Polarization dependent loss

6.4.1 Definition of polarization dependent loss

Polarization dependent loss (PDL) is another polarization effect in fiber optic communication systems. PDL refers to the fiber attenuation changes with input SOP. It can be expressed in the unit of dB as

$$PDL = 10 \cdot \log_{10}\left(\frac{P_{max}}{P_{min}}\right), \tag{6.10}$$

where P_{max} and P_{min} are the maximum and minimum power transmittance with different input SOP's. It can be shown that the two SOP's. which maximize or minimize the power transmission, are orthogonal [57].

6.4.2 Measurement of polarization dependent loss

Two methods of PDL measurement are widely used. One is called Polarization scanning method and the other is called Jones Matrix Eigenanalysis (JME) method [57]. Polarization scanning method uses a polarization controller between a light source (fully polarized) and the input of the fiber under test. The output power of the fiber is recorded when the polarization controller is scrambling. The difference of the maximum and the minimum output powers (in the unit of dBm) is the PDL of the fiber in the unit of dB.

The JME method is to measure the Jones matrix, $T(\omega)$, of the fiber under test. The PDL can be obtained from the two eigenvalues of the matrix $D(\omega) = T^{+}(\omega) \cdot T(\omega)$:

$$PDL = 10\left|\log_{10}\left(\frac{d_1}{d_2}\right)\right|, \tag{6.11}$$

where $T^{+}(\omega)$ is the hermitian of $T(\omega)$, d_1 and d_2 are the two eigenvalues of matrix $D(\omega)$.

6.5 Interaction of PDL and PMD

PMD and PDL usually co-exist in fiber optic communication systems. In the presence of both PMD and PDL the two PSP's are not necessary mutually orthogonal [9, 13], see Fig. 6.4. As a result, the lightwaves propagating along the two PSP's may interfere and produce anomalously large pulse broadening [13]. Due to the interaction of PMD and PDL, the following effects have been reported: 1) The two PSP's that are orthogonal in the absence of PDL are not orthogonal in general [9, 13]; 2) For a fiber consisting of two DGD elements sandwiched by a PDL element, the effective DGD of the fiber can be larger than the sum of the two DGDs. 3) The output pulse can be broadened in the presence of zero DGD and it can be narrowed in the presence of finite DGD [9, 18]; 4) In the absence of PDL the statistical distribution of DGD is a Maxwellian, however, it is the combination of Gaussian and Maxwellian functions in the presence of high PDL [17]; 5) The combined effect of PMD and PDL induces more severe system impairment than PMD or PDL alone [9, 62].

6.6 System impact due to PMD and PDL

PMD alone in a fiber optic system induces pulse broadening, see Fig. 6.5. A direct effect induced by the pulse broadening is the decrease of the pulse peak power. The other effect due to pulse broadening is that the optical power in one bit slot may spreads into adjacent slots causing intersymbol interference. PDL alone causes statistical global attenuation that induces power fluctuations in the system [13]. Both PMD and PDL show stochastic properties due to environment

perturbations. The properties and system impact of PMD and PDL are usually studied statistically. For analog systems, it has been shown that the pulse broadening due to the first order DGD is a Rayleigh distribution [20]. For digital systems, the impact of PMD has been studied by examining the distributions of eye-opening [11], system Q factor [21] and system outage probability [8]. The acceptable PMD value in a system is around 10% of the bit period including moderate chromatic dispersion and frequency chirp[8, 21]. In the presence of both PMD and PDL, it has been shown that the system BER gets higher than the case of PMD alone [9]. So far the system impact due to PDL alone and its combination with PMD has not been studied quantitatively in terms of system outage probability and the acceptable PMD value in the presence of PDL, which will be examined in this thesis.

6.7 Main work of part 2 of the thesis

Part 2 of the thesis examines the following aspects of PMD and PDL. Chapter 7 examines the statistical distributions of DGD in the presence of PDL and biased elliptical birefringence. A new waveplate model is proposed, which overcomes the limitations of the conventional waveplate model (DGD and PDL have upper limits). Chapter 8 studies the statistical distributions of PDL in the presence of PMD. Chapter 9 studies the high order DGD and PDL effects in fibers. The concepts of PMD, PDL and PSP for an optical pulse are proposed. The system impact due to the combined effect of PMD and PDL is studied in chapter 10 in terms of Q factor, BER and system outage probability. The acceptable PMD values in the presence of PDL at various power margins are discussed.

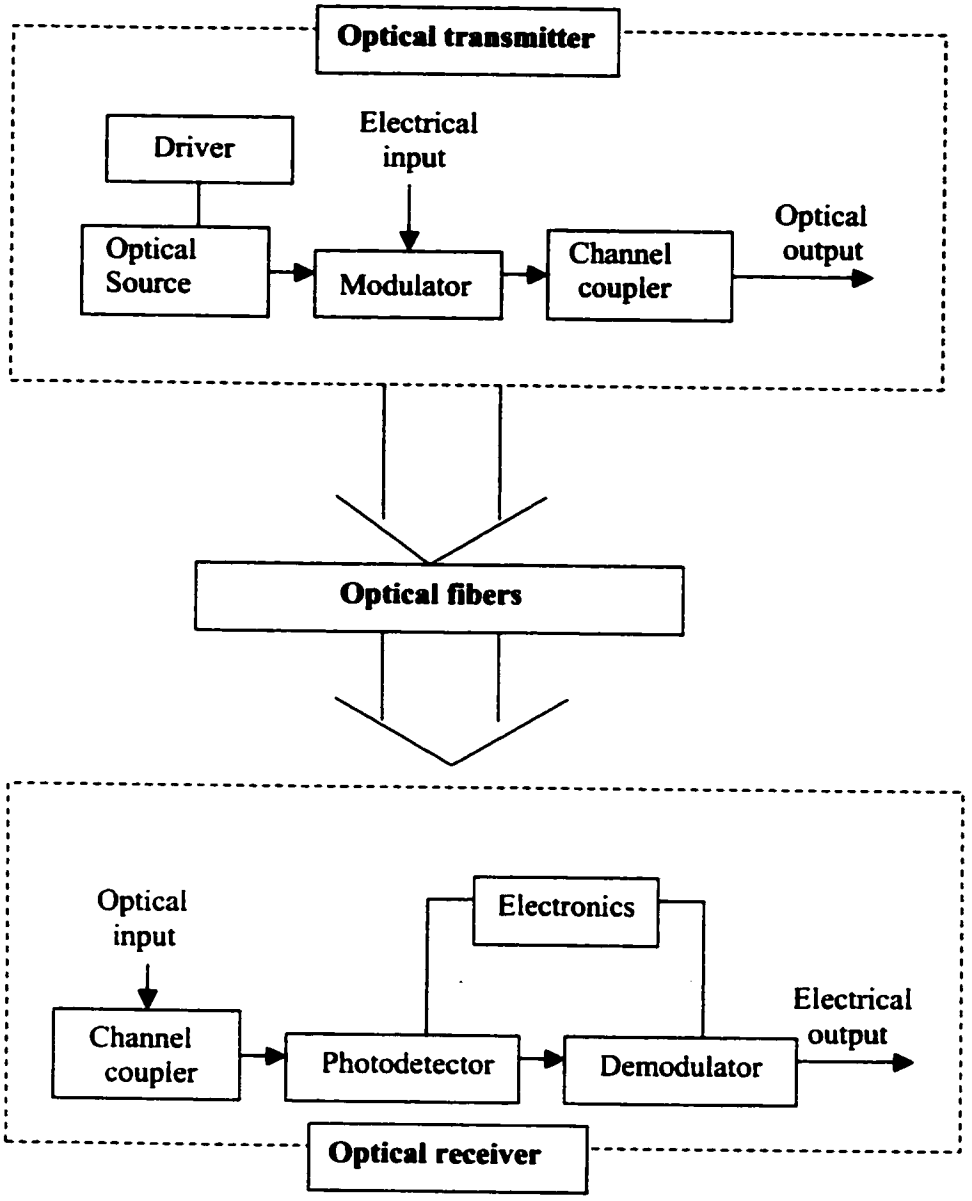

Figure 6.1 Block diagram of a typical fiber optic communication system.

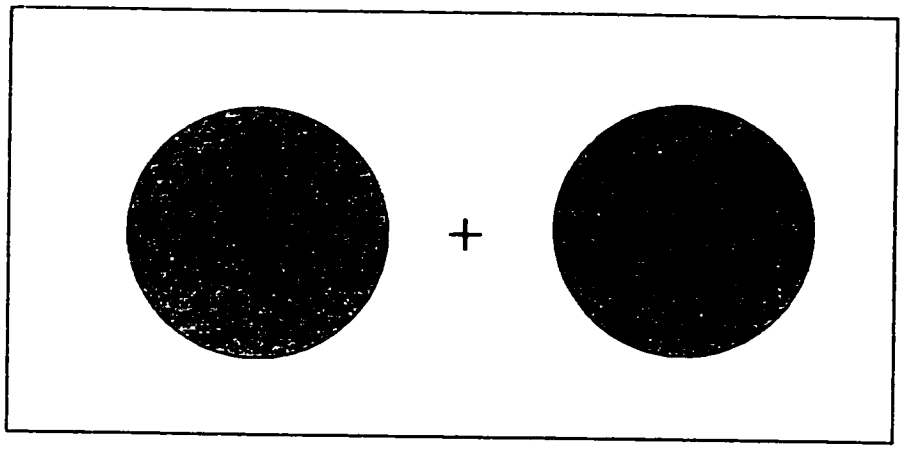

a) Two degenerate polarization modes in ideal fibers

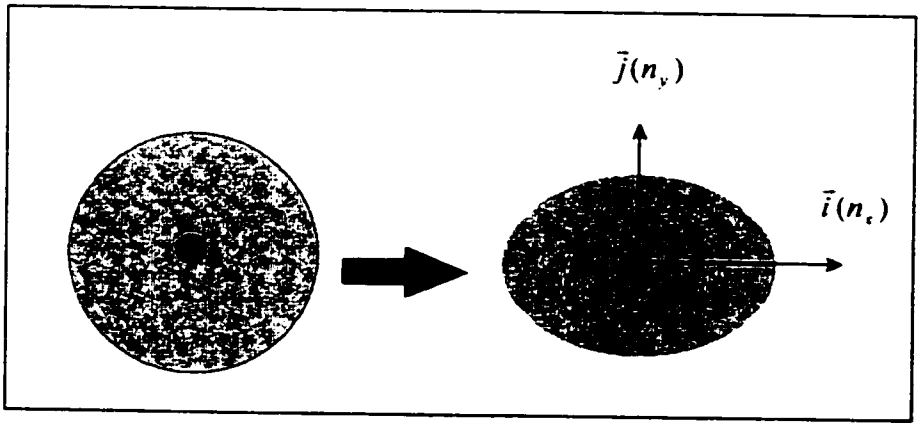

b) Birefringence due to the asymmetry of the fiber core

Figure 6.2 The polarization modes in ideal and practical fibers.

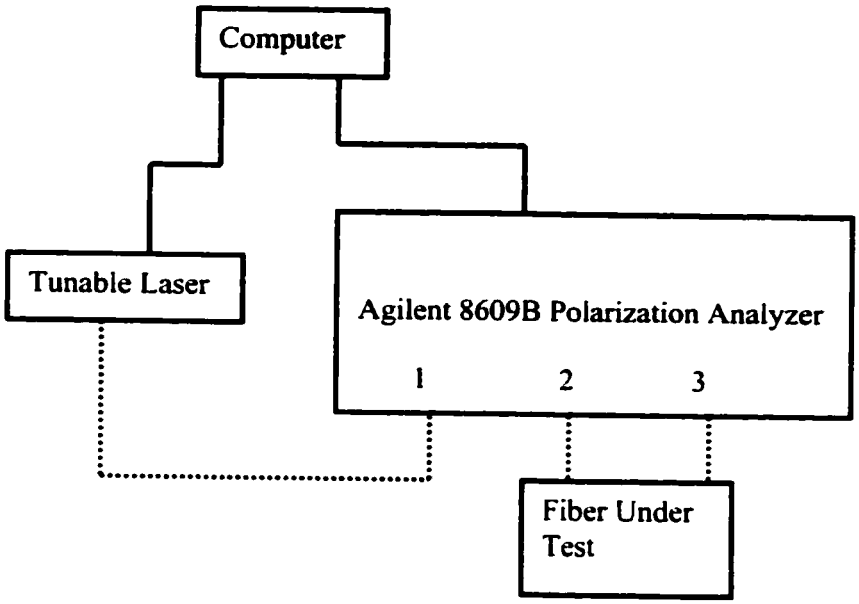

Figure 6.3 Block diagram of PMD measurement using JME method. The solid lines represent the connections made by electrical cables and the dashed lines represent connections made by optical fibers.

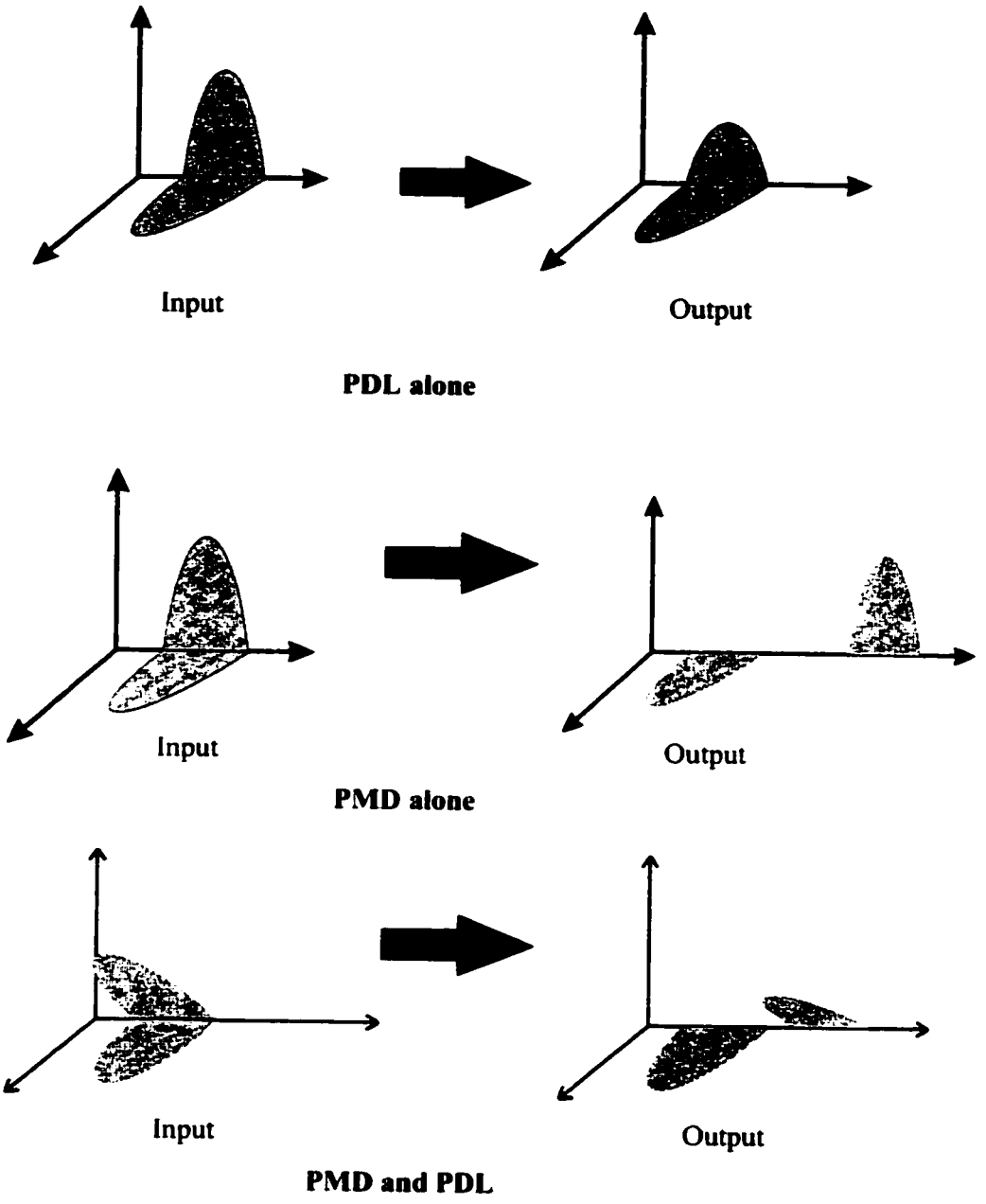

Figure 6.4 Effects of PMD and PDL on pulse transmission.

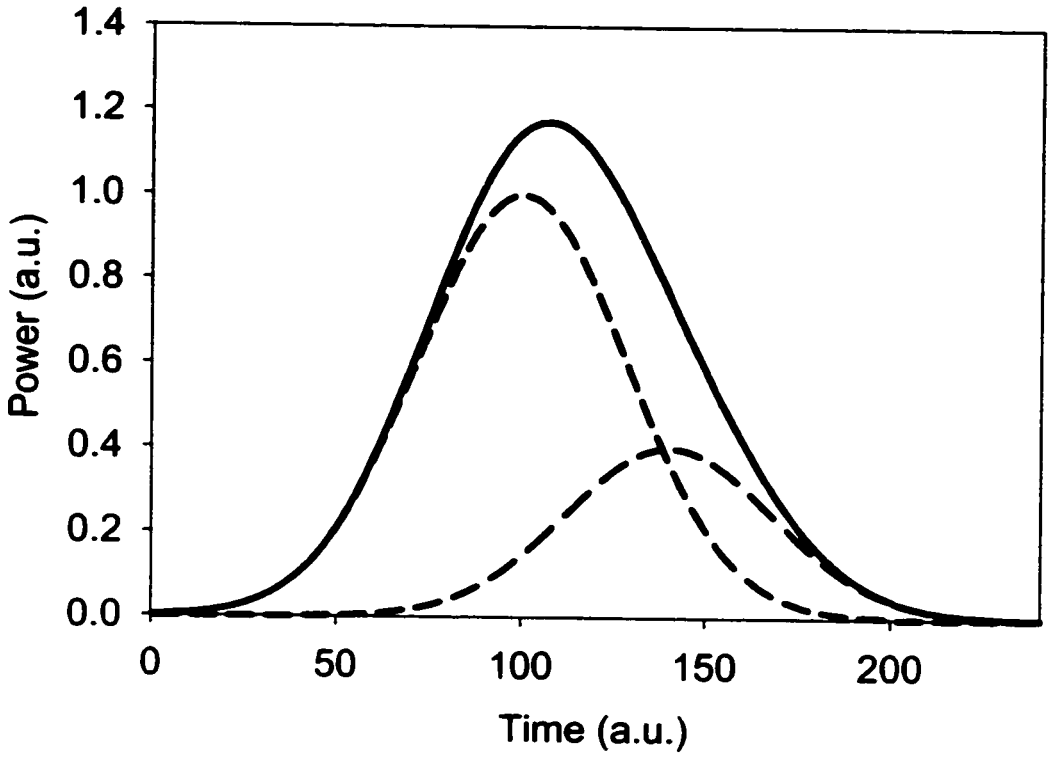

Figure 6.5 Birefringence induced pulse broadening in SM fibers. The input pulse splits into two pulses (dashed curves) due to birefringence, and the effective output pulse (solid curve) is broadened.

Chapter 7

Statistical Distribution of DGD

7.1 Introduction

PMD and PDL are two polarization effects in fiber optic communication systems and both of them show stochastic behavior due to environmental perturbations. The studies of PMD and PDL in fiber optic systems are usually based on the waveplate model [11, 13, 17, 20, 22, 23, 63, 64]. In this model a fiber is treated as a concatenation of N polarization maintaining fiber (PMF) segments with random coupling between any two adjacent segments, see Fig. 7.1. One assumption made in the waveplate model used previously is that the DGD of each PMF segment is uniformly distributed within a finite range [13, 17, 20, 23, 63, 64]. The other common practice made in the previous model is that the birefringence in the PMF segments is linear, even though the formulism covers the elliptical birefringence [13, 22, 23]. The limitation of the previous model is that it has a upper DGD limit. This would introduce errors in the calculation of system impact due to PMD because high bit error rate (BER) usually occurs in the large DGD region [9]. A new waveplate model is proposed in this chapter. The new model can generate any DGD values and the birefringence of the PMF segments is elliptical. The statistical distributions of DGD are studied in this chapter using both the new waveplate model and the previous waveplate model. The presentation of elliptical birefringence and the measurements of DGD vectors in single mode fibers and fiber components are described in section 7.2. Section 7.3 presents the statistical distribution of DGD using the previous model considering the case of biased elliptical birefringence. In section 7.4 a new waveplate model is proposed with the possibility of generating any DGD (PDL) values. The difference between the new model and the previous model is examined. For the two waveplate models used in this

chapter the influence of PDL on the statistical distribution of DGD is studied. A short conclusion is given in section 7.5.

7.2 Elliptical birefringence in fibers

7.2.1 Birefringence and Jones matrix with PMD and PDL

The Jones matrix $T(\omega)$ of a piece of polarization maintaining fiber at frequency ω in the presence of PMD and PDL can be written as [9, 13]

$$T(\omega) = \exp\left[\left(-i\vec{\beta}\omega + \vec{\alpha}\right)\cdot\vec{\sigma}/2\right], \tag{7.1}$$

where $\vec{\beta}$ is the birefringence vector in Stokes space, its amplitude is equal to the DGD of the fiber and its orientation is the direction of fast PSP, see Fig. 7.2. $\vec{\alpha}$ is the PDL vector, its amplitude is equal to the PDL of the fiber defined as $e^{2\alpha} = \frac{I_{max}}{I_{min}}$, where I_{max} (I_{min}) is the maximum (minimum) power transmission with different input states of polarization (SOP's) having same intensity. $\vec{\sigma}$ are the Pauli matrices: $\sigma_1 = \begin{pmatrix} 1 & 0 \\ 0 & -1 \end{pmatrix}$, $\sigma_2 = \begin{pmatrix} 0 & 1 \\ 1 & 0 \end{pmatrix}$, $\sigma_3 = \begin{pmatrix} 0 & -i \\ i & 0 \end{pmatrix}$. In Eq. 7.1 the polarization independent time delay and the global loss are ignored. If both θ and ϕ in Fig. 7.2 are zero (vector $\vec{\beta}$ is along the direction of S_1) and PDL is zero, the Jones matrix can be written as

$$T(\omega) = \exp\left(-i\beta\omega\cdot\sigma_1/2\right) = \exp\begin{bmatrix} -i\beta\omega/2 & 0 \\ 0 & i\beta\omega/2 \end{bmatrix} = \begin{bmatrix} \exp(-i\beta\omega/2) & 0 \\ 0 & \exp(i\beta\omega/2) \end{bmatrix}. \tag{7.2}$$

Eq. 7.2 is the expression of birefringence in a x-y-z coordinate system with fast PSP along the x-axis and the slow PSP along the y-axis and z-axis is the direction of light transmission.

If angle ϕ is zero but angle θ is not zero, then in the case of null PDL the Jones matrix is

$$T(\omega)=\cosh(-i\beta\omega/2)\cdot\begin{pmatrix}1&0\\0&1\end{pmatrix}+\sinh(-i\beta\omega/2)\cdot\sin\theta\cdot\begin{pmatrix}0&1\\1&0\end{pmatrix}+\sinh(-i\beta\omega/2)\cdot\cos\theta\cdot\begin{pmatrix}1&0\\0&-1\end{pmatrix}$$

$$=\begin{pmatrix}\cos(\theta/2)&\sin(\theta/2)\\\sin(-\theta/2)&\cos(\theta/2)\end{pmatrix}\cdot\begin{pmatrix}\exp(-i\beta\omega/2)&0\\0&\exp(i\beta\omega/2)\end{pmatrix}\cdot\begin{pmatrix}\cos(\theta/2)&\sin(-\theta/2)\\\sin(\theta/2)&\cos(\theta/2)\end{pmatrix}. \tag{7.3}$$

Comparing Eq. 7.3 to Eq. 7.2 we can see that the birefringence is still linear with the fast PSP rotating an angle of $\theta/2$ away from the x-axis [58]. Similarly, it can be shown that when $\phi=\pm\pi/2$ the birefringence is purely circular and when $0<|\phi|<\pi/2$ the birefringence is elliptical.

The Jones matrix of a fiber is the Jones matrix multiplication of the N PMF segments [13], that is

$$T=T_N T_{N-1}\cdots\cdots T_j\cdots\cdots T_2 T_1 \qquad (j=1,2,\ldots\ldots N). \tag{7.4}$$

In the previous waveplate model it is assumed that the DGD of each segment, β, is uniformly distributed from $-\beta_{max}$ to β_{max} [11, 23], where β_{max} is the maximum DGD in each PMF segment. As will be discussed in section 7.4 that this assumption has the limitation of characterizing the DGD distribution in a large DGD region. The other common practice made in the previous model is that the birefringence in the PMF segments is linear ($\phi=0$), even though the formulism covers the elliptical birefringence [13]. In the following experiments it is shown that the birefringence in a single-mode fiber and fiber components is elliptical in general. As a result, it is natural to assume that the birefringence in the PMF segments of the waveplate model is elliptical.

7.2.2 Measurements of DGD vectors

The measurement of DGD vector can be done by measuring the SOP vectors, $\vec{S}(\omega)$, in Stokes space at various frequencies and using the equation of $\partial\vec{S}(\omega)/\partial\omega = \vec{\Omega}(\omega)\times\vec{S}$ [61, 65, 66], see Fig. 7.3. $\vec{\Omega}(\omega)$ is the DGD vector at frequency ω. The amplitude of the DGD vector, $|\vec{\Omega}(\omega)|$, is the curvature of the SOP trace at frequency ω. If the DGD vector $\vec{\Omega}(\omega)$ is a constant, the SOP trajectory is a circle on the Poincaré sphere. The vector $\vec{\Omega}(\omega)$'s orientation is pointing to the circle center from the sphere center. Fig. 7.4 shows the SOP trajectory from the output end of a 2.64 m long polarization maintaining (PM) fiber (3M, Panda, DGD=2.76 ps) when a linearly polarized light is launched to the fiber input. The laser wavelength varies from 1550.7 to 1553.7 nm. We see that the birefringence of the PM fiber is linear ($\vec{\Omega}$ is on the S_1-S_2 plane) and it is frequency independent. Generally the trajectories of the output SOP's of single mode fibers and components with different frequencies are not circular and the DGD vector $\vec{\Omega}(\omega)$ is frequency dependent. Fig. 7.5 and Fig. 7.6 show the measurements of SOP trajectories with different frequencies of a fiber circulator (JDS Uniphase, CR5500) and a 86 km long single mode fiber (Cornning, leaf) respectively. The mean DGD of the circulator is 0.0076ps. For the measurement of SOP trajectory from the circulator, a fully polarized light from a tunable laser (Agilent, 8164A) is launched into port 1 of the circulator. After being reflected at the end of port 2 the light is collected by a polarization analyzer (Agilent 9509B) at port 3. The wavelength of the laser is tuned continuously from 1456 nm to 1583 nm. We can see that the SOP trajectory is a series of small and drifted overlapping circles. The DGD vector at frequency ω, $\vec{\Omega}(\omega)$, is pointing to the center of the small circle from the center of the sphere. As one can see from Fig. 7.5 that the DGD vector $\vec{\Omega}(\omega)$ of the circulator (dashed arrow) is frequency dependent and the birefringence is elliptical. Using the same tunable laser and the same polarization analyzer the SOP trajectory from the output of a 86 km long single mode fiber is measured in Fig. 7.6. The mean DGD of the fiber is 0.75 ps and the wavelength of the laser varies continuously from 1456 to 1550 nm. It is clear from Fig. 7.6 that the DGD vector of the single-mode fiber is frequency dependent and the birefringence is elliptical as well. From the

measurements of DGD vectors of the fiber circulator and the single mode fiber one can see that the birefringence in single mode fibers and components is elliptical in general. It is natural in the waveplate model to treat a fiber as a concatenation of elliptically birefringent PMF segments.

7.3 Statistical distribution of DGD

Considering the presence of elliptical birefringence in fibers and components discussed in the last section, this section examines the statistical distribution of DGD using Monte-Carlo simulations based on the previous waveplate model. The birefringence of the PMF segments in the model is elliptical. The influence of PDL on the statistics of DGD is studied as well.

7.3.1 Statistical DGD distribution with elliptical birefringence

In this subsection the fiber is assumed to have PMD only. Each fiber is treated as a concatenation of 20 PMF segments. The DGD of each segment is uniformly distributed from $-\beta_{max}$ to β_{max}. The birefringence of each segment is determined by angles θ and ϕ (Fig. 7.2). Angle θ is set to be uniformly distributed from 0 to 2π and angle ϕ is set to be uniformly distributed between zero and a maximum value ϕ_{max}, it is biased. This is the case when a birefringent fiber is twisted along one direction [10, 67], which is often encountered during fiber cabling.

The DGD of a fiber composed by N PMF segments can be obtained from the principal state vector $\vec{W}_N(\omega)$ [9, 17]

$$\begin{aligned}\vec{W}_N &= \beta_N \vec{e}_N + (\vec{e}_N \cdot \vec{W}_{N-1})\vec{e}_N + \cosh(\alpha_N - i\beta_N\omega)[\vec{W}_{N-1} - (\vec{e}_N \cdot \vec{W}_{N-1})\vec{e}_N] \\ &+ i\sinh(\alpha_N - i\beta_N\omega)\vec{e}_N \times \vec{W}_{N-1}\end{aligned} \tag{7.5}$$

where β_N and $\vec{e}_N$ are the birefringence amplitude (DGD) and orientation of the N-th segment respectively. $\vec{W}_{N-1}$ is the principle state vector of the concatenation of N-1 segments and α_N is the PDL of the N-th segment. In this subsection PDL is assumed to be zero. ω is 1.2×10^{15} rad/s corresponding to the communication wavelength around 1550 nm. The effective DGD of the fiber is the real part of χ where $\chi^2 = \vec{W}_N \cdot \vec{W}_N$. Fig. 7.7 shows the probability density distribution of DGD in an ensemble of 50,000 fibers. The birefringence in the PMF segments is linear ($\phi = 0$ in Fig. 7.2). The maximum DGD of each segment (β_{max}) is 2.236 ps that produces the *rms* DGD of the fiber to be 5 ps when $\phi = 0$. The solid line in Fig. 7.7 is the fitting curve using the normalized Maxwell function.

In the presence of a biased circular birefringence in each segment, the statistical distributions of DGD are examined with various values of angle ϕ_{max}. The maximum DGD of each segment is still set to be 2.236 ps. There are 50,000 fibers in each statistical ensemble with each fiber consisting of 20 PMF segments. It is found that the fitting curves of the DGD probability densities at various ϕ_{max} values are still Maxwellian with the mean DGD increasing with ϕ_{max}, see Figs. 7.8 and 7.9. This is due to the fact that the larger of angle ϕ_{max} the more bias (the less mode coupling) is added to the fiber (ϕ is uniformly distributed from 0 to ϕ_{max}, not from $-\phi_{max}$ to ϕ_{max}).

7.3.2 Statistical DGD distribution with PDL

In this subsection the probability density distribution of DGD is examined using Eq. 7.5 in the presence of PDL. There are 50,000 fibers in each statistical ensemble and each fiber consists of 20 PMF segments. The PDL in each section is uniformly distributed from $-\alpha_{max}$ to α_{max}. The maximum DGD of each segment is 2.236 ps. A typical probability density distribution of DGD in the presence of PDL is shown in Fig. 7.10. In this figure the mean PDL of the fiber is 8 dB and the angle ϕ is zero. The obvious difference between Figs. 7.7 and 7.10 is that the probability of zero DGD in Fig. 7.7 is zero but it is a finite value in the presence of PDL

(Fig.7.10). This property was reported before and the probability density of DGD was fitted by the combination of Gauss and Maxwell functions [17]. In the presence of circular birefringence, Fig. 7.11 shows the fitting curves of the DGD probability densities with various angles of ϕ_{max} in the presence of PDL (8 dB and 12 dB). We can see that the probability density functions of DGD are still the combination of Gauss and Maxwell functions with the probability of zero DGD increasing with PDL. The mean DGD increases with both PDL and angle ϕ_{max} even though the probability density of zero DGD increase with PDL, see Fig. 7.12.

In the above simulations the angle ϕ is assumed to be uniformly distributed between zero and a maximum value. An example of this situation is when a fiber is twisted along one direction, which is likely the case in fiber cabling. If the angle ϕ of each PMF segment is, however, uniformly distributed between $-\phi_{max}$ and ϕ_{max}, the simulation results show that the probability density of DGD is the same as that obtained with the assumption of linearly birefringent PMF segments ($\phi = 0$) and it does not depends on ϕ_{max}. This is not difficult to understand if one carefully examines the Eqs. 7.3 and Eq. 7.4. If all the Jones matrices of the PMF segments in a fiber are expressed as Eq. 7.3 (linear birefringence) and there are $2N$ PMF segments in the fiber. The products of T_2T_1, T_4T_3, ... $T_{2i}T_{2i-1}$, ... and $T_{2N}T_{2N-1}$ are not in the form of Eq. 7.3 in general. This means that the effective birefringence of $T_{2i}T_{2i-1}$ is elliptical in general and no bias is introduced. A concatenation of $2N$ linearly birefringent PMF segments is equivalent to a concatenation of N elliptically birefringent PMF segments. As a result, the statistical distribution of DGD is the same.

7.4 New waveplate model

7.4. 1 Model

The waveplate model used in section 7.3 assumes that a fiber is a concatenation of N PMF segments and each segment has a finite DGD uniformly distributed between $-\beta_{max}$ and β_{max} [13, 17, 20, 23, 63, 64]. This model produces a well known Maxwellian distribution of DGD

when DGD is not very large ($<N\cdot\beta_{max}$). In the range where DGD is larger than $N\cdot\beta_{max}$ this model will give zero probability because $N\cdot\beta_{max}$ is the maximum DGD value generated in this model and N cannot be infinite in a simulation. This model limits the simulations of DGD distribution and system impact when the DGD of a fiber optic system is very large.

In this section a new waveplate model is proposed. The probability distribution of DGD in each PMF segment is shown in Fig. 7.13 and it can be written as

$$\rho(\beta)=\begin{cases} Ae^{(\beta+\beta_m)/\beta_0} & where \quad \beta<-\beta_m \\ A & where \quad |\beta|<\beta_m \\ Ae^{(-\beta+\beta_m)/\beta_0} & where \quad \beta>\beta_m \end{cases}, \tag{7.6}$$

where $A=1/(2\beta_m+2\beta_0)$ is the normalization coefficient ($\int_{-\infty}^{+\infty}\rho(\beta)d\beta=1$). β_m and β_0 are two parameters that determine the probability distribution of DGD in each PMF segment. Fig. 7.14 shows the histogram of DGD with $\beta_m=0$, $\beta_0=0.5ps$ and N=100. The solid line is the fitting curve of the histogram using Maxwell function. It can be seen that the statistical distribution is a Maxwell distribution. The shadowed area S in Fig. 7.13 is determined by the value of β_m and β_0 and it can written as (the whole area between the curve of $\rho(\beta)$ and the DGD-axis is unitary)

$$S=2A\cdot\beta_m=\frac{\beta_m}{\beta_m+\beta_0}. \tag{7.7}$$

In the simulations it is found that N has to be large enough to be in a highly mode-coupled region. Fig. 7.15 shown the histograms of DGD at the extreme case of S=0 ($\beta_m=0$) and with N varying from 10 to 100. β_0 is set to be $5/\sqrt{N}$ ps. The solid curves in Fig. 7.15 are the fittings of histograms using Maxwell function. It is clear from Fig. 7.15 that, when $N\le 50$ the histogram cannot be well fitted by Maxwell function. In the following simulations in this

subsection with various β_m and β_0 values, N is always chosen to be 100 such that the system is in the highly mode-coupled region.

Fig. 7.16 shows the fitting curves of the statistical distributions of DGD using the new waveplate mode at various S values (Eq. 7.7). There are 200,000 fibers in each statistical ensemble and each fiber consists of 100 PMF segments ($N = 100$). The values of β_m and β_0 that are used in the simulations are listed in Table 7.1. At every S value, the pair of β_m and β_0 gives the same *rms* DGDs in the PMF segments. The mean DGDs and standard errors obtained from the simulations are listed in Table 7.1 as well. The standard error of DGD at each S value is obtained using the software "SigmaPlot". We can see from Fig. 7.16 that the fitting curves of the DGD distributions do not show evident dependence on S value. This means that the new model ($S < 1$) produces almost the same DGD distribution as that of the previous model (S=1). The mean DGDs obtained from the simulations and used in the fitting curves in Fig. 7.16 are plotted in Fig. 7.17.

As shown in Eq. 7.6 the new model has the ability of generating any DGD values. In order to see the difference between the new waveplate model and the previous model the DGD distributions (not the fitting curve) in large DGD range are shown in Fig. 7.18. For each model there are 1,000,000 fibers in the statistical ensemble and each fiber consists of 100 PMF segments. The values of β_m and β_0 used in the previous model are 0.866 ps and 0 respectively and they are 0.1152 ps and 0.3456 ps respectively in the new model, which give the same *rms* DGD in the PMF segments for both models. It is clear from Fig. 7.18 that the new model produces a slightly higher DGD probability at large DGD region.

7.4.2 Statistical DGD distribution with PDL

In the previous model the PDL in each PMF segment is uniformly distributed between a minimum value and a maximum value [13]. For a system with optical polarizers the previous model will not work because the PDL of a perfect polarizer is infinite, however, the maximum

Table 7.1 Parameters used in the simulations of DGD distributions for the new waveplate model and the mean DGDs with standard errors obtained in the simulations.

Simulation #	β_m (ps)	β_0 (ps)	S	DGD_{mean} (ps)
1	0.87	0	1	4.60 ± 0.02
2	0.71	0.13	0.85	4.63 ± 0.02
3	0.53	0.23	0.70	4.60 ± 0.02
4	0.36	0.29	0.55	4.65 ± 0.02
5	0.22	0.33	0.40	4.67 ± 0.02
6	0.12	0.35	0.25	4.59 ± 0.02
7	0.039	0.35	0.10	4.59 ± 0.02
8	0	0.35	0	4.62 ± 0.02

PDL that can be produced by the previous model is $N \cdot \alpha_{max}$. In order to overcome this, similar to the distribution of DGD (Eq. 7.6), the distribution of PDL in each PMF segment of the new waveplate can be written as

$$\rho(\alpha) = \begin{cases} Be^{(\alpha+\alpha_m)\cdot\alpha_0} & where \quad \alpha < -\alpha_m \\ B & where \quad |\alpha| < \alpha_m \\ Be^{(-\alpha+\alpha_m)\cdot\alpha_0} & where \quad \alpha > \alpha_m \end{cases}, \tag{7.8}$$

where $B = 1/(2\alpha_m + 2\alpha_0)$ is the normalization coefficient ($\int_{-\infty}^{+\infty} \rho(\alpha) d\alpha = 1$). In the presence of PDL the statistical distributions of DGD are studied using the new waveplate model (Eqs. 7.6 and 7.8). The parameters (β_m, β_0, α_m and α_0) used in each ensemble are different but the *rms* values of DGD and PDL are kept the same for all the ensembles with various S values, see table 7.2. Each ensemble consists of 200,000 fibers with each fiber consisting of 100 PMF segments.

Fig. 7.19 shows the fitting curves of the DGD distribution using a combination of Gauss and Maxwell functions with various S values. It can be seen that the fitting curve does not show evident dependence on the S value. The mean DGDs obtained from the simulations are plotted in Fig. 7.20. The standard error of the mean DGDs is 0.02 ps (obtained using the software of SigmaPlot).

Table 7.2 Parameters used in the simulations of DGD distributions with PDL for the new waveplate model

Simulation #	β_m (ps)	β_0 (ps)	α_m	α_0	S
1	0.87	0	0.18	0	1
2	0.71	0.13	0.15	0.027	0.85
3	0.53	0.23	0.11	0.048	0.70
4	0.36	0.29	0.076	0.062	0.55
5	0.22	0.33	0.047	0.070	0.40
6	0.12	0.35	0.025	0.074	0.25
7	0.039	0.35	0.0083	0.075	0.10
8	0	0.35	0	0.075	0

7.5 Conclusion

The statistical distributions of DGD are studied using two waveplate models. One has been used previously and the other is proposed in this chapter. The limitation of the previous model is that it produces zero DGD probability when DGD exceeds a certain value. The new waveplate model overcomes this limitation and it can generate any DGD values. Simulation results show that the two models produce almost the same DGD distributions except in large DGD region where the new model produces a slightly higher DGD probability than the previous model. The influence of PDL on the distribution of DGD is examined in this chapter.

In the presence of PDL the statistical distribution of DGD can be fitted by the combination of Gauss and Maxwell functions even in the presence of biased elliptical birefringence. The mean DGD increases with both PDL and the maximum biased angle.

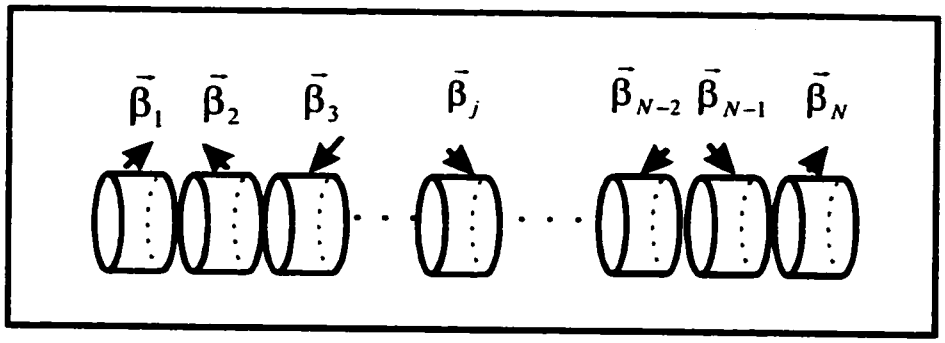

Figure 7.1 Waveplate model of birefringence in optical fibers

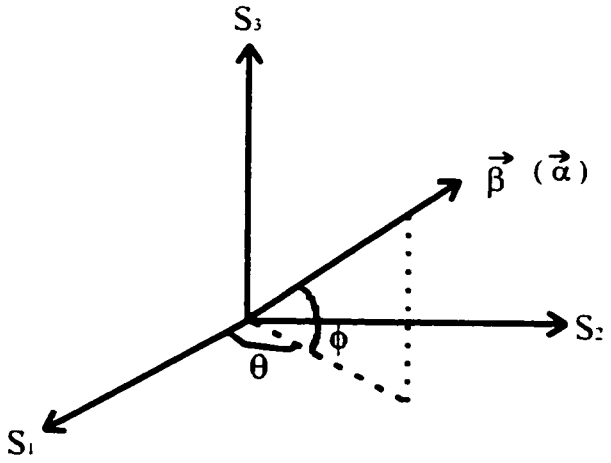

Figure 7.2 Representation of birefringence vector $\vec{\beta}$ and PDL vector $\vec{\alpha}$ in Stokes space.

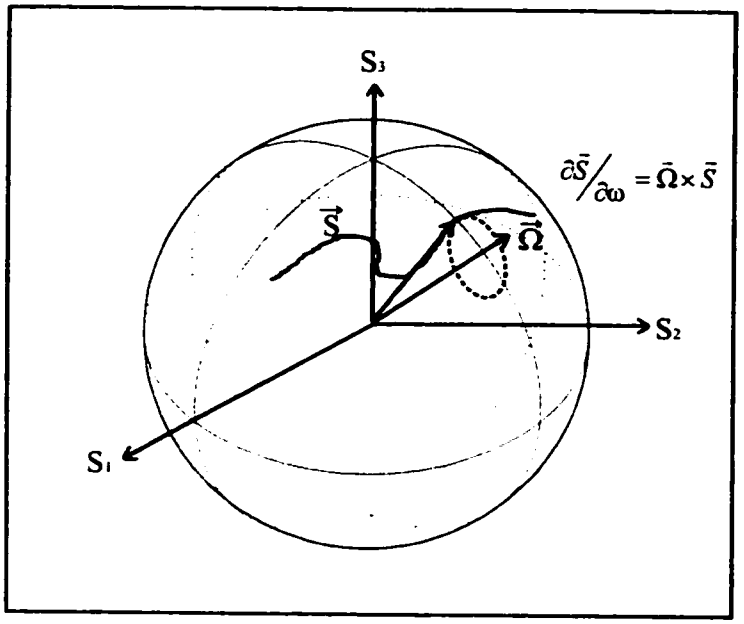

Figure 7.3 Relation between polarization state $\vec{S}$ and DGD vector $\vec{\Omega}$ in Stokes space.

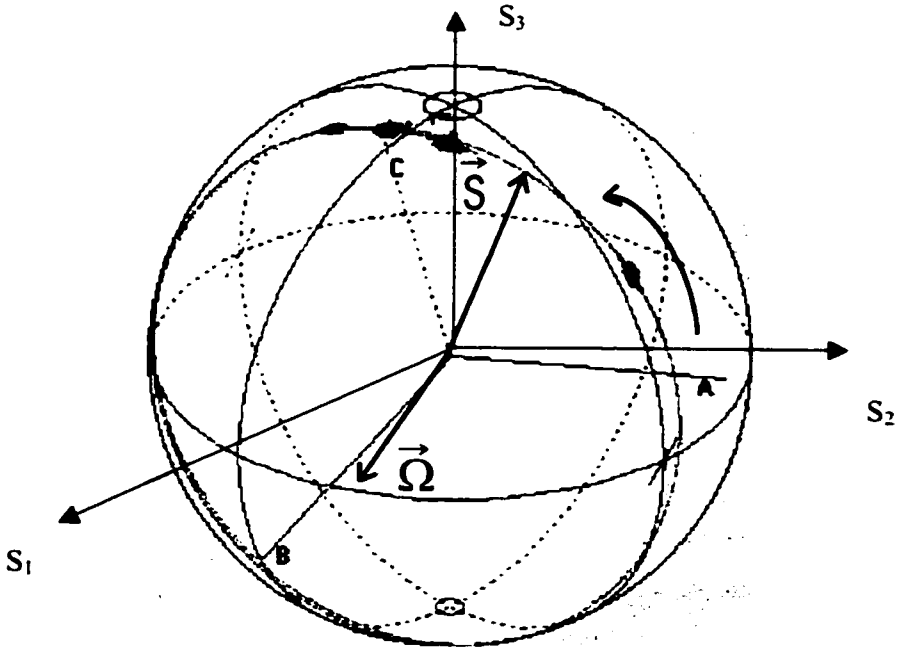

Figure 7.4 DGD vector $\vec{\Omega}$ of a polarization maintaining fiber.

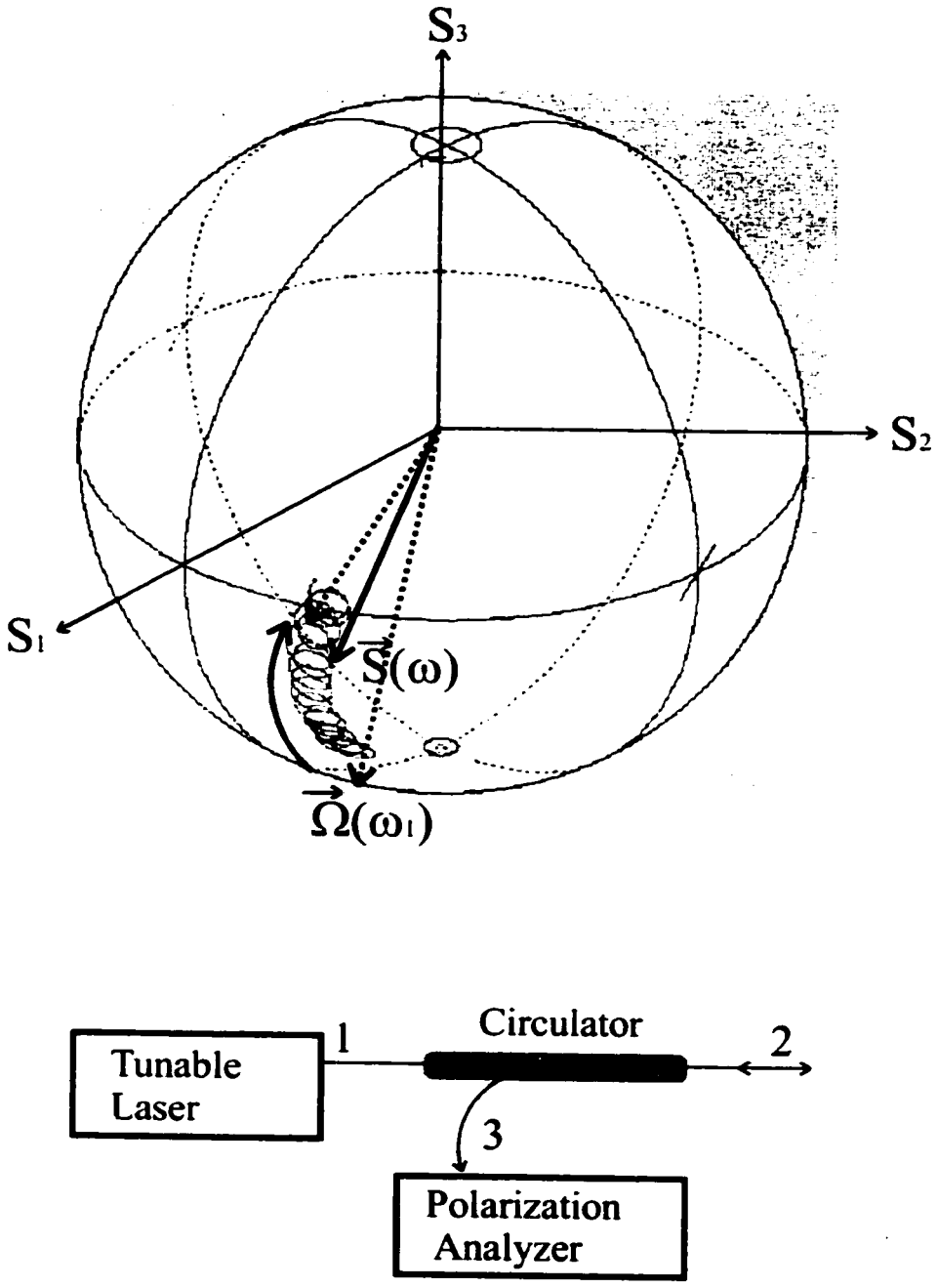

Figure 7.5 Measurement of DGD vector in a fiber circulator.

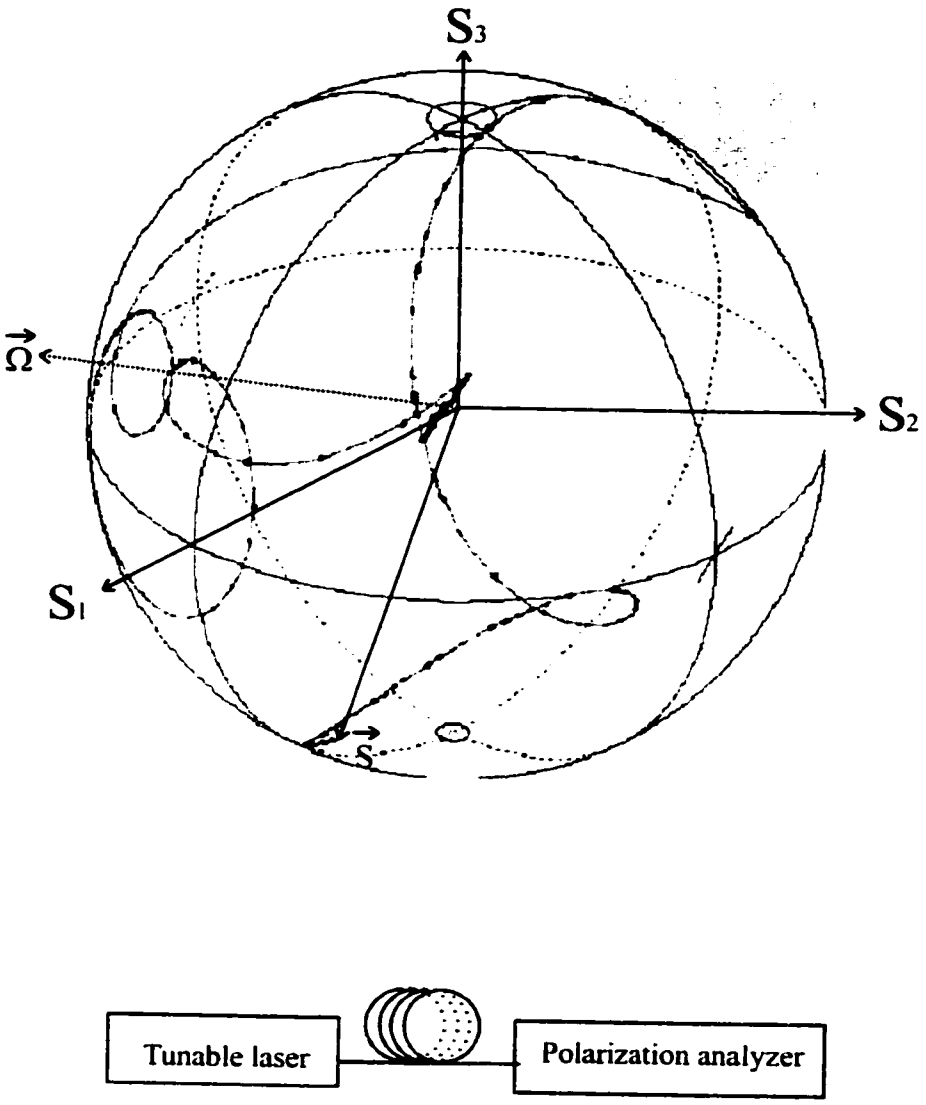

Figure 7.6 Measurement of the DGD vector of a 86 km single-mode fiber.

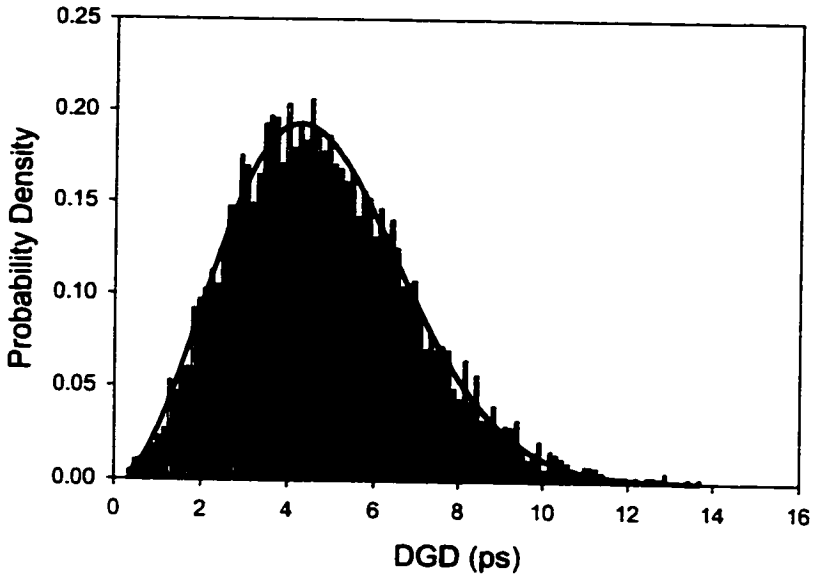

Figure 7.7 Probability density distribution of DGD of 50,000 fibers, each fiber is a concatenation of 20 PMF segments with linear birefringence.

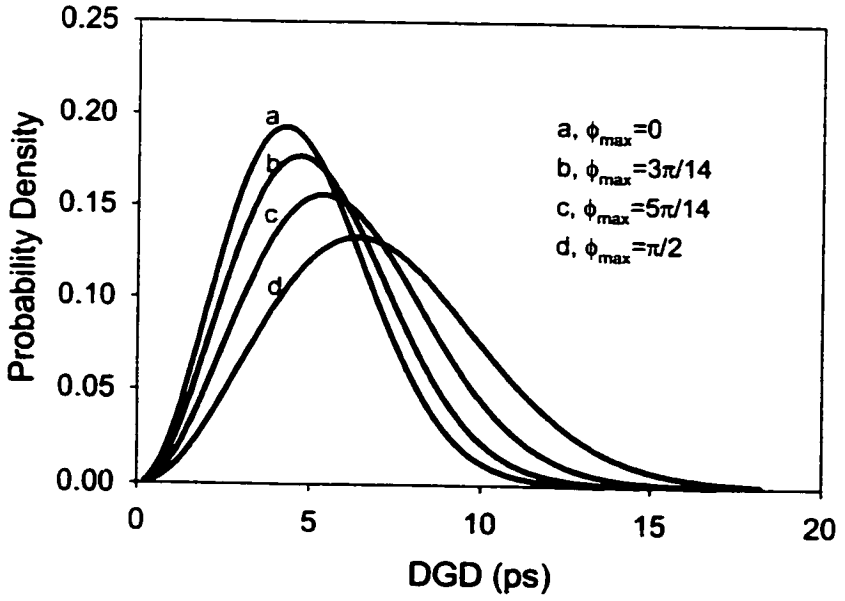

Figure 7.8 Statistical distribution of DGD in the presence of elliptical birefringence with various angles of ϕ_{max}.

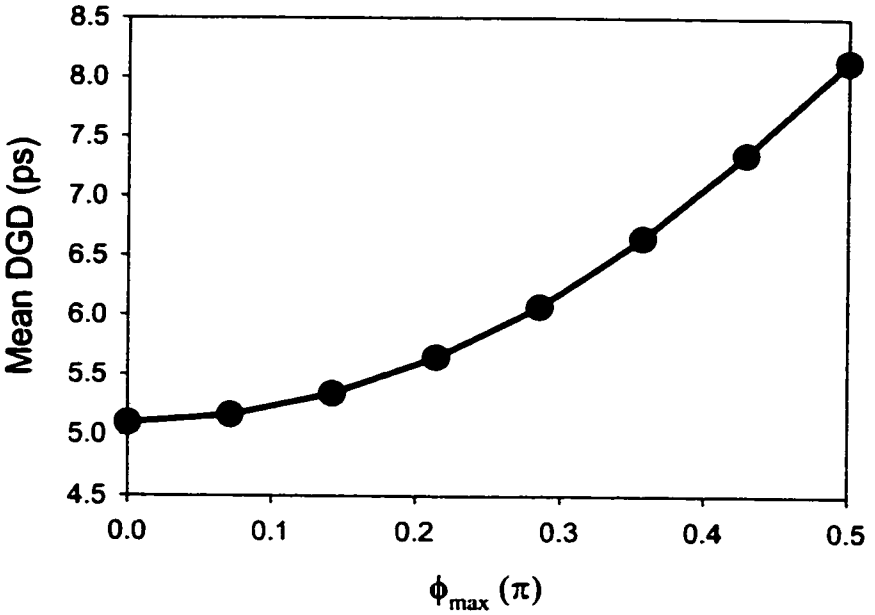

Figure 7.9 Mean DGDs at various angles of ϕ_{max} .

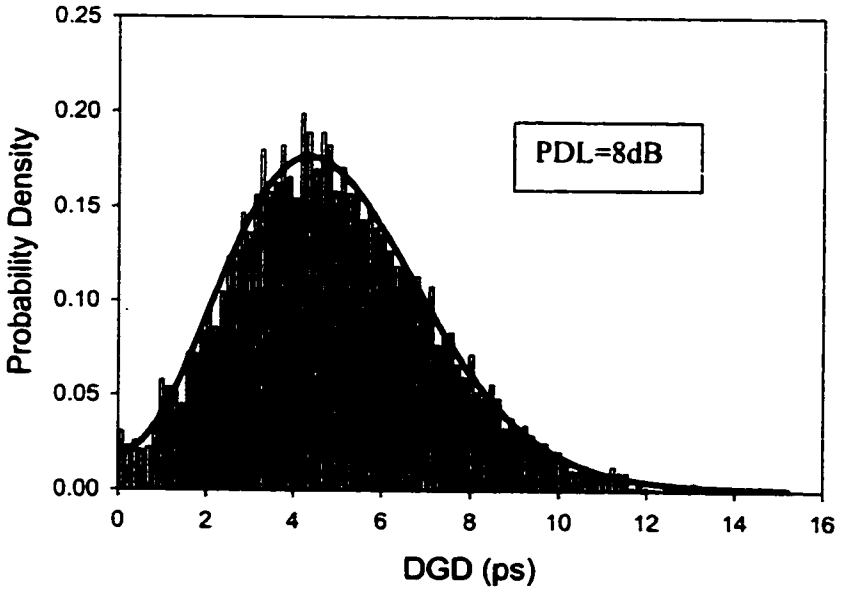

Figure 7.10 Statistical distribution of DGD in the presence of PDL. The mean PDL of the fiber is 8dB and the angle ϕ of each PMF segment in the fiber is zero. The solid curve is the fitting of the probability density using a combination of Gauss and Maxwell functions.

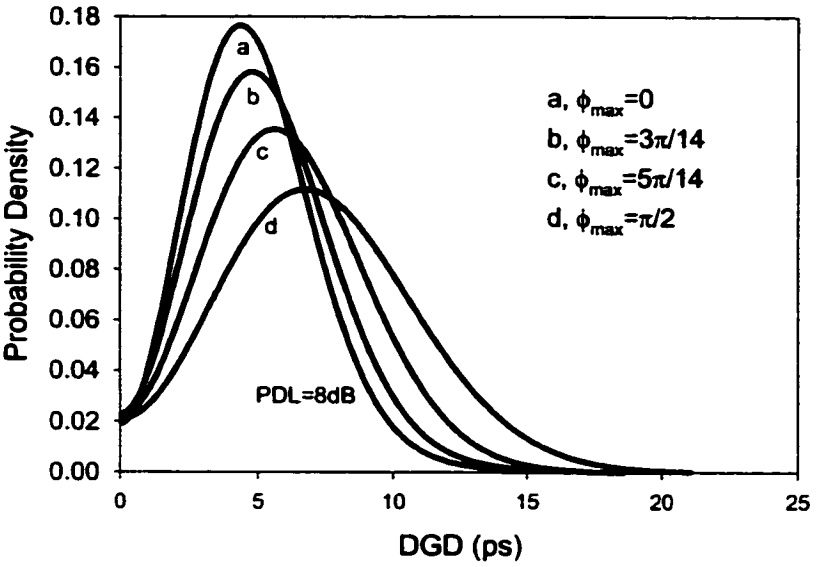

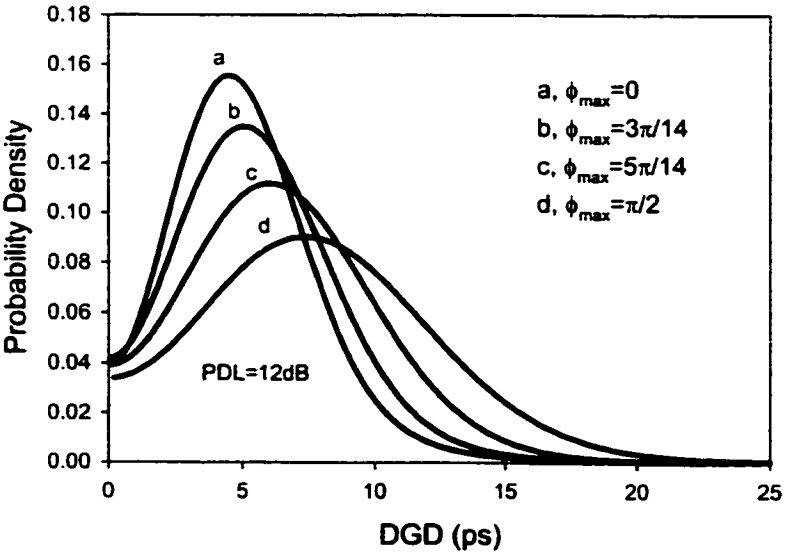

Figure 7.11 Statistical distributions of DGD in the presence of PDL at various angles of ϕ_{max}. The mean PDL of the fiber is 8dB and 12 dB respectively.

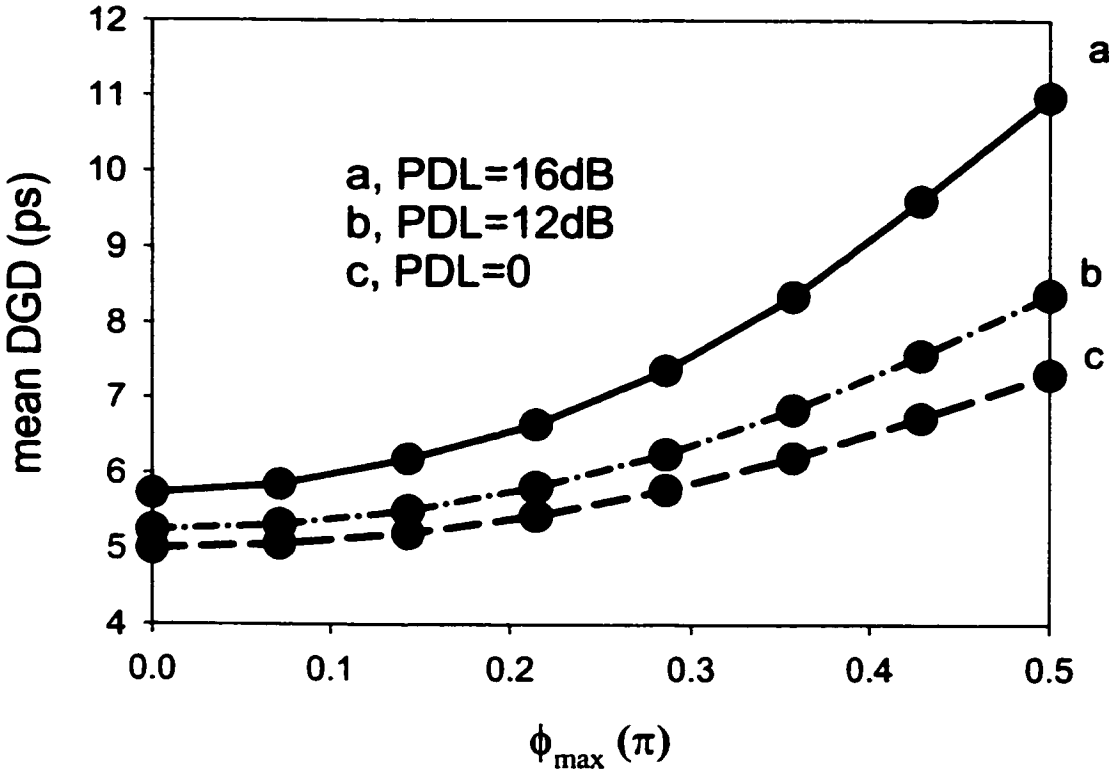

Figure 7.12 Mean DGD change with angle ϕ_{max} at various of PDLs.

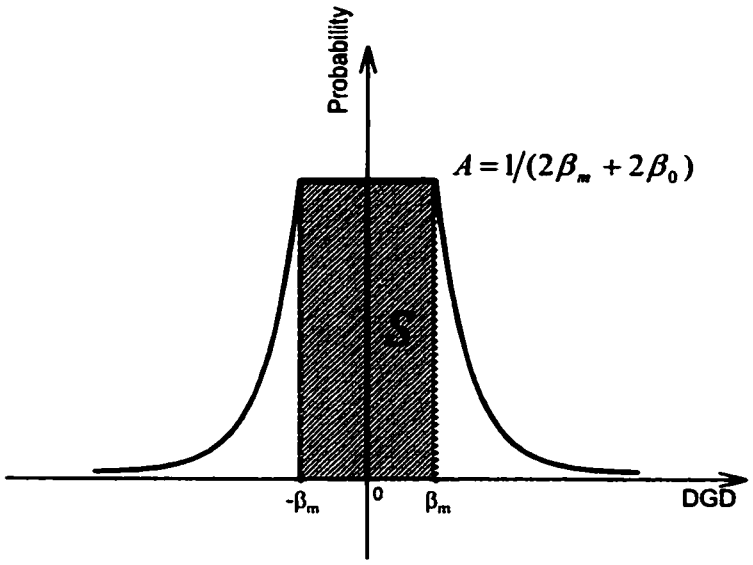

Figure 7.13 DGD distribution in each PMF segment of the new waveplate model.

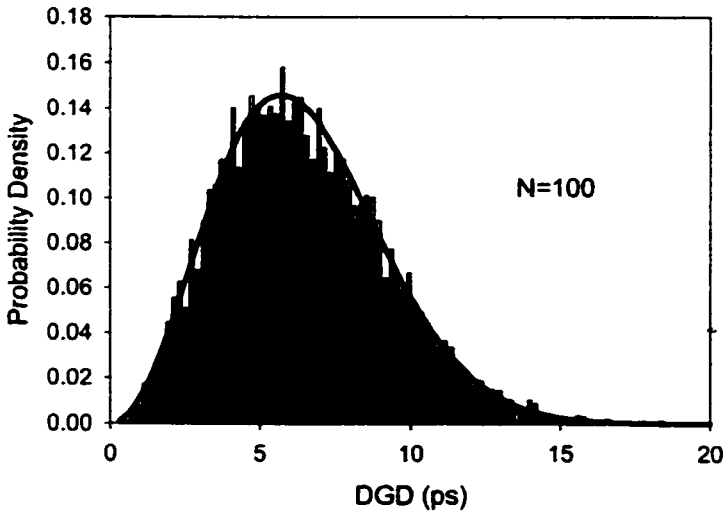

Figure 7.14 DGD probability density distribution based on the new model. There are 100 PMF segments in each fiber.

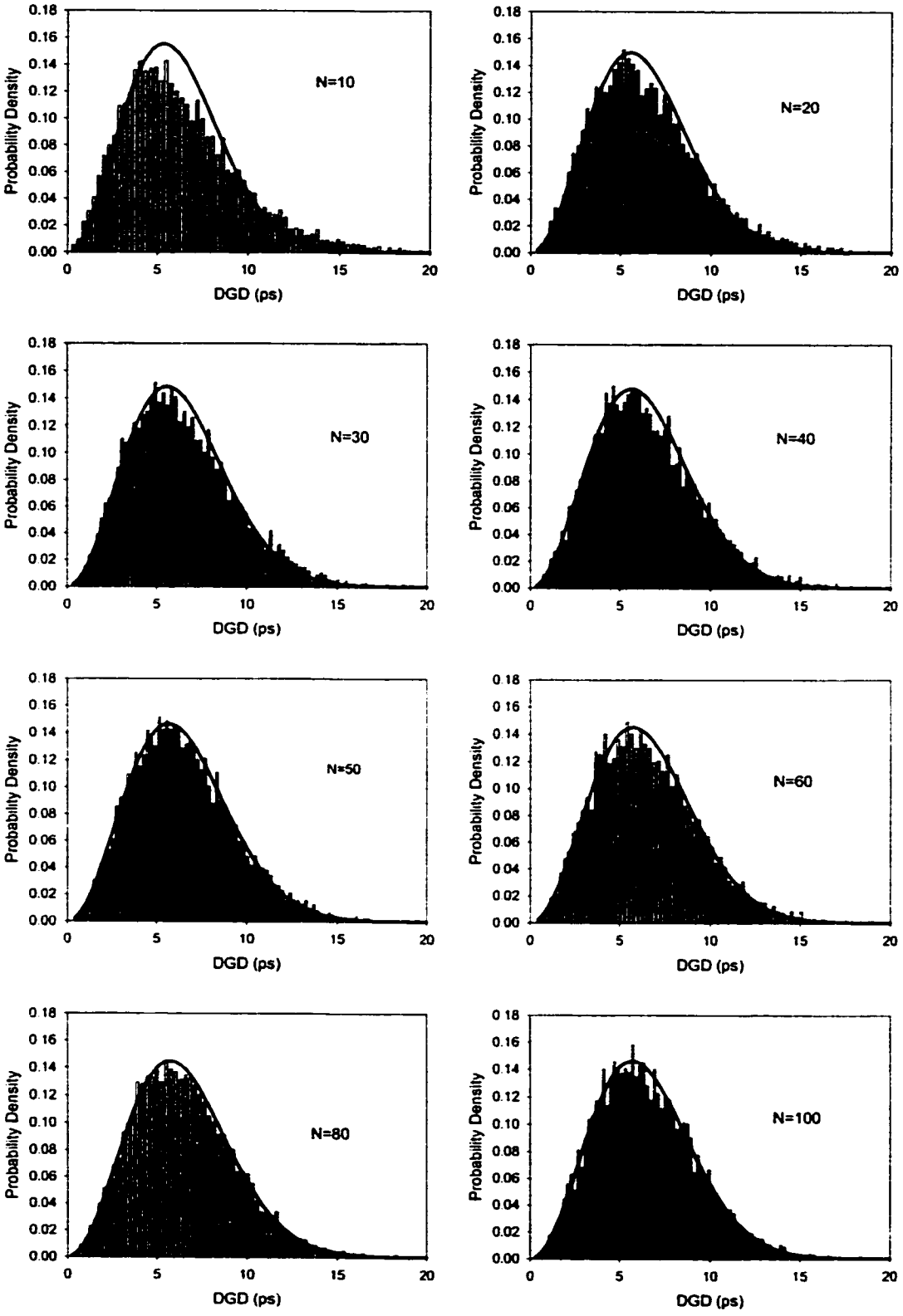

Figure 7.15 Histograms of DGD with various numbers of segments in each fiber.

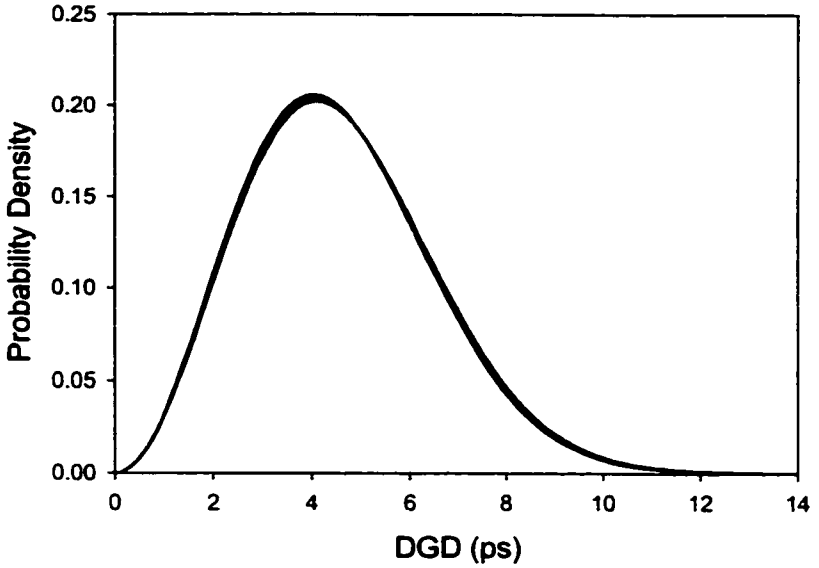

Figure 7.16 Fitting curves of the DGD probability density at various S values using the new waveplate model.

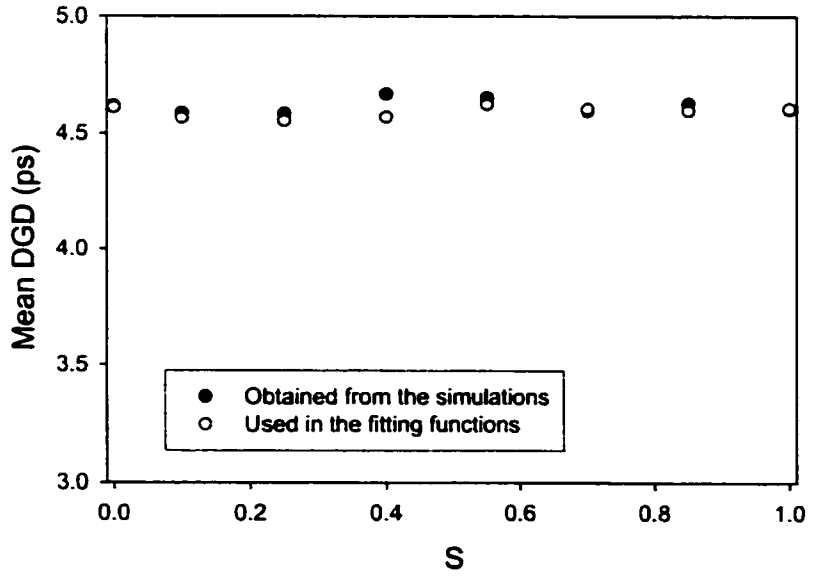

Figure 7.17 The mean value of DGD vs. the area of shadowed region S in Fig.7.13. The standard error of the mean DGD is less than 0.03 ps.

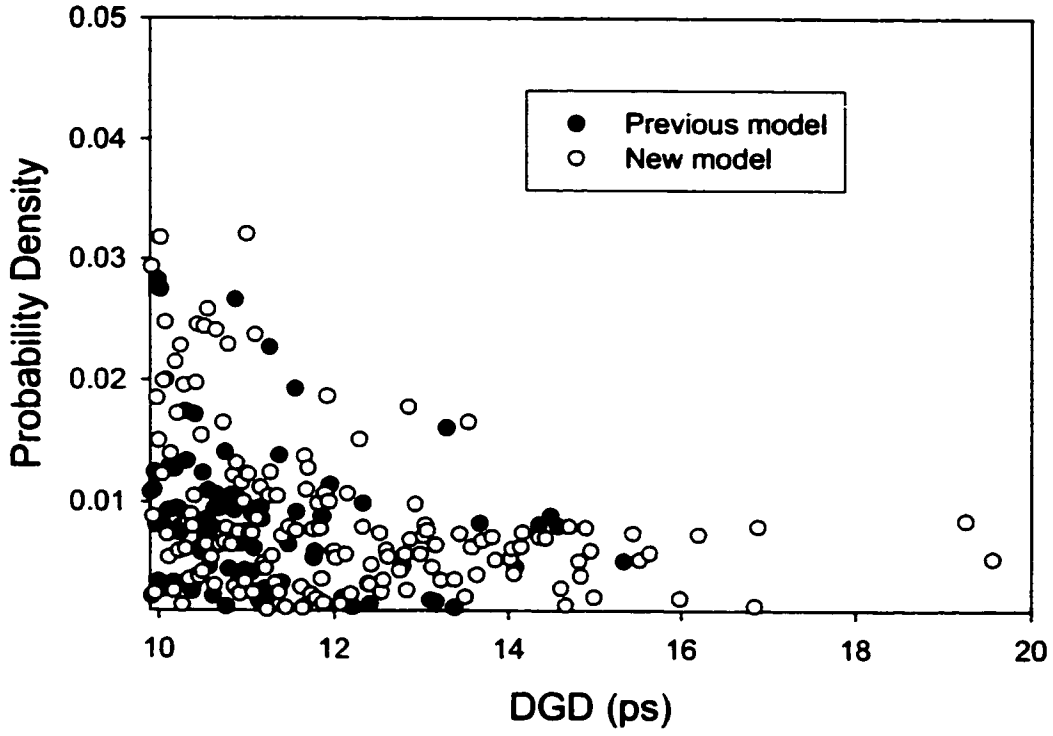

Figure 7.18 DGD Probability densities at the large DGD region with two different models.

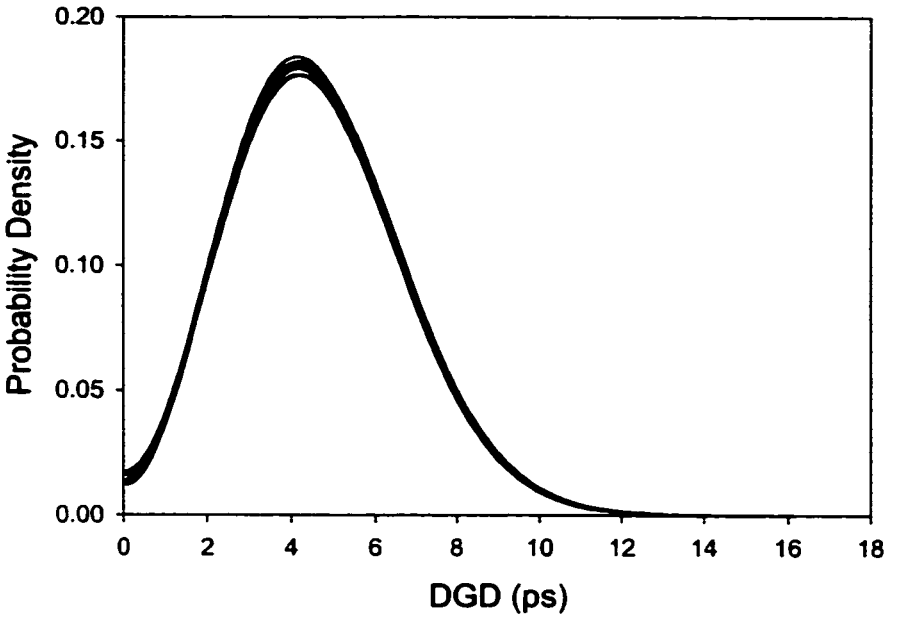

Figure 7.19 Statistical distributions of DGD in the presence of PDL using the new waveplate model.

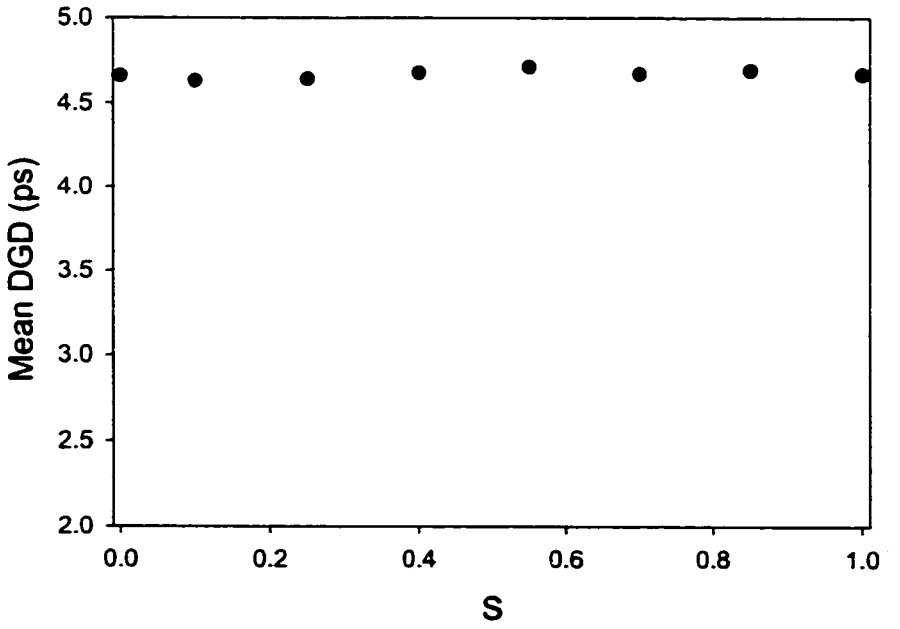

Figure 7.20 Mean DGDs at various values of S in the presence of PDL. Both the DGD and PDL in the model have the probability of infinite value. The standard error of the mean DGD is less than 0.03 ps.

Chapter 8

Statistical Distribution of PDL

8.1 Introduction

PMD and PDL are two polarization effects in fiber optic communication systems and both of them show stochastic behavior. In chapter 7 the statistical distribution of DGD is examined. It is also necessary to study the statistical distribution of PDL to evaluate the system impact due to the combined effect of PMD and PDL. PDL in single mode fibers can be ignored, but it is up to 0.4 dB in various fiber components [68, 69, 70, 71]. The studies of PDL are usually based on the waveplate model [13, 20, 71]. In the model a fiber (or a fiber system) is treated as a concatenation of many PMF segments. The PDL (or DGD) of each segment are uniformly distributed within a finite range. However, this model produces zero probability when PDL (or DGD) exceeds a certain value, which would induce errors of evaluating the system impact due to PDL (or DGD) because high bit error rate (BER) usually occurs at large PDL (or DGD) values. In chapter 7 a new waveplate model is proposed. In the new model the DGD and PDL of each PMF segment can take any values (Eqs. 7.6 and 7.8). In this chapter both waveplate models are used in examining the statistical distribution of PDL. Section 8.2 describes the calculation of PDL using Jones matrix and examines the statistical distribution of PDL using the previous model (DGD=0). Section 8.3 examines the influence of DGD on the statistical distribution of PDL using the previous model. A formula is proposed to evaluate the PDL of a system consisting of many PDL elements. Section 8.4 presents the statistical distribution of PDL in the presence of biased elliptical birefringence. In this thesis the biased birefringence means that the circular component of the birefringence is always positive (or negative). Section 8.5 examines the statistical distribution of PDL using the new waveplate model. The PDL

distributions produced by the two waveplate models are compared. Section 8.6 is a short conclusion of this chapter.

8.2 Statistical PDL distribution

The Jones matrix of a concatenation of N PMF segments is shown in Eq. 7.4 and the Jones matrix of the j^{th} segment in the presence of both PMD and PDL is

$$T_j(\omega) = \exp[(-i\vec{\beta}_j\omega + \vec{\alpha}_j)\cdot\frac{\vec{\sigma}}{2}], \qquad (j=1, 2, \ldots N) \tag{8.1}$$

where $\vec{\beta}_j$ and $\vec{\alpha}_j$ are the DGD and PDL vectors of the j^{th} segment in Stokes space, see Fig. 7.2. In this section the PDL of every PMF segment is assumed to be linear and PMD is zero ($\vec{\beta}_j = 0$ and $\vec{\alpha}_j$ is on the plane of S_1 and S_2 in Fig. 7.2). For a given Jones vector $E_j(\omega)\vec{e}$ at the input end of a fiber, the optical power at the fiber output is proportional to

$$P(\omega) = |E_j(\omega)|^2 \cdot \vec{e}_j^{\,*}(\omega)\cdot T^*(\omega)\cdot T(\omega)\cdot \vec{e}_j(\omega), \tag{8.2}$$

where $E_j(\omega)$ is the amplitude of the electric filed and $\vec{e}_j$ is the input SOP. $T(\omega)$ is the Jones matrix of the fiber expressed in Eq. 7.4. The input SOPs that give the maximum and minimum output power can be obtained by solving the equation of $\delta P(\omega) = 0$ with the constraint of $\vec{e}^{\,*}_j \cdot \vec{e}_j = 1$, where δ stands for the variation of $P(\omega)$ with input SOP, $\vec{e}_j$. The solution of this problem is equivalent to the following equation [72]:

$$\delta P - \lambda\delta(\vec{e}_j^{\,*}\cdot\vec{e}_j) = 0 \tag{8.3}$$

where λ is the Lagrangian Multiplier. Eqs 8.2 and 8.3 lead to the following equation:

$$[|E_i(\omega)|^2 T^+ \cdot T \cdot \vec{e}_i - \lambda \vec{e}_i]^+ \cdot \delta\vec{e}_i + \delta\vec{e}_i^{\,+} \cdot [|E_i(\omega)|^2 T^+ \cdot T \cdot \vec{e}_i - \lambda \vec{e}_i] = 0. \quad (8.4)$$

The solution of Eq. 8.4 is

$$|E_i(\omega)|^2 T^+ \cdot T \cdot \vec{e}_i = \lambda \vec{e}_i. \quad (8.5)$$

From Eq. 8.5 it is easy to show that the effective PDL in the unit of dB at frequency ω is

$$PDL = 10 \cdot \log_{10}(P(\omega)_{max} / P(\omega)_{min}) = 10 \cdot \log_{10}(\lambda_1 / \lambda_2), \quad (8.6)$$

where $P(\omega)_{max}$ ($P(\omega)_{min}$) is the maximum (minimum) power transmission with different input SOP's. λ_1 and λ_2 are the two eigenvalues of matrix $T^+(\omega) \cdot T(\omega)$ and $\lambda_1 \geq \lambda_2$. In this section the statistical distribution of PDL is studied by examining the statistical ensembles of fibers with various PDLs. For each ensemble the effective PDLs of 100,000 fibers are calculated using Eq. 8.6. Each fiber consists of 1000 PMF segments ($N = 1000$). For each segment, α_j is uniformly distributed between $-\alpha_{max}$ to α_{max}. The orientation of $\vec{\alpha}_j$ is uniformly distributed in the S_1-S_2 plane in Fig. 7.2, i.e. θ is uniformly distributed from 0 to 2π. Fig. 8.1 shows the probability density distribution of PDL with $\alpha_{max} = 0.0011$ (corresponding to the maximum PDL value of each segment to be $0.302/(1000)^{1/2}$ in dB). The solid curve in Fig. 8.1 is the fitting of the probability density distribution using Rayleigh function, that is

$$PDF(x) = \frac{\pi}{2 \cdot \bar{x}^2} \cdot x \cdot \exp\left(-\frac{\pi}{4 \cdot \bar{x}^2} \cdot x^2\right), \quad (8.7)$$

where x stands for PDL in the unit of dB and $\bar{x}$ is the mean value of PDL. It is clear in Fig. 8.1 that the statistical distribution of PDL is a Rayleigh function when PMD is zero.

8.3 Statistical PDL distribution with PMD

In the presence PMD the distributions of PDL are studied by examining many statistical ensembles with various PMDs and PDLs. For each ensemble we calculate the PDL values of 100,000 fibers with each fiber consisting 1000 birefringence segments (N=1000). The angular frequency ω is 1215.3 rad/ps corresponding to the wavelength of ~1550 nm. For each segment, the amplitudes of $\vec{\beta}_j$ and $\vec{\alpha}_j$ are uniformly distributed between 0 to β_{max} and 0 to α_{max} respectively. The orientations of $\vec{\beta}_j$ and $\vec{\alpha}_j$ are uniformly distributed on S_1-S_2 plane in Fig. 7.2 (linearly polarized). Fig. 8.2 shows the distributions of PDL with α_{max}=0.0011 and with $\beta_{max} = 5.69\times10^{-5}$ ps (a) and 3.16×10^{-4} ps (b), which correspond to the mean DGD of the fiber to be 0.0009 and 0.005ps respectively if there were no PDL ($\alpha_j = 0$) in the fiber. In fact the statistical distribution of PDL is examined for large mean DGD values up to β_{max}=0.474ps (corresponding to the mean DGD of 15 ps in the fiber) and it is found that there is no obvious influence of DGD on the PDL distribution when β_{max} is larger than 2×10^{-4} ps. The theoretical probability density function (PDF) of PDL is obtained by fitting the PDL distributions in Fig. 8.2. Comparing Figs. 8.1 and 8.2 one can see that, in the presence of PMD, the statistical distribution of PDL is not a Rayleigh function. The distribution of PDL may be fitted by a combination of Rayleigh and Maxwell functions, that is

$$PDF(x) = M\cdot\frac{\pi}{2\cdot\bar{x}^2}\cdot x\cdot\exp\left(-\frac{\pi}{4\cdot\bar{x}^2}\cdot x^2\right) + (1-M)\cdot\frac{32}{\pi^2\cdot\bar{x}^3}\cdot x^2\cdot\exp\left(-\frac{4}{\pi\cdot\bar{x}^2}\cdot x^2\right), \qquad (8.8)$$

where M is the distribution factor between 0 and 1 depending on the mean value of DGD, x stands for PDL in the unit of dB and $\bar{x}$ is the mean value of PDL. From the fitting curves in Figs. 8.1 and 8.2 we can see that the PDF of PDL is a Rayleigh function (M=1) when PMD is zero. In the presence of PMD in fibers (even though the PMD is very low compared to the PMD in communication fibers), the PDF of PDL is a combination of Rayleigh and Maxwell

functions. The factor M is 0.468 for $\beta_{max} = 5.69 \times 10^{-5}$ ps and is 0.01 for $\beta_{max} = 3.16 \times 10^{-4}$ ps. In order to examine the DGD dependence of M factor, the distributions of PDL with various DGDs are simulated and fitted with Eq. 8.8. Fig. 8.3 shows the distribution factor M at various values of β_{max}. From Eqs. 7.1, 7.4 and 8.1 we can see that the Jones matrix (and PDL) of a fiber depends on the product of DGD (β_j) and angular frequency ω. As we assumed in the simulations that β_j is uniformly distributed between 0 and β_{max}. β_{max} determines the *rms* DGD of the fiber, τ, as $\tau = \left(N\beta^2_{mean}\right)^{(1/2)}$, where β_{mean} is the *rms* DGD of each segment, $\beta_{mean} = \left\langle \beta^2 \right\rangle^{1/2} = \beta_{max} / \sqrt{3}$. The product of *rms* DGD τ and angular frequency ω is displayed in Fig. 8.3 instead of β_{max}. Fig. 8.3 shows that the value of M first drops very sharply and smoothly with τ. When τ is large than 0.0032 ps (corresponding to $\omega\tau \approx 4$) the value of M is less than 0.05, which means a dominating Maxwell distribution of PDL. It is well known that the PMD of optical fibers is much larger than 0.0032 ps for a span of a few kilometers. This indicates that a Maxwell distribution of PDL is expected in most optical fiber networks [73].

The distributions of PDL with α_{max}=0.00011 and α_{max}=0.011 are also examined and the distribution factor M seems to be independent of α_{max}, which means that distribution factor M depends only on $\omega \cdot \tau$. The factor M can be fitted as a function of $\omega \cdot \tau$ (see the solid line in Fig. 8.3) and the fitting curve can be written in the Lorenz form as:

$$M = \frac{1}{1 + (\omega \cdot \tau)^2} \tag{8.9}$$

Eq. 8.9 is very useful as one can determine the PDL distribution of a fiber optic system if the PMD of the system and the optical frequency are given.

It is well known that the total PMD of a concatenation of PMD elements is $<\tau>^2 = \sum_j <\tau_j^2>$, [74] where τ is *rms* DGD of the fiber and τ_j is the *rms* DGD of the j^{th} segment. Similar to this for each ensemble, we calculated the value of PDL_0 as

$$PDL_0 = \left(\sum_i PDL_i^2 \right)^{(1/2)}, \tag{8.10}$$

and compared it to the mean PDL value of the ensemble obtained using Eq. 8.6. The percentage differences between the mean PDL and PDL_0 are plotted in Fig. 8.4 for various β_{max}. We can see from Fig. 8.4 that the mean PDL is slightly larger than PDL_0 and it depends on the product of $\omega \cdot \tau$ (or β_{max}). When β_{max} is greater than 3×10^{-4} ps (τ=0.004ps) the mean PDL can be written as

$$\langle PDL \rangle = 1.04 PDL_0 \tag{8.11}$$

with an error of less than 1%. This is valid for α_{max} from 0.00011 to 0.011 that correspond to PDL_0 from 0.015dB to 1.5dB. Here we can say that Eq. 8.11 is a good approximation of evaluating the mean PDL value of a system with strong mode coupling and with PMD greater than 0.004 ps. which is mostly encountered in a practical fiber network.

As we know that the PDF of DGD is a Maxwell function for an ensemble of fibers or an ensemble of wavelengths on one fiber [15]. This statement is also valid for the PDF of PDL in the presence of PMD. This is confirmed by simulating the PDF of PDL both for an ensemble of fibers and an ensemble of wavelengths on one fiber and the same results are obtained.

8.4 Statistical PDL distribution with elliptical birefringence

The simulations in the above section assume that the birefringence in each PMF segment is linear. In this section the statistical distributions of PDL are studied with the assumption that the PDL and DGD vectors in the segment are not always on the S_1-S_2 plane (see Fig. 7.2). Angle ϕ is set to be uniformly distributed between zero and a maximum value ϕ_{max} ($\leq \pi/2$), i.e. it is biased. In each simulation there are 100,000 fibers with each fiber having 1000 PMF segments. Fig. 8.5 shows the probability density of PDL with zero PMD at various maximum angles, ϕ_{max}. It can be seen that when ϕ_{max} is small (0.15π, Fig. 8.5a) the PDL is not a Rayleigh distribution.

It is fitted by using both Maxwell function and the combination of Maxwell and Rayleigh functions. It can be seen that the PDL distribution fits with the combination of Maxwell and Rayleigh functions (except in the region near zero PDL). When ϕ_{max} is large (0.35π and 0.5π), the PDL distributions can be fitted by the combination of Maxwell and Rayleigh functions, see Fig. 8.5b and 8.5c. Fig. 8.6 shows the mean PDL at various angles of ϕ_{max}. It can be seen that the mean PDL increases with ϕ_{max} that is due to the bias of ϕ(we set it to be uniformly distributed between 0 and ϕ_{max}, not in $-\phi_{max}$ and ϕ_{max}).

In section 8.3 we know that the probability density distribution of PDL change from Rayleigh distribution to Maxwell distribution when the PMD of the fiber varies from zero to 0.005 ps. In the case when PDL of each PMF segment is elliptical, Fig. 8.7 shows some simulation results when $\phi_{max} = \pi/4$ and the PMD of the fiber is 0.0009 ps (a), 0.005 ps (b) and 0.1 ps (c) respectively. The solid curve in Fig. 8.7c is the fitting of the histogram using Maxwell function. At this DGD value (0.1 ps) the PDL distributions are examined with various angles of ϕ_{max} and it is found that the probability density distribution is independent of angle ϕ_{max}. The mean PDLs at various PMDs is shown in Fig. 8.8. It can be seen that the mean PDL increases with angle ϕ_{max} when PMD is small (<0.005 ps). When PMD is large ($\geq$0.1ps) the mean PDL shows no evident dependence on angle ϕ_{max}. This is consistent with ϕ_{max} independence of probability density distribution with large DGD ($\geq$0.1ps). The standard error of the mean PDL simulated in this subsection is less than 0.0001dB.

8.5 Statistical PDL distribution based on the new model

In section 7.4 a new waveplate model is proposed with the possibility of infinite DGD and PDL (Eqs.7.6 and 7.8). In this section the statistical distribution of PDL is calculated with the new model, in which Eqs.7.4, 7.6 and 8.6 are used. The DGD of each segment of the waveplate model is zero and the PDL vector of each segment is on the plane of S_1-S_2 in Fig. 7.2. For each ensemble there are 1,000,000 fibers and each fiber has 1000 PMF segments. The parameters of

α_m and α_0 (in Eq. 7.8) in the ensembles are listed in table 8.1. For each set of α_m and α_0, the mean of α^2 of each segment is kept constant. Similar to Eq. 7.7 the area S is defined here as:

$$S = \frac{\alpha_m}{(\alpha_m + \alpha_0)} \tag{8.12}$$

The area S for each set of parameters and the mean PDL obtained from the simulations are listed in table 8.1 as well. The simulations using different values of α_m and α_0, but the same $\langle \alpha^2 \rangle$ produce almost the same PDL distribution in the PDL range from 0 to 0.5 dB as that in Fig. 8.1 and all of the PDL histograms can be fitted by Rayleigh function, see Fig. 8.9. The mean PDLs obtained from all the statistical ensembles are almost the same (0.15 dB), see table 8.1. Fig. 8.9 only show the PDL distribution from 0 to 0.5 dB. In large PDL range, Fig. 8.10 shows the distributions of PDL with the previous model (S=1) and with the new model (S=0.55) in large PDL region. It is clear that the new model produces a higher PDL probability in the large PDL region.

In the presence of DGD the previous model show (section 8.3) that the probability density function of PDL changes from Rayleigh to Maxwell with the increase of DGD. For the new model the DGD dependence of PDL distribution is tested for two statistical ensembles. There are 1,000,000 fibers in each ensemble and there are 1000 PMF segments in each fiber. Fig. 8.11 shows the histograms of PDL in the presence of DGD. Parameters α_m and α_0 in the simulations are 1.46×10^{-4} and 4.39×10^{-4} respectively so that the mean PDL of the fiber is around 0.15 dB. The parameters of β_m, β_0 used in the two ensembles are $7.57\times10^{-6}\,ps$, $2.27\times10^{-5}\,ps$ and $4.105\times10^{-5}\,ps$, $1.26\times10^{-4}\,ps$ respectively that corresponding to the same mean DGDs used in the previous model in section 8.3 (0.0009 and 0.005 ps respectively). The solid curves in Fig. 8.11 are the fitting curves of the histograms using Eq. 8.8. It is clear from Fig. 8.11 that the distribution of PDL is a combination of Rayleigh and Maxwell distributions. With the increase of DGD the PDL distribution is a Maxwell distribution. Here one can

conclude that the two models give the same PDL distribution in the presence of DGD. As a result, Eqs. 8.9 and 8.11 are also valid for the new model.

Table 8.1 Parameters used in the simulation of PDL distributions. The PDL of each segment in the waveplate model has the possibility of infinite value

Simulation #	α_m	α_0	S	PDL_{mean} (dB)
	0.0011	0	1	0.15
2	0.00090	0.00016	0.85	0.15
3	0.00067	0.00029	0.70	0.15
4	0.00045	0.00037	0.55	0.15
5	0.00028	0.00042	0.40	0.15
6	0.00015	0.00044	0.25	0.15
7	0.000050	0.00045	0.10	0.15
8	0	0.00045	0	0.15

In the presence of biased elliptical birefringence, Fig. 8.12 shows the PDL distributions using the parameters of $\alpha_m, \alpha_0, \beta_m$ and β_0 the same as those used in Fig. 8.11. ϕ_{max} is $\pi/2$ and the mean DGDs of the fibers in the three ensembles are 0, 0.0009 and 0.005 ps respectively. The solid curves in Fig. 8.12 are the fittings of the PDL distributions using the combination of Rayleigh and Maxwell functions. It is shown in Fig. 8.12 that when $\phi_{max} = \pi/2$ and PMD is zero the PDL distribution is not Rayleigh, it can be fitted by the combination of Rayleigh and Maxwell functions. In the presence of PMD (>0.0009 ps) the PDL distribution is Maxwellian. It may conclude from the simulation results of section 8.3, 8.4 and this section that in the presence of DGD (>0.1 ps) the PDL distribution is Maxwellian including the presence of biased elliptical birefringence.

8.6 Conclusion

Two waveplate models are used in this chapter to study the statistical distribution of PDL. The one that was used previously assumes that the DGD (or PDL) in each PMF segment is uniformly distributed within a finite range. The limitation of the previous model is that it produces zero probability when DGD (or PDL) exceeds a certain value. The new model proposed in this thesis assumes that the DGD and PDL in each PMF segment can take any values. Simulation results lead to the following conclusions: 1) The probability density distribution of PDL is a Rayleigh function without PMD. The new waveplate model produces a higher PDL probability than the previous model in the large PDL range. 2) In the presence of PMD the probability density distribution of PDL can be fitted by the combination of Rayleigh and Maxwell functions. 3) The mean value of PDL increases with the maximum biased angle ϕ_{max} when PMD is zero. It does not show evident dependence on ϕ_{max} when PMD is larger than 0.1 ps.

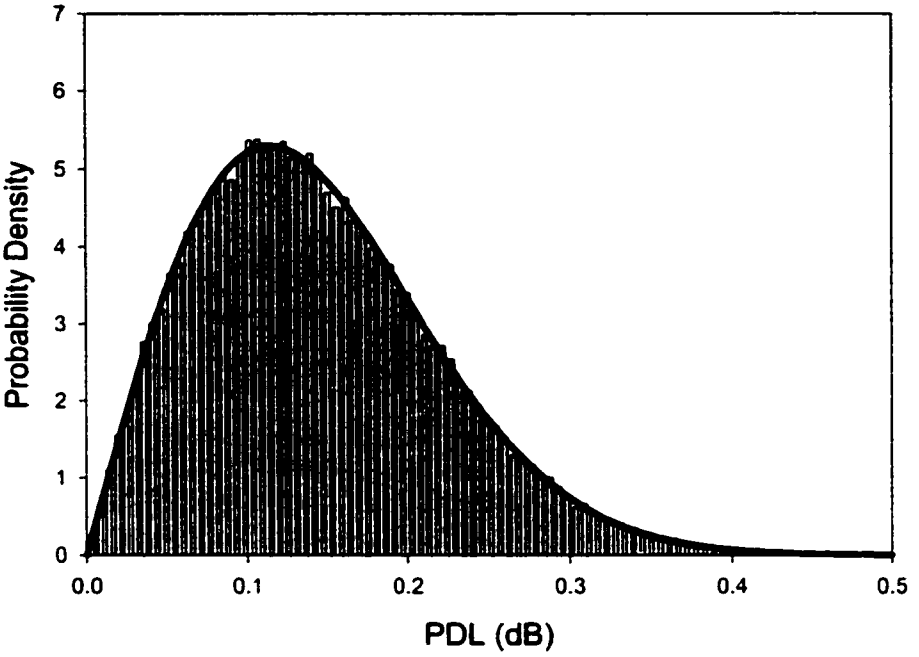

Figure 8.1 Probability density distribution of PDL with null PMD. The solid curve is the fitting of the PDL distribution using the Rayleigh function.

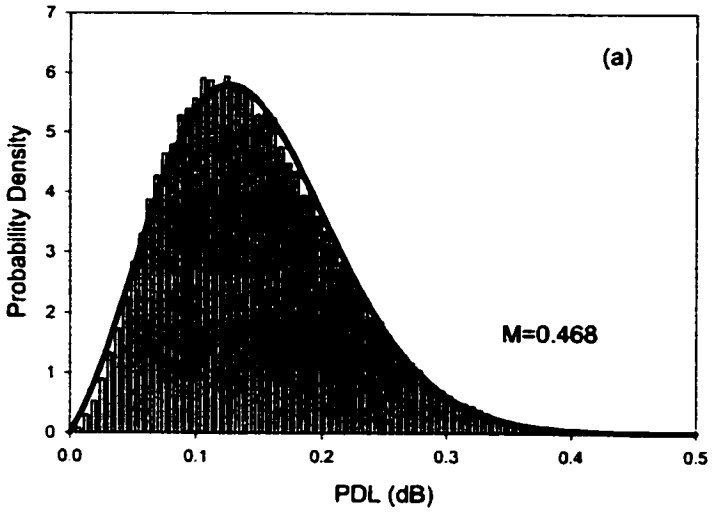

$$\beta_{max} = 5.69 \times 10^{-5}\,\text{ps}$$

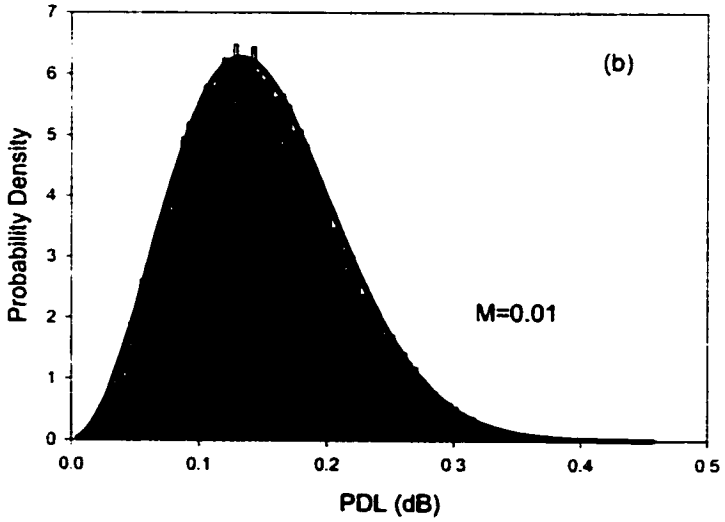

$$\beta_{max} = 3.16 \times 10^{-4}\,\text{ps}$$

Figure 8.2 Histograms of PDL in the presence of PMD. The solid curves are the fittings of the histograms using the combination of Maxwell and Rayleign distributions.

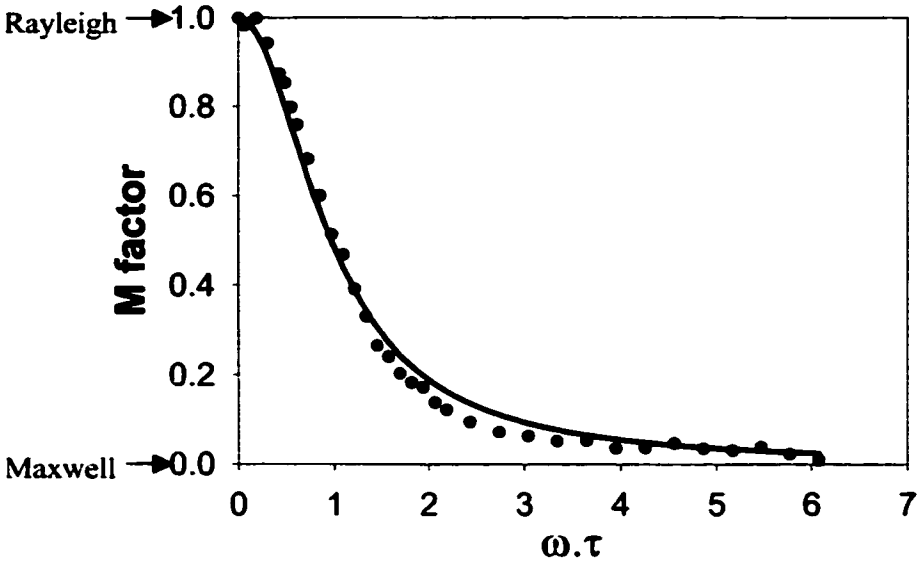

Figure 8.3 Distribution factor M of PDL with the product of carrier frequency and the mean DGD. The solid curve is the Lorenz function.

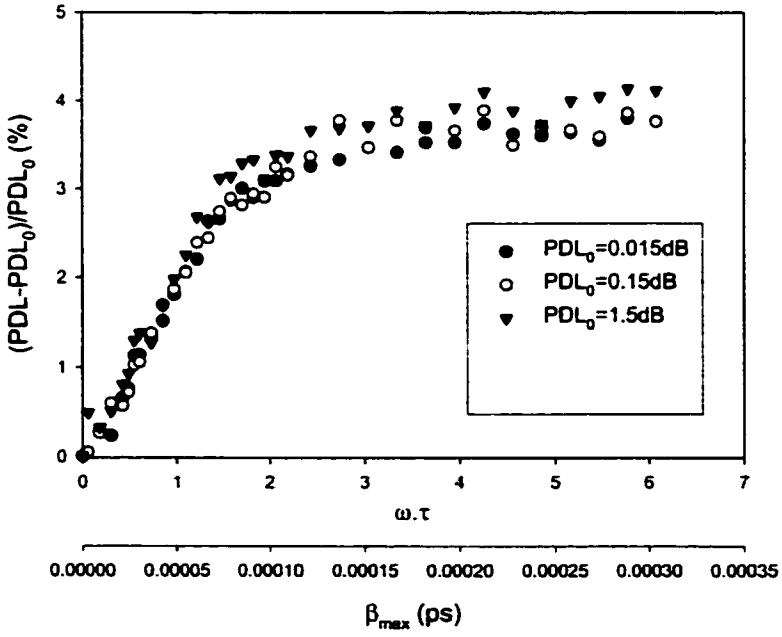

Figure 8.4 Difference between the mean PDL with PDL_0 defined by equation 8.10.

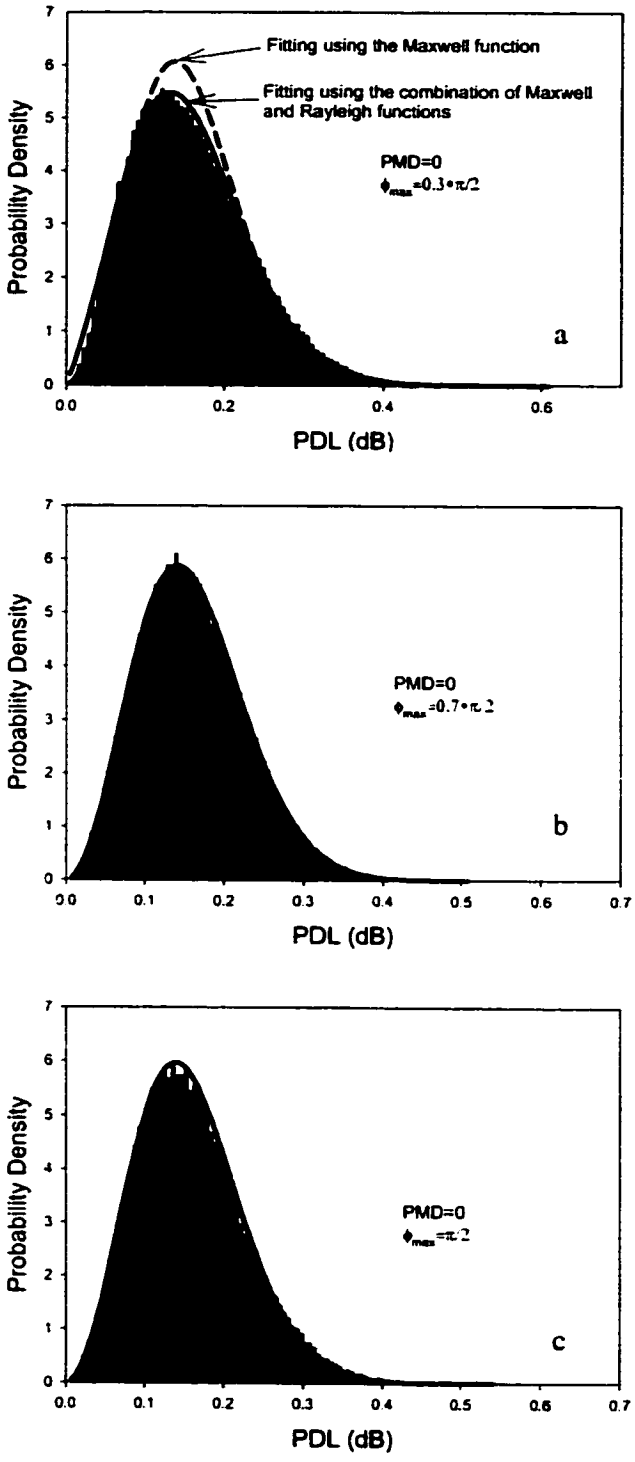

Figure 8.5 Statistical distributions of PDL with elliptical PDL vector at various maximum angles ϕ.

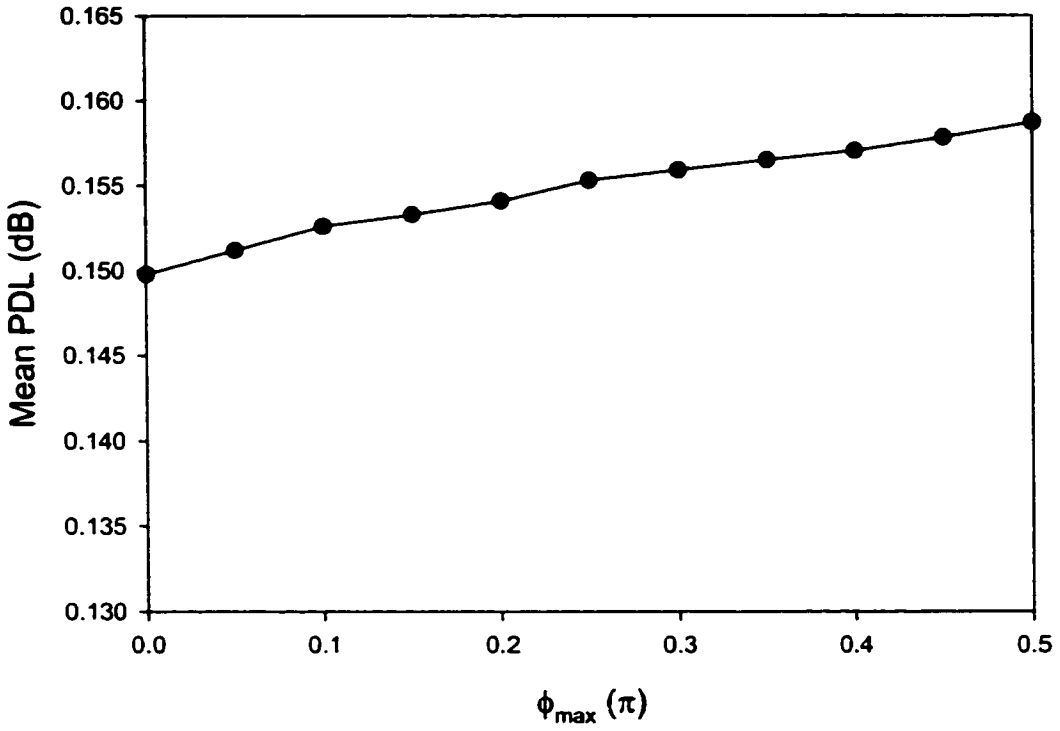

Figure 8.6 Mean PDLs with various angles of ϕ_{max}. The PMD of the fiber is zero.

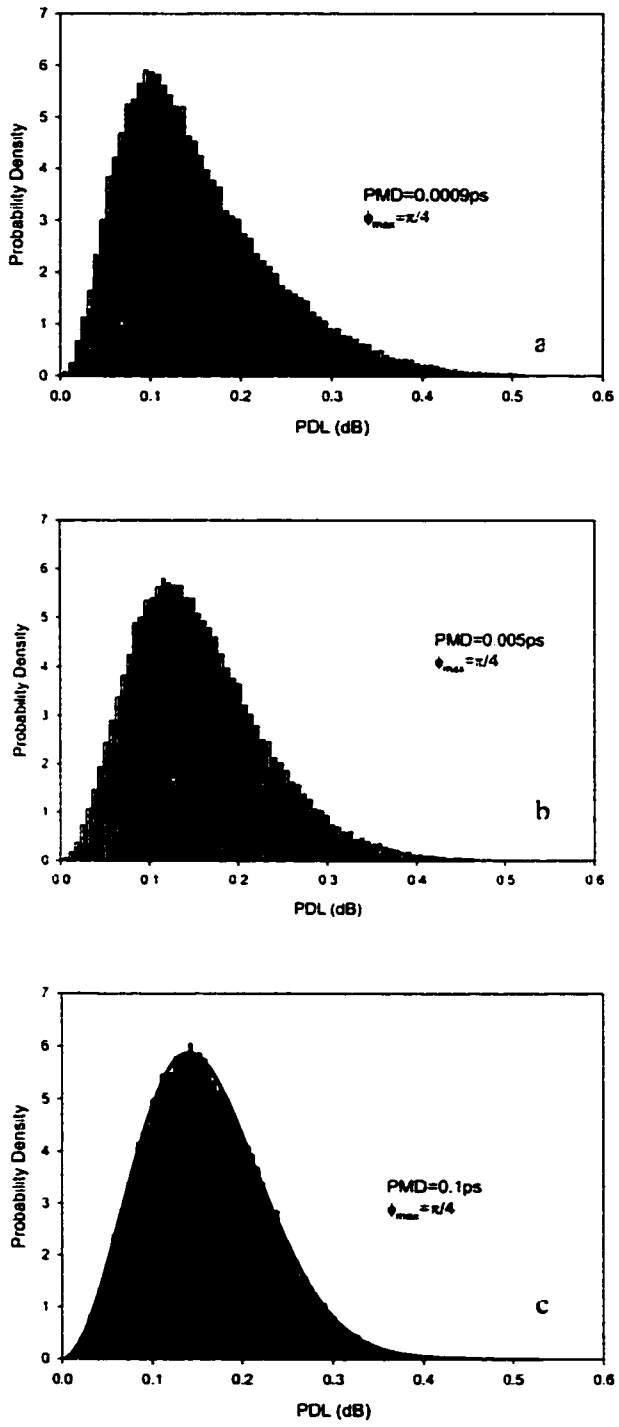

Figure 8.7 Statistical distributions of PDL at various PMD values when the PDL of each PMF segment is not linear. Solid line in c is the fitting curve with Maxwell function.

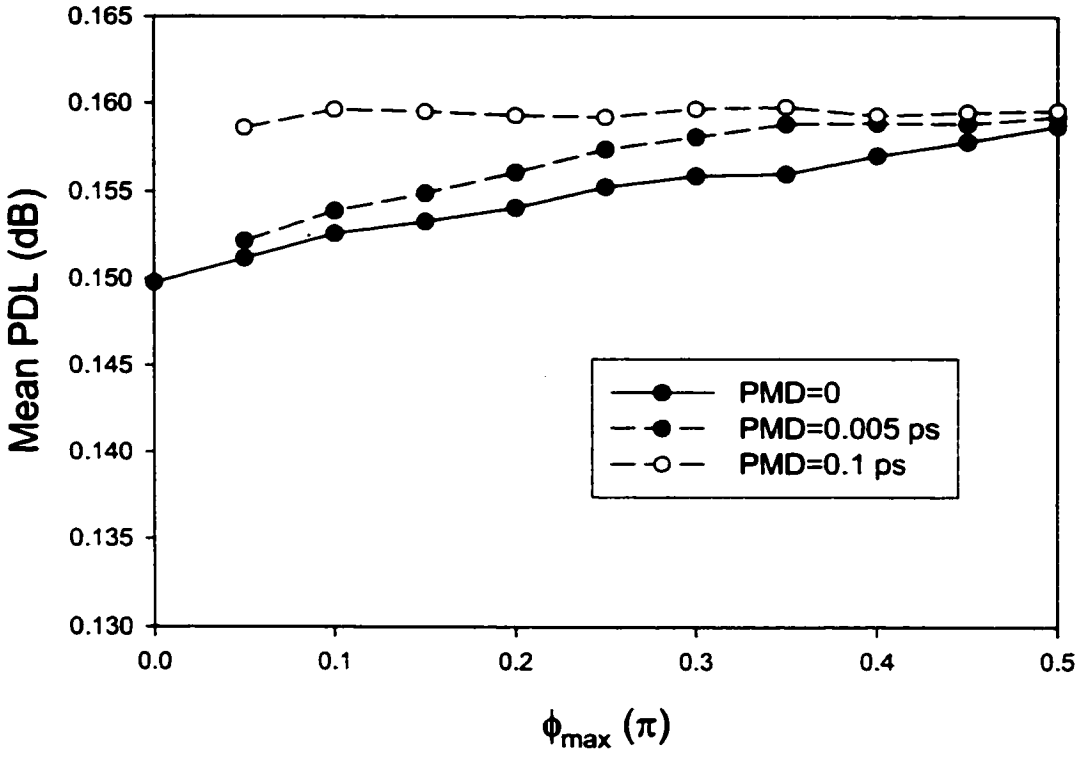

Figure 8.8 Change of mean PDL with angle ϕ_{max} at various PMDs. The standard error of the mean PDL is less than 0.0001dB

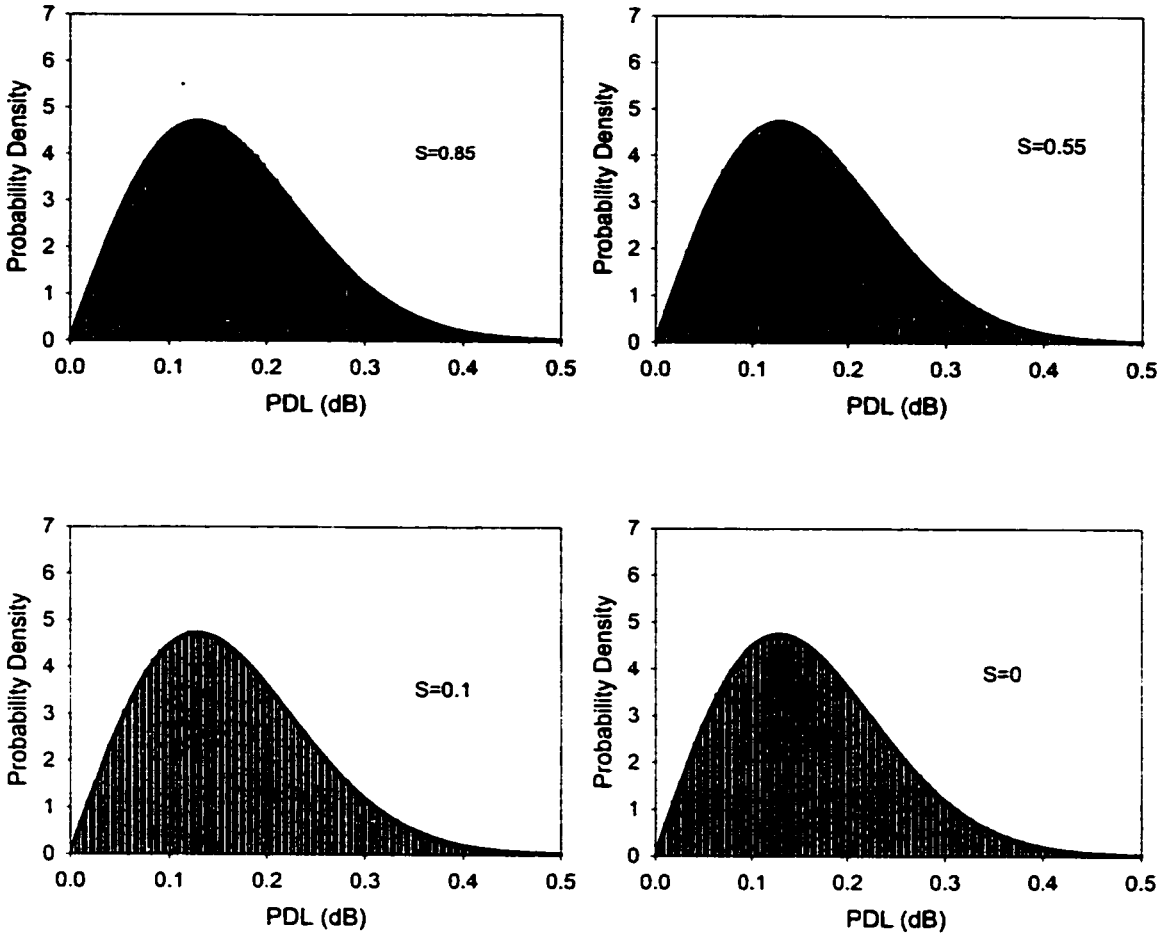

Figure 8.9 Statistical distributions of PDL at various values of S. The PDL in each segment of the waveplate model has the possibility of infinite value. The solid curves are the fitting curves of the PDL histograms with Rayleigh function.

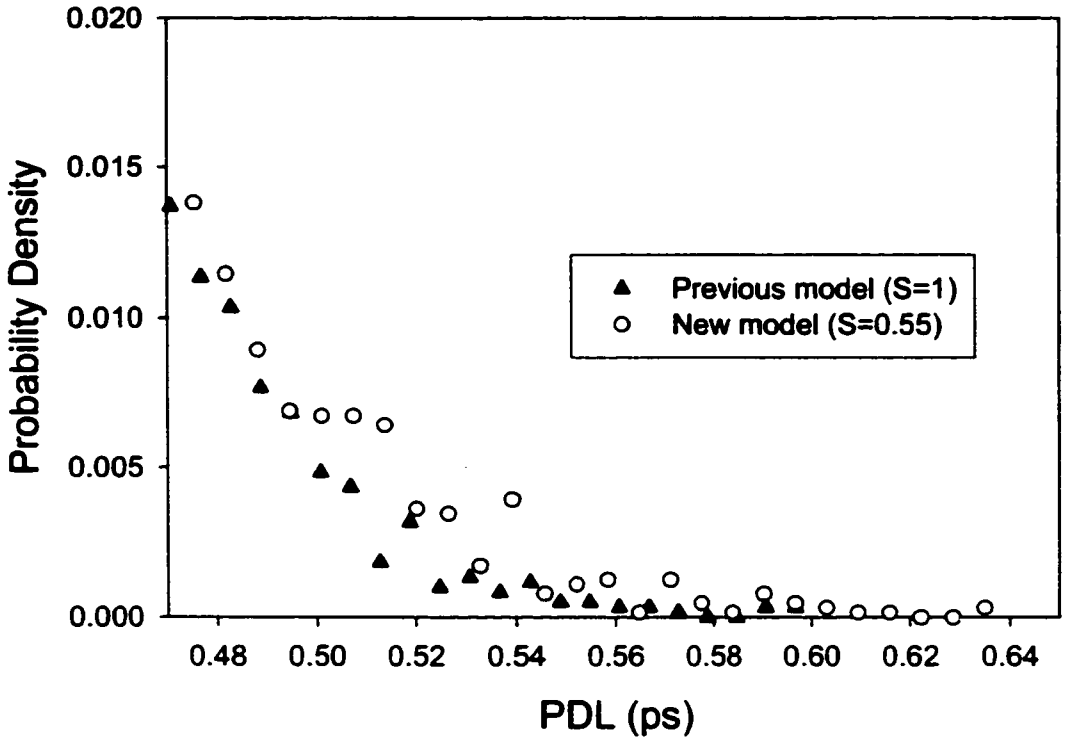

Figure 8.10 Comparison of the PDL distributions in the large PDL region with two different models.

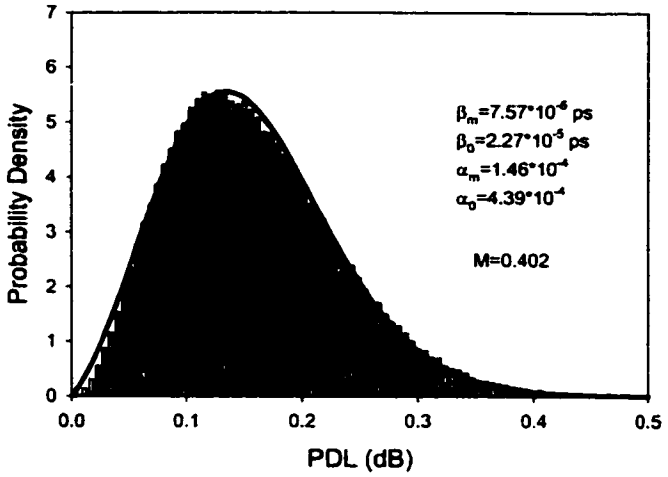

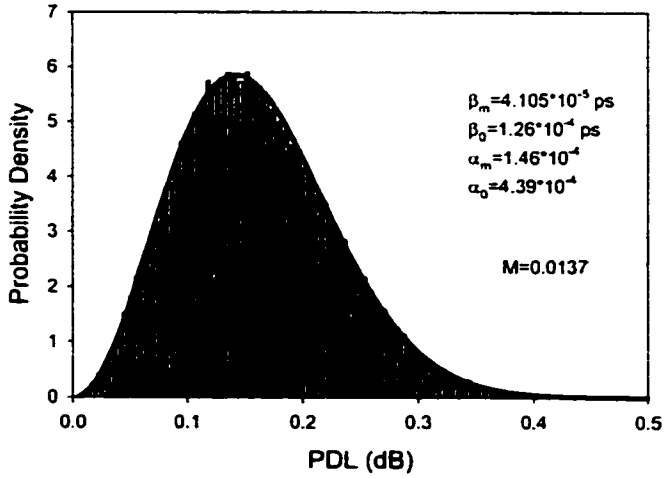

Figure 8.11 Statistical distributions of PDL with various DGDs. The PDL and DGD in the segments of the waveplate model have the possibility of infinite values.

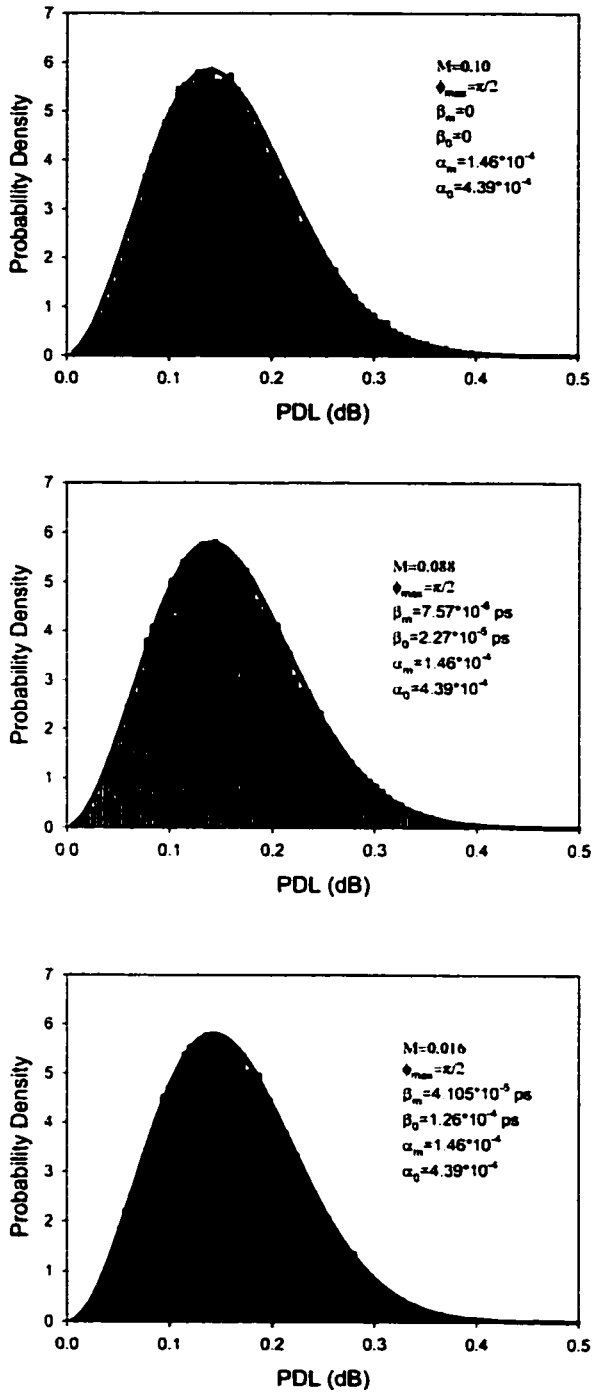

Figure 8.12 Statistical distributions of PDL in the presence of biased birefringence. The PDL and DGD in each segments of the waveplate model can be infinite.

Chapter 9

PMD and PDL for an Optical Pulse

9.1 Introduction

The properties of polarization mode dispersion (PMD) are described and understood with the concepts of principal states of polarization (PSP's) and differential group delay (DGD) [7]. In single mode fibers and fiber components, however, there is another polarization effect, i.e. polarization dependent loss (PDL). Due to the interaction of PMD and PDL the amplitude of DGD, its statistics and the two PSP's are different from those without PDL [13, 17]. Recent studies have shown that PDL can induce some anomalous phenomena in a pulse transmission, such as pulse narrowing with finite DGD [18] and pulse broadening with zero DGD [9]. However, the previous studies on PMD and PDL have been focused on the concepts of DGD, PDL and PSP's for a single frequency, even though generally they are frequency dependent [15]. This state of affairs is adequate for a system at relatively low speed, i.e. for a narrow bandwidth. With the development of high-speed optical fiber systems (10 Gbits/second and higher) the pulse durations are getting shorter and shorter and the frequency ranges in the pulses are becoming wider and wider. Clearly the assumption of narrow bandwidth is not applicable, as will be shown in this chapter. It is necessary to study the concepts of PSP, PMD and PDL for a pulse as a whole rather than its individual frequency component. The concept of PSP's for a pulse was first proposed by Shieh in 1999 [72] with the assumption of zero PDL. The two PSP's for a pulse are mutually orthogonal. In this chapter the concept of PSP for a pulse is extended to include PDL and the concepts of PMD and PDL for a pulse are proposed.

Section 9.2 describes the definitions of PSP, PMD and PDL for an optical pulse. Section 9.3

presents the PMD and PDL for a pulse in a fiber consisting of two PMF segments. Section 9.4 examines the statistical distribution of PMD and PDL for a pulse.

9.2 Theory

9.2.1 PDL for a pulse

When an optical pulse $\psi_{in}(t)$ is launched into a fiber, the two-dimensional output Jones vectors $\psi_{out}(\omega)$ (electrical fields at frequency ω) can be expressed as [58]

$$\psi_{out}(\omega) = T(\omega)\cdot\psi_{in}(\omega)\cdot\varphi\,, \tag{9.1}$$

where $T(\omega)$ is the 2×2 Jones matrix of the fiber described in Eq. 7.4. $\psi_{in}(\omega)$ (scalar) is the Fourier transform of the input pulse $\psi_{in}(t)$, φ is the input state of polarization (a 2×1 column vector, and $\varphi^{*}\cdot\varphi = 1$). In this chapter φ is assumed to be frequency independent, in other words, we assume that all the spectral components of the input pulse have the same polarization. If the fiber is a concatenation of N PMF segments and each segment has frequency-independent DGD and PDL, then $T(\omega)$ can be written as [12, 20] (here the polarization-independent loss and time delay are ignored)

$$\begin{aligned} T(\omega) = \exp(-\sum_{j=1}^{N}|\vec{\alpha}_j|/2)\cdot\exp[(-i\vec{\beta}_N\omega+\vec{\alpha}_N)\cdot\vec{\sigma}/2]\ldots \\ \times\exp[(-i\vec{\beta}_2\omega+\vec{\alpha}_2)\cdot\vec{\sigma}/2]\times\exp[(-i\vec{\beta}_1\omega+\vec{\alpha}_1)\cdot\vec{\sigma}/2] \end{aligned} \tag{9.2}$$

where $\vec{\beta}_j$ and $\vec{\alpha}_j$ are the DGD and PDL vectors of the jth segment and $\vec{\sigma}$ are the Pauli matrices, $\sigma_1 = \begin{pmatrix}1 & 0\\ 0 & -1\end{pmatrix}$, $\sigma_2 = \begin{pmatrix}0 & 1\\ 1 & 0\end{pmatrix}$, $\sigma_3 = \begin{pmatrix}0 & -i\\ i & 0\end{pmatrix}$. The directions of vectors $\vec{\beta}_j$ and $\vec{\alpha}_j$ in Stokes space are shown in Fig. 7.2 and they are described by two angles, θ_j and ϕ_j as

$$\vec{\beta}_j = \beta_j\left(\cos(\phi_j)\cdot\cos(\theta_j),\cos(\phi_j)\cdot\sin(\theta_j),\sin(\phi_j)\right)$$

$$\vec{\alpha}_j = \alpha_j\left(\cos(\phi_j)\cdot\cos(\theta_j), \cos(\phi_j)\cdot\sin(\theta_j), \sin(\phi_j)\right). \tag{9.3}$$

Here $\vec{\beta}_j // \vec{\alpha}_j$ is assumed for simplicity. This assumption still results in no-parallel DGD and PDL vectors in the fibers as discussed in chapter 7.

The output pulse power, P_{out}, from the fiber is

$$P_{out} = \int_{-\infty}^{\infty} \psi^*_{out}(t)\cdot\psi_{out}(t)dt, \tag{9.4}$$

where $\psi_{out}(t)$ is the inverse Fourier transform of $\psi_{out}(\omega)$ and $\psi^*_{out}(t)$ is the hermitian of $\psi_{out}(t)$. That is

$$\begin{aligned}\psi_{out}(t) &= \frac{1}{\sqrt{2\pi}}\int_{-\infty}^{\infty}\psi_{out}(\omega)\cdot\exp(i\omega t)d\omega \\ \psi^*_{out}(t) &= \frac{1}{\sqrt{2\pi}}\int_{-\infty}^{\infty}\psi^*_{out}(\omega)\cdot\exp(-i\omega t)d\omega.\end{aligned} \tag{9.5}$$

Substituting Eq. 9.5 to Eq. 9.4 the output pulse power is

$$\begin{aligned}P_{out} &= \frac{1}{2\pi}\int_{-\infty}^{\infty}d\omega\int_{-\infty}^{\infty}d\omega\psi^*_{out}(\omega)\cdot\psi_{out}(\omega')\int_{-\infty}^{\infty}\exp(i\omega' t - i\omega t)dt \\ &= \int_{-\infty}^{\infty}\psi^*_{out}(\omega)\cdot\psi_{out}(\omega')\delta(\omega'-\omega)d\omega d\omega' \\ &= \int_{-\infty}^{\infty}\psi^*_{out}(\omega)\cdot\psi_{out}(\omega)d\omega = \varphi^*\cdot D_{out}\cdot\varphi\end{aligned} \tag{9.6}$$

where $D_{out} = \int_{-\infty}^{\infty}T^*(\omega)\cdot T(\omega)\cdot|\psi_{in}(\omega)|^2\cdot d\omega$ is a 2×2 Hermitian matrix ($D^* = D$).

The maximum and minimum of output power can be obtained by solving the following equation with the constraint $\varphi^*\cdot\varphi = 1$ [72]

$$\delta P_{out} - \lambda\delta(\varphi^{+}\varphi) = 0, \tag{9.7}$$

where δ stands for the variation and λ is the Lagrangian multiplier. Eqs. 9.6 and 9.7 lead to the following equation:

$$(D_{out}\varphi - \lambda\varphi)^{+} \cdot \delta\varphi + \delta\varphi^{+} \cdot (D_{out}\varphi - \lambda\varphi) = 0 \tag{9.8}$$

The solution of Eq. 9.8 is

$$D_{out}\varphi = \lambda\varphi \tag{9.9}$$

The above equation defines the eigenstates and eigenvalues of matrix D_{out}. The two eigenstates are the two input SOP's that maximize/minimize the power transmission and the two eigenvalues are their corresponding maximum and minimum output power.

The effective PDL for a pulse is defined as the ratio between the maximum and the minimum of output power P_{out} in the decibel unit, that is

$$PDL_{eff} = 10 \cdot \log_{10}\left(\frac{(P_{out})_{\max}}{(P_{out})_{\min}}\right) = 10 \cdot \log_{10}\left(\frac{\lambda_1}{\lambda_2}\right), \tag{9.10}$$

where λ_1 and λ_2 are the two real eigenvalues of matrix D_{out} ($\lambda_1 > \lambda_2$), that is $D_{out} \cdot \varphi_{1,2} = \lambda_{1,2}\varphi_{1,2}$. $\varphi_{1,2}$ are the two eigenstates of D_{out}, they are the two orthogonal SOP's with minimum/maximum attenuation.

9.2.2 PMD and PSP for a pulse

The effective PMD for a pulse in the case of zero PDL is defined as the difference between

the maximum and the minimum time delay of a pulse in the fiber and the corresponding input SOP's are defined as the two orthogonal input PSP's [72].

In the presence of both PMD and PDL, the average time delay of a pulse in optical fibers can be written as (here the polarization-independent time delay is ignored)

$$\langle t \rangle = \frac{\int_{-\infty}^{+\infty} \psi_{out}^{*}(t) \cdot t \cdot \psi_{out}(t) \cdot dt}{\int_{-\infty}^{+\infty} \psi_{out}^{*}(t) \cdot \psi_{out}(t) \cdot dt}. \tag{9.11}$$

Using Eqs. 9.5, 9.6 and taking t as the form of $t = -i\frac{\frac{\partial}{\partial \omega}[\exp(i\omega t)]}{\exp(i\omega t)}$, Eq. 9.11 can be expressed as

$$\langle t \rangle = \int_{-\infty}^{\infty} \psi^{*}_{out}(\omega) \cdot i\frac{\partial}{\partial \omega} \psi_{out}(\omega) \cdot d\omega / P_{out} = (\varphi^{*} \cdot P_1 \cdot \varphi) / P_{out}, \tag{9.12}$$

where $P_1 = i\int_{-\infty}^{+\infty} [T^{*}(\omega) \cdot T'(\omega) \cdot |\psi_{in}(\omega)|^2 + T^{*}(\omega) \cdot T(\omega) \cdot \psi'_{in}(\omega)\psi^{*}_{in}(\omega)] \cdot d\omega$ is a 2×2 hermitian matrix, $T'(\omega)$ and $\psi'_{in}(\omega)$ are the derivatives of $T(\omega)$ and $\psi_{in}(\omega)$ with respect to frequency ω.

The PSP's for a pulse are defined as the SOP's, φ_{max} and φ_{min}, that maximize/minimize the time delay $\langle t \rangle$. Using the same procedure of obtaining Eq. 9.9, φ_{max} and φ_{min} can be solved from the following nonlinear eigenstate equation:

$$\left(\frac{P_1}{P_{out}} - \frac{D_{out} \cdot \varphi^{*} \cdot \varphi \cdot P_1}{(P_{out})^2} \right) \varphi = \lambda' \varphi, \tag{9.13}$$

where λ' is a Lagrangian multiplier. From Eq. 9.13 we can see that the two PSP's are not mutually orthogonal in general. The PMD for a pulse is the difference between the maximum and the minimum time delays:

$$PMD = \langle t \rangle_{\max} - \langle t \rangle_{\min} = \left(\varphi^{+} \cdot P_1 \cdot \varphi \Big/ \varphi^{+} \cdot D_{out} \cdot \varphi \right)_{\varphi=\varphi_{\max}} - \left(\varphi^{+} \cdot P_1 \cdot \varphi \Big/ \varphi^{+} \cdot D_{out} \cdot \varphi \right)_{\varphi=\varphi_{\min}} \tag{9.14}$$

9.2.3 Pulse broadening with different input SOP's

The interaction of PMD and PDL can cause pulse broadening or narrowing depending on the input SOP [9, 18, 23, 75]. Thus it is important to study the output pulse width as a function of input SOP so that we can search for the broadest and narrowest output pulse width. The effective mean squared output pulse width is defined as $\sigma^2_{eff} = \langle t^2 \rangle - \langle t \rangle^2$ [18] and

$$\langle t^2 \rangle = \frac{\int_{-\infty}^{+\infty} \psi_{out}^{*}(t) \cdot t^2 \cdot \psi_{out}(t) \cdot dt}{\int_{-\infty}^{+\infty} \psi_{out}^{*}(t) \cdot \psi_{out}(t) \cdot dt}. \tag{9.15}$$

Using Eq. 9.5 and $t = -i \dfrac{\dfrac{\partial}{\partial \omega}[\exp(i\omega t)]}{\exp(i\omega t)}$, the above equation can be written as

$$\langle t^2 \rangle = \frac{1}{P_{out}} \int_{-\infty}^{+\infty} [\psi^{*}{}'_{out}(\omega)] \cdot [\psi'_{out}(\omega)] \cdot d\omega = \frac{\varphi^{*} \cdot P_2 \cdot \varphi}{P_{out}}, \tag{9.16}$$

where $P_2 = \int_{-\infty}^{+\infty} \{ \frac{\partial}{\partial \omega} [\psi_{in}^{*}(\omega) \cdot T^{*}(\omega)] \} \cdot \{ \frac{\partial}{\partial \omega} [\psi_{in}(\omega) \cdot T(\omega)] \} d\omega$ is a 2×2 Hermitian matrix. Combining Eqs. 9.12 and 9.16 the mean squared output pulse width is

$$\sigma^2 = \varphi^{*} \cdot P_2 \cdot \varphi \Big/ P_{out} - \left(\varphi^{*} \cdot P_1 \cdot \varphi \Big/ P_{out} \right)^2. \tag{9.17}$$

The input SOP that maximizes/minimizes the mean squared output pulse width can be found via the equation $\delta(\sigma^2)-\lambda''\delta(\varphi^+\cdot\varphi)=0$ with the constraint $\varphi^+\cdot\varphi=1$ included. This leads to

$$\left\{\frac{P_2}{P_{out}}-\frac{D_{out}\varphi^+\varphi P_2}{(P_{out})^2}-2\left[\frac{P_1\varphi\varphi^+P_1}{(P_{out})^2}-\frac{\varphi^+P_1\varphi}{(P_{out})^3}D_{out}\varphi\varphi^+P_1\right]\right\}\varphi=\lambda''\varphi, \tag{9.18}$$

where λ'' is another Lagrangian multiplier.

9.3 PMD and PDL of a pulse for a concatenation of two PMF segments

This section demonstrates an example of PMD and PDL of a pulse for a fiber consisting two PMF segments (N=2). The DGDs of the two segments are 10 and 15ps respectively (i.e. $\beta_1=10ps$, $\beta_2=15ps$) and the PDLs of the two segments are 10 and 15dB respectively (i.e. $\alpha_1=1.15$, $\alpha_2=1.73$). $\vec{\alpha}_1$ and $\vec{\beta}_1$ are assumed to be parallel for simplicity in the calculation, and the same assumption is made for $\vec{\alpha}_2$ and $\vec{\beta}_2$. This assumption, however, doesn't affect the generality of the problem. This assumption naturally leads to the limit of highly coupled fibers of which the effective $\vec{\alpha}$ and $\vec{\beta}$ are not necessarily parallel (section 7.3.2). The values of angle ϕ_1 and angle θ_1 are set to be $\pi/2$ and zero respectively ($\vec{\beta}_1$ is in the direction of axis S_3). From the analysis in section 7.2 one can see that the first segment has pure circular birefringence and PDL. The value of θ_2 is set to be zero. We let the angle of ϕ_2 vary from $\pi/2$ to $-\pi/2$ ($\vec{\beta}_2$ rotates in the S_1-S_3 plane for an angle of π starting from the direction of axis S_3). This means that the birefringence of the second segment changes from circular ($\phi_2=\pi/2$), elliptical ($0<\phi_2<\pi/2$), linear ($\phi_2=0$), elliptical ($-\pi/2<\phi_2<0$) to circular with negative DGD value ($\phi_2=-\pi/2$). The input pulses launched to the fiber are assumed to be Gaussian, that is

$$\psi_{in}(\omega)=\left(\frac{2\tau_0^2}{\pi}\right)^{1/4}\cdot\exp\left(-\tau_0^2(\omega-\omega_0)^2\right), \tag{9.19}$$

where ω_0 is the optical carrier frequency and it is set to be $1.215\times10^{15} rad/s$ corresponding to communication wavelength of 1550 nm. The pulse widths, τ_0, used in this section are 100ps, 20ps and 5ps. The effective PDL and PMD of the two concatenated fibers at various pulse widths are shown in Figs. 9.1 and 9.2. We can see that both PMD and PDL show strong pulse width dependence. In other words, the PMD and PDL for a pulse are bandwidth dependent. The assumption of narrow bandwidth is not practical when PMD and PDL are considered for high-speed systems.

From Figs. 9.1 and 9.2 we can see clearly that both the effective PDL and the effective PMD for a pulse increase with input pulse width, τ_0. This is due to the effect of depolarization caused by higher order PMD and PDL [76]. The two PDLs of the two segments are 5dB and 10dB respectively and they are frequency-independent. If there is no PMD in either segment the PDL vector of the fiber is frequency-independent [12]. This means that PDL for a pulse is bandwidth independent. But in the presence of PMD the PDL vector is frequency dependent [13] (higher order PDL) except when the PMD and PDL vectors of the two segments, $\vec{\beta}_1$, $\vec{\beta}_2$ and $\vec{\alpha}_1$, $\vec{\alpha}_2$, are parallel or anti-parallel. Similarly, even when PDLs are zero the DGD vector of two concatenated PMD segments is frequency dependent as well, even though DGD value is a constant for all frequencies [18, 19]. Because of the frequency dependence of PDL and DGD vectors, the polarization states for a pulse which maximize/minimize the power transmission (maximize/minimize the time delay) cannot be identical for each frequency component in the pulse. Consequently the frequency components in the pulse cannot all reach their maximum/minimum power transmission (maximum/minimum time delay) for a given SOP. As a result, the PDL and PMD values for a pulse are generally less than those at a single carrier frequency. In order to see the pulse width dependence of the depolarization, here an example calculation of the output degrees of polarization (DOP's) is presented with various input pulse widths. The results are shown in Fig. 9.3. As we know that the output DOP depends on the input SOP. In this example the input pulses are assumed to be fully polarized (DOP=100%) and the input polarization states are chosen to have the maximum pulse power transmission for each angle ϕ_2. For a given input SOP and angle ϕ_2 the output SOP's are projected to the polarization

states which give the maximum power transmission, $\widetilde{P}_{max}$, and minimum power transmission, $\widetilde{P}_{min}$. The DOP is then given by

$$DOP = \left(\left(\widetilde{P}_{max} - \widetilde{P}_{min} \right) \Big/ \left(\widetilde{P}_{max} + \widetilde{P}_{min} \right) \right) \cdot 100\% . \tag{9.20}$$

From Fig. 9.3 we can see that at large pulse ($\tau_0 = 100ps$) the output pulse is almost fully polarized ($DOP \approx 100\%$). But at shorter pulses ($\tau_0 = 20ps$ and 5ps) the output pulses are partially polarized ($DOP < 100\%$). In the simulations it is found that when the pulse width is beyond $100ps$ the DOP is almost 100%, which corresponds to the limit of a single wavelength, and in this limit of CW the effective PDL/PMD can never be less than the PDL/DGD difference of the two fibers, however the effective PMD can still be larger than the sum of the DGDs of the two fibers.

Now let us examine some anomalous phenomena in Figs. 9.1 and 9.2. First, take a look at lines *a* and *b* in Fig. 9.2. In some cases the effective PMD of a pulse can be larger than the sum of DGD values of the two segments. The same phenomenon was also reported for the DGD of a single frequency and it is explained as the effect of destructive interference of light transmitted along the two PSP's as they are not orthogonal in the presence of PDL [19].

The other two anomalous phenomena appear in shorter pulse, $\tau_0 = 5$ps, lines c in Figs. 9.1 and 9.2. The effective PDL of a pulse can be smaller than the PDL difference of the two segments (Fig. 9.1) and the effective PMD of a pulse can be smaller than the DGD difference of the two segments (Fig. 9.2). These two phenomena are related to the interaction of PMD and PDL. In the case of null PMD, the effective PDL of a pulse is the same as that of one frequency because the PDL vector is frequency independent [20]. But in the presence of PMD the frequency-dependence of DGD and PDL vectors cause the output pulse being partially depolarized (Fig. 9.3) and thus the PDL is decreased. When the DOP of a short pulse decreases to a certain level the effective PDL for a pulse can be less than PDL difference of the two

segments. The phenomenon of effective PMD smaller than the DGD difference of the two segments may be explained as the constructive interference of two pulses propagating along the two PSP's. When a pulse is launched into a fiber it can be decomposed into two pulses, one transmits along the fast axis and the other transmits along the slow axis. In the presence of PDL the two PSP's for a pulse are not orthogonal in general. When constructive interference occurs, the overlap part of the two pulses gets stronger. As a result, the two pulses get closer and the time delay between the two pulses may be smaller then the DGD difference of the two segments.

PSP (for a single frequency or for a pulse) is a very useful concept when PDL is zero since the pulse distortion is minimum when a chirp-free pulse is launched into either of the two PSP's [72]. However this is no longer true in the presence of PDL. First let us see how the pulses are distorted when the pulses are launched along the two PSP's respectively. This simulation is done at the anomalous PMD region (see Fig. 9.2, $\theta_1 = \theta_2, \phi_1 = \pi/2$, $\phi_2 = -0.44\pi$, τ_0=5ps). The results are shown in Fig. 9.4. It is clear that the output pulse shapes are very different when the incident light is launched into different PSP's. One of the pulses (dashed line) actually include two humps. This kind of pulse distortion in the presence of PDL needs to be carefully studied when one tries to compensate PMD using the method of splitting the optical signal at the fiber output into polarization components that is aligned to only one PSP [11].

It is worthwhile to emphasize that the PSP's for a pulse without chirp are coincident with the SOP's giving the minimum pulse broadening in the case of zero PDL [72]. But PDL will lift this degeneracy. Fig. 9.5 shows the maximum pulse width, minimum pulse width and pulse widths when input pulses are launched along the two PSP's at different ϕ_2 angles. The input Gausian pulse width is 5 ps, $\theta_1 = \theta_2 = 0$ and $\phi_1 = \pi/2$. Fig. 9.5 shows that, when a pulse is launched along one of the two PSP's, the output pulse width is *not* the minimum in general. It is between the maximum and minimum pulse widths and is PSP dependent. This indicates that, in the presence of PDL, the distortion is not the minimum when a pulse is launched along either of the two PSP's (still have pulse spreading).

9.4 Statistical distribution of PMD and PDL for a pulse

Considering the statistical nature of PMD and PDL in fiber networks, the statistical distributions of PMD and PDL for a pulse are studied in this section.

9.4.1 Statistical distribution of PMD for a pulse

The statistical distribution of DGD for a single frequency is Maxwellian in the absence of PDL and it is the combination of Gauss and Maxwell function in the presence of high PDL [17]. In this subsection the statistical distribution of PMD for a pulse is studied by examining many statistical ensembles with 5,000 fibers in each ensemble and with 20 PMF segments in each fiber. First the PMD distribution is studied by examining three ensembles with the pulse widths of 40, 10 and 5 ps in the absence of PDL. The mean DGDs (single frequency) of the fiber is 5 ps. Fig. 9.6 shows the statistical PMD distributions with various pulse widths. The solid curves are the fittings of the PMD distributions using Maxwell function. It is clear from Fig. 9.6 that the distribution of PMD for a pulse is still Maxwellian with mean PMD value increases with pulse width. Secondly the distribution of PMD for a pulse is studied by examining three ensembles with both PMD and PDL. The DGD (single frequency) of each fiber is still 5 ps and the PDL (single frequency) of each fiber is 8 dB. Fig. 9.7 shows the distributions of PMD for a pulse with the *rms* pulse widths of 100, 40 and 5ps. From Fig. 9.7a one can see the probability distribution of PMD for a pulse in the presence of PDL is still a combination of Gauss and Maxwell functions for large pulse width (100ps), which is similar to case of the single frequency (Fig. 7.10). With the decrease of pulse width the probability distribution of PMD for a pulse is mainly a Maxwellian ($\tau_0 = 5ps$, Fig. 9.7c). This PMD distribution at small pulse width is due to the depolarization effect with small pulse width (Fig. 9.3).

9.4.2 Statistical distribution of PDL for a pulse

The statistical distribution of PDL for one frequency is the Rayleigh function in the absence of PMD (Fig. 8.1). In the absence of PMD the distribution of PDL for a pulse is the same as that for single frequency because in each segment in the fiber the PDL is assumed to be frequency

independent. In the presence of PMD the distribution of PDL is studied in this subsection by examining four ensembles with different PMD values and different pulse widths. There are 5,000 fibers in each ensemble and there are 20 PMF segments in each fiber. The DGD (single frequency) in the first two ensembles is 0.0001ps and the pulse widths are 10 and 5 ps respectively. Fig. 9.8 shows the distributions of PDL for a pulse of the first two ensembles. The solid curves are the fitting curves of the PDL distribution using Eq. 8.8. It is clear that, similar to the PDL distribution for a single frequency, the distribution of PDL for a pulse is the combination of Rayleigh and Maxwell functions in the presence of small PMD. When DGD in the fibers increases to 0.01ps, Fig. 9.9 shows the statistical distribution of PDL for a pulse with pulse widths of 10 and 5 ps respectively. From the fitting curves one can see that the PDL distribution is mainly Maxwellian (the distribution M factors (Eq. 8.8) are 0.034 and 0.041 respectively). This is similar to the distribution of PDL for a single frequency---with the increase of PMD the PDL distribution changes from Rayleigh to Maxwell functions.

9.5 Conclusion

The concepts of PSP, PMD and PDL for an optical pulse are proposed and discussed in this chapter. The PMD and PDL of a pulse for a fiber consisting of two PMF segments are calculated. The results show that the PMD and PDL of a pulse are strongly pulse-width dependent for short pulse. Due to the depolarization of lightwave and the interaction of PMD and PDL, two anomalous results are found: a) The effective PDL of a pulse can be smaller than the PDL difference of the two fibers. b) The effective PMD for a pulse can be either larger than the sum of the DGDs of the two fibers or less than the DGD difference of the two fibers, depending on the input pulse width. Also, the pulse distortion is not the minimum when a pulse is launched into either of the PSP's in the presence of PDL. This calls extra caution in first order PMD compensation in which the input pulses are launched into one of the PSP's [11].

The statistical distributions of PMD and PDL for a pulse are studied. The probability density distribution of PMD for a pulse is still a Maxwell in the absence of PDL. In the presence of high PDL the PMD distribution is a combination of Gauss and Maxwell functions at larger pulse

width (100ps) and it is mainly Maxwellian at short pulse width (5ps). The probability of PDL for a pulse is similar to the single frequency case—the PDL distribution is a combination of Rayleigh and Maxwell distributions.

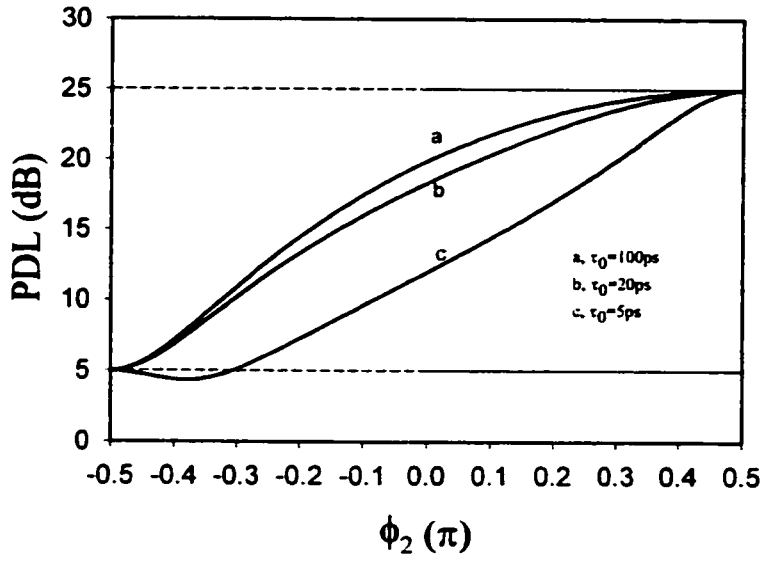

Figure 9.1 Effective PDL for s pulse of two concatenated fibers. PDL_1=10dB, PDL_2=15dB, β_1=10ps, β_2=15ps, $\phi_1 = \pi/2$, θ_1=0 and θ_2=0. The upper dashed line is the sum of the two PDLs (25dB) and the lower dashed line is the difference of the two PDLs (5dB).

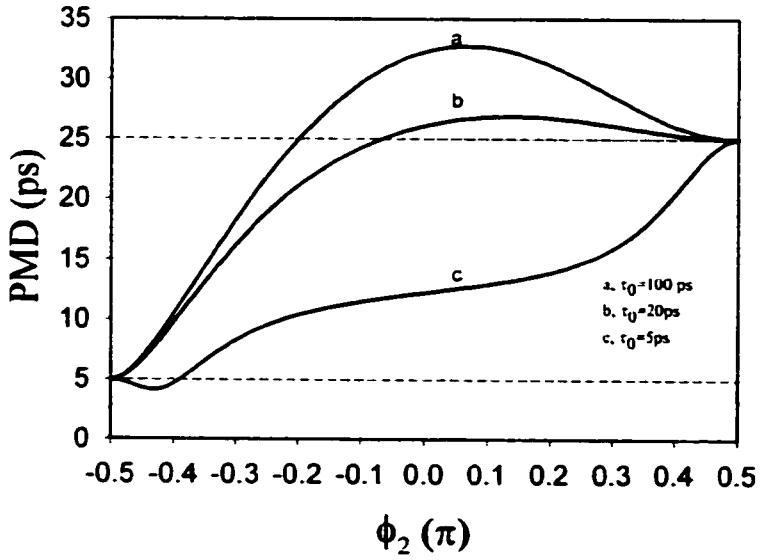

Figure 9.2 Effective PMD for a pulse of two concatenated fibers. PDL_1=10dB, PDL_2=15dB, β_1=10ps, β_2=15ps, $\phi_1 = \pi/2$, θ_1=0 and θ_2=0. The upper dashed line is the sum of the two DGDs (25dB)and the lower dashed line is the difference of the two DGDs (5dB).

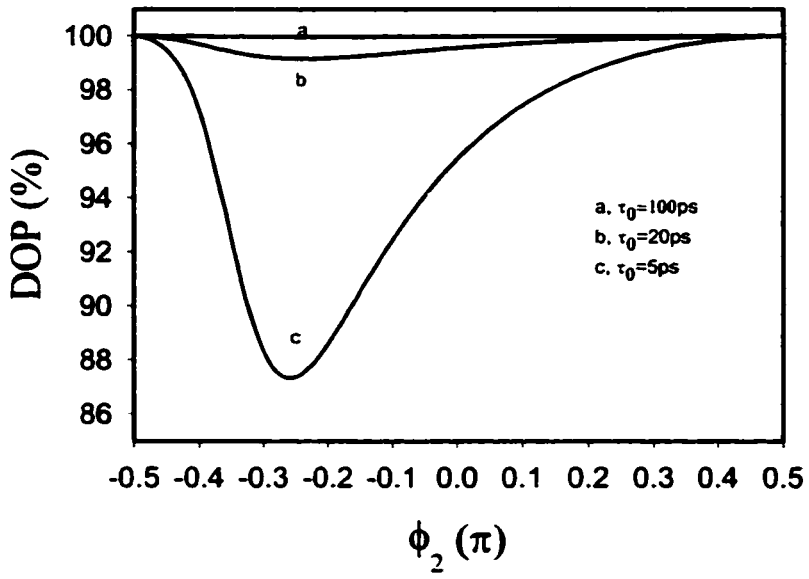

Figure 9.3 Degree of polarization of the output pulses when the input states of polarization maximize power transmission. PDL_1=10 dB, PDL_2=15 dB, β_1=10 ps, β_2=15 ps $\phi_1 = \pi/2$, θ_1=0 and θ_2=0.

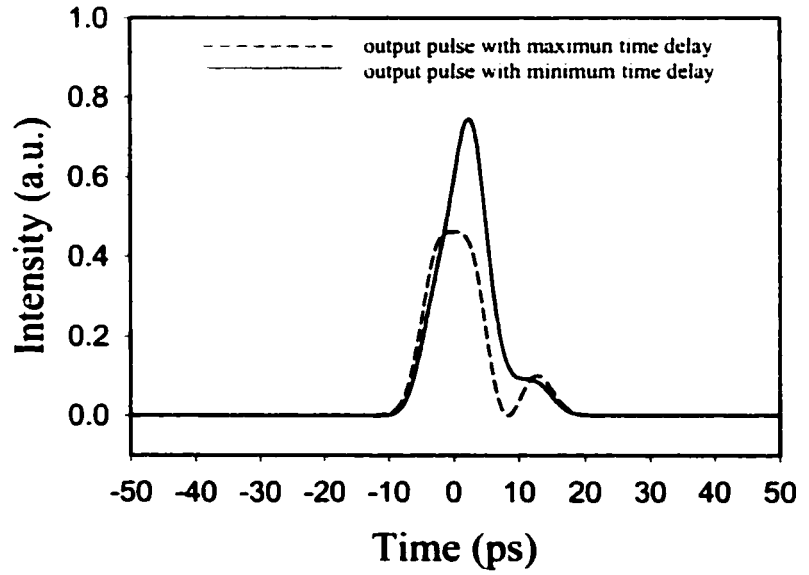

Figure 9.4 Pulse distortions when input Gausian pulses are launched to the two PSP's. The *rms* input pulse width is 5 ps. The value of ϕ_2 is chosen for the case of effective PMD less than the DGD difference of the two segments (ϕ_2=-.44π, $\theta_1 = \theta_2 = 0, \phi_1 = \pi/2$).

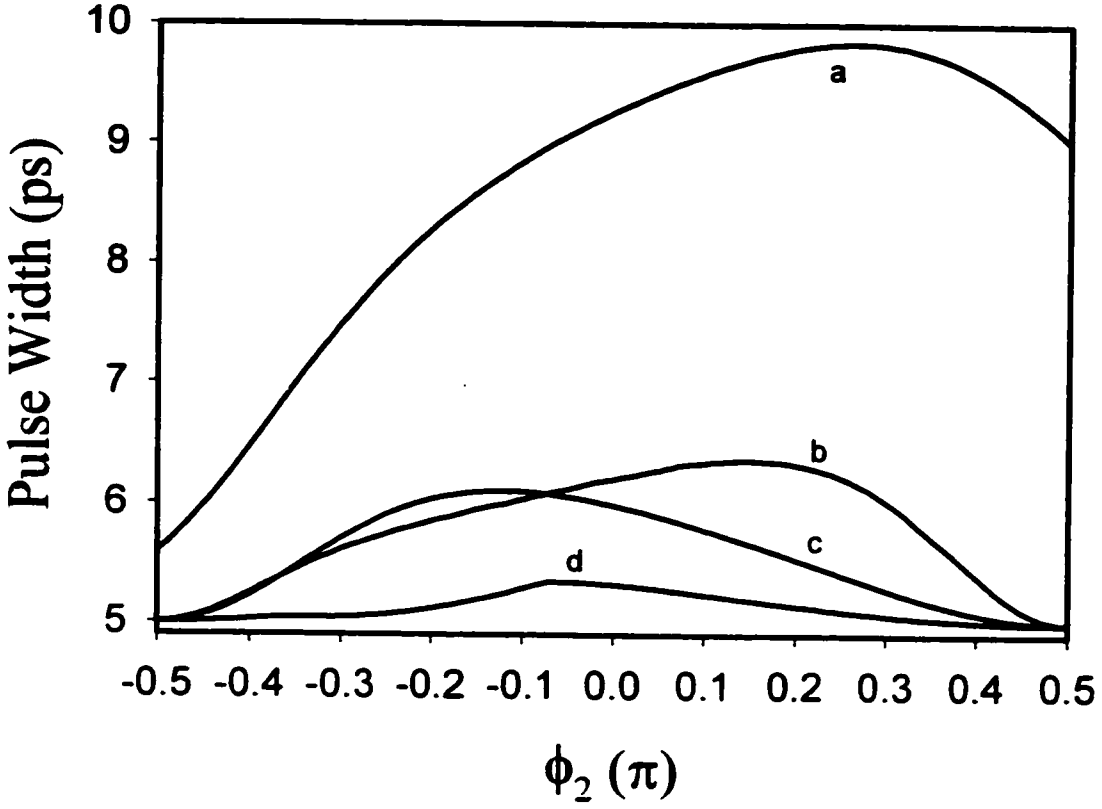

Figure 9.5 Output pulse widths with various input states of polarization.

a, SOP with maximum pulse width.

b, SOP with minimum time delay (fast axis).

c, SOP with maximum time delay (slow axis).

d, SOP with minimum pulse width.

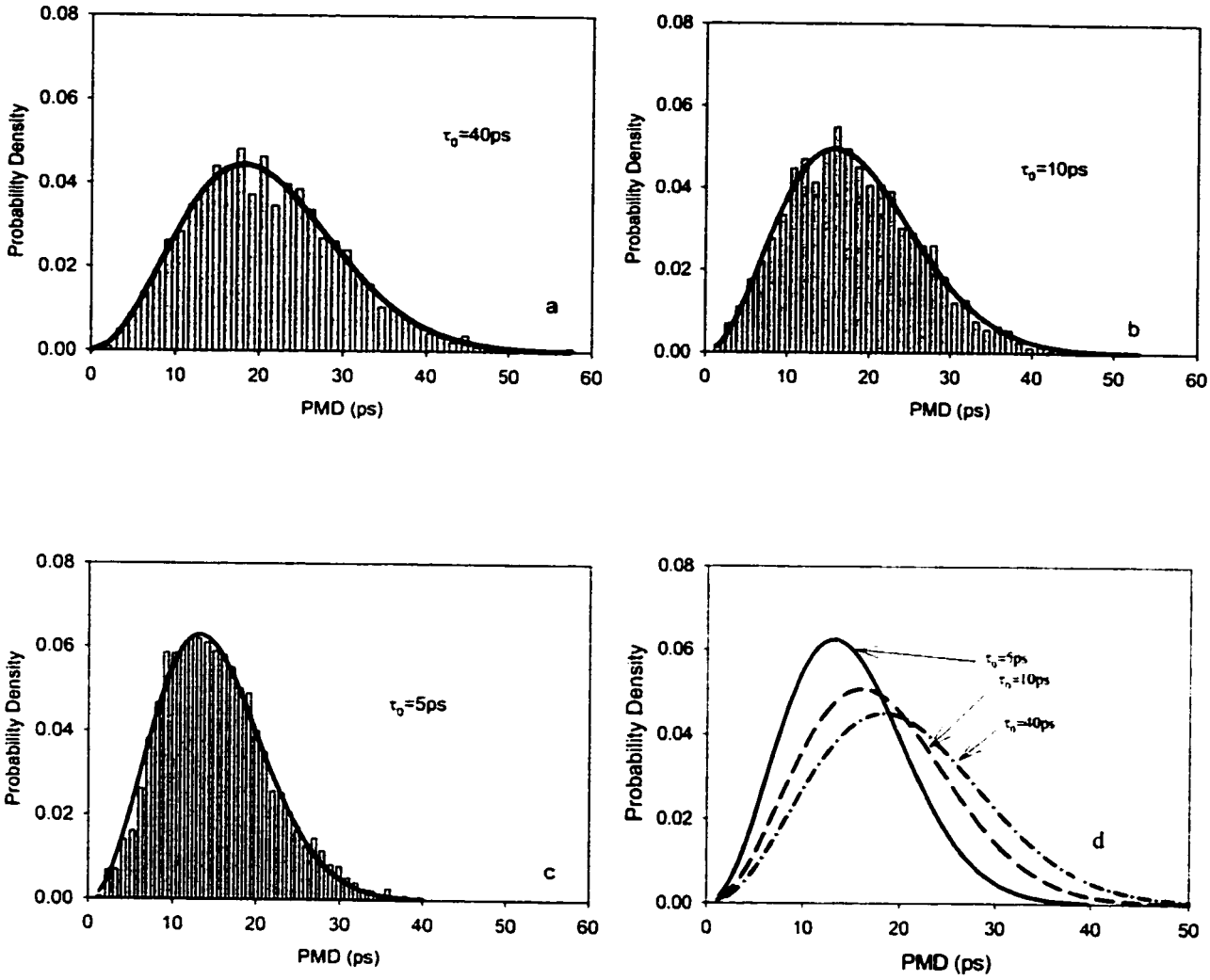

Figure 9.6 Statistical distributions of PMD for a pulse at various pulsewidths. The solid curves in a), b) and c) are the fitting of the PMD distribution using Maxwell function. d) is the fitting curves of PMD distribution at all three pulsewidths.

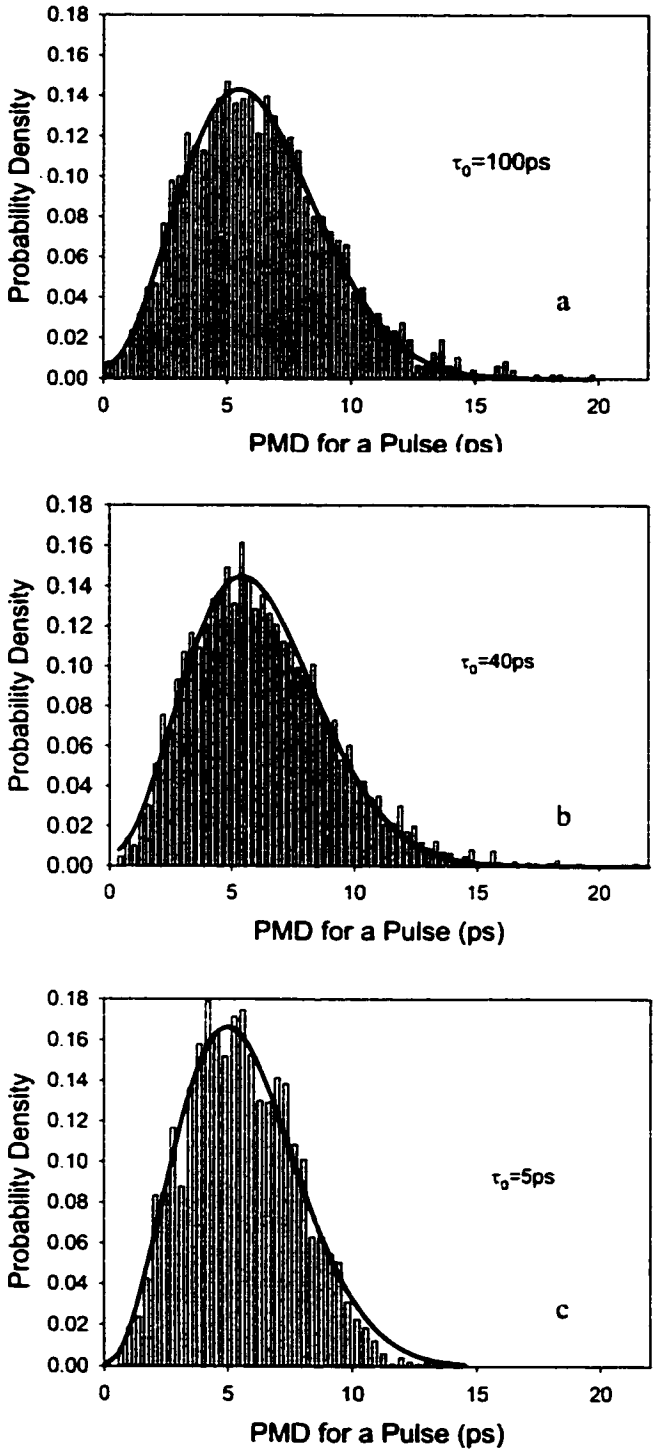

Figure 9.7 Statistical distributions of PMD for a pulse in the presence of PDL (8dB) at various pulse widths.

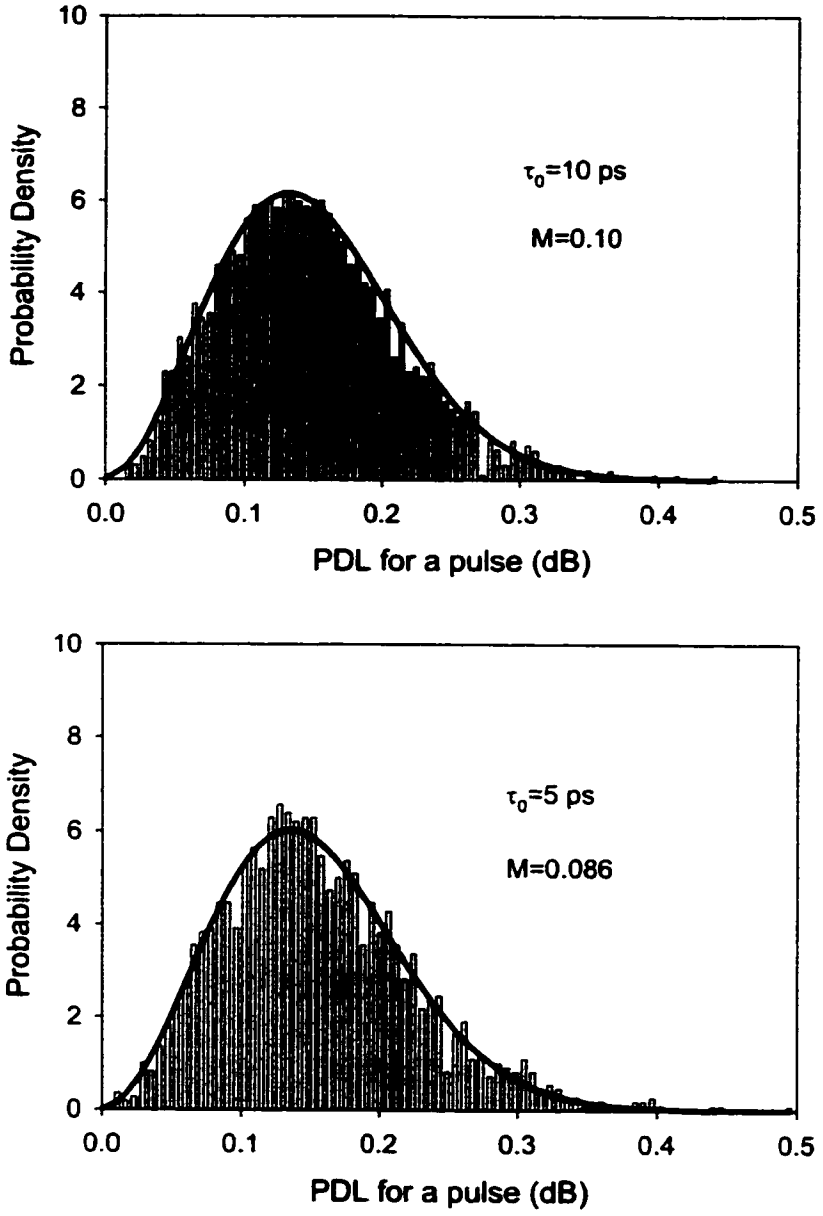

Figure 9.8 Statistical distributions of PDL for a pulse with small DGD (0.0001ps). The solid curves are the fittings of the PDL distributions using the combination of Rayleigh and Maxwell functions.

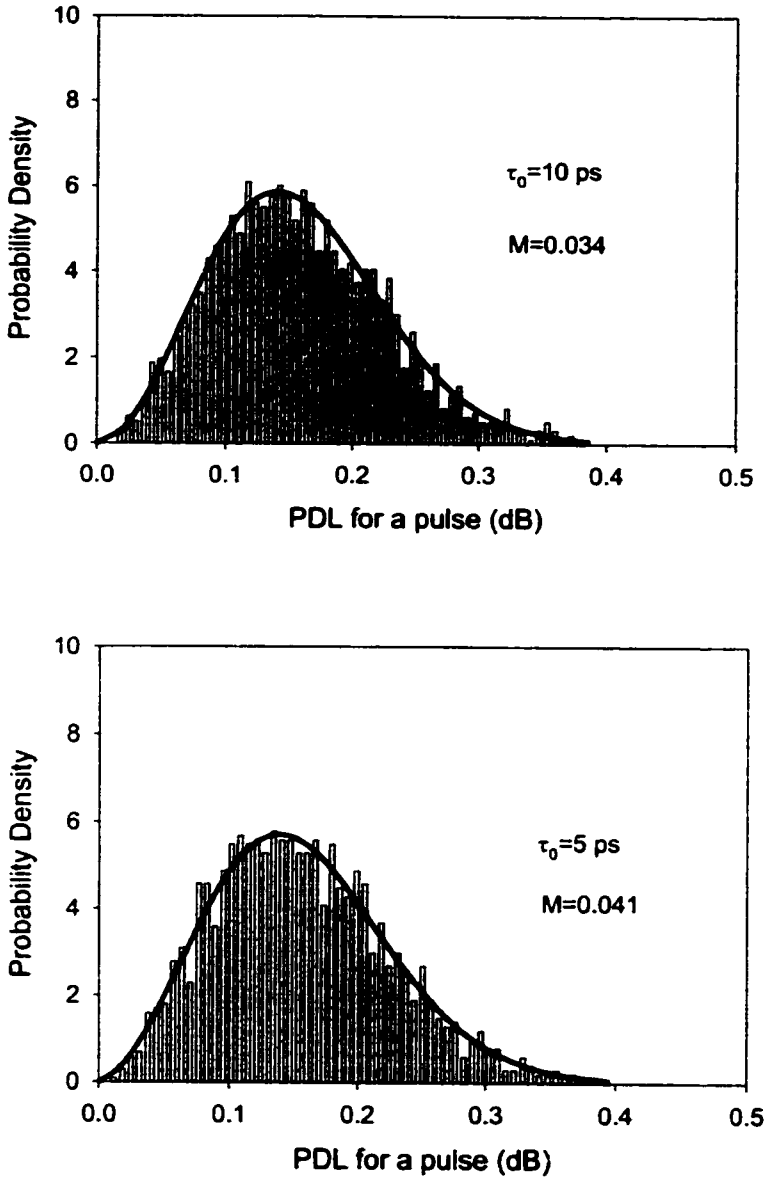

Figure 9.9 Statistical distribution of PDL for a pulse with PMD (0.01ps). The solid curves are the fittings of the PDL distributions using the combination of Maxwell and Rayleigh functions.

Chapter 10

System Impact of PMD and PDL

10.1 Introduction

When fiber attenuation and chromatic dispersion are compensated, PMD and PDL are the two major factors that limit the capacity of fiber optic communication systems at high bit rate (>10 Gbits/second). The system impact due to PMD alone has been studied both theoretically [7, 8, 21, 23, 77] and experimentally [24, 78, 79]. With the development of high capacity communication systems, the fiber networks are becoming more complicated as more fiber components are used. Fiber components, such as optical add-drop multiplexers, fiber Bragg gratings, wavelength-division multiplexers and demultiplexers, have both PMD and PDL [9, 13, 62]. It has been shown that the system impact due to the combined effect of PMD and PDL is more severe than PMD or PDL acting alone [9, 13, 62]. However, the system impact due to PDL alone and that due to the combination of PMD and PDL have not been studied quantitatively. The system PMD limit in the presence of PDL has not been examined and the power margin for PDL compensation has not been reported. In this chapter the combined effects of PMD and PDL are studied by examining the transmissions of the "010" and "101" bit patterns in a fiber optic communication system (10 Gbits/second) using the waveplate models presented in chapters 7 and 8.

Section 10.2 presents the modeling of a typical *intensity modulation with direct detection* (IM-DD) fiber optic communication system with PMD and PDL. The transmissions of the "101" and "010" bit patterns in this system are discussed. Section 10.3 studies the system impact due to PDL alone (PMD=0), which includes the distributions of system Q factor, BER and the system outage probability. The PDL induced Q factor distribution is measured experimentally and then is compared to the numerical simulation. Section 10.4 presents the

system impact due to PMD with the chromatic dispersion and the frequency chirp (PDL=0). The interactions of PMD with the chromatic dispersion and the frequency chirp are examined. The combined PMD and PDL effect on system impact is studied in section 10.5. The PMD and PDL interactions are presented and the system PMD limit in the presence of PDL is discussed. The system Q factor distribution with PMD and PDL is measured experimentally and is compared to the numerical simulation. Section 10.6 is a short conclusion of this chapter.

10.2 Modeling

The model used in this chapter to simulate the system impact due to PMD and PDL is shown in Fig. 10.1. This is a typical IM-DD fiber optic communication system that consists of an optical transmitter, optical fibers and components, an optical amplifier with an optical filter, and a photo detector with an electrical filter. The pulses from the transmitter are assumed to be Gaussian, that is

$$P(t) = A_0 \sqrt{2\pi}\tau_0 \exp\left(-\frac{t^2}{2\tau_0^2}\right), \tag{10.1}$$

where A_0 is a constant depending on the optical power from the transmitter and τ_0 is the *rms* pulse width. The electrical field that corresponds to the pulse is [6]

$$\vec{E}(t) = E(t)\vec{\varphi} = \left(2\pi\tau_0^2 A_0^2\right)^{\frac{1}{4}} \exp\left(-\frac{1+iC}{4}\left(\frac{t}{\tau_0}\right)^2\right)\exp(i\omega_0 t)\vec{\varphi}, \tag{10.2}$$

where C is the linear frequency chirp parameter imposed on the pulse, it is the derivative of frequency with respect to time, t. ω_0 is the optical carrier frequency and $\vec{\varphi}$ is a unitary vector standing for the input state of polarization (SOP).

The Jones vector (electrical field at frequency ω) corresponding to the pulse shown in Eq. 10.2 can be expressed as

$$\vec{E}(\omega) = E(\omega)\vec{\varphi} = \left(\frac{8\pi {A_0}^2 {\tau_0}^6}{(1+iC)^2}\right)^{\frac{1}{4}} \exp\left(-\frac{(\omega-\omega_0)^2 {\tau_0}^2}{(1+iC)}\right)\vec{\varphi}, \qquad (10.3)$$

where $E(\omega)$ is the Fourier Transform of $E(t)$, $E(\omega) = \frac{1}{\sqrt{2\pi}} \int_{-\infty}^{\infty} E(t)\exp(-i\omega t)dt$.

The system impact due to PMD and PDL is studied in this chapter by examining the distortions of "010" and "101" bit patterns. The electrical fields of "010" and "101" bit patterns from the transmitter can be written as

$$\begin{aligned} \vec{E}_{1in}(t) &= \vec{E}(t) && \text{("010" pattern)} \\ \vec{E}_{0in}(t) &= \vec{E}(t+T) + \vec{E}(t-T) && \text{("101" pattern),} \end{aligned} \qquad (10.4)$$

where T is the bit period. The Fourier transforms of $\vec{E}_{1in}(t)$ and $\vec{E}_{0in}(t)$, $\vec{E}_{1in}(\omega)$ and $\vec{E}_{0in}(\omega)$, are the corresponding Jones vectors of "010" and "010" bit patterns, respectively.

The output Jones vectors that correspond to "010" and "101" patterns are [58]

$$\begin{aligned} \vec{E}_{1out}(\omega) &= T(\omega)\vec{E}_{1in}(\omega) && \text{("010" pattern)} \\ \vec{E}_{0out}(\omega) &= T(\omega)\vec{E}_{0in}(\omega) && \text{("101" pattern),} \end{aligned} \qquad (10.5)$$

where $T(\omega)$ is the Jones Matrix of the system and it can be written in the forms of Eqs.7.1 and 7.4. The inverse Fourier transforms of $\vec{E}_{1out}(\omega)$ and $\vec{E}_{0out}(\omega)$ are the output electrical fields in time domain, $\vec{E}_{1out}(t)$ and $\vec{E}_{0out}(t)$. The output optical powers of "010" and "101" patterns are

$$\begin{aligned} P_{1out}(t) &= \left|\vec{E}_{1out}(t)\right|^2 && \text{("010" pattern)} \\ P_{0out}(t) &= \left|\vec{E}_{0out}(t)\right|^2 && \text{("101" pattern).} \end{aligned} \qquad (10.6)$$

The currents of the photo detector produced by "010" and "101" patterns are proportional to the optical powers of "010" and "101" patterns. They can be written as [80]

$$I_1(t) = RGP_{1out}(t) \qquad \text{("010" pattern)}$$
$$I_0(t) = RGP_{0out}(t), \qquad \text{("101" pattern),} \tag{10.7}$$

where $R = \eta q / h\nu$ is the responsivity of the photo detector, η is the quantum efficiency, q is the charge of electron, $h\nu$ is the photon energy and G is the gain of the optical amplifier.

Noises in a practical communication system mainly include detector thermal noise, shot noise and the beatings of amplifier spontaneous emission against itself, signal and shot noise [80]. In a system where optical amplifiers are used the dominating noises are the spontaneous-signal and the spontaneous-spontaneous beating noises, other noises can be ignored [6, 8, 58]. The spontaneous- spontaneous beating noise and the spontaneous-signal beating noise can be expressed as [80]

$$\sigma^2_{sp-sp} = (q\eta G F_n)^2 \Delta\nu_{opt} \Delta f$$
$$\sigma^2_{sig-sp} = 2(q\eta G)^2 F_n P_s \Delta f / h\nu, \tag{10.8}$$

where F_n is the noise figure of the optical amplifier and it can be written as [81]

$$F_n = 2\frac{N_2(G-1)}{(N_2 - N_1)G} \approx \frac{2N_2}{N_2 - N_1}, \tag{10.9}$$

where N_1 and N_2 are the populations in the ground and excited states of the optical amplifier. $\Delta\nu_{opt}$ is the bandwidth of the optical filter. Δf is the bandwidth of the electrical filter. $P_s = P_{1out}(t)$ or $P_{0out}(t)$ is the optical power of pattern "010" or "101".

The system Q-factor is determined by the eye opening ($I_1 - I_0$) and the noise at decision time t_d. It is defined as [82]

$$Q = \left.\frac{I_1 - I_0}{\zeta_1 + \zeta_0}\right|_{t=t_d}, \tag{10.10}$$

where ζ_1 and ζ_0 are the effective noises of patterns "010" and "101" respectively

$$\begin{aligned}\zeta_1 &= \left((q\eta GF_n)^2 \Delta\nu_{opt}\Delta f + 2(q\eta G)^2 F_n P_{1out}\Delta f / h\nu\right)^{1/2} \\ \zeta_0 &= \left((q\eta GF_n)^2 \Delta\nu_{opt}\Delta f + 2(q\eta G)^2 F_n P_{0out}\Delta f / h\nu\right)^{1/2},\end{aligned} \tag{10.11}$$

The bit-error-rate (BER) is associated to the system Q-factor by [82]

$$BER = \frac{1}{2} erfc\left(\frac{Q}{\sqrt{2}}\right), \tag{10.12}$$

where erfc is the complementary error function. Q-factor and BER are two equivalent parameters of evaluating the system performance. In this chapter the impact of PMD and PDL is discussed using both system Q factor and BER.

The parameters used in Eqs.10.1 to 10.8 are based on a practical fiber optic communication system. A_0 in Eqs.10.1~10.3 depends on the average output power from the transmitter, P_0. P_0 is set to be 0 dBm for all the simulations. The global loss of the system is set to be 30dB. The occurrences of bit "1" and bit "0" are assumed to have the same possibility. The energy with each bit "1", A_0, is

$$A_0 = 2TP_0 \tag{10.13}$$

The *rms* input pulse width τ_0 in Eq. 10.1 is 40 ps (4×10^{-11} seconds) that corresponds to return-to-zero (RZ) pulses of OC192 (10 Gbits/second). Optical carrier frequency ω_0 in Eqs.10.2 and 10.3 is $1.2153\times10^{15}\,rad/s$ that corresponds to a wavelength around 1550 nm. The SOP, $\vec{\varphi}$, from the transmitter is always set to be $\frac{1}{\sqrt{2}}\begin{pmatrix}1\\1\end{pmatrix}$. Bit period T in Eq. 10.4 is 100 ps. The quantum efficiency η of the photo detector is 100% (an ideal detector) and the photo energy $h\nu$ is the energy of photon at wavelength of 1550 nm. The gain of the optical amplifier, G, is 20 dB and noise figure F_n is 5 dB (the ideal is 3 dB). The bandwidth of the optical filter, $\Delta\nu_{opt}$, is 125GHz (1 nm channel spacing) and the bandwidth of the electrical filter, Δf, is 6 GHz. These two bandwidths are chosen for the practical channel spacing of the WDM system and the optimized electrical SNR of a photo detector [8, 62]. The decision time t_d in Eq. 10.10 is chosen to give the maximum eye-opening ($I_1 - I_0$).

PMD and PDL in fiber networks show stochastic properties due to environmental perturbations. In the following sections the system impacts due to PMD and PDL are studied in terms of the statistical distributions of Q factor, BER and the system outage probability. The system outage probability is defined as the cumulative probability that the BER exceeds the value of 10^{-12} [8].

10.3 System impact due to PDL

10.3.1 System Q factor and BER (previous model)

PDL induces power fluctuation in fiber optic communication systems. As a result, the system Q factor and BER change with time. In this section the PDL impact is studied by examining many statistical fiber ensembles with various PDL values. There are 10,000 fibers in each ensemble and each fiber consists of 40 PMF segments. The PDL in each segment is uniformly distributed within a finite range that depends on the mean value of PDL in the system.

Fig. 10.2 shows the eye diagrams of an OC192 system with the mean PDLs of 0.25 dB and 0.35 dB. We can see that PDL introduces more power fluctuations in bit "1" than in bit "0". With the increase of PDL the optical power of bit "1" decreases due to PDL induced global attenuation in the system [13]. In Fig. 10.2 we can see that the power of "101" bit pattern at time $t \approx 0$ is higher than that of "010" pattern at both edges, which is due to the interference of two pulses in "101" pattern (Eq. 10.4). This effect can be cancelled if the "010" pattern is replaced with "10101" pattern. However, this effect will not affect the calculations in this chapter because the decision time, t_d, is chosen to have the maximum eye-opening ($t_d \approx 0$). The optical powers at the two edges of "010" pattern are not used in the calculations. Fig. 10.3 shows the statistical distributions of system Q-factor and BER with mean PDL of 0.25dB. The solid line in Fig. 10.3a is the fitting curve using a normalized Gauss function, that is

$$PDF = \frac{2}{\pi\bar{x}} \exp\left(-\frac{4(x-\bar{x})^2}{\pi\bar{x}^2} \right), \tag{10.14}$$

where x stands for Q factor, $\bar{x}$ stands for the mean value of x and PDF stands for probability density function. It can be seen that the statistical distribution of Q factor due to PDL is Gaussian. The BER probability decreases very quickly with BER, see Fig. 10.3b. With mean PDLs of 0.12, 0.25, 0.35, 0.50, 0.65 dB, Figs.10.4 and 10.5 show the fitting curves of Q factor distributions and the histograms of BER respectively. It is clear from Fig. 10.4 and 10.5 that the system Q-factor and BER strongly depends on PDL. When mean PDL increases from 0.12 to 0.65dB the mean Q factor drops from ~9.3 to ~7.6.

10.3.2 System Q factor and BER (new model)

In section 7.4 a new waveplate model is proposed. This model can generate any DGD and PDL values. Section 8.5 shows that in the medium PDL range the new model and the previous model produce the same PDL distribution (Fig. 8.9). In large PDL region the new model produces a slightly higher PDL probability (Fig. 8.10). In this section the system impact of PDL

is studied using the new model. For the purpose of comparison, the previous model is used as well with the same *rms* PDL as that of the new model. Fig. 10.6 shows the probability distributions of system Q-factor and Fig. 10.7 shows the probability distributions of BER using two waveplate models. The average of PDL square, $\langle a^2 \rangle$, of each PMF section for both models is the same (3.183×10^{-6}), which corresponds to $\alpha_m = 0.00309$, $\alpha_0 = 0$ for the previous model and $\alpha_m = 0.00141$, $\alpha_0 = 0.000993$ for the new model. There are 10,000 fibers in each statistical ensemble and each fiber consists of 80 PMF segments. It is clear from Fig. 10.6 and 10.7 that the new model produces a lower mean system Q-factor and a higher mean BER than the previous model. This is consistent with result discussed in section 8.5 that the new model produces slightly higher PDL probability than the previous model in larger PDL range (Fig. 8.10).

10.3.3 System outage probability

The system outage probability is defined as the cumulative probability that the BER degradation exceeds to the value of 10^{-12} (Q<7.0324). The PDL induced outage probability is studied in this subsection by examining many statistical ensembles using the new waveplate model with various PDL values. There are 10,000 fibers in each statistical ensemble and each fiber consists of 100 PMF segments. The input optical power at the photo detector are set to be 0.3 to 1 dB higher than the power that provides BER of 10^{-12} when PDL=0, i.e. the power margin is from 0.3 to 1 dB. The outage probabilities due to PDL with various power margins are shown in Fig. 10.8. From Fig. 10.8 we can see that the PDL range, ΔPDL, that corresponds to sharp rise in the outage probability increases with power margin, see Fig. 10.9. Fig. 10.8 shows that for each power margin the outage probability drops to almost zero when PDL decreases to a certain value. This PDL value is considered as the maximum PDL that can be compensated by the corresponding power margin. Fig. 10.10 shows the maximum PDLs that produce the outage probability of less than 1% at various power margins. We can see that the maximum PDL has a linear relation with power margin.

10.3.4 Measurement of system Q factor distribution

The experimental distribution of Q factor is reported in this subsection. Fig. 10.11 shows the block diagram of the experimental setup. One part of the signal from an OC12 transmitter (Nortel Networks, 0.625 Gbits/second) is used to trigger the communication analyzer (83480A, Agilent) and the other part of the signal is used to generate a 10 Gbits/second signal (OC192). The 10 Gbits/second signal is amplified and then is launched to a polarization controller (11896A, Agilent). After going through a PDL source (VPLS-Q-03-FC, Taliescent) the signal is collected by the communication analyzer where the system Q factor is measured. The polarization controller and the communication analyzer are controlled by a personal computer through a GP-IB bus. The procedure of measuring the system Q factor is as follows: First the polarization controller scrambles for 10 seconds and stops, then the communication analyzer starts to measure the Q factor. After 30 seconds when the Q factor is stable (within the variation of less than 1%) it is recorded. After the Q factor is saved the polarization controller starts scrambling again and the whole procedure repeats. It takes about 50 seconds to obtain one Q factor data. The optical power to the communication analyzer is −10 dBm. The PDL value of the PDL source is 0.24 dB and its PMD value is less than 0.005 ps. The PMD value of the polarization controller is less than 0.005 ps but its PDL value varies from 0.1 to 0.7 dB depending on the rotation angles of its four waveplates. Total of 2000 Q factor values are measured (it takes two days and one night) and the Q factor distribution is shown in Fig. 10.12a. It is clear that the Q factor distribution is not Gaussian. This is due to the fact that in sections 10.3.1 and 10.3.2 we assume that there are at least 40 PMF segments in each fiber, but in the experiment there are only two PDL elements—the PDL source and the polarization controller. If we assume that each waveplate of the polarization controller has a PDL value of 0.175 dB (produces a maximum PDL of the polarization controller of 0.7 dB) and the rotation angles of the four waveplates changes randomly when the polarization controller is scrambling, the simulation result is shown Fig. 10.12b. Comparing Fig. 10.12a with Fig. 10.12b we can see that the simulation result reasonably agrees with the experimental result.

10.4 System impact due to PMD

First order [77, 83] and high order [8, 23, 84, 85] PMD effects in digital systems have been studied by many researchers, which include the statistics of Q factor, the PMD limit with chromatic dispersion [23] and the system outage probability [8]. In this section the system impact of PMD are studied in the presence of both chromatic dispersion and frequency chirp. The statistical distributions of system Q factor and BER are examined by using two waveplate models. The system outage probabilities are simulated using the new waveplate model with various power margins.

10.4.1 Interaction of PMD with frequency chirp

The electrical fields of a chirped pulse in time and frequency domains are expressed in Eqs.10.2 and 10.3 respectively. In the frequency domain a chirped pulse is broader than that of a non-chirp pulse (called *transform-limited* pulse). If there are no chromatic dispersion, PMD or non-linear effect in the system, frequency chirp has no system impact since the pulse width in time domain is still the same as that of the non-chirped pulse [6]. In the presence of high order PMD and chromatic dispersion the group velocity is frequency and polarization dependent, as a result the pulse is broadened or narrowed in time domain [6]. Using the parameters discussed in section 10.2, Fig. 10.13 shows the degradation of eye-diagrams with PMD (10 ps) and various frequency chirps (no chromatic dispersion). It can be seen that when frequency chirp increases the eye diagram is getting slightly worse. Fig. 10.14 shows the statistical distributions and mean values of system Q factor with PMD of 10 ps and with C=0, 0.2, 0.4 and 0.6. We can see that with the increase of frequency chirp the Q factor distribution gets wider and the standard deviation is larger. Without PMD, chromatic dispersion and chirp, the Q factor using the parameters discussed in section 10.2 is 9.6916. From Fig. 10.14 it can be found that, in the presence of chirp and PMD, the Q factor can be either higher or lower than 9.6916. Higher Q factor is due to the pulse narrowing induced by the interaction of chirp and high order PMD (or PMD induced chromatic dispersion) [76, 85, 86]. This effect was studied experimentally by Poole in 1988 [87]. Fig. 10.15 shows an example of pulse narrowing in the presence of chirp and PMD. In order to see this effect clearly the chirp and PMD are enlarged (C=2,

PMD=30ps). The statistical distribution of pulse broadening ($\sigma^2 - \sigma_0^2$, where σ_0 and σ are the input and output pulse widths respectively) induced by the interaction of PMD (10 ps) and frequency chirp is shown in Fig. 10.16. As we can see that in the presence of both chirp and PMD there is a finite possibility of pulse narrowing ($\sigma < \sigma_0$) and this probability increases with chirp. In the case of pure PMD (C=0) there is no pulse narrowing.

10.4.2 Interactions of PMD with frequency chirp and group velocity dispersion

Chromatic dispersion effects in the system can be expressed by rewriting Eq. 10.5 as

$$\begin{aligned} \vec{E}_{1out}(\omega) &= T(\omega)\vec{E}_{1in}(\omega)\exp(i(\beta(\omega)-\beta(\omega_0))L) \qquad \text{("010" pattern)} \\ \vec{E}_{0out}(\omega) &= T(\omega)\vec{E}_{0in}(\omega)\exp(i(\beta(\omega)-\beta(\omega_0)L)) \qquad \text{("101" pattern)} \end{aligned} \tag{10.15}$$

and

$$\beta(\omega)-\beta(\omega_0) = \beta_1(\Delta\omega)+\frac{1}{2}\beta_2(\Delta\omega^2)+\frac{1}{6}\beta_3(\Delta\omega^3)+\cdots\cdots \tag{10.16}$$

where $\beta_m = \left(\frac{d^m\beta}{d\omega^m}\right)_{\omega=\omega_0}$ and L is the fiber length. β_1 is the inverse group delay and this term does not lead to pulse distortion [11]. β_2 and β_3 are the coefficients for first- and second-order chromatic dispersion respectively. β_2 is usually referred as group velocity dispersion (GVD). In this subsection only first-order chromatic dispersion (β_2) is considered. The PMD values used in this subsection are 10, 15, 20 and 25 ps. The frequency chirp, C, is 0.6 and the product of GVD and fiber length L ($\beta_2 L$) is $-1400\ ps^2$. The two parameters, C and $\beta_2 L$, are chosen for the special case of pulse narrowing when PMD is zero. Fig. 10.17 shows the distributions of pulse broadening at various PMD values. It can be seen that when PMD is small (10, 15 ps) the output pulse width is always less than the input pulse width, but when PMD is large (20, 25 ps) the distribution of pulse broadening is getting wider and the output pulse width can be either larger or less than that of the input pulse. The statistical distributions of system Q-factor at various PMD values are shown in Fig. 10.18. Without chromatic dispersion, chirp and PMD in

the system the Q-factor is 9.6916 (this is the effect of detector noises etc.). Simulation results show that with small PMD (10, 15 ps) the Q-factor is always larger than 9.6916 due to the pulse narrowing. With large PMD value (20, 25 ps) the Q-factor can be either smaller or larger than 9.6919. From the above simulations in the presence of chromatic dispersion, chirp and PMD we can conclude that frequency chirp in a system can either impair or improve the system performance. Careful design of frequency chirp and chromatic dispersion can improve the system performance even in the presence of PMD.

10.4.3 Distribution of system Q factor due to PMD (new model)

In section 7.4 a new waveplate model is proposed. In the new model a fiber has the possibility of taking any DGD values. The new model produces almost the same DGD distribution as the previous models in medium DGD range. In large DGD region the new model produces a slightly higher DGD probability (Fig. 7.18). In this subsection the new model is used to examine the system impact due to PMD. The statistical ensemble includes 10,000 fibers with each fiber consisting of 100 segments. The parameters of β_m and β_0 in Eq. 7.6 are: $\beta_m = 1ps$ and $\beta_0 = 0.6112ps$, which give the mean of $\langle \beta^2 \rangle$ in each PMF segment of 1.333 ps^2 (the *rms* PMD of fiber is 11.5ps). The statistical distribution of Q factor is shown in Figs.10.19. For the purpose of comparison, the Q factor distribution using the previous model ($\beta_m = 2ps$, $\beta_0 = 0$ that gives the same $\langle \beta^2 \rangle$ in the segments) is also plotted in Fig. 10.19. It can be seen that the two models produce almost the same Q-factor distribution in medium Q factor range (Fig. 10.19a), but in small Q factor region the new model produces a slightly higher Q-factor distribution (Fig. 10.19b). This is consistent with DGD distributions using the different models (Fig. 7.18).

10.4.4 System PMD impact with biased elliptical birefringence

In chapter 7 the statistical distribution and the mean value of DGD are studied for the case of biased elliptical birefringence. Generally the mean DGD increases with the maximum biased angle, ϕ_{max} (Fig. 7.9) and this conclusion is still valid in the presence of PDL (Fig. 7.12). In this

subsection the system impact of PMD is examined considering the case of biased birefringence. Fig. 10.20 and Fig. 10.21 show the eye diagrams and Q factor distributions when $\phi_{max} = 0$, $\pi/4$ and $\pi/2$. The mean DGD in each fiber of the statistical ensembles is 10 ps when $\phi_{max} = 0$. It is clear from Figs.10.20 and 10.21 that with the increase of biased birefringence angle the eye diagrams get worse and the probability density of Q-factor is higher at small Q range. This is consistent with the results in section 7.3 that the probability density of DGD at large DGD range increases with maximum angle ϕ_{max} (Fig. 7.8). High bias means less mode coupling. The result here shows that high mode coupling is better in terms of system impact.

10.4.5 System outage probability

The outage probability due to PMD is simulated in this subsection by examining many statistical ensembles with various PMD values using the new waveplate model. There are 10,000 fibers in each statistical ensemble and each fiber consists of 100 PMF segments. The input optical power are set to be 0.3 to 1 dB higher than the power that provides BER of 10^{-12} when PMD is zero. The outage probabilities due to PMD are shown in Fig. 10.22 with various power margins. We can see that when PMD is larger than 10 ps there is a certain percentage of outage probability even at the power margin of up to 1dB. This indicates that other methods, other than increasing power margin, should be studied for PMD compensation when PMD is larger than 10 ps. This is consistent with the commonly acceptable PMD value (10% of bit period, 100 ps for 10Gbits/second system) [8, 23]. In order to test the method of PMD compensation by increasing the optical power, the maximum PMD values that induce outage probability less than 1% at various power margins are plotted in Fig. 10.23. It can be seen that with the increase of the maximum PMD the power margin increase exponentially. This means that increasing optical power is not an effective way for PMD compensation.

10.5 System impact due to the combined effect of PMD and PDL

PMD and PDL are the two polarization effects in fiber optic communication systems and

both of them degrade system performance. The combined effect of PMD and PDL produces more severe system impairment than PMD or PDL alone [9, 13, 62]. The system impact due to the combination of PMD and PDL are studied in terms of statistical distributions of system Q factor, BER and the system outage probability using two waveplate models.

10.5.1 Distributions of system Q factor and BER (previous model)

In this subsection the previous waveplate model is used. The distributions of Q factor and BER due to the combined effect of PMD and PDL are examined through many statistical ensembles with various PMD and PDL values. There are 10, 000 fibers in each ensemble and there are 100 PMF segments in each fiber. First, four statistical ensembles with same PMD but with different PDLs are examined. The PMD of the four ensembles is 10 ps and the PDLs are 0, 0.2, 0.4 and 0.6 dB respectively. Fig. 10.24 shows the eye diagrams at various PDL values. As we can see that with the increase of PDL the eye opening decreases due to the PDL induced global attenuation. The noise in bit "1" increases with PDL because the power fluctuation increases with PDL. Fig. 10.25 and Fig. 10.26 show the statistical distributions of Q-factor and BER at various PDLs. It is clear from the two figures that PDL has a strong impact on the system in the presence of PMD. When PDL=0, 0.2, 0.4 and 0.6dB the mean Q-factors are 9.6, 8.5, 7.5 and 6.7 respectively and the maximum BERs are 7×10^{-17}, 1.3×10^{-14}, 1.4×10^{-11} and 5.8×10^{-9} respectively. The solid curves in Fig. 10.25 are the fittings of Q distributions using Eq. 10.14. It can be seen that the distribution of Q factor is Gaussian even in the presence of PMD (10 ps).

Secondly the combined effects of PMD and PDL are examined with same PDL but different PMDs. The PDL of each ensemble is 0.4 dB and the PMDs of the four ensembles are 0, 10, 15 and 20 ps respectively. Fig. 10.27 shows the eye diagrams at different PMDs (0, 10, 15 and 20 ps) but the same PDL (0.4 dB). It can be seen that with the increase of PMD the "eyes" get noisier due to PMD induced pulse broadening [9]. Fig. 10.28 and Fig. 10.29 show the statistical distributions of Q factor and BER. From the two figures we can see clearly that the Q factor decrease (BER increase) with PMD. The mean Q factors are 7.60, 7.52, 7.42 and 7.27 and the

maximum BERs are 9×10^{-16}, 5×10^{-11}, 4×10^{-10} and 4×10^{-8} respectively when PMDs are 0, 10, 15 and 20 ps. Fig. 10.25 shows that in the presence of PDL ($\geq 0.2dB$) and PMD (10ps) the statistical distribution of Q factor can be fitted with Gauss function, but from Fig. 10.28 we can see that when PMD gets larger ($\geq 15ps$) the distribution of Q factor is not Gaussian.

10.5.2 Distributions of system Q factor and BER (New model)

The same statistical ensembles used in the previous model are used for the new waveplate model in this subsection. First the eye diagrams and the distributions of Q-factor and BER with the same PMD (10 ps) but different PDL values are examined. The parameters, α_m, α_0, β_m and β_0 used in the simulations are listed in table 10.1. The mean value of PDL square, $\langle\alpha^2\rangle$, and DGD square, $\langle\beta^2\rangle$, in each fiber are kept the same as that used for the previous model in above subsection for the purpose of comparison. The eye diagrams, statistical distributions of Q factor and BER at various PDLs are shown in Figs.10.30, 10.31 and 10.32. Comparing the simulation results in this subsection with the results of the previous subsection we can see the two models give the similar results.

Table 10.1 Parameters used in the simulations with various PDLs

	α_m	α_0	β_m	β_0
(PDL=0)	0	0	1.0	0.61
(PDL=0.2dB)	0.0023	0.0014	1.0	0.61
(PDL=0.4dB)	0.0046	0.0028	1.0	0.61
(PDL=0.6dB)	0.0069	0.0042	1.0	0.61

Secondly the eye diagrams and the distributions of Q-factor and BER with the same PDL but different PMD values are examined. The parameters, α_m, α_0, β_m and β_0 used in the simulations are listed in table 10.2. The mean value of PDL square, $\langle\alpha^2\rangle$, and DGD square,

$\langle \beta^2 \rangle$, in each fiber are kept the same as used in the previous model for the purpose of comparison. The eye diagrams, statistical distributions of Q factor and BER are shown in Figs.10.33, 10.34 and 10.35. Again we can see that these results are similar to those using the previous model in above subsection.

Table 10.2 Parameters used in the simulations with various DGDs.

	α_m	α_0	β_m	β_0
(PMD=10ps)	0.0046	0.0028	1.0	0.61
(PMD=15ps)	0.0046	0.0028	1.5	0.92
(PMD=20ps)	0.0046	0.0028	2.0	1.22

From the simulation results in sections 10.3 and 10.4 we know that when PDL or PMD acting alone the new model gives higher Q factor probability density than the previous model in the small Q region (Figs.10.6 and 10.19). In the presence of both PMD and PDL, Fig. 10.36a shows the distributions of Q factor using two waveplate models. For the previous model $\alpha_{max} = 0.004605$, $\beta_{max} = 2ps$, and for the new model $\alpha_m = 0.0023025$, $\alpha_0 = 0.0014073$, $\beta_m = 1ps$ and $\beta_0 = 0.6112ps$. These parameters ensure that the *rms* PDL and PMD in the two models are the same. It is clear from 10.36a that, unlike the cases of pure PMD or PDL, the new model produces a lower probability density of Q factor in small Q factor range (<8.5). This counterintuitive result may be due to the reasons of 1) As we will see in next paragraph that the average values of PMD and PDL amplitudes in the new model is less than that in the previous model if the *rms* PMD and PDL of the two models are the same. 2) The interaction of PMD and PDL in the previous model is slightly stronger than that in the new model.

In the simulations of this subsection it is assumed that the averages of PDL square, $<\alpha^2>$, and PMD square, $<\beta^2>$, of the PMF segments in the two waveplate models are the same. Using Eqs.7.6 and 7.8 the averages of β^2 and α^2 for the new model are

$$\langle \alpha^2 \rangle_{new} = 2\alpha_0{}^2 + \frac{1}{3}\alpha_m{}^2 + \frac{2\alpha_0\alpha_m{}^2}{3(\alpha_m + \alpha_0)}$$

$$\langle \beta^2 \rangle_{new} = 2\beta_0{}^2 + \frac{1}{3}\beta_m{}^2 + \frac{2\beta_0\beta_m{}^2}{3(\beta_m + \beta_0)}, \tag{10.17}$$

The averages of PDL and PMD amplitudes for the new model are

$$\langle |\alpha| \rangle_{new} = \alpha_0 + \frac{\alpha_m{}^2}{2(\alpha_m + \alpha_0)}, \text{ and } \langle |\beta| \rangle_{new} = \beta_0 + \frac{\beta_m{}^2}{2(\beta_m + \beta_0)}. \tag{10.18}$$

For the previous model the averages of PMD and PDL squares are

$$\langle \beta^2 \rangle_{pre} = \frac{1}{3}\beta_{\max}{}^2, \text{ and } \langle \alpha^2 \rangle_{pre} = \frac{1}{3}\alpha_{\max}{}^2. \tag{10.19}$$

The averages of PMD and PDL amplitudes for the previous model are

$$\langle |\beta| \rangle_{pre} = \frac{1}{2}\beta_{\max}, \text{ and } \langle |\alpha| \rangle_{pre} = \frac{1}{2}\alpha_{\max}. \tag{10.20}$$

Combining Eqs.10.17 to 10.20 the ratios of $\langle |\alpha| \rangle_{new}$ to $\langle |\alpha| \rangle_{pre}$ (or the ratios of $\langle |\beta| \rangle_{new}$ to $\langle |\beta| \rangle_{pre}$) for the case of same $\langle \alpha^2 \rangle$ (or same $\langle \beta^2 \rangle$) in both models can be calculated at various S values (Eq. 8.12 or Eq. 7.7), see Fig. 10.37. It is clear the mean DGD (or PDL) in each PMF segment of the new model is less than that in the previous model.

In the cases of pure PMD or PDL, on the one hand the new model has the possibility of producing large PMD or PDL values, but on the other hand the mean PMD or PDL of each PMF segment is less than that of the previous model. The net result of these two effects is that the new model produces a slightly stronger system impact than the previous model (Figs.10.6

and 10.19). In the presence of both PMD and PDL the interaction of PMD and PDL in the previous model is stronger than that in the new model, as a result the new model produces slightly weaker system impact than the previous model. In order to verify this conclusion, Fig. 10.36b shows the statistical distributions of DGD in the presence of PDL using the two models. For the previous model $\alpha_{max} = 0.004605$, $\beta_{max} = 2ps$, and for the new model $\alpha_m = 0.0023025$, $\alpha_0 = 0.0014073$, $\beta_m = 1ps$ and $\beta_0 = 0.6112ps$. These parameters ensure that the *rms* DGD and PDL of the two models are the same. As we know that without PDL the new model produces a slightly higher probability density than the previous model in large DGD region (Fig. 7.18) and the interaction of PMD and PDL leads a higher DGD probability density in large DGD region (compare the two graphs in Fig. 7.11). In the presence of PDL Fig. 10.36b does not show evident difference of DGD distributions in large DGD region using the two models. It is clear that the interaction of PMD and PDL in the previous model is stronger than that in the new model.

10.5.3 System outage probability

In sections 10.3.3 and 10.4.5 the system outage probabilities due to PDL and PMD alone are studied. In this subsection the system outage probability due to the combined effects of PMD and PDL is examined using the new waveplate model by examining many statistical ensembles with various PMD and PDL values. There are 10,000 fibers in each statistical ensemble and each fiber consists of 100 PMF segments. The input optical power is 0.5 dB higher than the power that provides BER of 10^{-12}. Fig. 10.38a shows the outage probabilities induced by PDL when PMD is 0, 2, and 5 ps respectively. Fig. 10.38b shows the outage probabilities induced by PMD when PDL is 0, 0.02 and 0.04 dB respectively. Fig. 10.38 clearly shows the interaction of PMD and PDL. First, from Fig. 10.22 we can see that when PMD in the system is less than 5 ps the outage probability due to PMD is almost zero when power margin is larger than 0.3 dB. Fig. 10.38a shows that with power margin of 0.5 dB and in the presence of PDL the influence of PMD (2 and 5 ps) on system outage probability is evident. Second, it is clear from Fig. 10.8 that the outage probability induced by PDL is almost zero when PDL is less than 0.05 dB with the power margin of larger than 0.3 dB. Fig. 10.38b show that in the presence of PMD there is a

stronger influence of PDL (<0.05 dB) on the system outage probability. The simulation results in this subsection agree with the conclusion that the combined effect of PMD and PDL is more severe than PMD or PDL acting alone [9, 13].

10.5.4 PMD limit in the presence of PDL

The commonly accepted PMD limitation of a fiber optic communication system is 10% of the bit period [8, , 23]. Fig. 10.38 shows that the combined effect of PMD and PDL on system impact is more severe than PMD and PDL acting alone due to the strong interaction between PMD and PDL. The PMD limit in a fiber communication system would be reduced because of PDL. In this subsection the PMD limit in the presence of PDL is studied by using the new waveplate model. For a certain value of power margin the combination of PMD and PDL that produces the same system outage probability as PMD alone (10 ps) is searched by the following procedures: 1) The system outage probability when PMD is 10 ps and PDL is zero is obtained. 2) For a given PMD value (< 10 ps) some statistical ensembles are examined with various PDL values and the corresponding system outage probabilities are calculated. 3) The data of outage probability versus the corresponding PDL values are plotted and the curve is fitted, see Fig. 10.39. 4) From the fitting curve the PDL value that produces the same outage probability as PMD alone (10 ps) is obtained. Using this procedure the PMD limits in the presence of PDL with the power margins of 0.3 and 0.4 dB are obtained, see Fig. 10.40. As we can see the PDL strongly affect the system limit of PMD even in small PDL range (<0.1dB). By increasing the power margin the PMD limit can be increased due to the fact that PDL can be compensated by increasing power margin (Fig. 10.8).

10.5.5 Measurement of system Q factor distribution

The experimental setup of measuring the Q factor distribution due to PMD and PDL is the same as that shown in Fig. 10.11 except there is a PMD emulator (EM550, EXFO) inserted between the PDL source and the Communication analyzer. The PMD of the PMD emulator is 8.67 ps. The procedure of measuring the Q factor is the same as described in section 10.3.4. Total of 2118 Q factors are measured and the Q factor distribution is shown in Fig. 10.41a.

In the simulation of this experiment the PDL value of the PDL source is 0.24dB and the optical power to the communication analyzer is −10 dBm. The polarization controller is considered as four waveplates with PMD of 0.00125 ps and with PDL of 0.175dB in each waveplate. The rotation angles of the four waveplates are random when the polarization controller is scrambling. The PMD emulator used in this experiment is a concatenation of nine PMF segments with unknown rotation angle between any two adjacent segments. In the simulation the PMD of each PMF segment is set to be 2.89 ps ($9\times 2.89^2 = 8.67^2$). The rotation angles of each PMF segment is determined by the following procedure: 1) The rotation angle of each PMF segment is set to be a random value between 0 to 2π. 2) The effective PMD of the simulation is calculated by using Eq. 7.5. 3) If the effective PMD is not equal to 8.67 ps, then repeat procedures 1) and 2). 4) If the effective PMD of the emulator is equal to 8.67 ps, then the nine rotation angles are saved and used in the simulation. The simulation result is shown in Fig. 10.41b. It can be seen that the simulation gives almost the same Q factor range as that from the experiment. At small and large Q factor region the simulated probability density is relatively lower than that from the experimental measurement. This may due to the following reasons: 1) The rotation angles of the PMF segments of the PMD emulator are not determined exactly. 2) The PDL of each waveplate of the polarization controller is not correctly characterized. 3) The PDL value of the PDL source, the PMD value of the PMD emulator and the PDL of the polarization controller may fluctuate during the measurement (two days and one night). 4) The optical power may fluctuate during the experiment.

10.6 Conclusion

This chapter examines the system impact due to PMD and PDL in terms of statistical distributions of Q factor and BER and system outage probability. Simulation and experimental results lead to the following conclusions: 1) In the case of only PDL the statistical distribution of the system Q factor is Gaussian. The outage probability due to PDL shows strong power margin dependence. The power margin for PDL compensation has a linear relationship with PDL. 2) Due to the interactions of PMD with chromatic dispersion and frequency chirp, PMD

may be compensated by introducing certain amounts of chromatic dispersion and frequency chirp with opposite signs. When PMD is higher than 10% of bit period, it can't be effectively compensated by increasing power margin. 3) There is a strong interaction between PMD and PDL. Because of this interaction more power margin is needed to compensate PDL in the presence of PMD and the PMD limit drops significantly in the presence of PDL. 4) Compared to the previous model, the new waveplate model produces slightly more severe system impact than those with PMD or PDL acting alone. In the presence of both PMD and PDL the system impact produced by the new waveplate model is slightly weaker when the *rms* DGD and PDL in the two models are the same. 5) The distributions of system Q factor induced by PDL and the combination of PDL and PMD are measured experimentally. The simulation results show fairly good agreement with the experimental results.

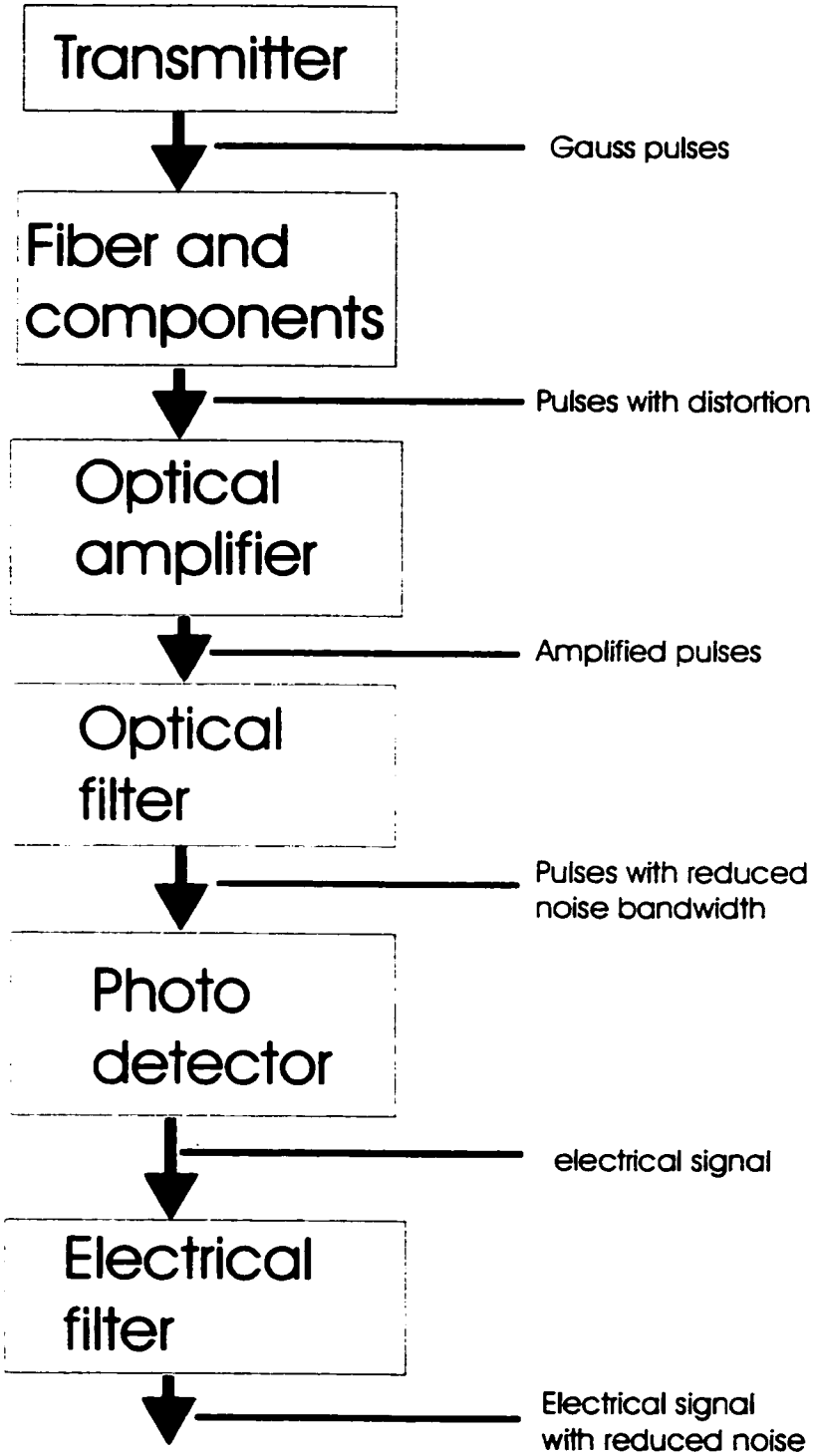

Figure 10.1 Block diagram of an IM-DD system.

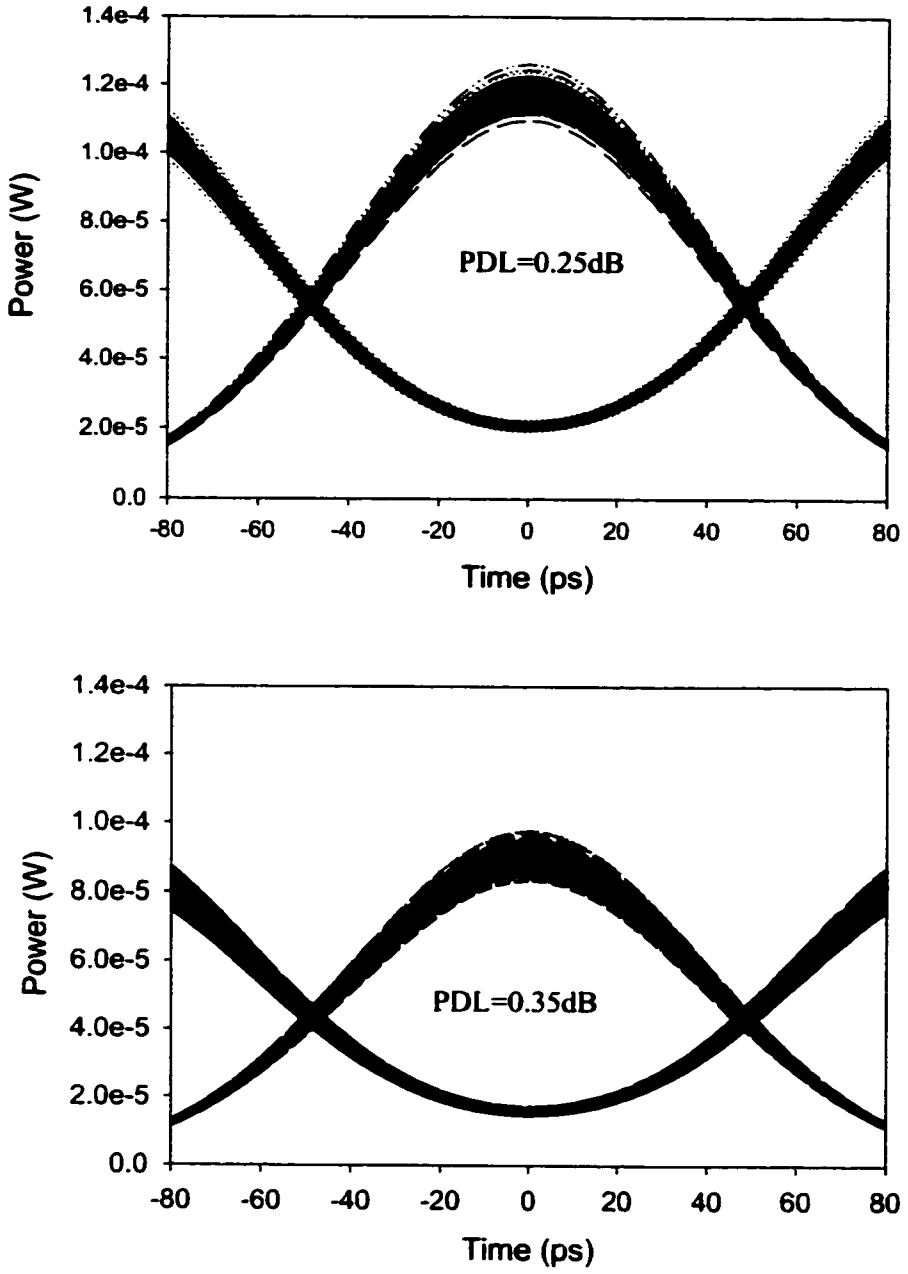

Figure 10.2 Eye diagrams of a 10 Gbites/second system in the presence of PDL.

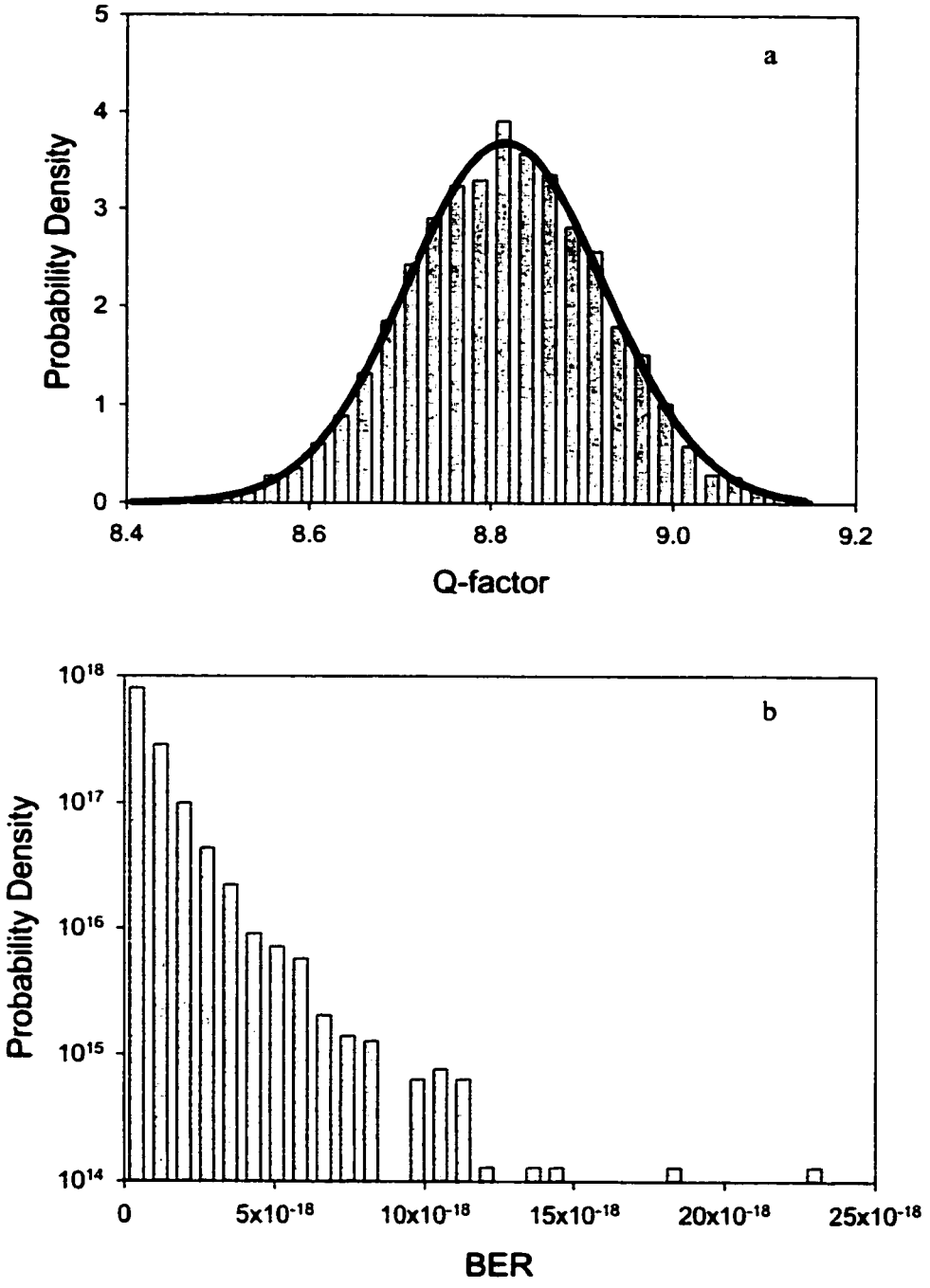

Figure 10.3 Statistical distributions of system Q-factor and BER in the presence of PDL with a mean value of 0.25 dB.

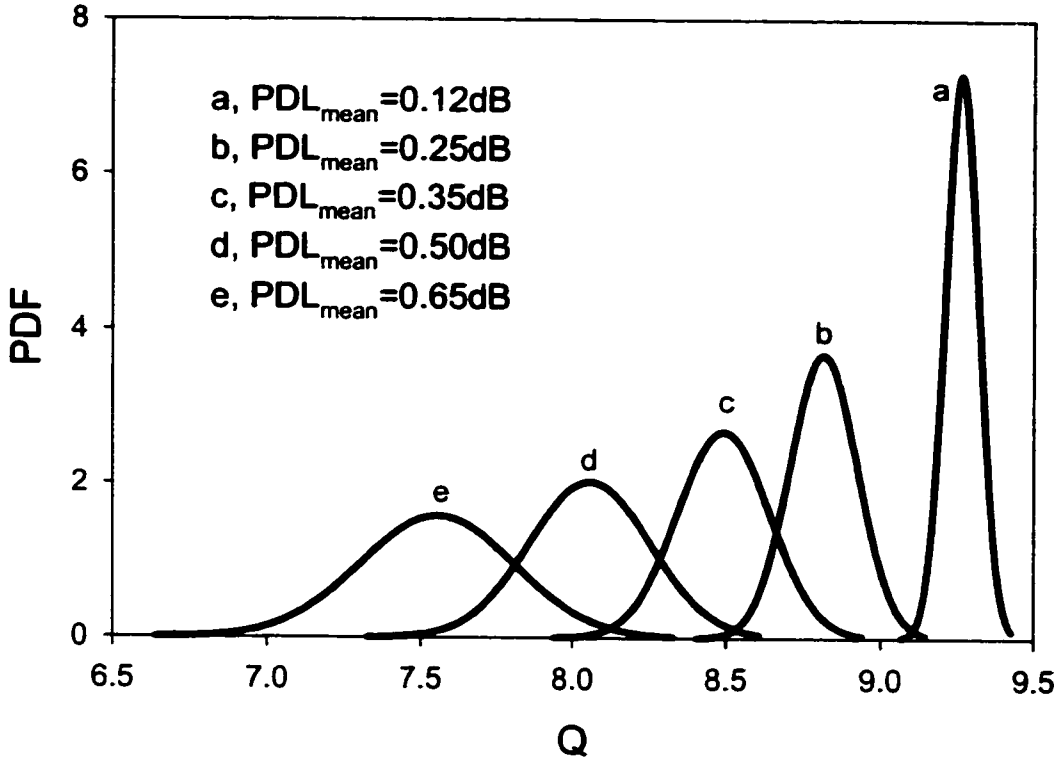

Figure 10.4 Fitting curves of Q-factor distributions with various PDL values.

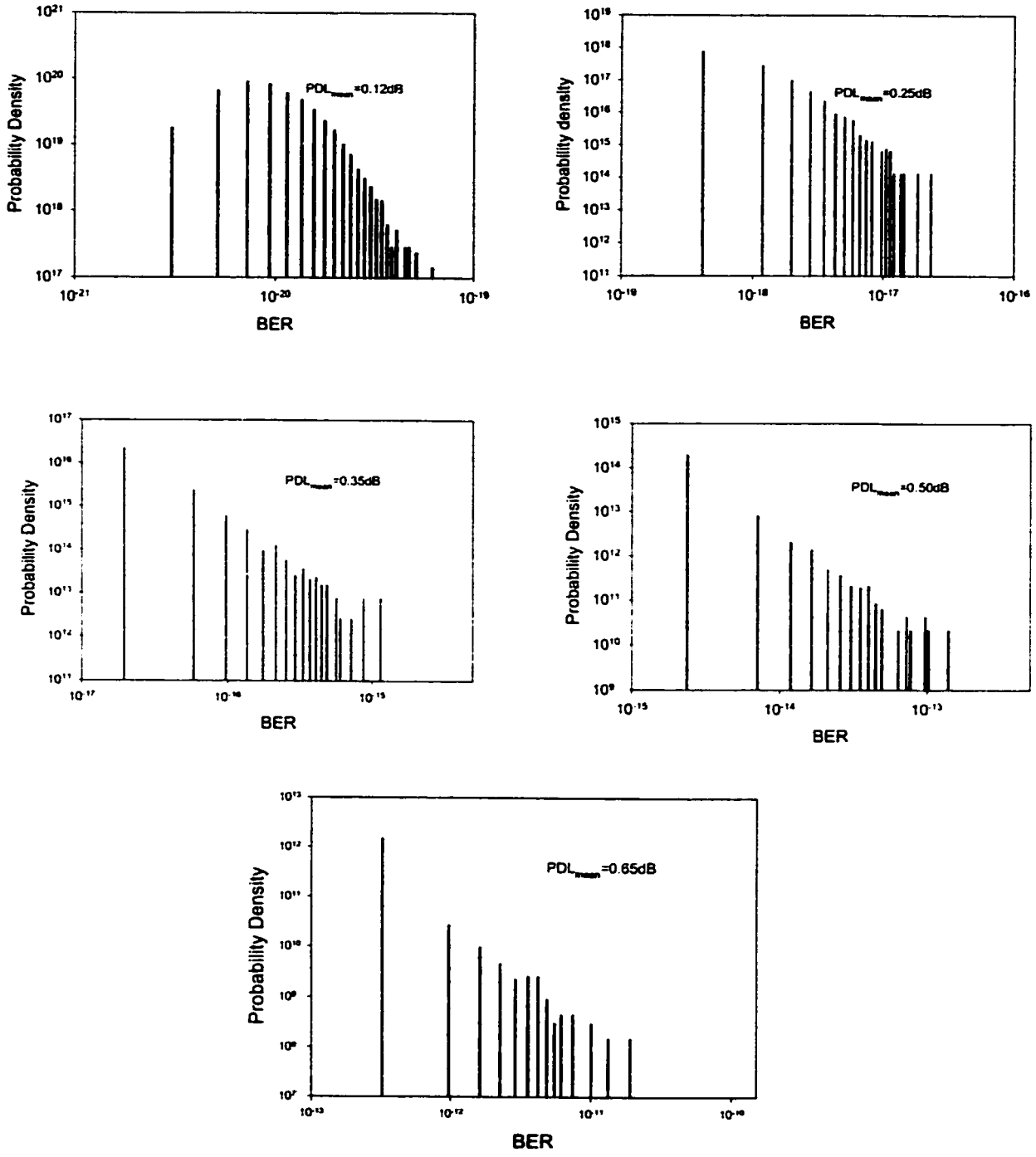

Figure 10.5 Statistical distributions of BER in the presence of various PDL values.

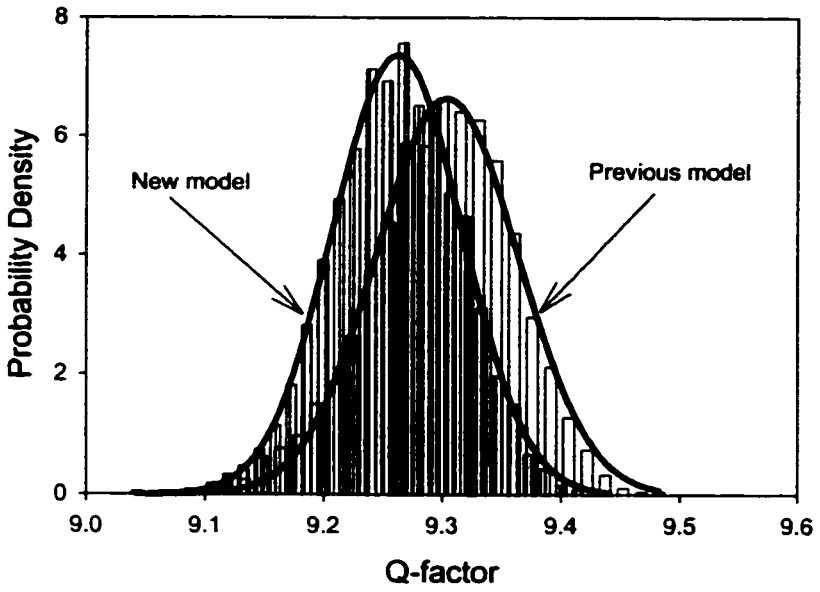

Figure 10.6 Statistical distributions of system Q factor using two waveplae models with the same *rms* PDL in each PMF segment.

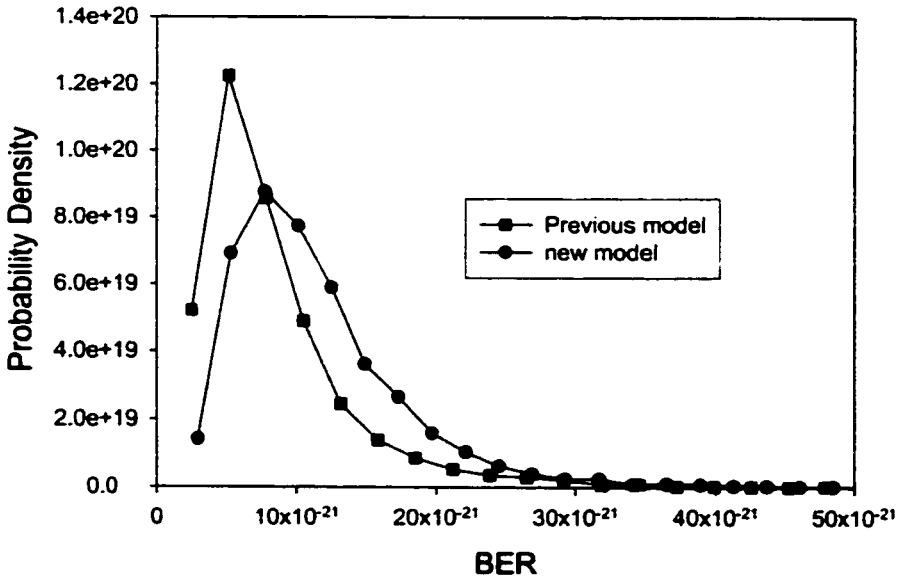

Figure 10.7 Statistical distributions of the BER using two waveplate models with same *rms* PDL in each PMF segment.

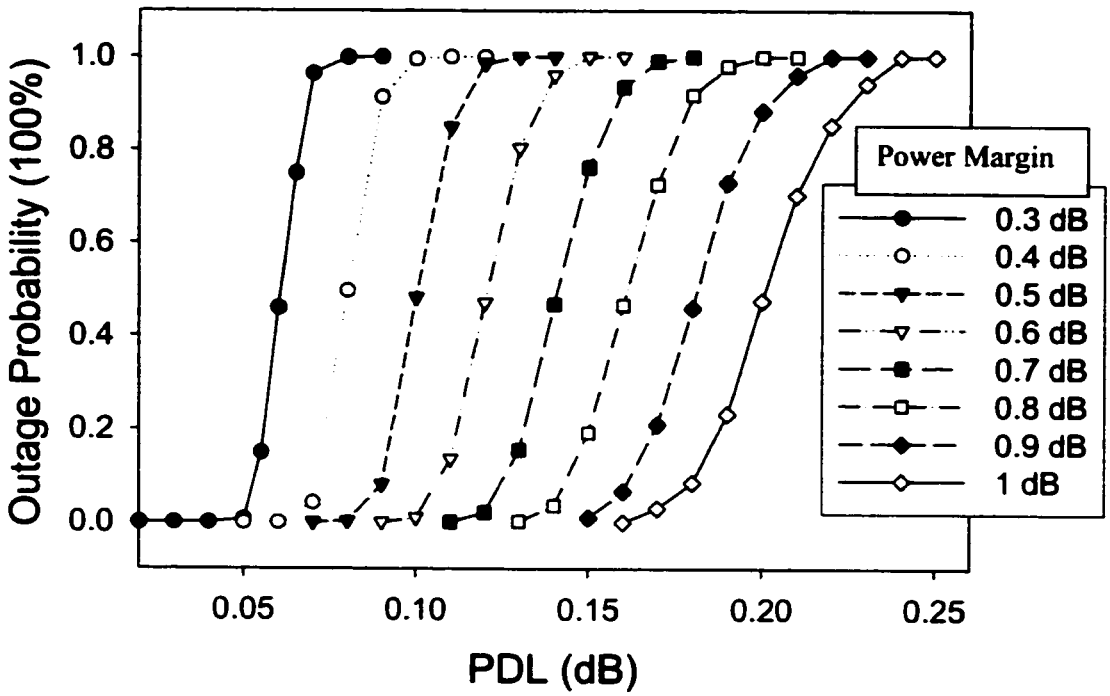

Figure 10.8 Outage probability due to PDL at various power margins.

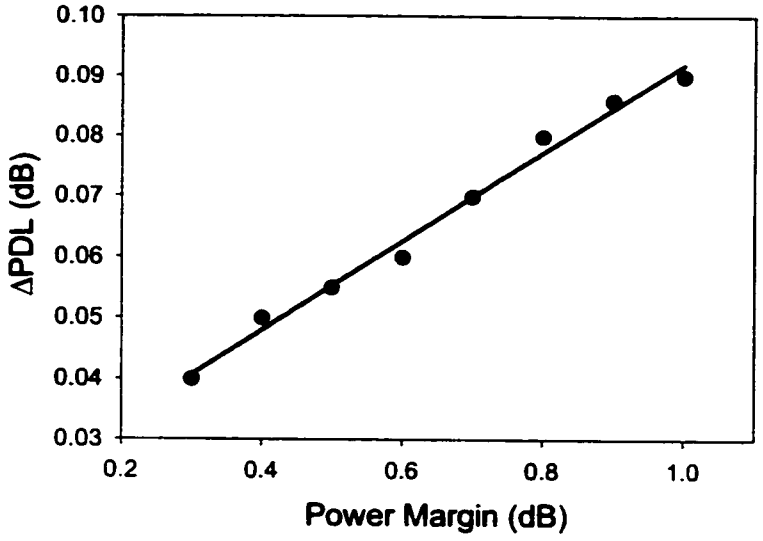

Figure 10.9 PDL ranges that induce outage probability from 0 to 100% at various power margins.

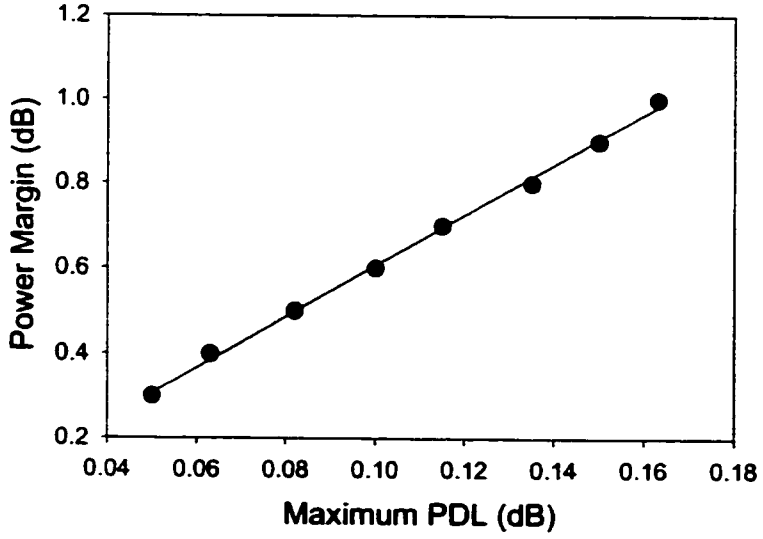

Figure 10.10 Power margin that is required for PDL compensation with outage probability less than 1%.

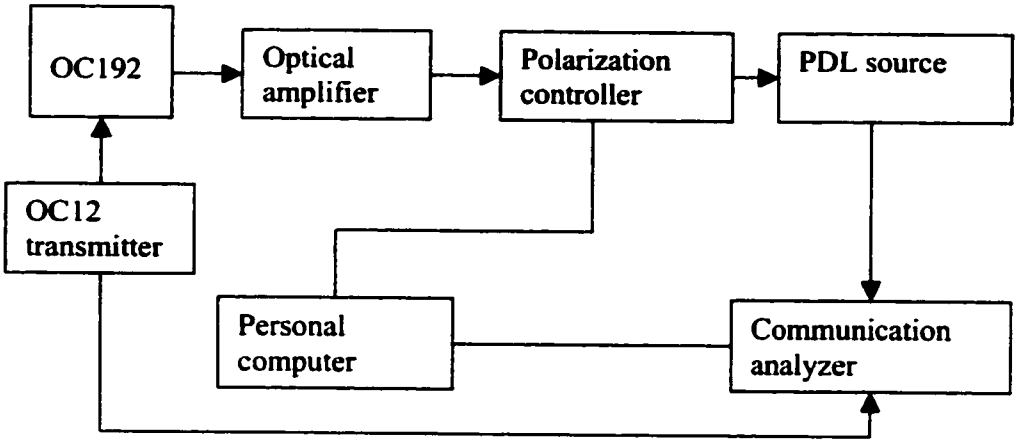

Figure 10.11 Experimental setup for measuring the Q factor distribution due to PDL.

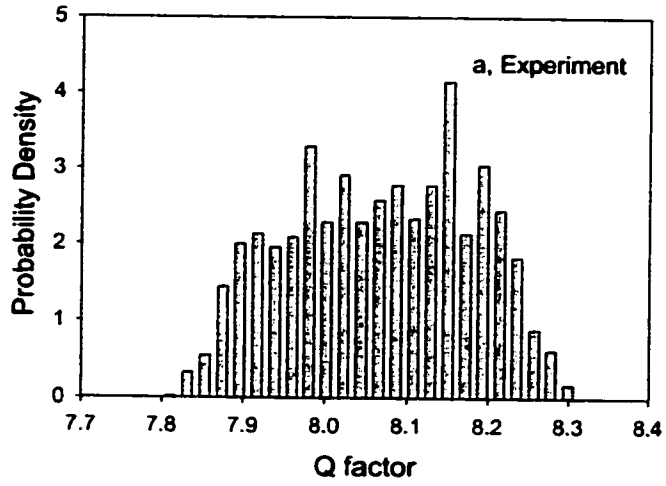

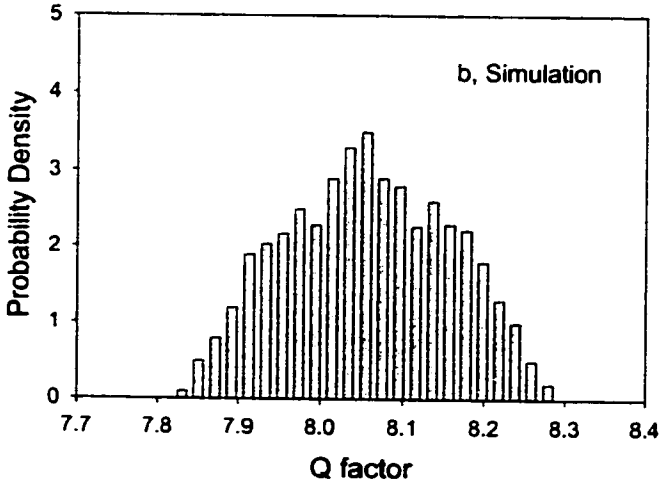

Figure 10.12 Experimental and simulation results of system Q factor distributions due to PDL.

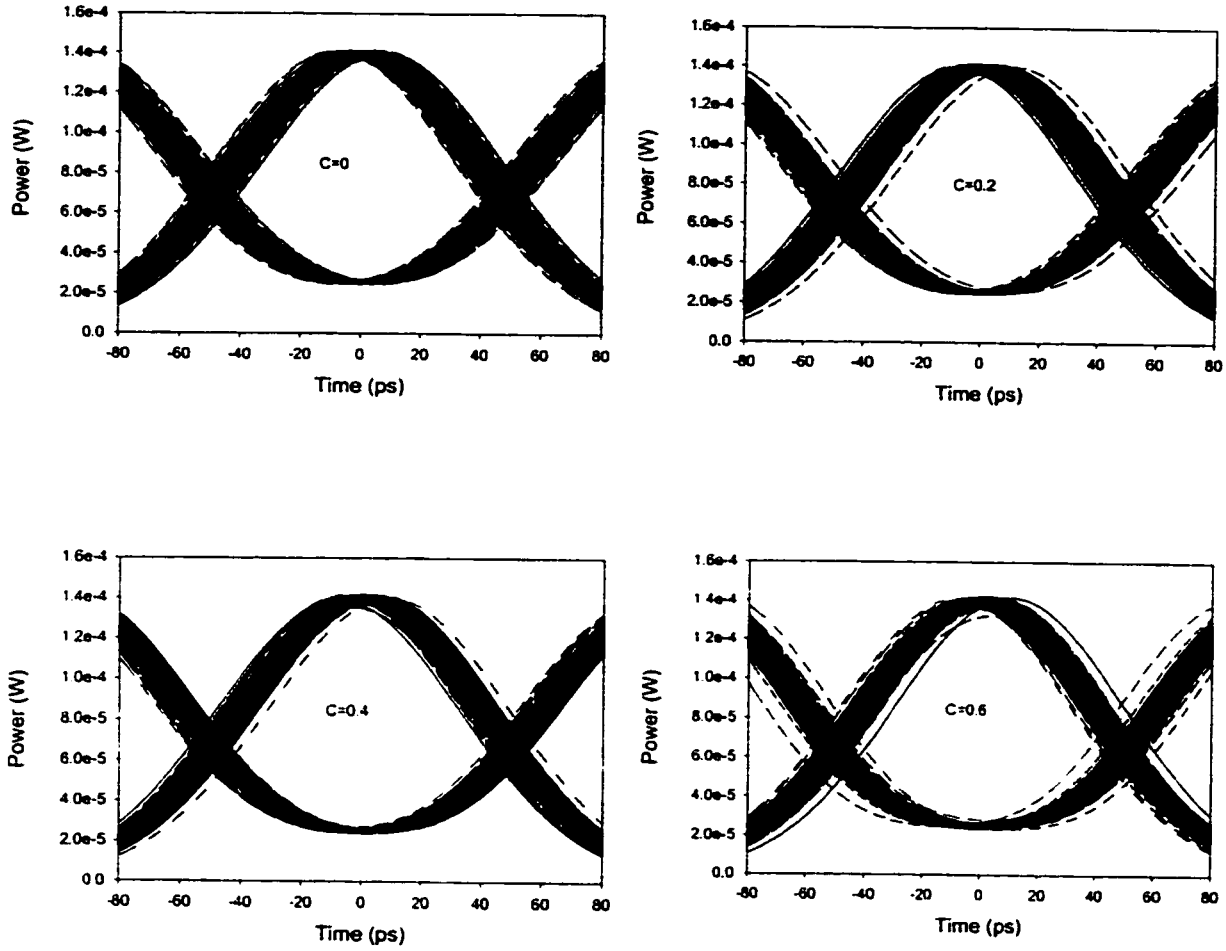

Figure 10.13 Eye diagrams in the presence of PMD (10 ps) and various chirp values.

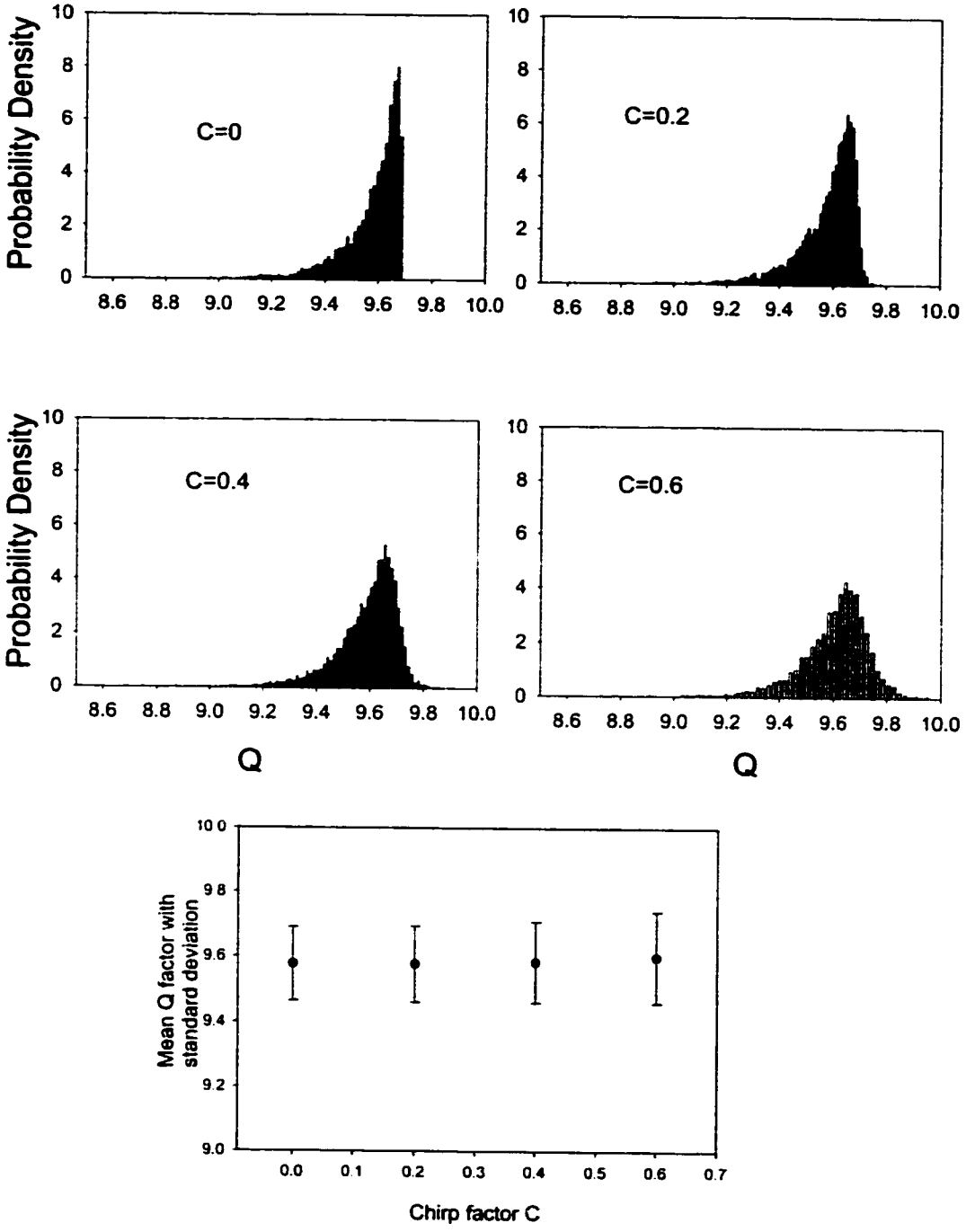

Figure 10.14 Statistical distributions and mean values of system Q factor with PMD (10 ps) and various frequency chirp values.

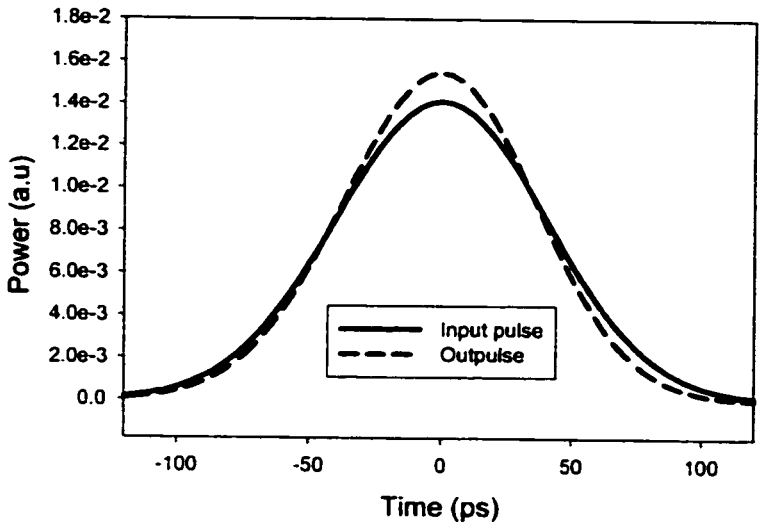

Figure 10.15 Pulse narrowing in the presence of chirp and PMD. The output pulse is shifted in order to compare the two pulse widths.

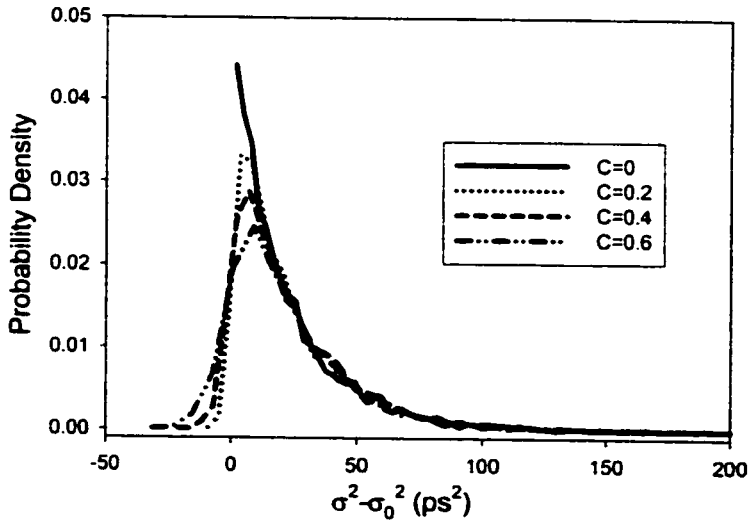

Figure 10.16 Statistical distribution of pulse broadening with PMD (10 ps) and frequency chirp.

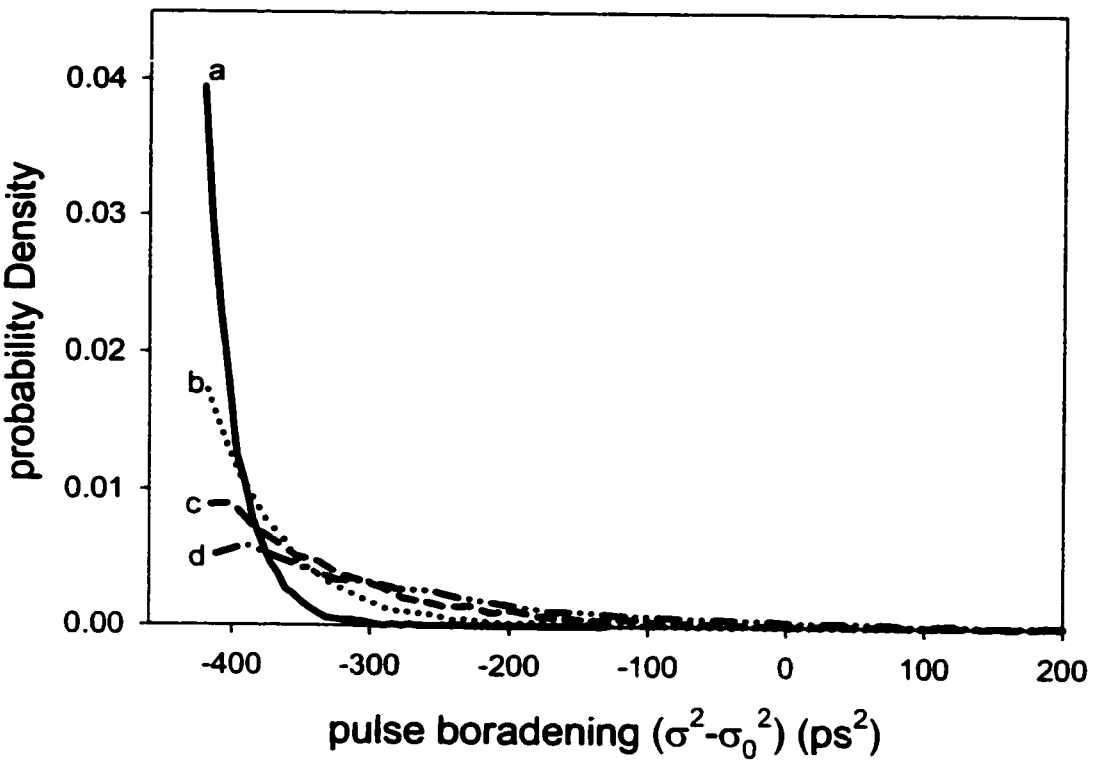

Figure 10.17 Pulse broadening in the presence of chirp (C=0.6), group velocity dispersion ($\beta_2 L = -1400 ps^2$) and various PMDs. a) PMD=10, b) PMD=15ps, c) PMD=20ps and d) PMD=25ps.

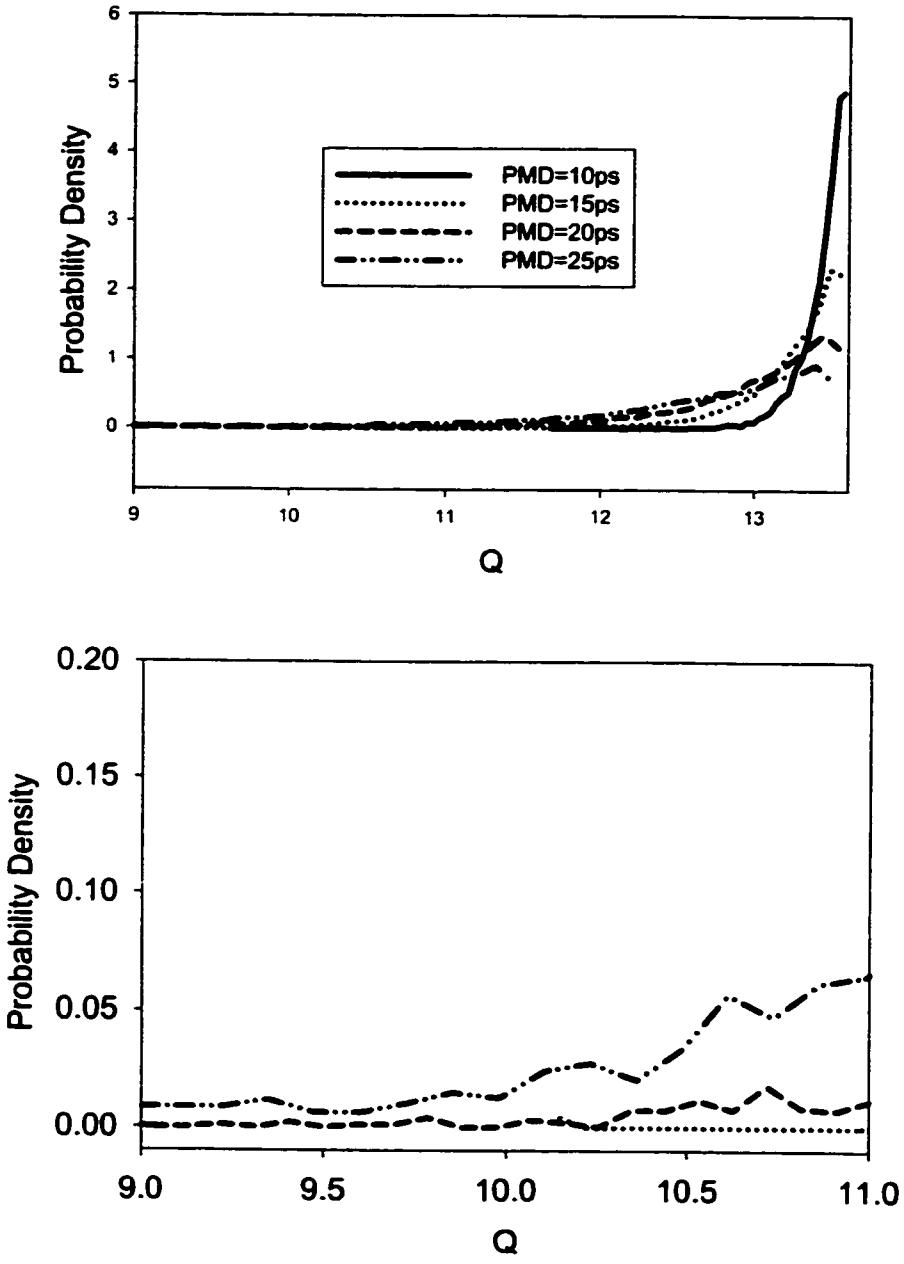

Figure 10.18 Statistical distribution of system Q-factor in the presence of chirp (C=0.6), group velocity dispersion ($\beta_2 L = -1400 ps^2$) and various PMDs.

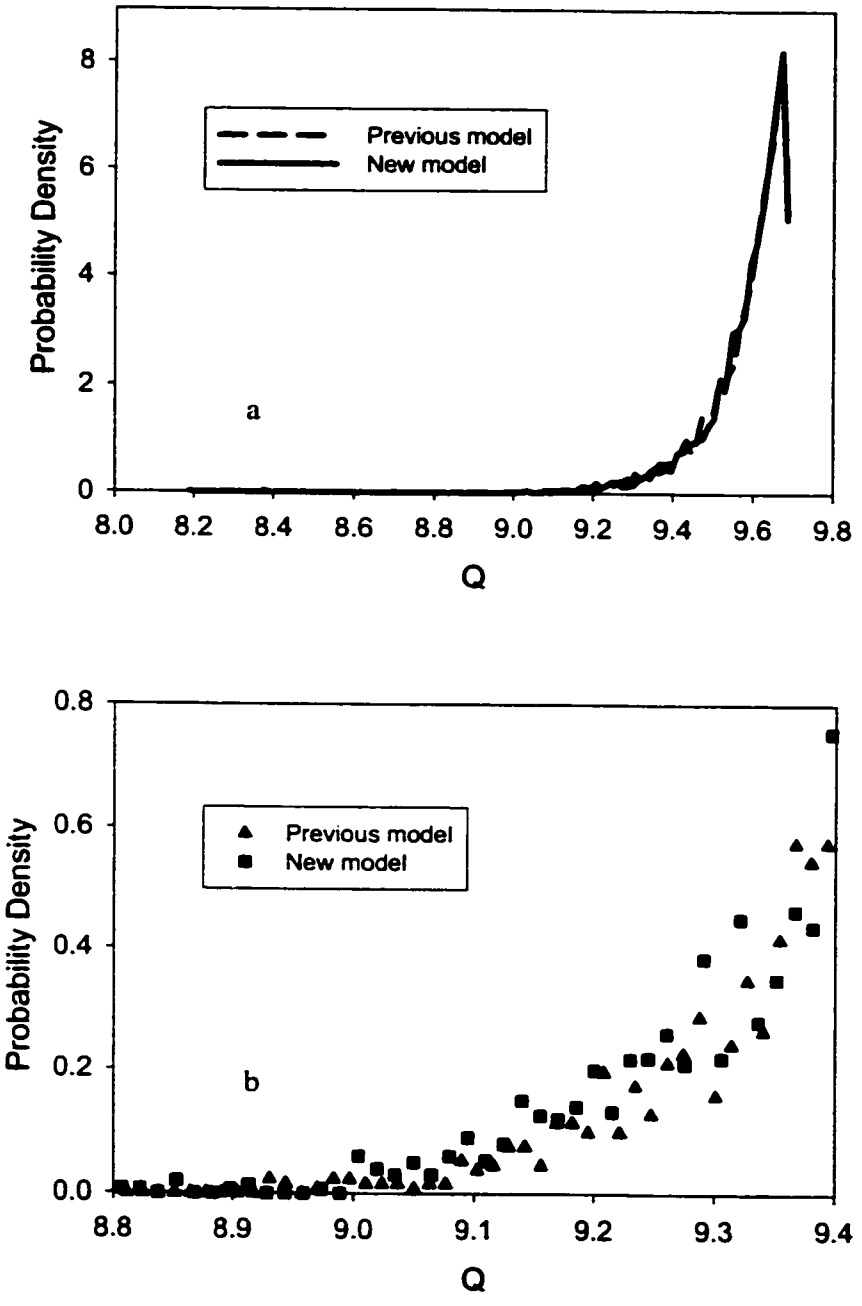

Figure 10.19 Distribution of Q factor in the presence of PMD using two different models with the same PMD square in each PMF segment.

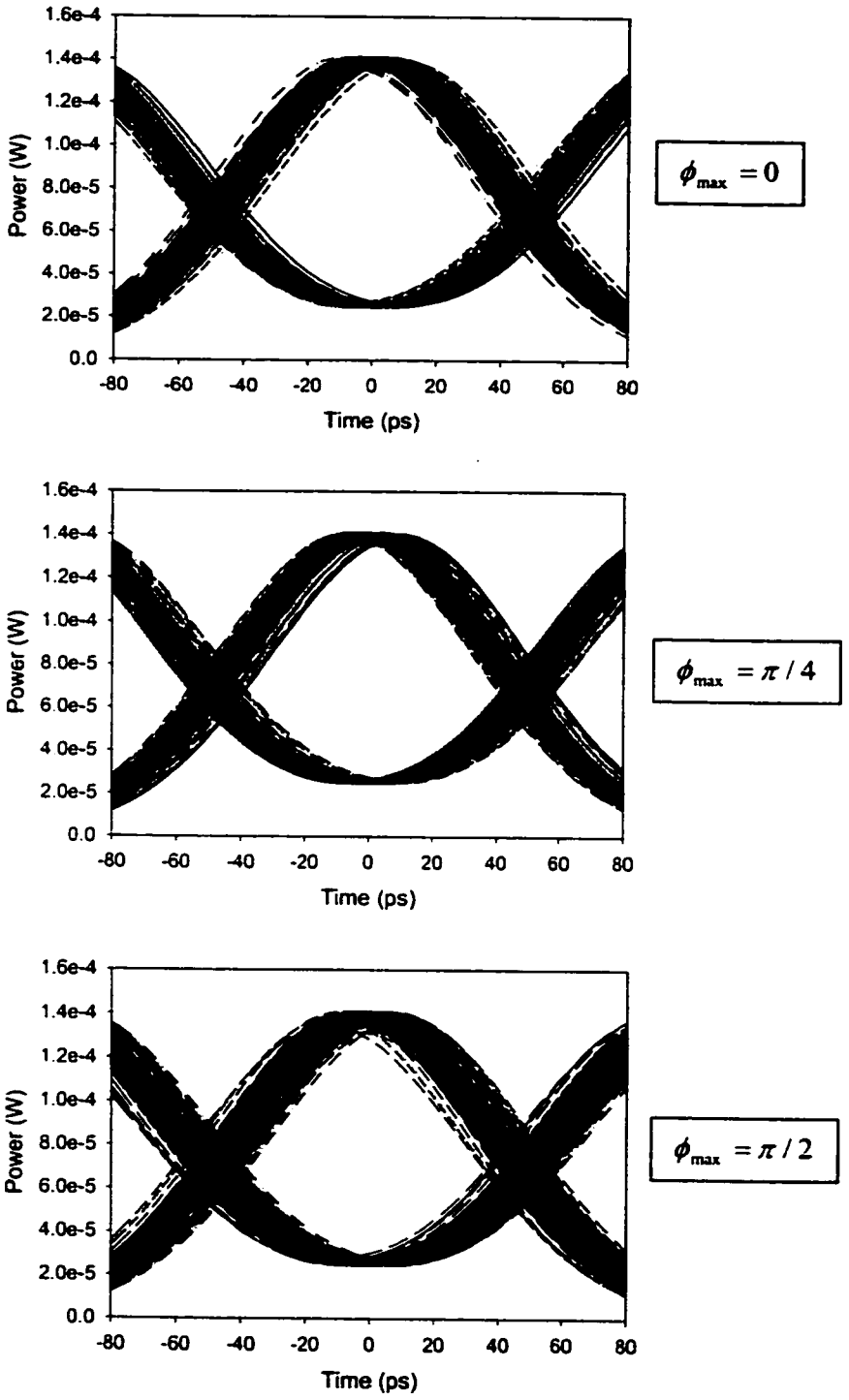

Figure 10.20 Eye diagrams in the presence of biased PMD (10 ps) at various maximum biased angles, ϕ_{max}, in the PMF segments.

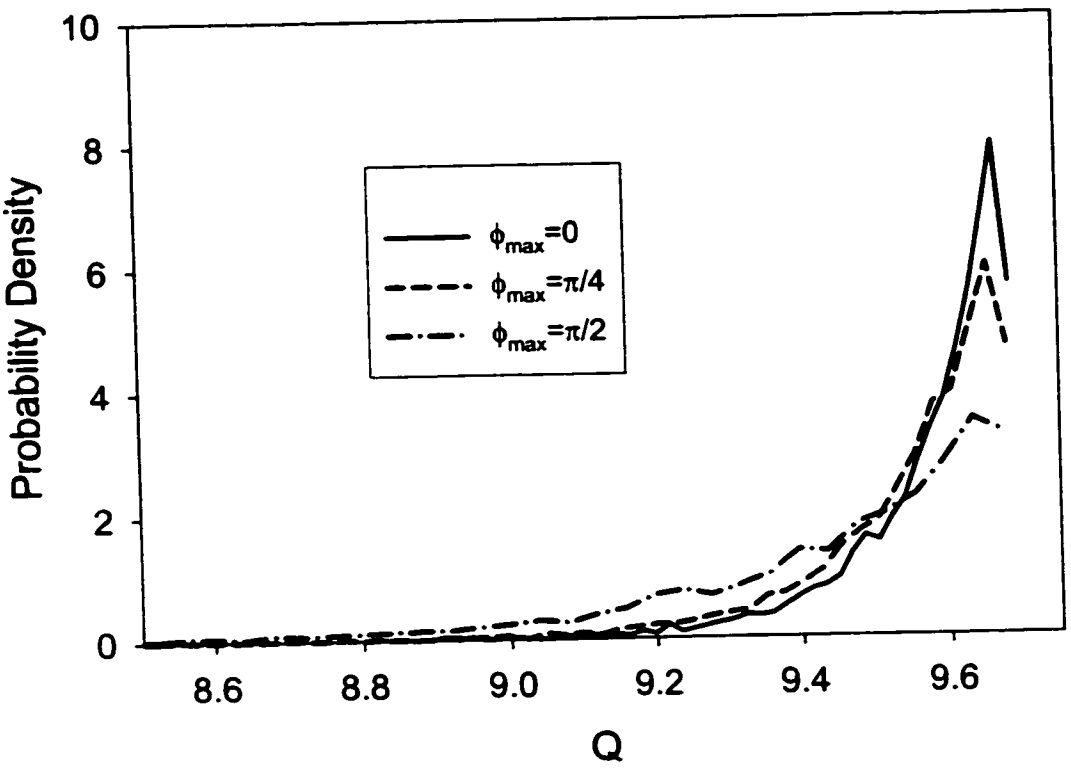

Figure 10.21 Statistical distributions of Q-factor in the presence of biased PMD (10 ps) at various maximum biased angles , ϕ_{max} , in the PMF segments.

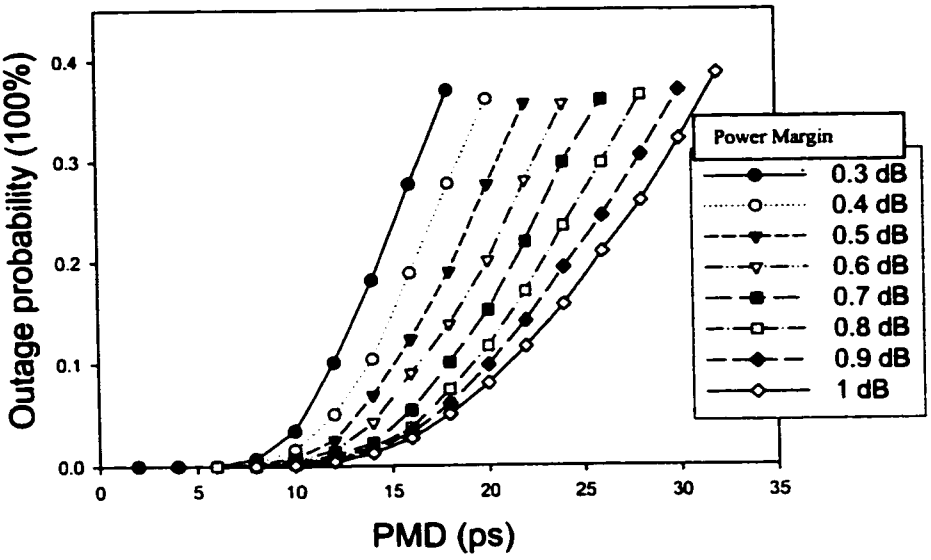

Figure 10.22 System outage probabilities due to PMD at various power margins.

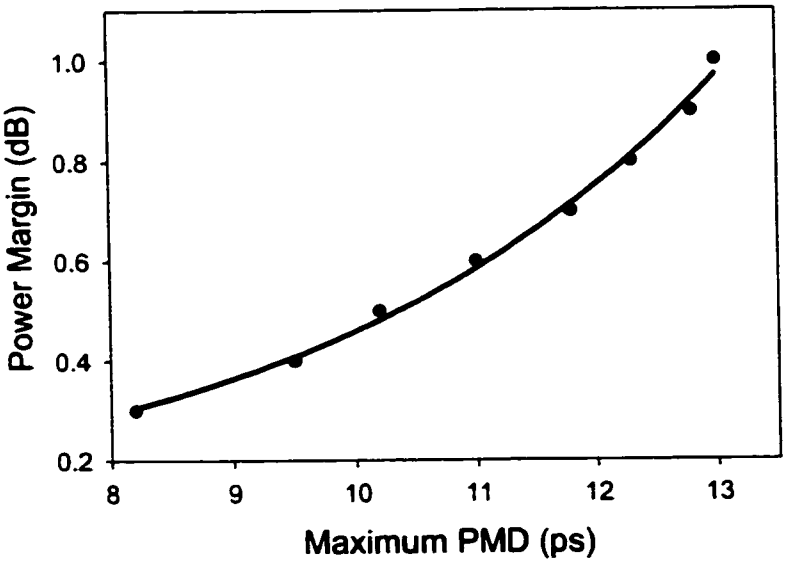

Figure 10.23 Maximum PMDs that induce 1% outage probability at various power margins.

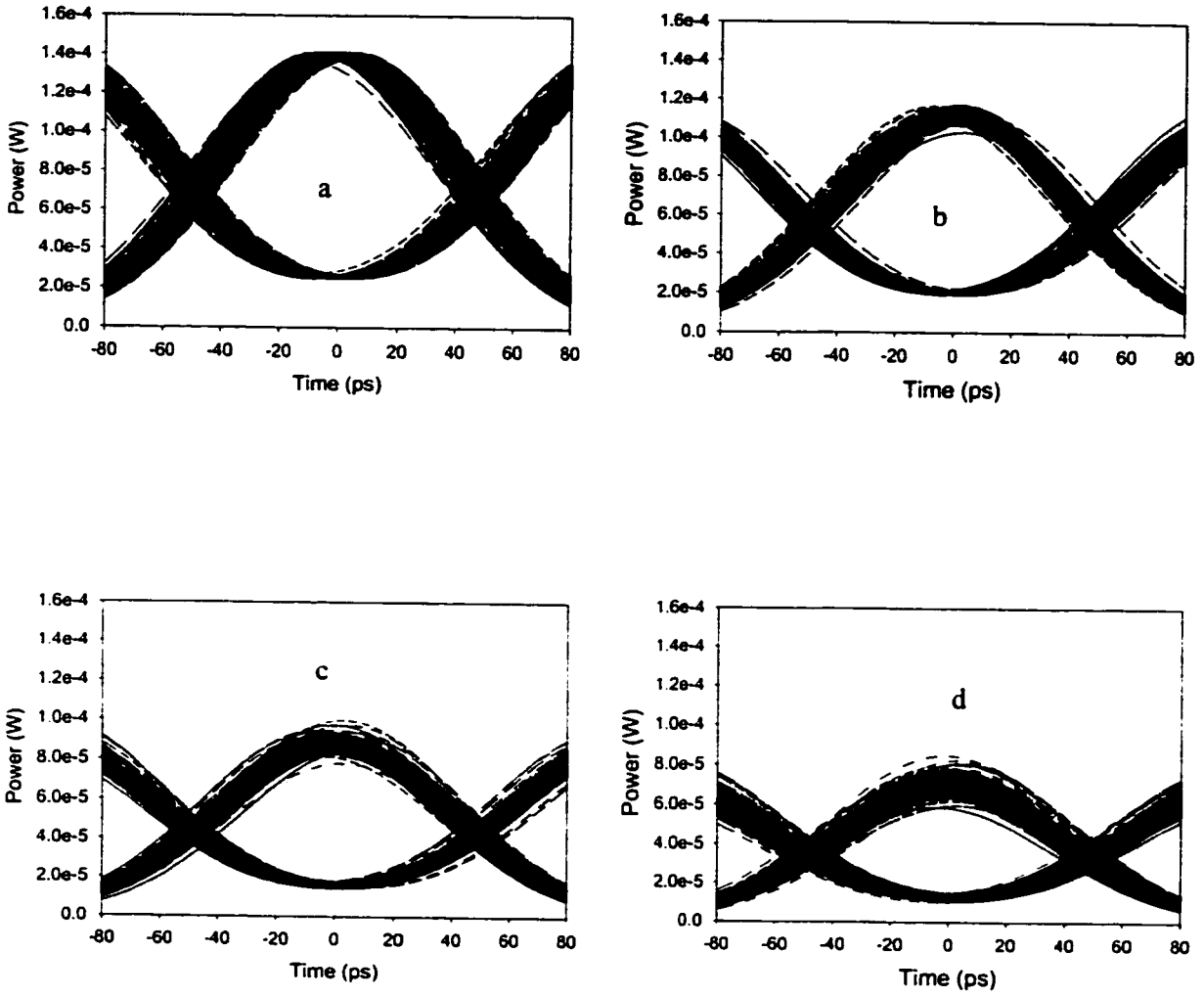

Figure 10.24 Eye diagrams in the presence of PMD and PDL based on the previous model. The PMD of each ensemble is 10 ps and the PDL is a) 0, b) 0.2 dB, c) 0.4 dB, d) 0.6 dB.

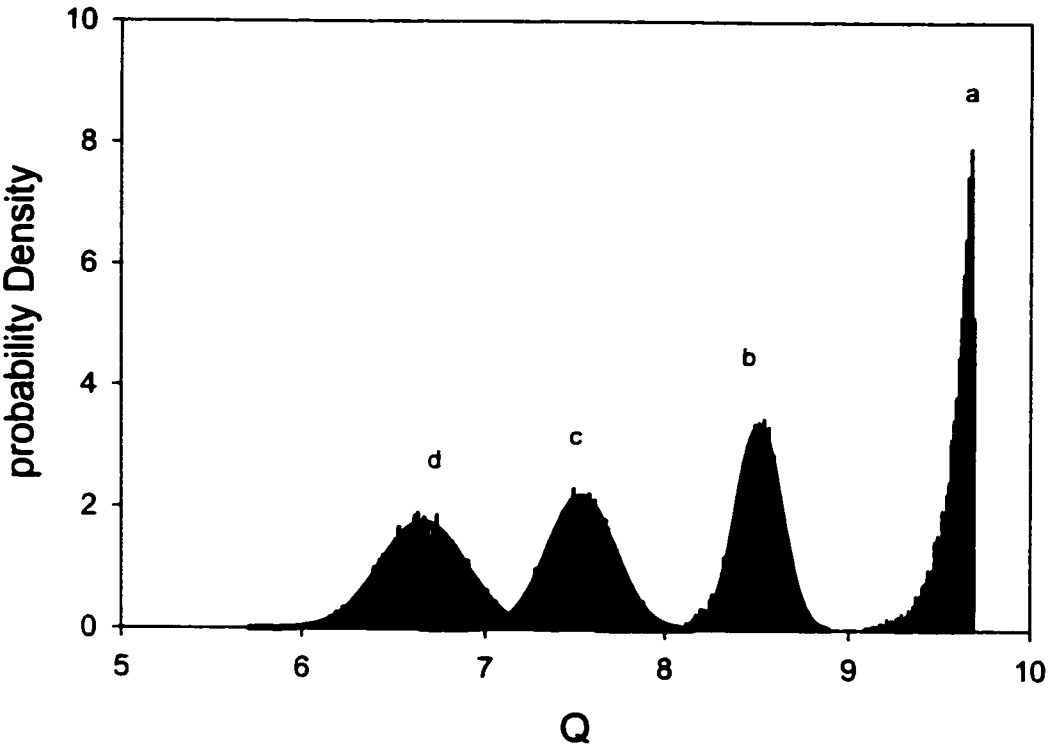

Figure 10.25 Statistical distribution of system Q factor in the presence of PMD and PDL. The PMD of each statistical ensemble is 10ps, the PDL is a) 0, b) 0.2 dB, c) 0.4 dB, d) 0.6 dB.

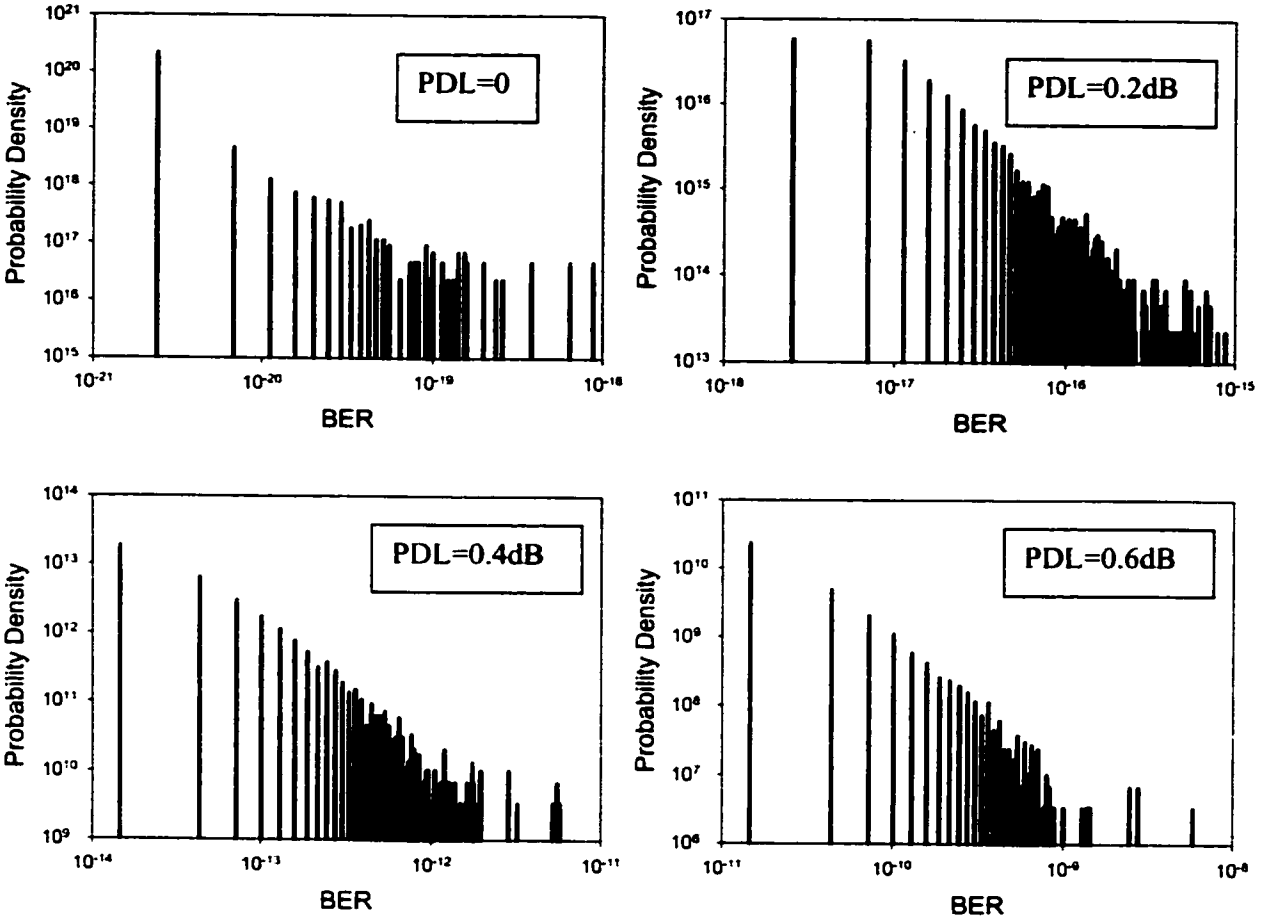

Figure 10.26 Statistical distribution of BER in the presence of PMD and PDL (Previous model). The PMD of the each ensemble is 10 ps and the PDL varies from 0 to 0.6 dB.

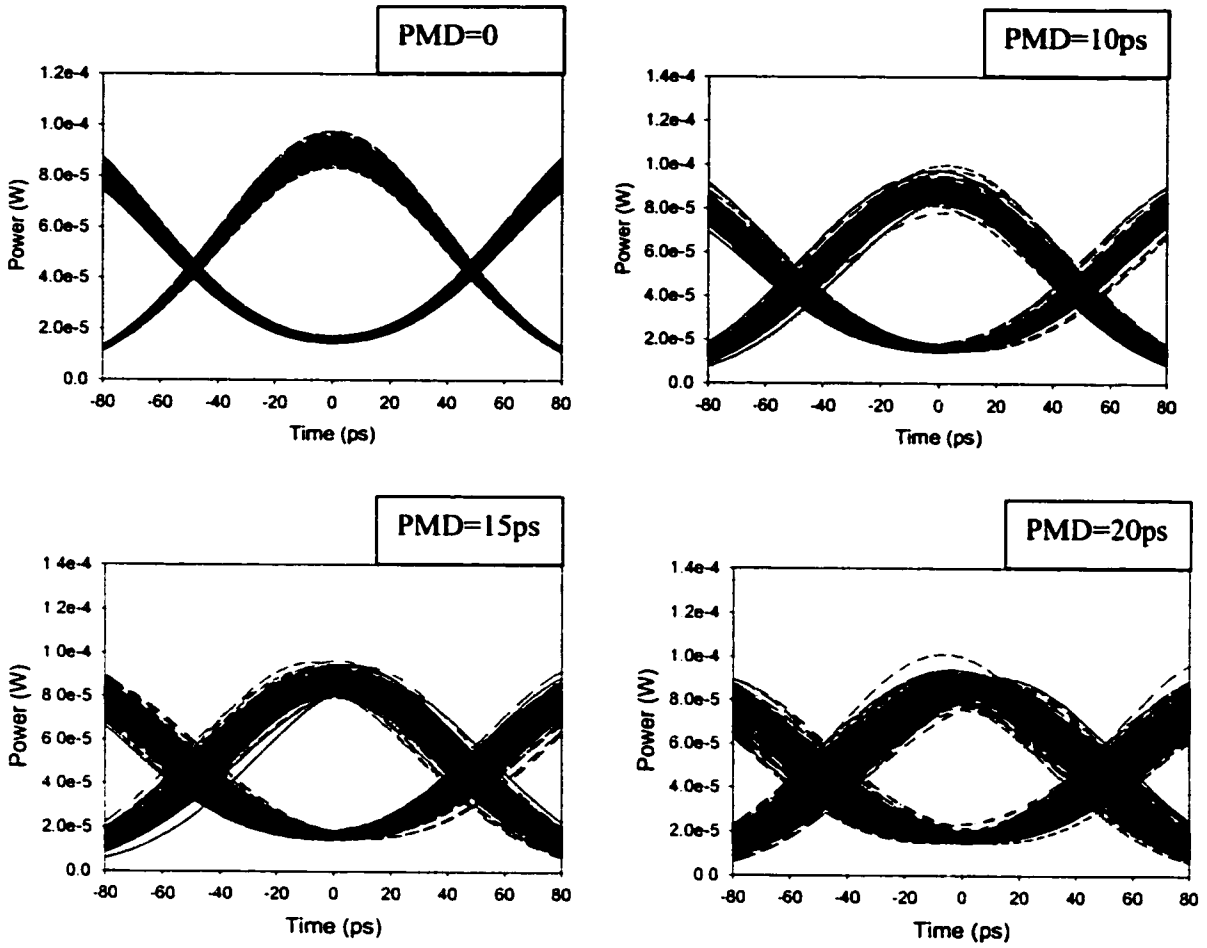

Figure 10.27 Eye diagrams using the previous model in the presence of PMD and PDL. The PDL is 0.4 dB and the PMD is 0, 10, 15 and 20 ps.

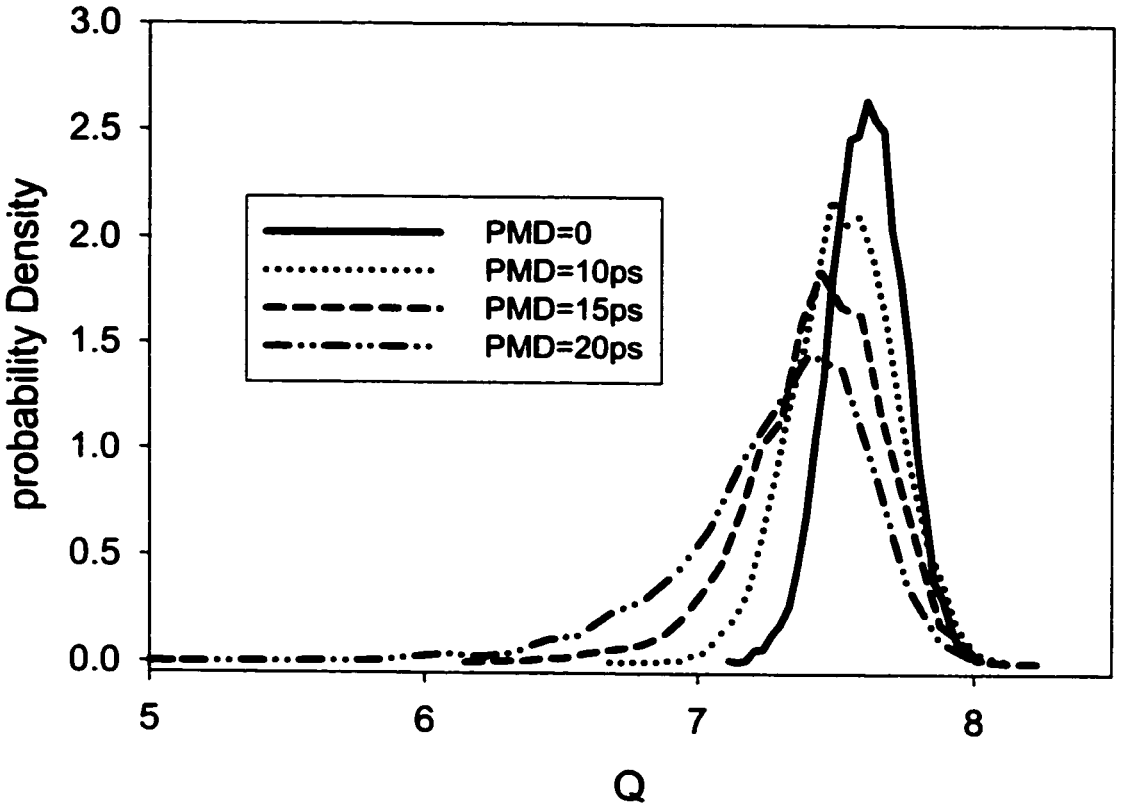

Figure 10.28 Statistical distribution of system Q-factor using the previous model in the presence of PMD and PDL. The PDL of each ensemble is 0.4 dB and the PMD change from 0 to 20 ps.

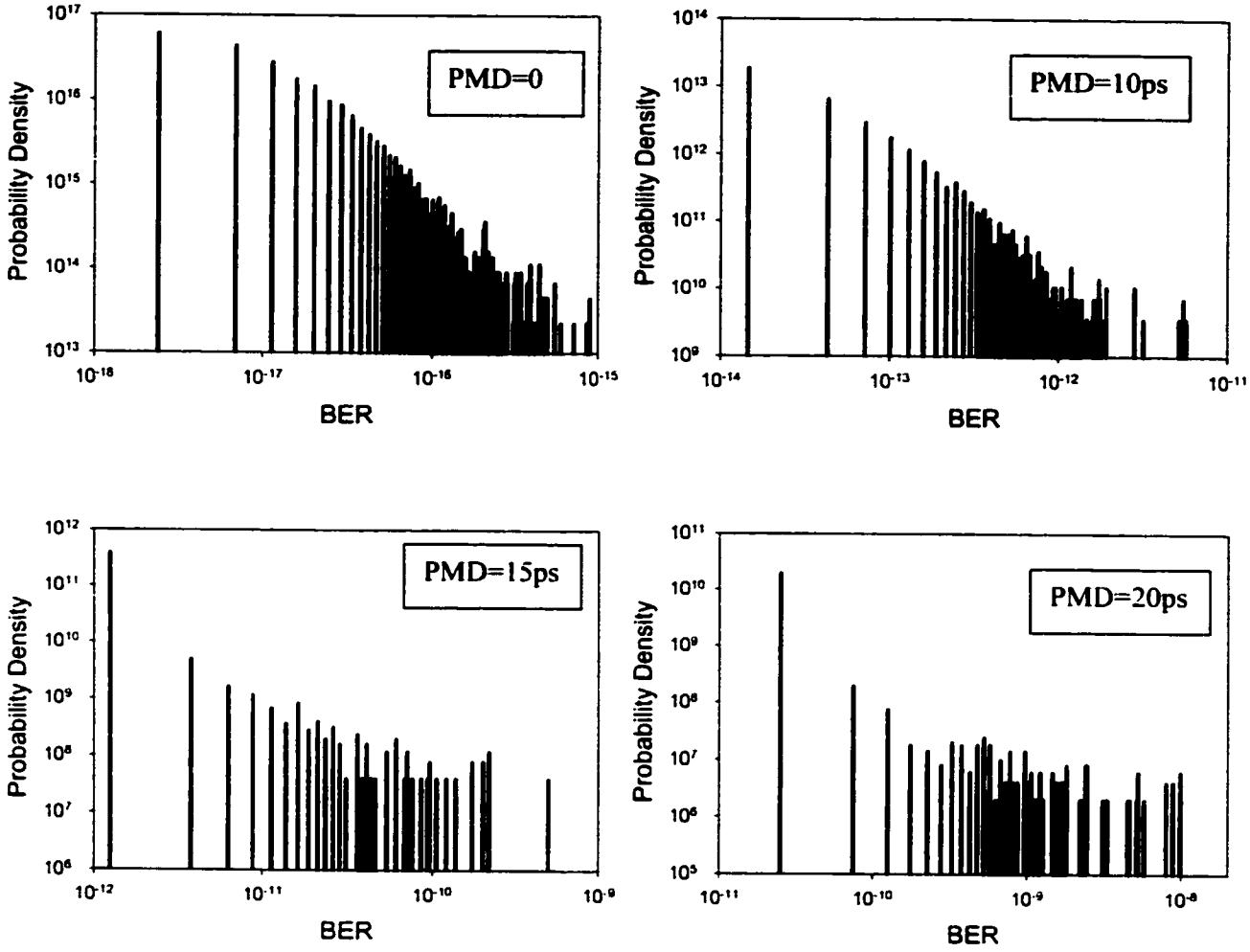

Figure 10.29 Statistical distribution of BER in the presence of PMD and PDL (previous model). The PDL of the fibers is 0.4 dB and the PMD varies from 0 to 20 ps.

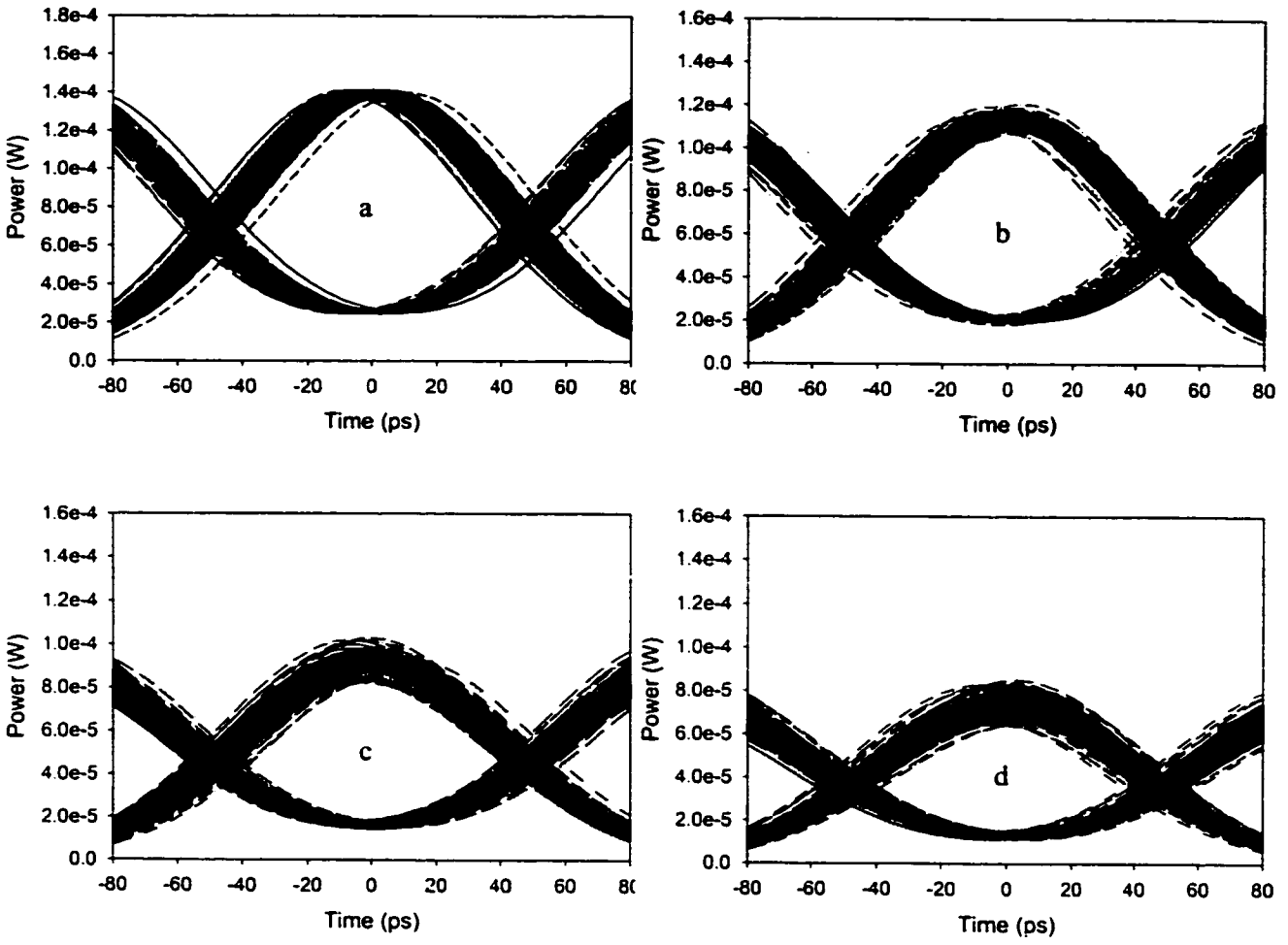

Figure 10.30 Eye diagrams using the new model at various PDLs and with the same PMD (10 ps). a) $\alpha_m = 0$, $\alpha_0 = 0$, b) $\alpha_m = 0.0023$, $\alpha_0 = 0.0014$ c) $\alpha_m = 0.0046$, $\alpha_0 = 0.0028$, d) $\alpha_m = 0.0069$, $\alpha_0 = 0.0042$.

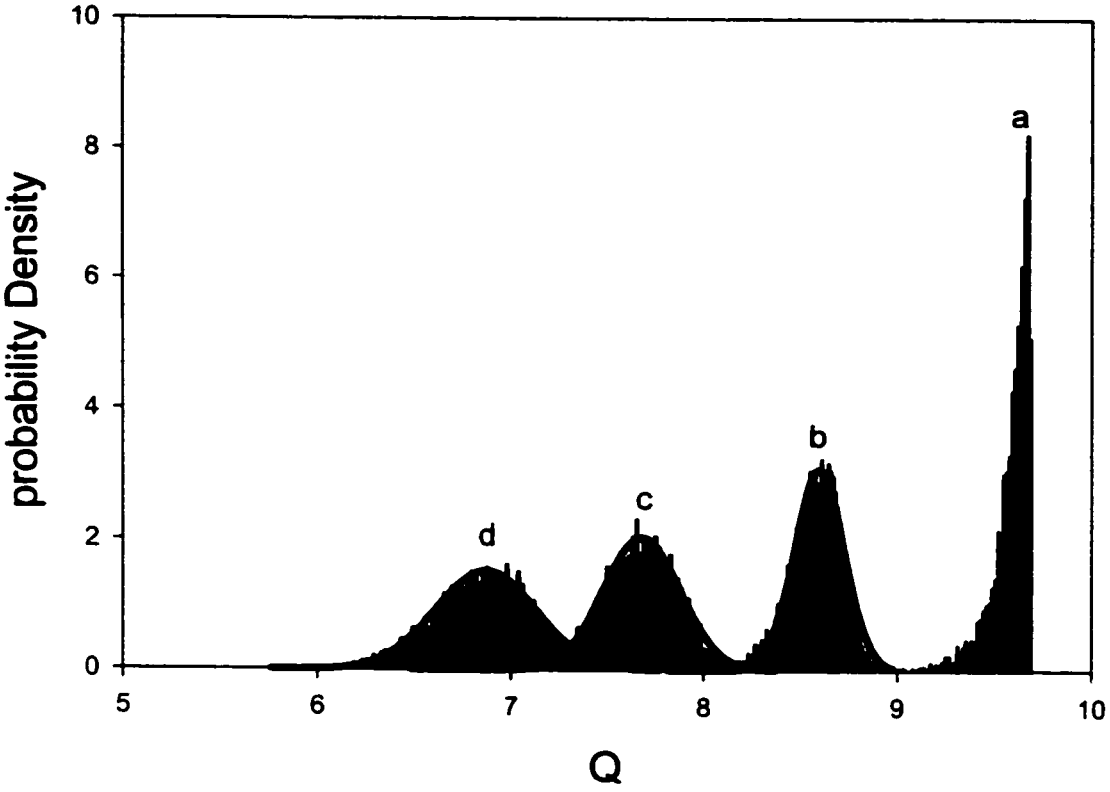

Figure 10.31 Statistical distribution of Q factor using the new model at various PDLs but with the same PMD (10 ps). a) $\alpha_m = 0$, $\alpha_0 = 0$, b) $\alpha_m = 0.0023, \alpha_0 = 0.0014$, c) $\alpha_m = 0.0046$, $\alpha_0 = 0.0028$ d) $\alpha_m = 0.0069$, $\alpha_0 = 0.0042$.

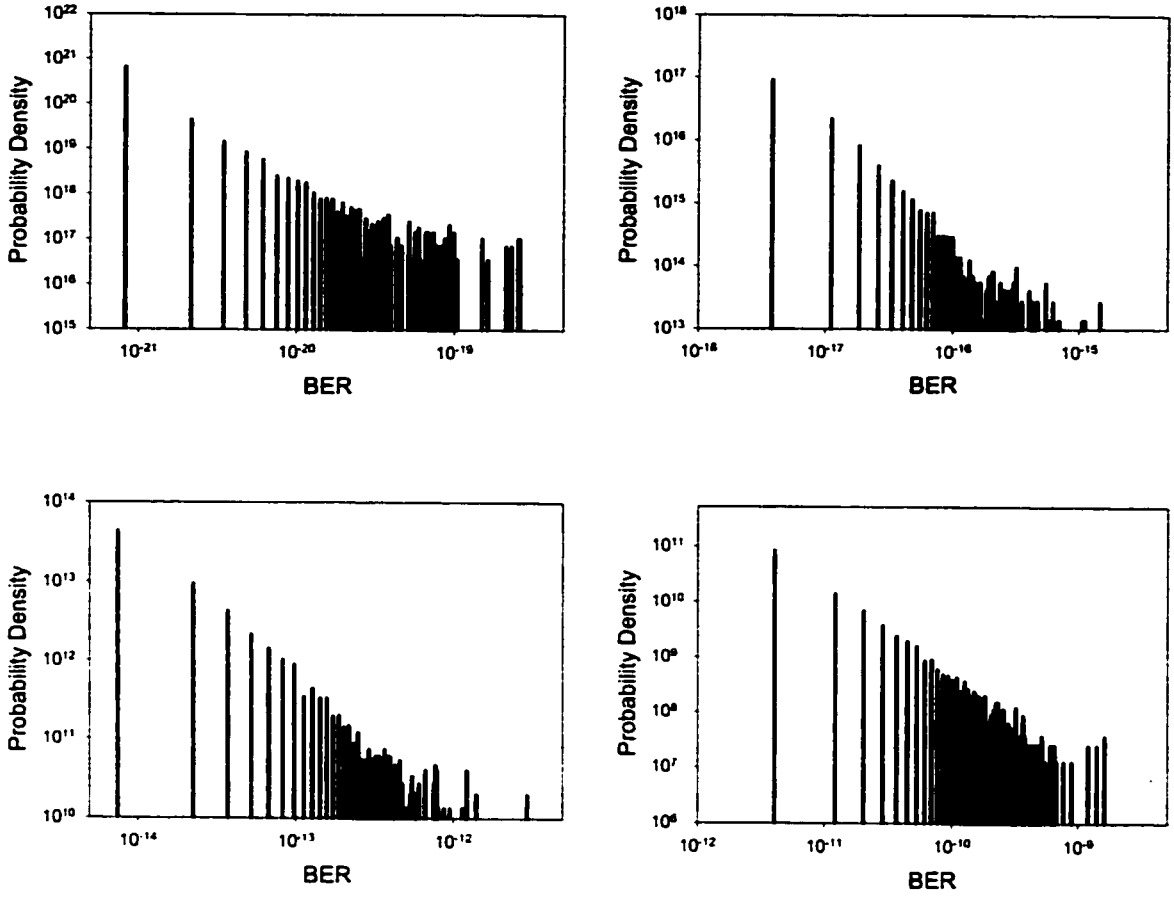

Figure 10.32 Statistical distribution of BER with PMD and PDL using the new model. a) $\alpha_m = 0$, $\alpha_0 = 0$, b) $\alpha_m = 0.0023, \alpha_0 = 0.0014$ c) $\alpha_m = 0.0046$, $\alpha_0 = 0.0028$, d) $\alpha_m = 0.0069$, $\alpha_0 = 0.0042$.

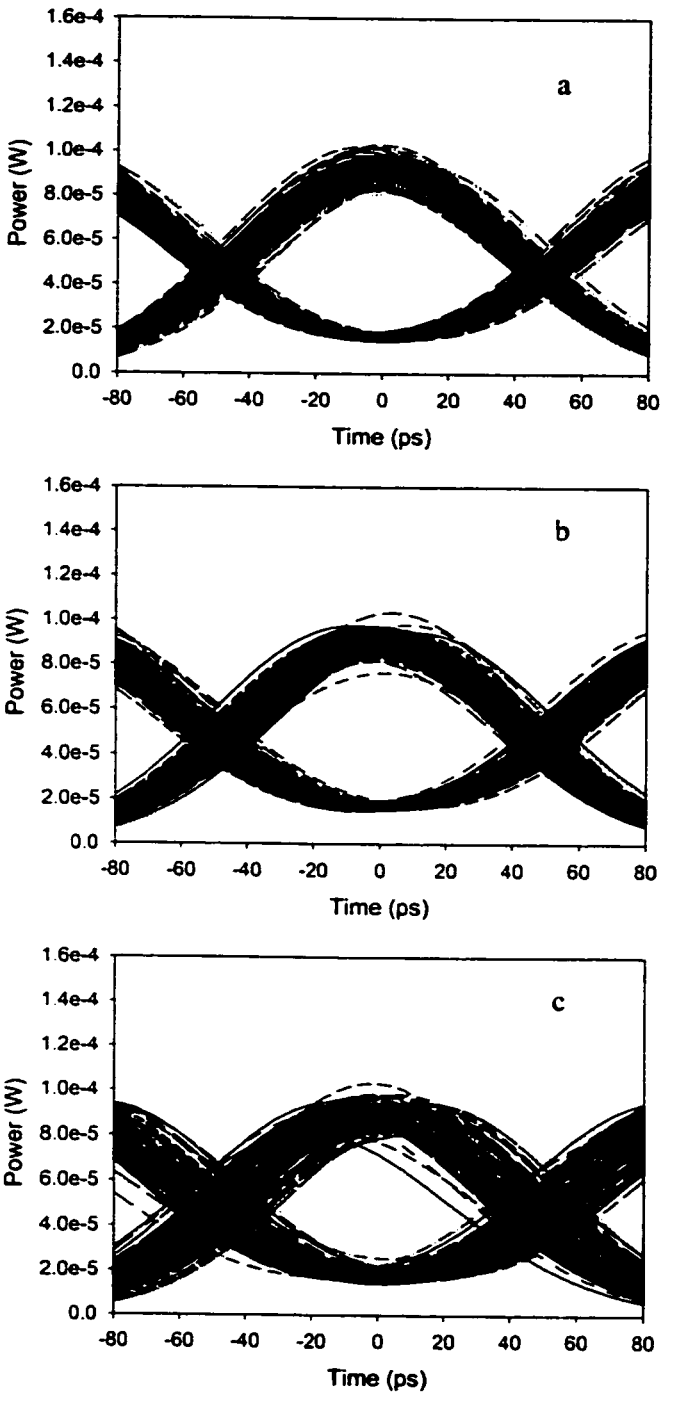

Figure 10.33 Eye diagrams using the new model at various PMDs with the same PDL. a) $\beta_m = 1.00ps, \beta_0 = 0.61ps$, b) $\beta_m = 1.50ps, \beta_0 = 0.92ps$, c) $\beta_m = 2.00ps, \beta_0 = 1.22ps$.

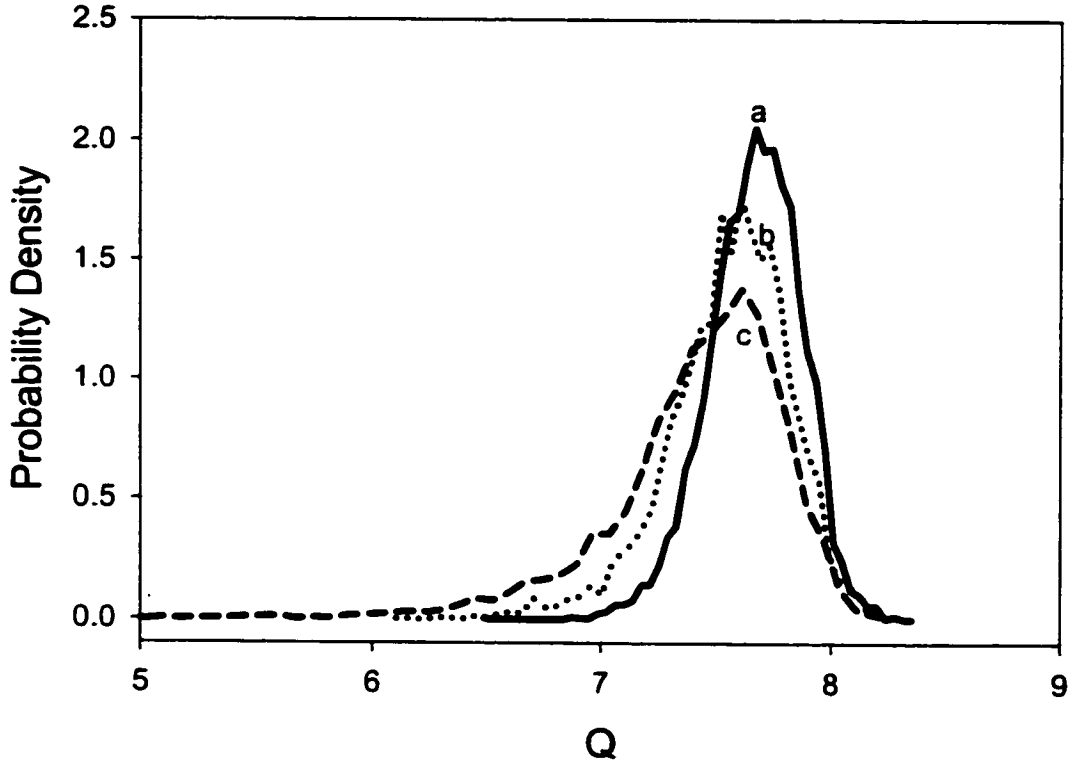

Figure 10.34 Statistical distribution of Q factors using the new model in the presence of same PDL and various PMDs. a) $\beta_m = 1.00ps, \beta_0 = 0.61ps$, b) $\beta_m = 1.50ps, \beta_0 = 0.92ps$, c) $\beta_m = 2.00ps, \beta_0 = 1.22ps$.

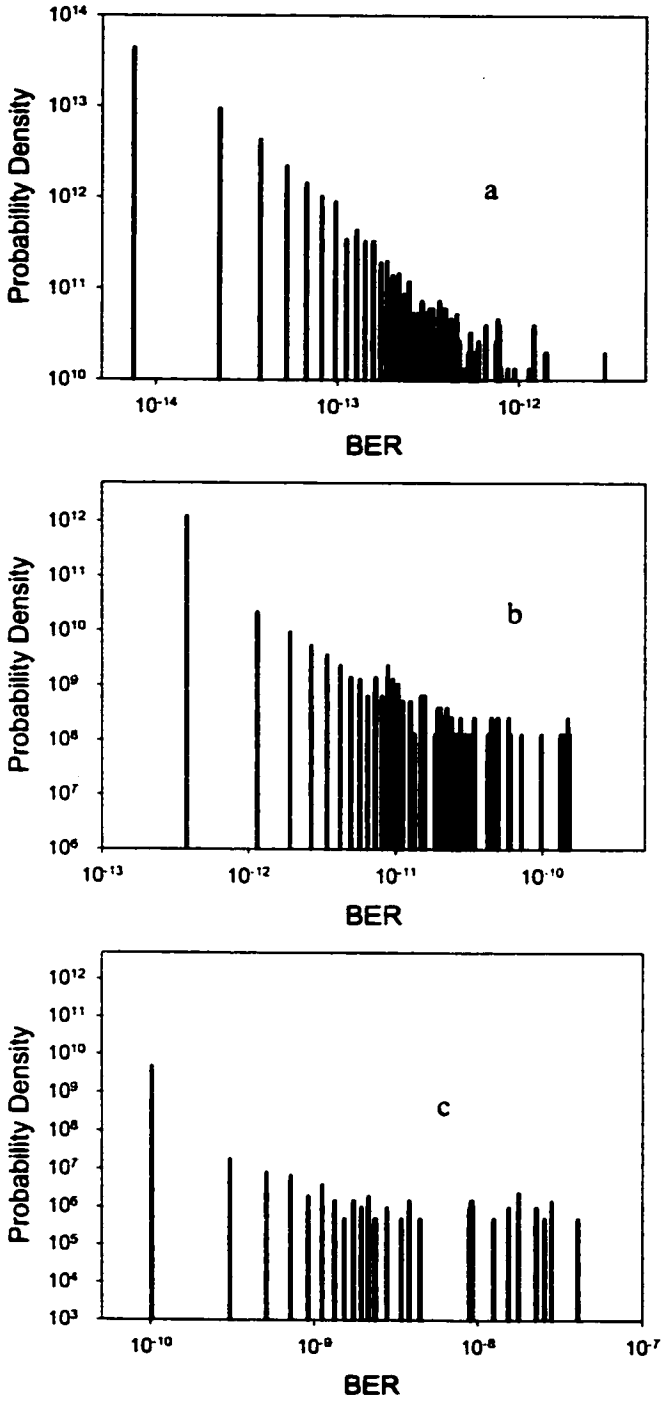

Figure 10.35 Statistical distribution of BER in the presence of PMD and PDL using the new model. a) $\beta_m = 1.00ps, \beta_0 = 0.61ps$,

b) $\beta_m = 1.50ps, \beta_0 = 0.92ps$, c) $\beta_m = 2.00ps, \beta_0 = 1.22ps$.

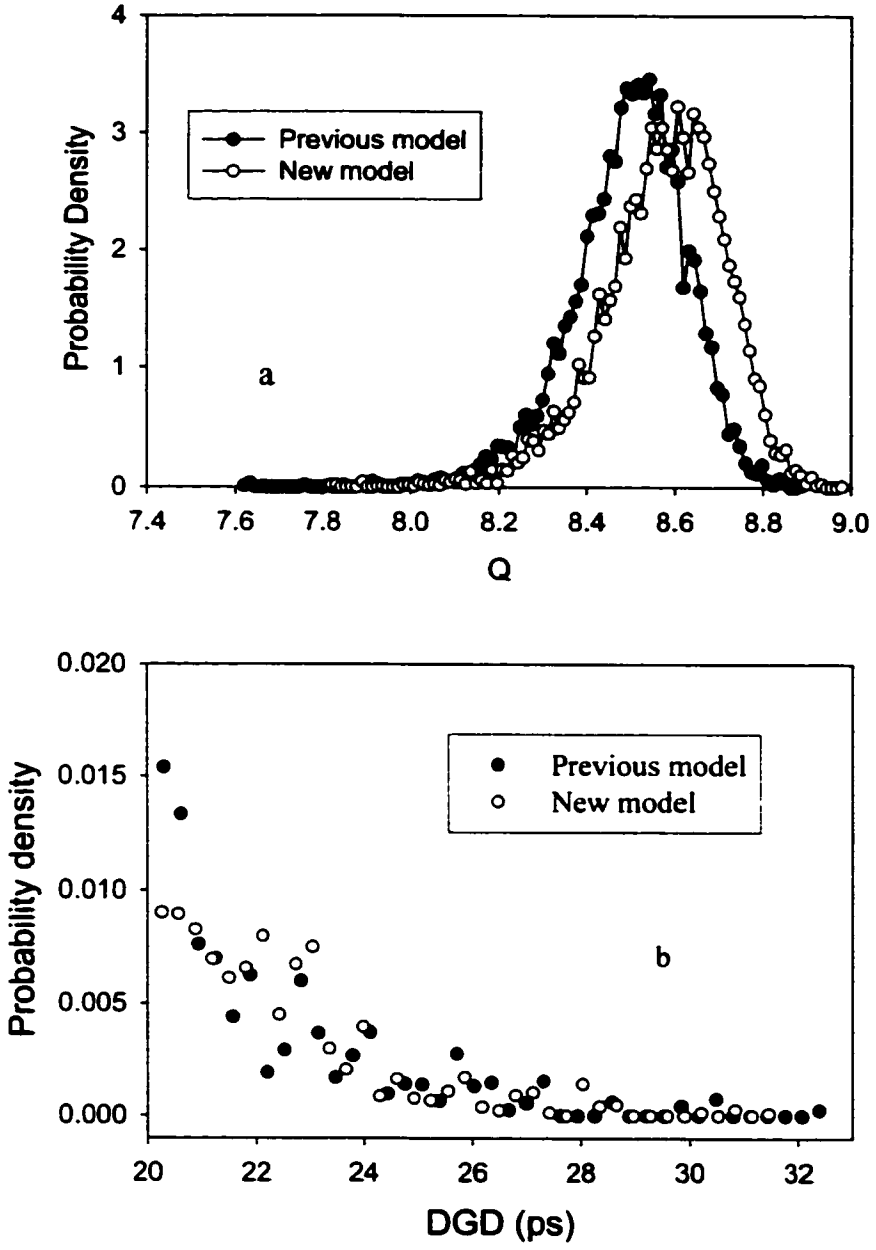

Figure 10.36 Comparison of the interactions of PMD and PDL in two waveplate models. a) Statistical distributions of Q factor using different waveplate models with PMD and PDL. b) Statistical distributions of DGD in the presence of PDL using different models.

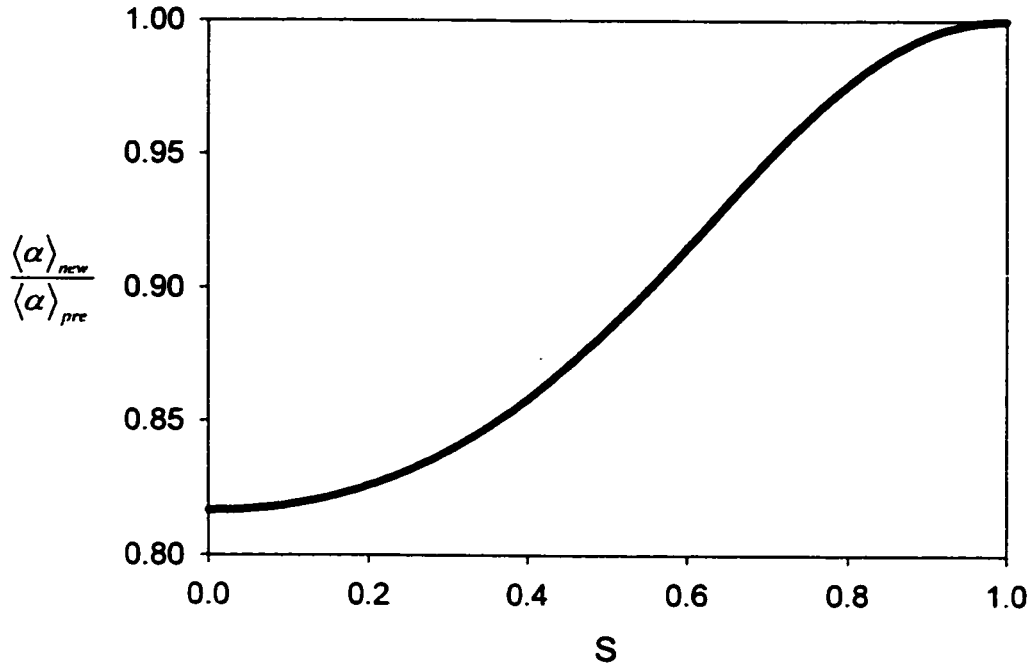

Figure 10.37 The ratio of the average PDLs (or PMDs) for the two models at various S values in the case that the average PDL (or PMD) squares of the PMF segments are kept the same.

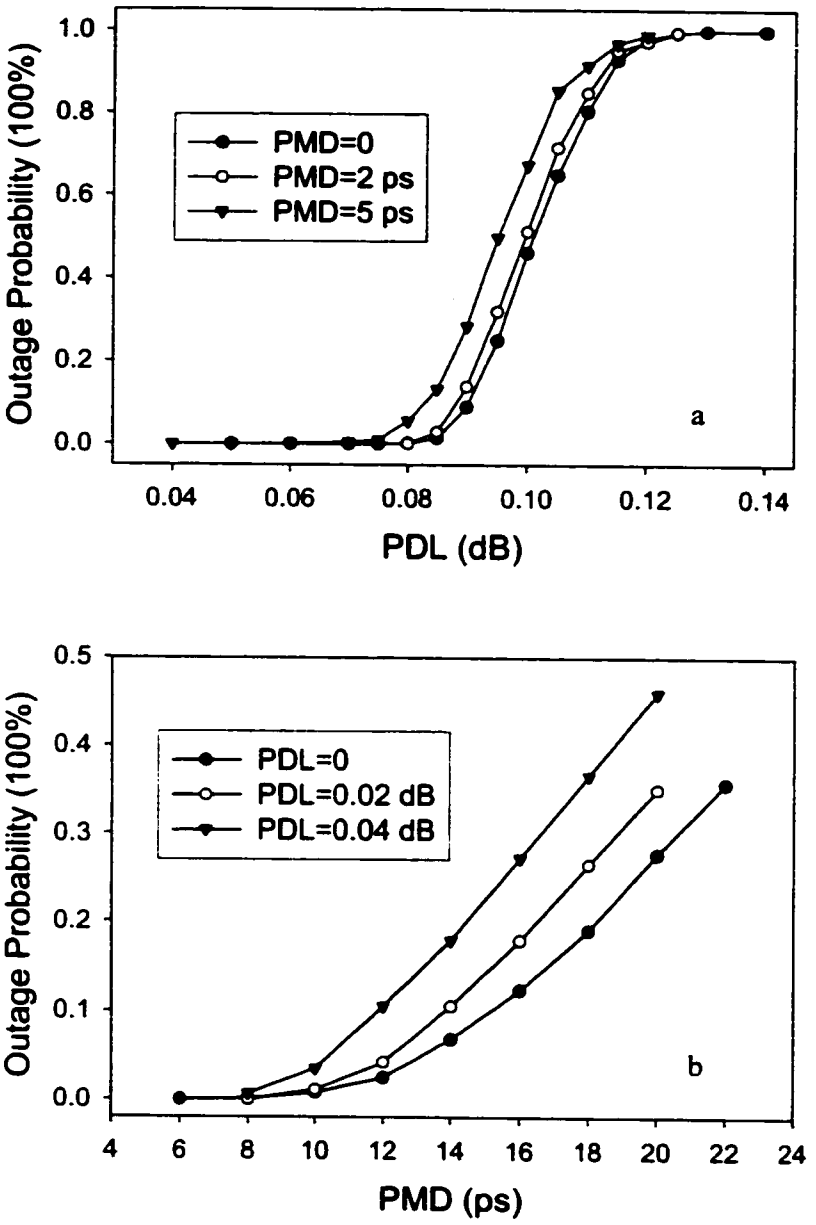

Figure 10.38 Outage probability due to the combined effect of PMD and PDL with a power margin of 0.5 dB.

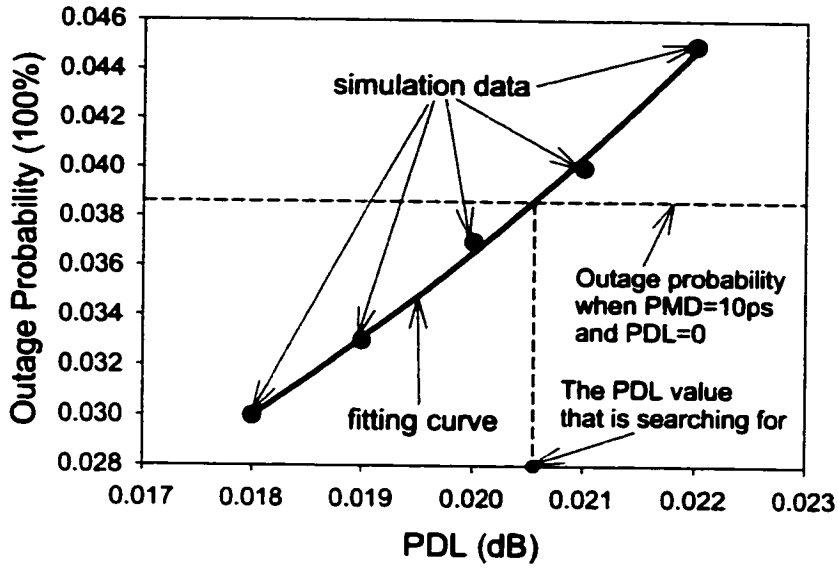

Figure 10.39 For a given PMD value (< 10 ps) and power margin, the method of obtaining the appropriate PDL value that gives the same outage probability as that when PMD=10 ps and PDL=0.

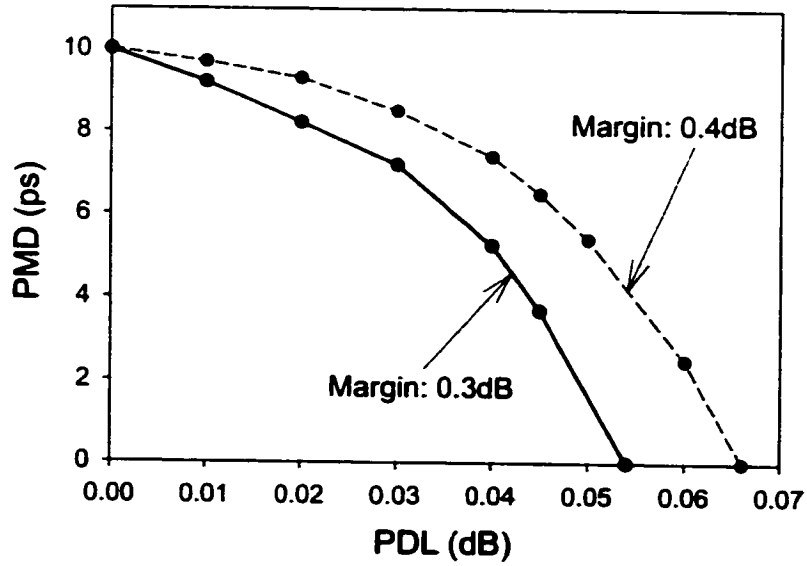

Figure 10.40 PMD limit in the presence of PDL for a 10 Gbits/second system.

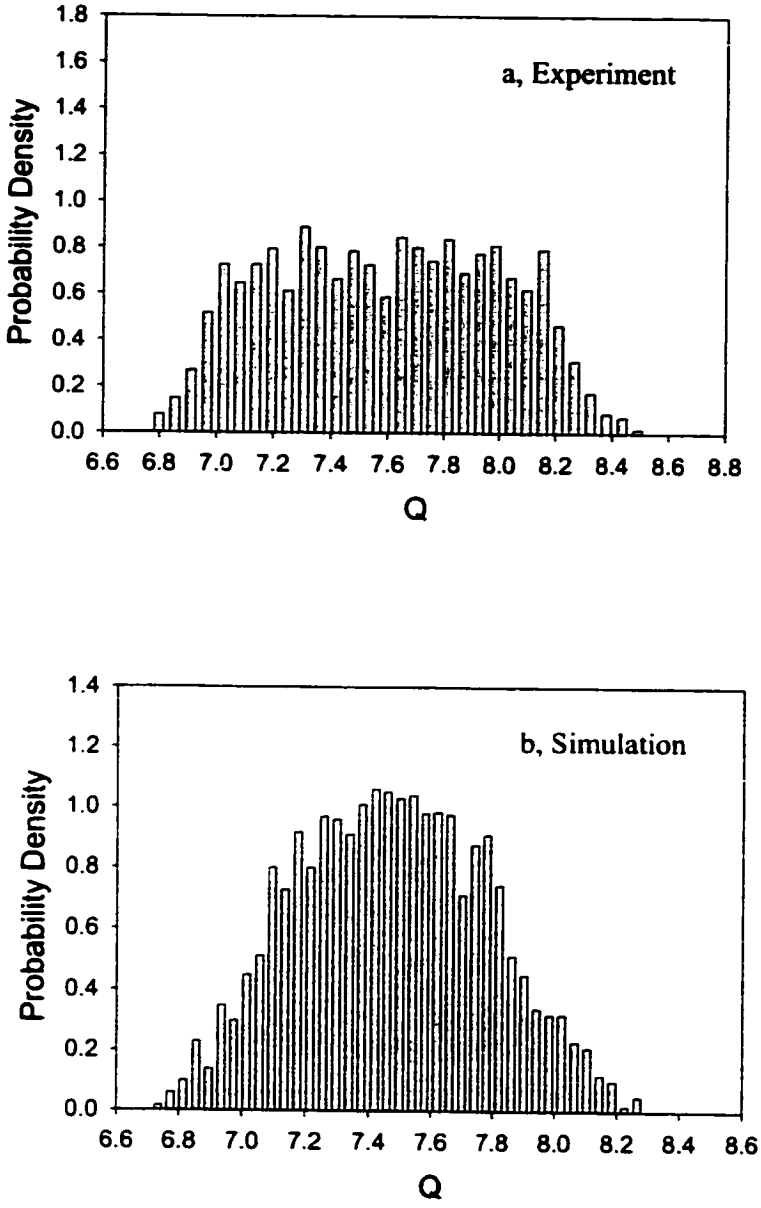

Figure 10.41 Experimental and simulation results of system Q factor distribution in the presence of PMD and PDL.

Chapter 11

Summary and Future Work

This thesis consists of two research directions: 1) Optical fiber applications for gas concentration and radiation dose measurements; and 2) Investigation of polarization effects in fiber optic communication systems.

11.1 Summary of part I

Two applications of optical fibers are presented in part 1 of the thesis. One is the application of infrared fibers in the measurement of gas concentrations in a CVD chamber, and the other is the application of optical fibers in the measurement of radiation dose.

In the semiconductor industry, silica thin films are deposited on substrates in a CVD chamber. The reactive gases are not uniformly distributed in the CVD chamber, and certain unstable intermediate species are appreciable only within a thin boundary layer near the substrate surface (a few millimeters). The intermediate species are known to play a critical role in the thin film formation process, and properly measuring these species can reduce the data processing time for real-time thin film deposition control. Current system using the technique of FT-IR spectroscopy has two major drawbacks that limit the realization of real-time monitoring and control of thin film deposition. One is the low collecting efficiency of infrared radiation from a source and the other is the large light beam divergence in the CVD chamber. These two drawbacks prevent effective sampling the gases in the thin boundary layer above the substrate, and it requires 30 seconds to acquire one gas absorption spectrum (the whole thin film deposition time is usually a few minutes). In this thesis the current system has been improved by using a semi-ellipsoid mirror and an infrared fiber bundle. The specially designed

semi-ellipsoid mirror has a major radius of 70 cm and a minor radius of 30 cm, and its inner surface was coated with gold to increase its reflectivity. Compared to parabolic mirror, the semi-ellipsoid mirror has more than doubled the collecting efficiency of the spectrometer. The infrared fiber bundle consists of two types of infrared fibers: silver halide and zirconium fluoride fibers. It covers the wavelength range from visible to 20 μm. Two modified SMA connectors were specially designed and fabricated for this fiber bundle, thus eliminating the need of epoxy for mounting fibers, which would otherwise introduce strong absorption peaks in the mid-infrared wavelength range. Linking the spectrometer to the CVD chamber, the fiber bundle has reduced both the focal spot size (from 12 mm to 4 mm) and beam divergence (from 0.4 to 0.1 rad) in the CVD chamber. These improvements have allowed the system to measure gas concentrations in a region closer to the substrate surface.

Gamma radiation induces ionization and the formation of color centers in optical fibers, which increases the fiber loss. This effect has been employed to investigate fiber optic radiation sensors in this thesis. The gamma radiation induces loss spectra of various fibers have been studied. Among the fiber samples, P-doped fiber (5% of P_2O_5) is the most radiation-sensitive due to its large core diameter (40 μm) and high P_2O_5 doping concentration (5%). At the wavelength of 502 and 540 nm, the radiation-induced loss in P-doped fiber shows a linear relationship with the total dose without dose-rate dependence, while the radiation induced losses in normal multi-mode and Ge-doped fibers are dose rate dependent. Compared to normal single-mode fiber (SMF 28), P-doped fiber is more than 100 times sensitive to gamma irradiation. This suggests that P-doped fiber is a good candidate for fiber optic radiation sensor operating at 502 or 540nm in radiation therapy applications.

11.2 Summary of part II

Part II of the thesis presents an investigation of the polarization effects in fiber optic communication systems using two waveplate models. In the conventional waveplate model a fiber is treated as a concatenation of many polarization maintaining fiber (PMF) segments, the differential group delay (DGD) (or polarization dependent loss (PDL)) in each PMF segment is

uniformly distributed within a finite range. The drawback of this model is that it produces zero DGD (or PDL) probability when DGD (or PDL) exceeds a certain value. To overcome this drawback a new waveplate model is proposed. The DGD in each PMF segment of the new waveplate model has the ability of taking any values.

Using both waveplate models, chapter 7 has examined the statistical DGD distribution. Simulation results show that the new waveplate model produces the same DGD distribution as that of the conventional waveplate model except in the large DGD region where the new waveplate model produces a slightly higher DGD probability density. In the presence of PDL, the statistical DGD distribution is a combination of Gaussian and Maxwellian distributions. This conclusion is valid for both waveplate models even in the presence of biased elliptical birefringence. In this thesis a biased elliptical birefringence means that the circular component of the birefringence is always positive (or negative) in Stokes space.

In chapter 8, the waveplate models have been used to study the statistical PDL distribution, which is found to be a combination of the Rayleigh and Maxwellian distributions in the presence of DGD. Without DGD the PDL distribution is a Rayleigh distribution and when PMD is larger than 0.005 ps it is mainly Maxwellian. The new model produces the same PDL distribution as the conventional waveplate model except in the large PDL region where the new waveplate model produces a slightly higher PDL probability density.

The high order frequency dependent DGD and PDL effects have been studied in chapter 9. The concepts of PMD and PDL for an optical pulse are proposed for the first time. The PMD and PDL of a pulse for a fiber consisting of two PMF segments are calculated. The results show that the PMD and PDL for a short pulse are strongly pulse-width dependent. Due to the lightwave depolarization and the interaction of PMD and PDL, two anomalous results are found: 1) The effective PDL for a pulse can be smaller than the PDL difference of the two PMF segments; and 2) The effective PMD for a pulse can be either larger than the sum of the DGDs of the two PMF segments or less than the DGD difference of the two PMF segments, depending on the input pulse width. Pulse broadenings with various input polarization states are studied. It

is found that the output pulse width is not the minimum when a pulse is launched into either of the two PSP's in the presence of PDL. This calls extra caution for first order PMD compensation in the presence of PDL. The statistical distributions of PMD and PDL for a pulse are studied by examining many statistical ensembles. It is found that the distribution of PMD for a pulse is Maxwellian when PDL is zero, while it is a combination of Gaussian and Maxwellian functions in the presence of PDL. The distribution of PDL for a pulse is the same as that of single frequency (the Rayleigh distribution) when PMD is zero, it is mainly Maxwellian in the presence of PMD (>0.01 ps).

The system impact due to PMD and PDL has been studied in chapter 10 in terms of Q factor, BER and system outage probability using the previously mentioned waveplate models. First, the system impact due to PDL alone is studied. It is found that the statistical distribution of Q factor due to PDL alone is Gaussian. When the *rms* PDLs in each PMF segment of the two models are equal, the new waveplate model produces a higher BER than the conventional model. This is expected due to none zero DGD probabilities at large DGD values generated by the new waveplate model. The outage probabilities due to PDL are examined using the new waveplate model for various power margins. Simulation results show that the PDL induced outage probability strongly depends on power margin. Therefore, PDL can be compensated by a certain amount of power margins. Second, the system impact of PMD is studied in the presence of chromatic dispersion and frequency chirp. The new waveplate model produces higher BER than the conventional model when the *rms* DGDs in each PMF segment of the two models are equal. The pulse narrowing induced by the interaction of frequency chirp and higher order PMD is examined. Due to the interaction of chromatic dispersion and frequency chirp, PMD may be compensated by introducing certain amounts of chromatic dispersion and frequency chirp with opposite signs. The outage probabilities due to PMD are examined using the new waveplate model for various power margins. It is found that when PMD is larger than 10% of the bit period, it cannot be compensated by increasing the power margin. This is consistent with the conclusion that the acceptable PMD value in a system is around 10% of the bit period. Third, the combined effect of PMD and PDL on system limitation has been studied. Unlike the cases of PMD or PDL alone, the new waveplate model produces a slightly lower BER in the presence

of both PMD and PDL than the conventional waveplate model. This is due to the two facts: 1) The mean DGD (or PDL) of each PMF segment in the new waveplate model is less than that in the conventional waveplate model when the *rms* DGDs (or PDLs) in each PMF segments in the two models are equal; and 2) The interaction of PMD and PDL is slightly stronger in the new waveplate model than that in the conventional waveplate model. The outage probability in the presence of both PMD and PDL is examined using the new waveplate model. Simulations show the strong interaction between PMD and PDL. For given power margin, the system outage probability due to small PMD (or small PDL) alone is almost zero, but it is a finite value with both PMD and PDL. The system limit of PMD is also studied in the presence of PDL. It is found that PDL significantly decrease the PMD limit even at 0.1 dB of PDL value. The distributions of system Q factors due to PDL and its combination with PMD are measured experimentally and compared with numerical simulations with good agreement.

11.3 Future work

For the study of infrared fibers in the monitoring of chemical process in the CVD chamber, the further work will focus on improving the performance of the whole system and will include examinations of bundles formed with different mid-infrared fibers and tests using improved material for the spectrometer beam-splitter and chamber windows. For the studies of fiber optic dosimeter, further work may study the induced loss by other high-energy particles, such as electrons and neutrons. The spatial resolution of the fiber optic dosimeter needs to be studied because this technique has the potential of making a distributed dosimeter system.

For the studies of PMD and PDL effects in fiber optic communication systems, future work may include the followings: 1) Measurement of PDL distribution in the presence/absence of PMD. 2) PMD compensation in the presence of PDL. 3) Examining the interaction of PMD and PDL in a higher bit rate system, such as OC768 (40 Gbits/second).

Bibliography

[1] Whidden, T. K. et al, In Situ Mid-Infrared Analyses of Reactive Gas-Phase Intermediates in TEOS/Ozone SAPCVD, Proceedings of the 1998 International Conference on Characterization and Metrology for ULSI Technology, AIP Press, New York, 1998.

[2] Whidden, T.K. et al, In Situ Studies of TEOS/Ozone CVD: Experimental Considerations for Probing Reaction Boundary Layers in Commercial CVD Equipment, The 194th Meeting of the Electrochemical Society, Boston, MA, Nol. 1-6, 1998.

[3] Romet, R., Couturier, M. F. and Whidden, T. K., Modeling of Silicon Dioxide Chemical Vapor Deposition from Tetraethoxysilane and Ozone, Journal of The Electrochemical Society, Vol. 148, No. 2, pp. G82–G90, February 2001.

[4] Rogina, B. M., and Vojnovic, B, Application of Optical-Fiber Sensors for Radiation-Dosimetry, Radiation Measurements, Vol. 26, No. 4, pp599-602, 1996.

[5] Bueker, H., Haesing, F. W., Pfeiffer, F., and Schmitz, H. J., A Fiber-Optic Twin Sensor for Dose Measurements in Radiation Therapy. Optical Review, Vol.4(1A), pp130-132, 1997.

[6] Agrawal, Govind P., Fiber Optic Communication Systems, second edition, sections 2.4, 2.5 and 2.6, John Willey & Sons, Inc, New York, 1997.

[7] Poole, C. D., and Wagner, R. E., Phenomenological Approach to Polarization Dispersion in Long Single-Mode Fibers, Electronics Letters, Vol. 22, No. 19, Sept., pp1029-1030, 1986.

[8] Bulow, Henning, System Outage Probability Due to First- and Second-Order PMD, IEEE Photonics Technology Letters, Vol. 10, No. 5, pp696-698, May 1998.

[9] Huttner, B., Geiser C., and Gisin, N., Polarization-Induced Distortion in Optical Fiber Networks with Polarization-Mode Dispersion and Polarization-Dependent Losses, IEEE Journal of Selected Topics in Quantum Electronics, Vol., 6, No. 2, pp317-329, 2000.

[10] Rashleigh, S.D., Origins and Control of Polarization Effects in Single-Mode Fibers, Journal of Lightwave Technology, Vol. LT-1, No. 2, pp912-931, June 1983.

[11] Chameron, J., PhD thesis, Physics Department, University of New Brunswick, 2000.

[12] Gisin, N., Statistics of Polarization Dependent Losses, Optics Communications, Vol. 114, pp399- 405, February, 1995.

[13] Gisin, N. and Huttner B., Combined Effects of Polarization Mode Dispersion and Polarization Dependent Loss in Optical Fibers, Optics Communications, Vol.142, pp119-125, 1997.

[14] Yan, L. S., Yu, Q., Xie, Y., and Willner A. E., Statistical Measurement of the Combined Effect of PMD and PDL Using a 10-Gb/s Recirculating Loop Testbed, OFC'2001, Proc. Of Optical Fiber Communication Conference, WT5, 2001.

[15] Gisin, N. and Pellaux, J. P., Polarization Mode Dispersion: Time versus Frequency Domains, Optics Communications, Vol. 89, pp316-323, 1992.

[16] Galtarossa, A., and Palmieri, L., Relationship Between Pulse Broadening due to Polarization Mode Dispersion and Differential Group Delay in Long Single Mode Fibers, Electronics Letters, Vol. 34, pp492-493, 1998.

[17] Chen, L., Cameron, J., and Bao, X., Statistics of Polarization Mode Dispersion in Presence of the Polarization Dependent Loss in Single Mode Fibers, Optics Communications, Vol. 169, pp69-73, 1999.

[18] Chen, L., and Bao. X., Polarization-Dependent Loss-Induced Pulse Narrowing in Birefringent Optical Fiber with Finite Differential Group Delay, Journal of Lightwave Technology, Vol. 18, No. 5, pp665-667, 2000.

[19] Huttner, B., and Gisin, N., Anomalous Pulse Spreading in Birefringent Optical Fibers with Polarization-Dependent Loss, Optics Letters, Vol. 22, No. 8, pp504-506, April 1997.

[20] Elbers, J. -P., Glingener, C., Duser, M., and Voges, E., Modeling of Polarization Mode Dispersion in Singlemode Fibers, Electronics Letters, Vol. 33, No. 22, pp1004-1005, October 1997.

[21] Beltrame, D., Matera, F., Settembre, M., Galtarossa, A., Pizzinat, A., Favre, F., Guen, D. Le and Henry, M., Impact of Polarization Mode Dispersion on the Statistics of Q factor in Optical Transmission Systems, Electronics Letters, Vo. 36, No. 16, pp1400-1401, Aug.2000.

[22] Gisin, N., and Huttner B., Influence of Polarization Dependent Loss on Birefringent Optical Fiber Networks, OFC'2000, Proc. of Optical Fiber Communication Conference, TuG1, 2001.

[23] Cameron, J., Chen, L., and Bao, X., Impact of Chromatic Dispersion on the System Limitation Due to Polarization Mode Dispersion, IEEE Photonics Technology Letters, Vol. 12, No. 1, pp47-49, January 2000.

[24] Bulow, H., Operation of Digital Optical Transmission System with Minimal Degradation Due to Polarization Mode Dispersion, Electronics Letters, Vol. 31, No. 3, pp214-215, Feb. 1995.

[25] Griffiths, Peter R. and Haseth, James A. de, Fourier Transform Infrared Spectrometry, John Wiley & Sons, New York, 1986.

[26] Mattson, David R., Sensitivity of a Fourier Transform Infrared Spectrometer, Applied Spectroscopy, Vol. 32, No. 4, pp335-338, 1978.

[27] Loudon, R., The Quantum Theory of Light, second edition, Clarendon press, oxford, pp10, 1983.

[28] Borodovski, P. A. etc., Microwave Technique for Measurement of Electron Mobility in P-$Ca_xHg_{1-x}Te$, Infrared Physics and Technology, Vol. 37, pp513-515, 1996.

[29] Lang, Weihe etc., TiP-seeding Technique Applied in Bulk Growth of HgCdTe, Laser & Infrared, Vol. 23, No. 6, pp37-39, 1993.

[30] Lu, Chunsheng, Photoelectric Detection Technique and Applications (in Chinese), Science and Technology press, 1992.

[31] Nemirovsky, Y. etc., Trapping Effects in HgCdTe, Journal of Vacuum Science and Technology, Vol. B10, pp1602-1610, 1992.

[32] Tang, Dingyuan, The Present Status of the Development of Infrared Detectors, Laser and Infrared, Vol. 21, No.1, pp5 - 11, 1995.

[33] Whidden, T. K., Private Communication. 1997.

[34] Saito, Mitsunori and Kikuchi, Katsuhiro, Infrared Optical Fiber Sensors, Optical Review, Vol. 4, No. 5, pp524-538, 1997.

[35] Kinslow, Roy H. Amorphous Materials Inc., 1991. (http://amorphousmaterials.com/As_S.htm).

[36] Technical data sheet from Galileo Corp., Galileo Park, P. O. Box 550, MA, USA, 1998.

[37] Technical data sheet from CeramOptec Industries Inc. 515 A Shaker Road, East Longmeadow, MA, USA, 1998.

[38] Friebele, E. J., Long, K. J., Askins, C. G., Gingerich, M. E., Marrone, M. J., and Griscom D. L., Overview of Radiation Effects in Fiber Optics. Proc. of SPIE. Vol. 541, Radiation Effects In Optical Materials, pp70-88, 1985.

[39] Griscom D. L., Nature of Defects and Defect Generation in Optical Glasses. Proc. of SPIE. Vol. 541, Radiation Effects In Optical Materials, pp38-59, 1985.

[40] Berghmans, F., Deparis, O., Coenen, S., and Decreton M., Optical Fibers in Nuclear Radiation Environments. O.D.D. Soares (ed), Trends in Optical Fiber Metrology and Standards. pp131-156, 1995.

[41] Kyoto, M., Chigusa, Y., Ohe, M., Go, H., Watanabe, M., Matsubara, T., Yamamoto, T., and Okamoto, S., Gamma-Ray Radiation Hardened Properties of Pure Silica Core Single-Mode Fiber and Its Data Link System in Radioactive Environments, Journal of Lightwave Technology, Vol. 10, No. 3, pp289-293, 1992.

[42] Deparis, O., Megret, P., Decreton, M., and Blondel, M., The Radiation-Induced Absorption Band at 600nm and Its Impact in Fibroscopy. Proc. RADECS'95, pp507-511, 1995.

[43] Bueker, H., Haesing, F. W., Physical Properties and Concepts for Applications of Attenuation-Based Fiber Optic Dosimeters for Medical Instrumentation, Proc.of SPIE. Vol. 1648, Fiber Optical Medical and Fluorescent Sensors and Applications, pp63-70, 1992.

[44] Fiore, L. D., Grado, A., and Russo, P., Fiberoptic Sensors for Radiation Dosimetry, Proc. of SPIE, Vol. 2360, pp580-583, 1994.

[45] Henschel, H., Kohn, O., Metzger, S., Decreton, M., Devos, P., and Deparis, O., Neutron Fluence and Dose Measurements by Optical Fibers, 5th International Conference on Applications of Nuclear Techniques, 1996.

[46] Bueker, H., Gripp, S., and Haesing, F. W., "Temperature Effects of Fiber-Optic Dosimeters for Radiotherapy", Proc. of SPIE, Vol. 1572, pp410-413, 1991.

[47] Griscom, D. L, Friebele, E. J., and Long, K. J., Fundamental Defect Centers in Glass: Electron Spin Resonance and Optical Absorption Studies of Irradiation Phosphorus-Doped Silica Glass and Optical Fibers. Journal of Applied Physics, Vol. 54, No. 7, pp3743-3762., 1983.

[48] Griffiths, Peter R., Interferometers vs Monochromators: Separating the Optical and Digital Advantages, Applied Spectroscopy, Vol. 31, No. 6, pp485-495, 1977.

[49] Eyal Ophir, private communication, 1997.

[50] Anoikin, E. V., Mashinsky, V. M., Neustruev, V. B., Sidorin Y. S., Effects of Exposure to Photons of Various Energies on Transmission of Germanosilicate Optical Fiber in the Visible to Near IR Spectral Range. Journal of Non-crystalline Solids. Vol. 179, pp243-253, 1994.

[51] Griscom D. L., γ-Ray-Induced Optical Attenuation in Ge-Doped-Silica Fiber Image Guides. Journal of Applied Physics, Vol. 78, No. 11, pp6696-6704, 1995.

[52] Deparis, O., Megret, P., Decreton, M., and Blondel M., Gamma Radiation Tests of Potential Optical Fiber Candidates for Fibrscopy. IEEE Transactions on Nuclear Science, Vol.43, No. 6, pp3027-3031, 1996.

[53] Agrawal, Govind P., Fiber Optic Communication Systems, second edition, sections 1.3 and 1.4, John Willey & Sons, Inc, New York, 1997.

[54] Agrawal, Govind P., Fiber Optic Communication Systems, second edition, section 8.6, John Willey & Sons, Inc, New York, 1997.

[55] Agrawal, Govind P., Fiber Optic Communication Systems, second edition, sections 2.2, John Willey & Sons, Inc, New York, 1997.

[56] Poole, C.D., Tkach, R.W., Chraplyvy, A. R., and Fishman, D. A., Fading in Lightwave Systems due to Polarization-Mode Dispersion, IEEE Photonics Technology Letters, Vol. 3, pp68-70, 1991.

[57] Derickson, D., editor, Fiber Optic Test and Measurement, Hewlett-Packard Company, 1998.

[58] Jones, R. C., A New Calculus for the Treatment of Optical Systems, Journal of the Optical Society of America, Vol. 31, pp488-493, 1941.

[59] Heffner, B. L., Automated Measurement of Polarization Mode Dispersion Using Jones Matrix Eigenanalysis, IEEE Photonics Technology Letters, Vol. 4, pp1066-1069, 1992.

[60] Gisin, H., Vonder Weid J. P. and Pellaux, J. P., Polarization Mode Dispersion of Short and Long Single-Mode Fibers, IEEE Journal of Lightwave Technology, Vol. 9, pp821-827, 1991.

[61] Poole, C. D., Winters, J. H., and Nagel, J. A., Dynamical Equation for Polarization Dispersion, Optics Letters, Vol. 16, No. 6, pp 372-374, March 15, 1991.

[62] Wang, D and Menyuk, C. R., Calculation of Penalties Due to Polarization Effects in a Long-Haul WDM System Using a Stokes Parameter Model, Journal of Lightwave Technology, Vol. 19, No. 4, pp487-494, April 2001.

[63] Forno, A. O. Dal, Paradisi, A., Passy, R., and von der Weid, J. P., Experimental and Thoretical Modeling of Polarization-Mode Dispersion in Single-Mode Fibers, IEEE Photonics Technology Letters, Vol. 12, No. 3, pp296-298, March 2000.

[64] Curti, F., Daino, B., Mao, Q., and Matera, F., Concatenation of Polarization Dispersion in Single-Mode fibers, Electronics Letters, Vol. 25, No. 4, pp290-291, 1989.

[65] Poole, C. D., Measurement of Polarization-Mode Dispersion in Single-Mode Fibers with Random Mode Coupling, Optics Letters, Vol. 14, No. 10, pp523-525, May 1989.

[66] Eickhoff, W., Yen Y., and Ulrich R., Wavelength Dependence of Birefringence in Single-Mode Fibers, Applied Optics, Vol. 20, No. 19, pp3428-3435, October 1981.

[67] Ulrich R., Simon, A., Polarization Optics of Twisted Single-Mode Fibers, Applied Optics, Vol.18, No. 13, pp2241-2251, July 1979.

[68] Bhatti, M. A., and Siddiqui, A. S., Measurement of Polarization Dependent Loss in Optical Fiber and Bulk Optical Devices, Proc. Of OFMF,95, 3rd Optical Fiber Measurement Conference, Liegi, Belgium, pp25-26, Sept., 1995.

[69] Mihailov, S. J., Walker, R. B., Stocki, T. J., and Johnson, D. C., Fabrication of Tilted Fiber-Grating Polarization-Dependent Loss Equalizer, Electronics Letters, Vol. 37, No. 5, pp284-286, March 2001.

[70] Ducos L., Clin, R., Blanchard, P., and Gautier, F., Polarization Dependent Loss of Passive Optical Components, Proc. Of OFMF,95, 3rd Optical Fiber Measurement Conference, Liegi, Belgium, pp25-26, Sept., 1995.

[71] El Amari, A., Gisin N., Perny, B., Zbinden, H., and Zimmer, C. W., Statistical Prediction and Experimental Verification of Concatenation of Fiber Optic Components with Polarization Dependent Loss, Journal of Lightwave Technology, Vol. 16, No. 3, pp332-339, March 1998.

[72] Shieh, W., Principal States of Polarization for an Optical Pulse, IEEE Photonics Technology Letters, Vol. 11, No. 6, pp677-679, 1999.

[73] Menyuk, C. R., Wang, D., and Pilipetskii, A. N., Repolarization of Polarization-Scrambled Optical Signals Due to Polarization Dependent Loss, IEEE Photonics Technology Letters, Vol. 9, No. 9, pp1247-1249, 1997.

[74] Curti, F., Daino, B., De Marchis, G. and Matera, F., Statistical Treatment of the Evolution of the Principal States of Polarization in Single-Mode Fibers, Journal of Lightwave Technology, Vol.8, No. 8, pp1162-1166, 1990.

[75] Chen, L., Yanez, M., Huang, C., and Bao, X., Pulsewidth Compression in Optical Components with Polarization Mode Dispersion Using Polarization Control, Journal of Lightwave Technology, Vol. 19, No. 6, pp830-836, 2001.

[76] Foschini, G. J., Jopson, R. M., Nelson, L. E., and Kogelnik, H., The Statistics of PMD-Induced Chromatic Fiber Dispersion, Journal of Lightwave Technology, Vol. 17, No. 9, pp1560-1565, September 1999.

[77] Djupsjobacka, A., Calculation of Signal Outage Due to Polarization Mode Dispersion, IEEE Photonics Technology Letters, Vol. 13, No. 7, pp660-662, 2001.

[78] Sunnerud, H., Karlsson, M., and Andrekson, P. A., A Comparison Between NRZ and RZ Data Formats with Respect to PMD-Induced System Degradation, IEEE Photonics Technology Letters, Vol. 13, No. 5, pp448-450, May 2001.

[79] Nelson, L. E., Nielsen, T. N. and Kogelnik, H., Observation of PMD-Induced Coherent Crosstalk in Polarization_Multiplexed Transmission, IEEE Photonics Technology Letters, Vol. 13, No. 7, pp738-740, July 2001.

[80] Agrawal, Govind P., Fiber Optic Communication Systems, second edition, section 8.6, John Willey & Sons, Inc, New York, 1997.

[81] Agrawal, Govind P., Fiber Optic Communication Systems, second edition, section 8.1, John Willey & Sons, Inc, New York, 1997.

[82] Agrawal, Govind P., Fiber Optic Communication Systems, second edition, section 4.5, John Willey & Sons, Inc, New York, 1997.

[83] Chen, C. J., System Impairment Due to Polarization Mode Dispersion, OFC'99, WE2, 1999.

[84] Ciprut, P., Gisin, B., etc, Second-Order Polarization Mode Dispersion Impact on Analog and Digital Transmissions, Journal of Lightwave Technology, Vol. 16, No. 5, pp757-771, May 1998.

[85] Foschini, G. J., Nelson, L. E., Jopson, R. M., and Kogelnik, H., Probability Densities of Second-Order Polarization Mode Dispersion Induced Polarization Dependent Chromatic Fiber Dispersion, IEEE Photonics Technology Letters, Vol. 12, No. 3, pp293-295, March 2000.

[86] Khosravani, K., and Willner A. E., System Performance Evaluation in Terrestrial Systems with High Polarization Mode Dispersion and the Effect of Chirp, IEEE Photonics Technology Letters, Vol. 13, No. 4, pp296-298, April 2001.

[87] Poole, C.D. and Giles, C. R., Polarization-Dependent Pulse Compression and Broadening Due to Polarization Dispersion in Dispersion-shift Fiber, Optics Letters, Vol. 13, pp155-157, 1988.

[88] Bruyere, F., Impact of First- and Second-order PMD in Optical Digital Transmission Systems, Optical Fiber Technology, Vol. 2, pp.269-280, 1996.

Vita

Candidate's full name: Ping Lu

Universities attended:

Jilin University (Changchun, China)
B.Sc. (Physics) 1984 - 1988
M.Sc. (Physics) 1988 - 1991

University of New Brunswick
(1997-1999)
University of Ottawa (transferred from UNB)
(1999-2001)

Publications:

Journal Papers

David Waddy, **Ping Lu**, Liang Chen and Xiaoyi Bao, Fast State of Polarization Changes in Aerial Fiber under Different Climate Conditions. ***IEEE Photonics Technology Letters***, Vol. 13, No. 9, Sept., 2001, P1035-1037.

Ping Lu, Liang Chen and Xiaoyi Bao, Polarization Mode Dispersion and Polarization Dependent Loss for a Pulse in Single Mode Fibers. ***J. of Lightwave Technology***, Vol. 19, No. 6, June, 2001, P856-860

Ping Lu, Liang Chen and Xiaoyi Bao, Statistical Distribution of Polarization-Dependent Loss in the Presence of Polarization-Mode Dispersion in Single-Mode Fibers, ***IEEE Photonics Technology Letters***, Vol. 13, No. 5, May, 2001, P451-453

Ping Lu, Xiaoyi Bao, Kellie Brown and Narayan Kulkarni, Gamma-induced Attenuation in Normal Single-and Multi-Mode, Ge-doped and P-doped Optical Fibers: A Fiber Optic Dosimeter for Low Dose Levels, ***Canadian Journal of Physics,*** Vol. 78, 2000, P.89-97

Ping Lu, Xiaoyi Bao and Tom Whidden, Application of a Mid-Infrared Fiber Bundle in Remote Measurement of Gas Concentrations in a Chemical Vapor Deposition Chamber, ***Applied Optics,*** Vol. 39, Is.7, March 1, 2000, P1112-1117.

Ping Lu, Xiaoyi Bao, Narayan Kulkarni and Kellie Brown, Gamma Ray Radiation Induced Visible Light Absorption in P-doped Silica Fibers at Low Dose Levels. ***Radiation Measurements***, Vol.30, Is. 6, P725-733, 1999.

Conferences

Ping Lu, Liang Chen and Xiaoyi Bao, Pulse Width Dependence of Polarization Mode Dispersion and Polarization Dependent Loss for a Pulse and Their Impact of Pulse Broadening, ***OFC'2001***, ThA6, 2001.

David Waddy, **Ping Lu**, Liang Chen and Xiaoyi Bao, The Measurement of Fast State of Polarization Changes in Aerial Fiber, ***OFC'2001***, ThA3

Ping Lu, Liang Chen and Xiaoyi Bao, Principal States of Polarization for an Optical Pulse in the Presence of Polarization Mode Dispersion and Polarization Dependent Loss, 2000 International Conference on Applications of Photonic Technology (ICAPT'2000), June 12-16, 2000, Quebec City, Canada.***Proc. of SPIE***, pp372-378, 2000

Ping Lu, Xiaoyi Bao and Tom Whidden, Mid_IR Fiber Bundles for Remote Monitoring and Control of Chemical Processing in a CVD Chamber. ***Proc. of SPIE***, Vol. 3849, 1999. P67-73.

Ping Lu, Xiaoyi Bao and Tom Whidden, Mid_IR Reflector for Enhancing the Light Collection of FTIR Spectrometer in Gas Concentration Monitoring. ***Proc. of SPIE***, Vol. 3859, 1999, P63-66.

Narayan Kulkarni, **Ping Lu**, Xiaoyi Bao and Kellie Brown, Characterization of A Miniature Fiber Optic Detector for Radiation Therapy, 45th Annual Scientific Meeting, ***Canadian Organization of Medical Physicists***, June 16_19, 1999, P26-28.

Ping Lu, Xiaoyi Bao, Narayan Kulkarni , and Kellie Brown, Experimental Study of Optical Fibers for the Application of Fiber Radiation Sensor, ***Proc. of SPIE***, Vol. 3534, p510-518, 1998.

Xiaoyi Bao, **Ping Lu** and Tom Whidden, A Novel Way of Improving the Collection Efficiency and Image Quality of Globar to Mid-IR fibers, ***Proc. of SPIE***, vol. 3416, p213-219, 1998.

Patents

Tom Whidden, Sun Yong Lee, Xiaoyi Bao, **Ping Lu**, Jim Taylor, Apparatus and Method for Infrared Light Transmission and System and Method for Infrared Analysis of the Fluid, 1999 (US09/415,395)